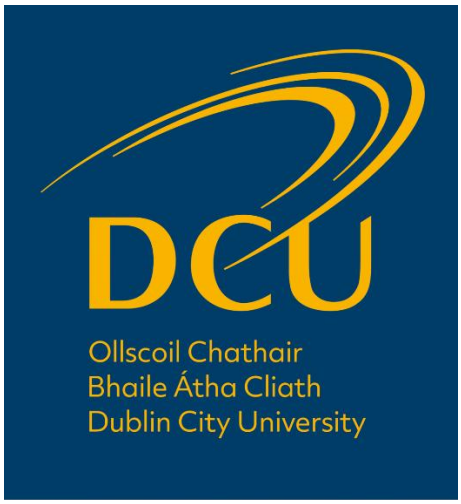

Versatile Cell Membrane Models: Biomimetic Suspended Lipid Bilayers designed for protein/DNA membrane dynamics and detection

---

A thesis submitted to Dublin City University for the award of PhD,

by

Guilherme Berselli, M.Sc.

Under the supervision of Prof. Tia E. Keyes

School of Chemical Sciences

Dublin City University - Dublin, Ireland

July 2021

Declaration

I hereby certify that this material, which I now submit for assessment on the programme of study leading to the award of PhD is entirely my own work, that I have exercised reasonable care to ensure that the work is original, and does not to the best of my knowledge breach any law of copyright, and has not been taken from the work of others save and to the extent that such work has been cited and acknowledged within the text of my work.

Signed: 

ID No.: _____16210727_____

Date: _____03/09/2021_____

Acknowledgements

First and foremost, I would like to thank my supervisor Prof. Tia E. Keyes and the Science Foundation Ireland, under the grant number 14/IA/2488, for giving me the opportunity to be one of her PhD's students, for her support, encouragement and time over the years. Thank you so much, Tia.

I would like to extend my gratitude to the staff of the School of Chemical Sciences, people which without their help my time at DCU would never been as good as it was. I would like to thank Ambrose for his assistance and great humour every day at the hatch and for saving me every time I needed! Also, I would like to thank the amazing staff that used to support me during my demonstration duties. Thank you John, Vinnies, Catherine and Damien for all the superb atmosphere you always brought to the labs, and for the great work in preparing and organising the undergraduate labs. I would like to extend my gratitude to Veronica, chief of the technical staff, for her extreme professionalism and for being a fantastic supervisor during my Teaching Assistant role. I really appreciate all help and time you spent with us during meetings and looking forward our duties. Thank you Veronica! Last but not the least, I can't forget to mention Dr. Aoife Morrin for getting me on her group as a Research Assistant while I was preparing for my Viva. Thanks Aoife, it was a fantastic experience working with you! I wish you and your group all the best!

I would like to thank Tia Keyes' group for all their help, from past to present. I would start by the person how introduced me to the fantastic world of FCS: Siva, thank you so much for your patience and knowledge and for teaching me the basics I needed to walk by myself though the fantastic lipidland. I really appreciate your time and effort during those afternoons in the laser room re-aligning the lasers on the microscope. Also, thank you Sean for introducing me to the world of lipids and how to use the LB. Thanks Nirod for introducing me to the great world of electrochemistry. Kho, I will never forget your enthusiasm and curiosity about science and research. Without a question, those are the best values a scientist can pass to others! Thank you guys for the trainings, discussions and learning you gave me. I would have never get to here without those unvaluable moments. I extend my gratitude to the PhDs at Keyes' group, again past to present: Agata, Jack, John, Karmel, David, Darragh, Aisling, Aurelien, Chris, Kho, Rubin, Rhianne and Amarutha. Cheers lads, in a way or another you all contributed to this.

During my PhD I got the opportunity to work, collaborate and socialize with people from different research groups, which all add something nice to me. Thanks to all of PhDs in the Chemistry department that I could meet, talk or have a laugh during the coffee morning, the casual pints, chemistry days or sports days! Colm, thanks for the weekends we end up together in the laser room. Liam, cheers for being a such a great lad. Sinead and Brionna, always good craic when you are passing by Nubar and are welcome to grab a drink with you! Thanks Peter for organising the clay pigeon shooting club in DCU, that was always fun! The football lads, from past to present, thank you for those lovely winter matches that made the pints after a game pay the price for the cold and the pouring rain. Thank you guys, I can't nominate all amazing people I met in DCU but I definitely remember you all.

I would extend my gratitude to those people that were there with me at some memorable moments. It is hard to nominate those legends but let's start with the Goldenboi. Dr. Aurelien "goldenboi' Gimenez! I could say here that you are a fantastic scientist, unvaluable for the group, that your patience in training people or your effort to develop new techniques for the group were, without a question, key elements that I could benefit to progress and progress to end up with a great PhD! Or even that the experience we exchanged at every discussion made me grow as a scientist and that I learn unvaluable things from you. But I won't. I will talk about the lovely and great person you are! That being with you was like being in a sunny Montpellier. That you could understand me when no one else would! That talking to you was never a problem, it was always a pleasure! Merci bien l'ami, on se retrouvera certainement dans un endroit ensemble! Ca ira le Gimenez-Berselli mec! Merci de m'avoir aidé tout au long de mon doctorat con, sérieux mec t'es une étoile d'or!

Next, I would like to point out another great scientist I had the pleasure to share my work with. The big RuRu chief, Dr. Chirstopher Burke. Lad, it is hard to mention the uncountable moments you made me laugh or when you just listen to me talking about my work, life, football... I don't need to mention the fantastic moments around pints, oh dear there were a few, or beer festivals, for introducing me to the fantastic world of craft beers and whiskey! I regret I couldn't do the same to you regarding wine but I believe you'll get there at some point! For being a great football player, for teaching me chemistry, for teaching me that and ah sure look it's just the taste! Cheers lad! Ah and the Dr. Steve Lyons, the Sligoboi! Thank you so much for your friendship, Steve! I will never

forget that since my first day in Ireland you were there to cheer me up! Thanks for showing me the another nice part of Ireland, your hometown and your family. That was some St. Pats. From all those moments lads I can say: we had to put time and effort to build this friendship together. And it was worthed. It really was! Cheers lads!

Finally, to my lovely close family in Ireland, Poland and Brazil. I can't start without saying thank you to one of the best person I ever met. Eithne, I can't say enough about what a brilliant person you are! Clever (and clever clogs), kind and always with a great sense of humour, you made my life in Ireland brighter. Thank you for all the great moments we had together, all the good times laughing and singing and playing with Bailey. I learnt so much with you that I can't even say it! Thanks Chief! You are a legend! To my love, Kasia, for supporting me throughout the years, for being with me every time I needed support, for embarking on this adventure together till the end. Thank you so much for bringing balance to my life! Love you lots! And to my family, that even from a distance always believed that this chapter of my life will end well. And it did! Cheers to my brother Renato and to my sister Priscila that came to visit me during my PhD. Renato, ainda temos muito que visitar por aqui, estou esperando a próxima viagem! Pri e Du, espero que vocês tenham aproveitado bem Londres. E que show aquele ein, Bob Dylan e Neil Young, quem diria! Mae e Pai, amo muito vocês! Saudade incalculável!

Research output

Publications

O'Connor, D., Byrne, A., Berselli, G., Long, C., Keyes, T.E. Mega-Stokes Pyrene Ceramide Conjugates for STED Imaging of Lipid Droplets in Live Cells. *Analyst*. 2019, 5, 3671-3682.

Berselli, G. B., Sarangi, K. N., Ramandurai, S., Murphy, P. V., Keyes, T. E. Microcavity-Supported Lipid Membranes: Versatile Platforms for Building Asymmtric Lipid Bilayers and for Protein Recognition. *ACS Appl. Bio Mater*. 2019, 2, 8, 3404-3417.

Robinson, J., Berselli, G. B., Ryadnov, M. G., Keyes, T. E. Annexin V Drives Stabilization of Damaged Asymmetric Phospholipid Bilayers. *Langmuir*. 2020, 36, 5454-5465.

Berselli, G. B., Sarangi, K. N., Gimenez, A. V., Murphy, P. V., Keyes, T. E. Microcavity Array Supported Lipid Bilayer Models of Ganglioside – Influenza Hemagglutinin$_1$ binding. *Chemical Communications.* 2020, 56, 11251-11255.

Berselli, G. B., Gimenez, A. V., O'Connor, A., Keyes, T. E. A Robust Photoelectric Biomolecular Switch at a Microcavity Supported Lipid Bilayer. Submitted, 2021.

Kho, K. W., Berselli, G. B., Keyes, T. E. A nano-plasmonic assay of oligonucleotide-cargo release from cationic lipoplexes. Small, 2021, 2005815.

Berselli, G.B., Sarangi, N. K., Robinson, J., Dransart, E., Zadah, M. S., Ludger, J., Keyes, T. E. Gal3 targets the inactive α5β1 integrin to oligomerize and trigger membrane reorganization in a GSLs-dependent manner. In preparation.

Oral Presentation

Science Foundation Ireland Mid-Term Project Review. "Microcavity-Supported Lipid Bilayers as a versatile tool to study protein-GSL binding and aggregation". Oral presentation. September 2018, DCU, Dublin, Ireland.

Chemical Research Symposium. "Building a biomolecular machine using Microcavity Supported Lipid Bilayers". Oral presentation. June 2020, DCU, Dublin Ireland.

Poster Presentation

19th IUPAB and 11th EBSA Congress. "Biomimic domain forming cell membrane models for dynamic studies of cholera toxin interactions". Poster presentation. July 2017, Edinburgh, Scotland.

Thesis Publication

Chapter	Title	Status	Authors	Contribution
2	Microcavity-Supported Lipid Membranes: Versatile Platforms for Building Asymmtric Lipid Bilayers and for Protein Recognition	*ACS Appl. Bio Mater*. 2019, 2, 3404-3417	Berselli, G. B., Sarangi, K. N., Ramandurai, S., Murphy, P. V., Keyes, T. E.	Manuscript primary author. Primary contributor to experimental design and execution
3	Microcavity Array Supported Lipid Bilayer Models of ganglioside-Influenza Hemagglutinin Binding	*Chem. Commun.,* 2020, 56, 11251-11254	Berselli, G. B., Sarangi, K. N., Gimenez, A. V., Murphy, P. V., Keyes, T. E.	Co-author of manuscript. Primary contributor to experimental design and execution
4	Photoelectrical activity of biomolecular switch reconstituted at fluidic Microcavity-Array Supported Lipid Bilayers	*Appl. Mat. Int.* Submitted Fev. 2021.	Berselli, G. B., Gimenez, A. V., O'Connor, A., Keyes, T. E.	Manuscript primary author. Primary contributor to experimental design and execution
5	A NanoPlasmonic Assay of Oligonucleotide-Cargo Delivery from Cationic Lipoplexes	Small, 2021, 17, 12, 2005815	Kho, K. W., Berselli, G. B., Keyes, T.E.	Co-author of manuscript with Dr. K. W. Kho. Designed and executed experimental lipoplex characterization. Conducted FLCS, FLCCS and FLIM experiments and analysis.

Signed: ---------- ----------

Candidate Supervisor

03/09/2021

Date

Table of Contents

Guilherme Berselli

Versatile Cell Membrane Models: Biomimetic Suspended Lipid Bilayers designed for protein/DNA membrane dynamics and detection

Thesis Abstract

The cell membrane, comprised mainly of phospholipid, sphingolipids, sterols and proteins, is a complex, but molecularly ordered, semi-permeable barrier between the intracellular and extracellular environments. It plays a vital role in cell adhesion, signalling and transport. To understand its functions, in many cases to reduce experimental complexity in the study of lipids and proteins several model membrane systems have been developed in the past years. This thesis explores the application of one such model Microcavity-Supported Lipid Bilayers, or MSLBs, as a versatile platform for the preparation and the study of asymmetric lipid bilayers containing gangliosides. The overall objective of the thesis is therefore to explore the application of microcavity supported lipid bilayers and their use as versatile platforms to the preparation of highly fluidic lipid membranes to study important biophysical aspects of membranes such lipid asymmetry, protein-binding, protein incorporation to suspended lipid membranes and protein aggregation. In addition, the lipid bilayers spanned over microcavity arrays were used as a model for oligonucleotide endosomal escape from cationic lipoplexes.

Chapter 1 describes the background to this work and overviews the current state of the art in model membranes. In chapter 2, describes experimental studies at the MSLBs to evaluate fluidity of symmetric and asymmetric lipid bilayers in parallel with an interrogation of binding of Cholera Toxin subunit b (CTb) to its receptor GM1. It was found that transmembrane asymmetry affects the lipid bilayer fluidity in MSLBs. The lateral clustering of CTb was observed at the nanomolar range in fluidic and gel-phase membranes. As will be discussed, the high lateral fluidity of the MSLBs along with their multimodal addressability makes them really well suited to building both asymmetric bilayers, in analogy to the real cell membrane. And in particular to the study of aggregation processes involving lateral movement of lipid and/or membrane protein. Aggregation

is a feature of a number of key biological processes including infection and, in this work, MSLBs are applied to two infection models: cholera toxin and in chapter 3 hemagglutinin.

In chapter 3, the binding of hemagglutinin (HA1) from influenza virus was demonstrated to be dependent on the type of ganglioside and on the lipid bilayer composition. The affinity of three glycolipids GDa1, GM1 and GM3 for the subunit HA1 suggested that GDa1 showed highest affinity at DOPC bilayers, even though the diffusivity of GDa1-HA1 complex was approximately half of that obtained for GM1 and GM3-HA1 complexes suggesting differences in HA1 assembly dimensions or penetration into the lipid bilayer. Although the affinity of HA1 for GM1 appears unaffected by lipid bilayer composition, the lower mobility of HA1 in bilayers containing sphingomyelin and cholesterol suggests association with Lo domains. These results suggest that the affinity of HA1 is dictated by GSL and lipid membrane composition and might suggest that these characteristics could influence the target cell for influenza infection.

Another key advantage of MLSBs is that they offer a substantial aqueous volume above and below the lipid membrane and so unlike SLBs, can support both structurally and in terms of diffusion transmembrane proteins. Chapter 4, membrane protein reconstitution was explored using bacteriorhodopsin as a photo-active proton pump to create a simple photoresponsivity machine from MSLB focused on the insertion of a photo-activated proton pump, bacteriorhodopsin (bR), into artificial cavity-spanning lipid bilayers. It was found that the photo-activation of lipid bilayers containing bR generate an electric response, which is dependent on frequency of the transient photo-signal and environmental pH.

Chapter 5 expands the use of MSLBs and explores the use of MSLBs to study the delivery and release of oligonucleotide-cargo from lipoplexes to microcavities to stablish a proof-of-concept assay for oligonucleotide endosomal escape platform using SERS and FLCS. In order to mimic as close as possible a typic mammalian cell membrane, a quaternary membrane composition was used. It was found that the fastest oligonucleotide cargo release was obtained for the cationic lipoplexes comprised of DOTAP/DOPE. This indicates a new direction of the use of MSLBs to the study of nanocarrier gene delivery. Finally, chapter 6 focused on building a model of Galectin-3 (Gal3) binding to integrin α5β1 and to gangliosides. The insertion of α5β1 into MSLBs was used to determine its lateral diffusion coefficient and aggregation. It was found that Gal3 reorganizes

the spatial distribution of GSLs in an oligomerization-dependent manner, and the bounding of Gal3 to integrin leading to an increase in α5β1 mobility.

Chapter 1: Introduction

1.1. Lipid membranes: structural barrier of cells

The cell membrane is an ordered but complex semipermeable matrix, responsible for protecting the cell from its surroundings by separating the interior of the cell to its outside environment. Cell membranes are fluidic lipid bilayers which one of the key components of the membrane are phospholipids. Lipid bilayers are 3-dimentional structures formed by two layers of amphiphilic lipid and sterol molecules. The lipid molecules, or phospholipids, contain a hydrophilic polar head attached to a hydrophobic tail. To form a lipid bilayer, the tail regions, repelled by water, are attracted to each other, while the polar heads interact with the surround water molecules. Although lipid membranes may be seen as a simplistic design, they are essential structures for all cells and live organisms.

Over the years, different models were proposed to explain how lipid molecules are organised into lipid membranes. Initially, it was believed that the lipids would spontaneously arrange into lipid bilayers while proteins were adsorbed at the membrane. This was proposed as the Davson-Danielli model (1935), also known as the paucimolecular model, or "Sandwich model". The model describes a lipid bilayer as a hydrophobic zone containing a layer of proteins, and the hydrophilic zone, on each side of the membrane. The Davson-Danielli model assumed all membranes were uniform, with constant-protein ratio. Also, it was proposed that protein were static at the lipid matrix. The model was supported by electron microscopy images, showing two dark parallel lines, suggested as protein layers, with a lighter region in between, believed to be a lipid bilayer. However, much evidence was contrary to the model, for example membrane proteins were discovered to be insoluble in water, therefore it was not clear how forming an interfacial hydrophilic layer over the lipid bilayer was possible. In addition, fluorescence antibody tagging revelled that membrane proteins were not static, on the contrary, they were found to be mobile within the lipid membrane.

In light of these contradictions, the first model that describes the cell membrane as a complex two-dimensional fluid was proposed by Singer and Nicolson in 1972 (*Figure 1.1*). This model describes the phospholipid bilayer as two-dimensional homogenous mixture of diffusing molecules.[1] They proposed that lipids are held together by non-covalent forces with proteins embedded in the membrane as a "mosaic". This model addresses the main issues to arise from the "sandwich" model, therefore it was well accepted as a more realistic model of cell membrane behaviour. Since its introduction, the mosaic model has expanded to accommodate the evolving experimental and theoretical insights into the membrane particularly related to its complex organization. For instance, plasma membranes have a variable transversal lipid composition in which the lipid leaflets differ in composition.[2]

In addition, experimental observations have suggested that the lipid membrane is not a homogenous structure, but rather formed by a complex mixture of heterogeneous phases. In artificial membranes lipid phases, or domains, are dynamic molecular assemblies in constant formation and disruption within the lipid membrane. In disordered phases, lipids are in a more fluidic state. Ordered phases are well packed lipid rigid region enriched in sphingolipids and sterols. In biological membranes, the concept of lipid self-organization into dissimilar fluid domains was driven by two main experimental observations from cells. First, lipid residues enriched with sphingomyelin, cholesterol and membrane proteins were observed as insoluble fractions in non-ionic detergents, therefore called detergent-resist-membranes (DRMs), implying in heterogeneities of cells.[3–5] Second, the observation of macroscopic phase separation on biomimetic lipid mixtures.[6]

Phase transition of lipid models have been widely explored since 1970.[7] Recently the introduction of fluorescence techniques allowed to visualize lipid phase separation on artificial lipid models. Nowadays, lipid rafts are believed to serve as platform for proteins involved in multiple-cell actions, such signal transduction, membrane trafficking and cytoskeletal organization.[8] Although no evidence of rafts in cells, lipid models have shown this direction. Due to the nanoscale nature of lipid rafts it is very challenging to observe them in biological membranes. Although the high spatiotemporal resolution required to study nanoscale assemblies of lipids and proteins in living cells, many effort has been made to allow the direct observation of lipid segregation in vivo. [9] However, there is no direct evidence of lipid rafts in living cells.[10]

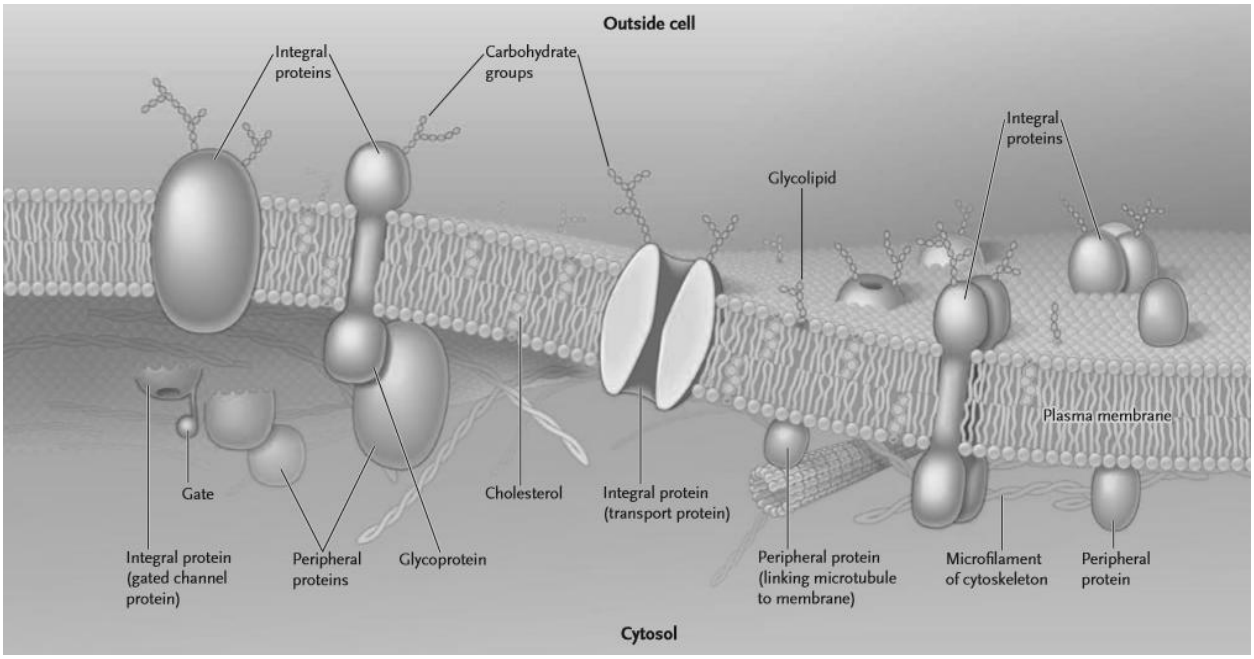

Figure 1.1. Illustration of the different components of the cell membrane. Figure reproduced from reference.[11]

1.2. The main components of the cell membrane

Cell membranes are composed of phospholipids, proteins, sterols and glycolipids. Each component plays a role structurally and functionally to the cell. For instance, while the phospholipids and sterols provide the structure of the lipid bilayer, membrane proteins and glycolipids are involved in cell signalling and trafficking. Phospholipids are amphiphilic molecules, containing a hydrophilic head group attached to two hydrophobic fatty acid chains. When phospholipids are exposed to aqueous environment, due to their amphiphilic nature, they spontaneously self-arrange such that their hydrophobic tails are repealed from the water and the hydrophilic polar heads are attracted to bulk milieu, resulting in the formation of micelles, vesicles or bilayers. In cells, the phospholipid membrane forms a stable barrier between the cytoplasm and the exterior of the cell. Proteins and glycolipids embedded to the membrane provide key functions, such junction, recognition and membrane transport.

1.2.1. Lipids

The main component of the cell membrane, amphiphilic lipids, are the building block of membranes, being responsible for its double layer structure. Two main properties of lipids influence the packing within the lipid membrane and have impact on lipid lateral diffusion. The carbon tail length and saturation. The shorter the faster it diffuses. The hydrophobic carbon tails usually consist of 14 to 24 carbons length, and the shorted the tail easier the lipid diffuses within the bilayer. Also, the extent of saturation of the hydrocarbon chains can influence the diffusion. One or more unsaturated, or double bonds in the hydrocarbon chain of the lipid increase the fluidity of the membrane due to the disruption of lateral interactions between the hydrophobic tails of surrounding lipids. In addition, the shape of lipids can affect the local curvature of the membrane. Lipids with conical shape may induce positive or negative membrane curvature and lipids with cylindrical shape tend to form planar membranes. There are thousands of naturally occurring phospholipids mostly divided into 2 main groups: glycerophospholipids and sphingolipids.

- Glycerophospholipids

Among lipids, the most abundant are Glycerophospholipids. A simple molecule such as choline, serine, glycerol or ethanolamine attach to a phosphate group to form the polar head group. The two fatty acid chains are covalently linked to the same phosphate group with a glycerol backbone to form the non-polar tail. Their structure is comprised of three carbon glycerol with two long fatty acid chains. The third carbon is attached to a hydrophilic head groups, such phosphatidylcholine (PC), phosphatidylethanolamine (PE), phosphatidylserine (PS), are the predominant phospholipids encounter in the membrane, phosphatidylinositol (PI) and cardiolipin are present in smaller quantities (*Figure 1.2*). The most abundant glycerophospholipids is PC therefore is the most used in artificial models of lipid membranes.

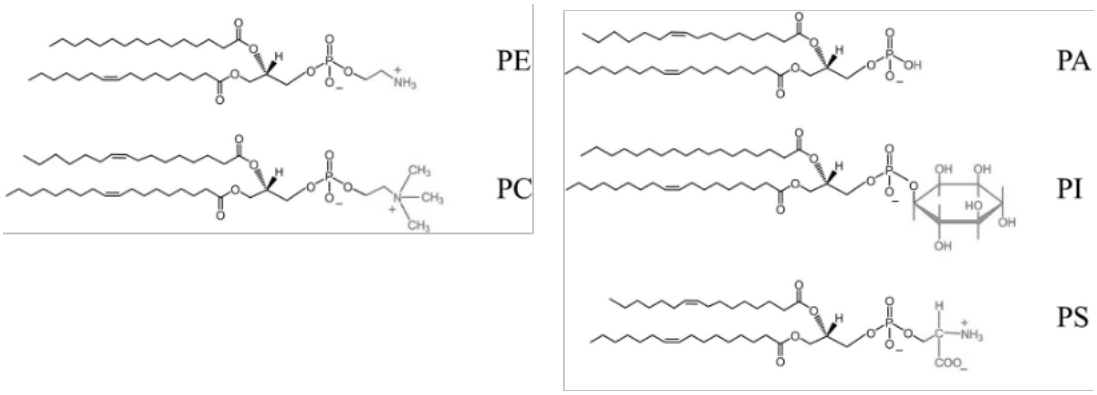

Figure 1.2. Molecular structure of most abundant glycerophospholipids.

- Sphingolipids

Another class of lipids are the sphingolipids, a large family where possession of a ceramide tail is a core feature. The main component of sphingolipids is sphingomyelin, which is formed by a sphingosine as a backbone (*Figure 1.3*). The presence of amide bridge and hydroxyl groups contributes to its headgroup polarity/amphiphilicity and facilitates formation of H-bonds with other proteins and lipids. The saturated ceramide tails promote the lateral packing of sphingolipids, therefore increasing its melting temperature.

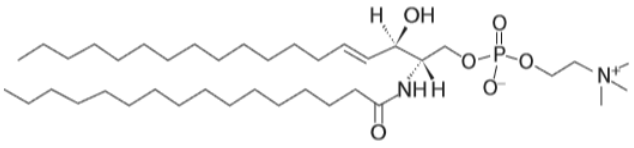

Figure 1.3. Structure of a sphingolipid, sphingomyelin.

- Glycosphingolipids

An important sub-category of sphingolipids are glycosphingolipids or GSLs, also known as gangliosides. GSLs exhibit a structure containing a sphingoid base, mostly sphingosine, attached to a glycan chain.[12] They are subdivided in four series of GLSs, according to the their biosynthesis,

resulting in different sialylated glycan chains, usually composed of 1-8 saccharides (*Figure 1.4*).[13] Found in the glycocalyx of cells, a layer enriched with glycolipids and glycoproteins, GSLs are mainly distributed in the extracellular leaflet of plasma membranes. GSLs are particularly more abundant expressed in the nervous system, constituting 5 to 10% of the lipid mass of brain cell membranes.[14] The most abundant gangliosides are GM1, GD1, and GT1 which represent more than 90% of GSLs in the brain of all mammals.[13]

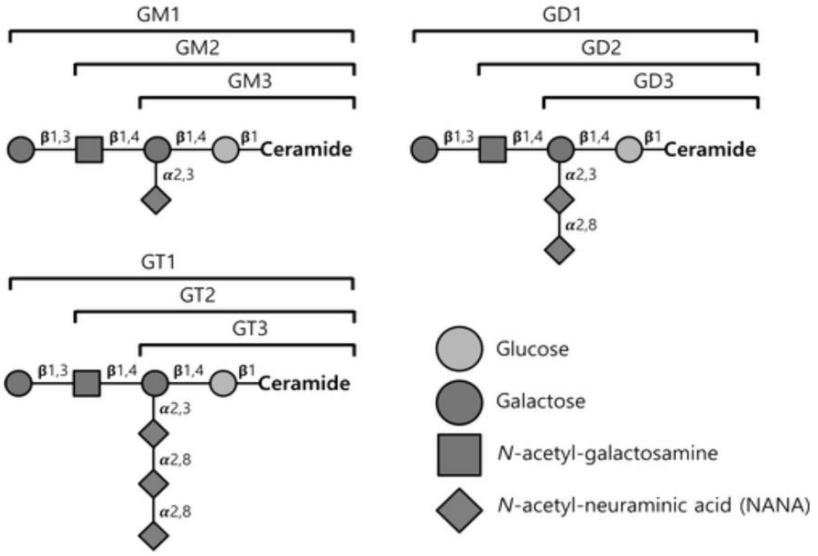

Figure 1.4. General structure of gangliosides commonly found in biological cells. Figure adapted from reference.[15]

GSLs are essential components of eukaryotic cells, playing an important role in many biological process, including mediating cell-cell interactions and protein-to-cell recognition through carbohydrate-carbohydrate or carbohydrate-protein interactions.[16] Also, GSLs may form clusters, or GSL-enriched microdomains (GEM), in presence of sphingomyelin and cholesterol, which could serve as floating platform for cell signalling and function.[17–19]

In addition, GSLs are receptors for microbial infection and toxins. The specific protein-carbohydrate recognition to GSLs is used by certain proteins to gain entry to the cell. For example, cholera toxin and shigella toxin associates with GM1 and Gb3, respectively, to bind to cell

membrane.[20–22] Viruses infections, such as Influenza virus, use glycans to mediate their attachment at cells via glycan binding due to carbohydrate-receptors in viral particles.[23] Influenza A viruses recognizes sialic acid residues of gangliosides in the cell membrane for invasion and infection of host cells through hemagglutinin-ganglioside binding.[12,24] Therefore, gangliosides are in important component of cell membranes with significant biomedical impact, which is discussed further in chapters 2 and 3.

1.2.2. Cholesterol

Cholesterol is the most abundant sterol found in cell membranes and is a major component of mammalian plasma membrane, comprised of up to 30% of mammalian plasma membranes.[25] Like many constituents of the membrane it is amphiphilic, comprised of four fused hydrocarbon rings with a non-polar aliphatic tail at one end and a polar hydroxyl group at the other end. Its planar and rigid structure to the molecule plays an important structural role in the plasma membrane (*Figure 1.5*).[26] Cholesterol is oriented in the membrane with the hydrophobic carbon tail embedded in the membranes and the hydroxyl group oriented to the ester carbonyl group of phospholipids. As well as its structural role cholesterol regulates membrane fluidity, compressibility, water penetration and curvature of lipid bilayers.[27]

Cholesterol influences the membrane fluidity of lipid bilayers by acting as a "membrane buffer" which modulates the fluidity of a lipid membrane. For example, when the cell faces an increase in temperature, the amount of cholesterol may increase in the membrane to balance the membrane fluidity. For example, at higher temperatures the intermolecular separation of lipids increases, which causes an increase in the membrane fluidity. Therefore, cholesterol can be inserted in between lipid molecules, felling intermolecular spaces, tightening the membrane to preserve the integrity of the membrane. On the other hand, at lower temperatures, cholesterol disrupt the molecular packing of tight packed lipids to maintain the necessary membrane fluidity for cell function.

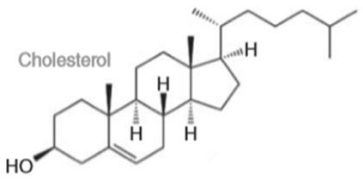

Figure 1.5. Structures of the predominant sterol in mammalian cells, cholesterol.

1.2.3. Membrane proteins

While lipids are responsible for the structure of the cell membrane, membrane proteins are the key active components that mediate the cell interaction with its surrounding environment. Proteins are responsible for many of the important cell functions, which include signalling and traffic, transport and anchoring the cell. In living cells, membrane proteins may contribute from 50 to 80% of the total weight of the lipid membrane.[28,29] Membrane proteins are characterised according to the nature of their assembly at the membrane, where they may be fully inserted, also known as integral proteins, or partially inserted, such peripheral proteins, as indicated in *Figure 1.6*.

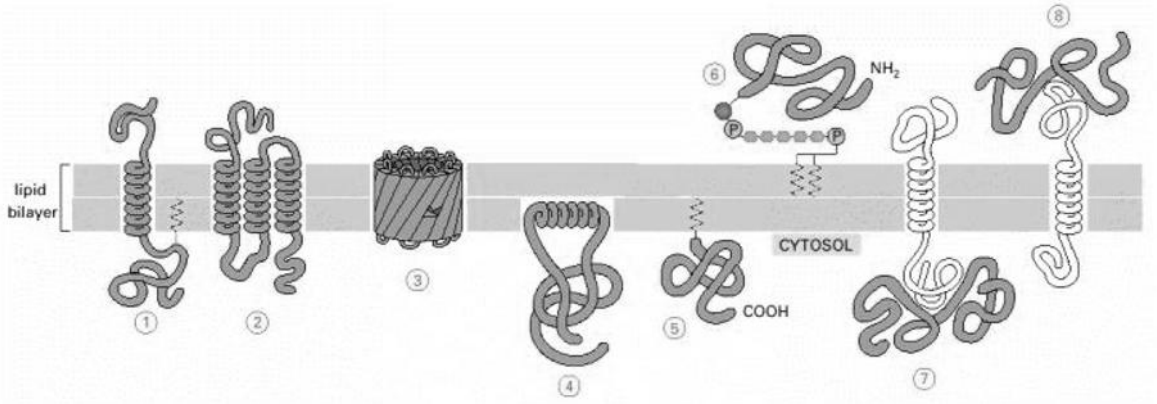

Figure 1.6 : Different types of proteins found at cell membranes. Full inserted proteins as single alpha helix (1), multiple alpha helices (2), or as rolled beta-sheets (3). Peripheral proteins can be anchored to the cytosolic surface (4), attached to lipid in the cytosolic monolayer (5), linked to phosphatidylinositol (6) or to other proteins (7), (8). Figure reproduced from reference.[30]

The activity of integral membrane proteins is usually dependent on the presence of a lipidic environment, which serve as a support, or 'solvent' to proteins. Some proteins may interact non-specifically with the bulk lipid bilayer, while others might have specific interactions to a small number of lipids in order to maintain protein activity, also called annular protein-lipid interactions. These interactions can be related to hydrophobic effects, hydrogen bonding or charge transfer and are related to protein orientation and function.[31] For example, it has been postulated that protein-lipid interactions can be crucial for correct insertion, folding and topology of membrane proteins.[32] studies have indicated that the presence of positively charged amino acids in cytoplasm region of proteins interact with negatively charged phospholipids and may help protein insertion to membrane and orientation.[33] For instance, anionic phospholipids, such PE, are required by LacY to maintain the active transport of lactose, due to topological orientation in presence of PE.[34] Similarly, MscL requires annular anionic phospholipids to stabilizes its open state, which can be disrupted in presence cationic/zwitterionic lipids.[35,36] In similar fashion, peripheral proteins may require specific lipid environment to function. An example are annexins that binds to the surface of lipid bilayers via negative lipids, such PS and PE, in a Ca^{2+} dependent manner.[37,38] Also, physical properties of lipid bilayers, such membrane fluidity or tension, are required guarantee lateral mobility to promote protein activity.[31] For example, due to their lateral mobility in a membrane, the linear peptide gramicidin self-assemble to form protein-pore complex (~ 4Å) forming ion channels that can accommodate the passage of monovalent cations.[39,40]

The lipid membrane is also required to aggregation of proteins. This is particularly important to multivalent proteins which are able to bind to more than one lipid receptor at the cell membrane, such Cholera Toxin (CT), Shiga Toxin (ST) and others.[20,21] CT cross-link with GM1 in order to promote stabilization and to facilitate protein uptake into cells.[41] After binding to one lipid molecule, the protein can diffuse within the lipid membrane to encounter other receptors, stabilizing the bound protein to promote cell infection.[42] This is discussed in Chapter 2. In addition, the initial complex formed by Amyloid-β peptide and GM1 oligomerizes leading to fibrils which are responsible for the formation of aggregates that triggers Alzheimer's disease.[43]

Overall, proteins are active parts of the cell membrane that requires the cell membrane in order to perform a certain activity. The next chapter will cover the main models used to mimic the cell

membrane to explore the properties of lipid membranes along with the assembly of peripheral and integral proteins.

1.3. Artificial models of the cell membrane

Cellular membranes are by nature complex, and the lipid diffusivity can be influenced by lipid-lipid interactions, domain formation, protein and cytoskeleton interactions.[44] To overcome the complexity of biological cells and gain access to the understanding of the structure and dynamics of biological membranes, artificial membrane models have been greatly used to determine the influence of lipid membrane composition, domain formation and other on the lateral mobility of lipids. Bioartificial models of the cell membrane are an important field of studies to provide more understanding about lipid dynamics and organization, and lipid-proteins interactions in a compositionally controlled system, separated from the very complex cell environment. Specifically, understanding the role of protein recognition by lipid membranes has an important value for disease, both for understanding unique processes in disease mechanisms involving membrane but also in devising therapy. Many components gain access to the cytoplasm by specific signalling processes at the cell membrane. This information is usually promoted by a particular receptor, typically mediated by proteins or glycolipids. However, due to the complexity of the cell membrane, one can be difficult to isolate and analyse a specific it many experimental approaches were developed during the last decades to address particular cell membrane properties.

To accurately evaluate protein-membrane interactions in artificial lipid bilayers, a fluidic membrane model is required to guarantee the natural mobility of lipids and protein receptors. This is particularly important in processes that involve aggregation or network formation due to the need for lateral mobility. In this context, suspended lipid bilayers have increasingly become of interest in biomimicry of membranes. In addition to that, the stability of the bilayer is crucial to promote protein reconstitution avoiding denaturation of the membrane. Currently, different lipid membrane models are being used to build artificial bilayers in vitro.

The most studied types of lipid membrane established for lipid membranes are lipid vesicles or liposomes, Black Lipid Membranes (BLMs) and SLBs. Recently, pore suspended lipid membranes have been introduced, expanding the possibilities to explore from different perspectives and

pushing further the limits of the lipid membranes understanding and applications. Despite the natural cell membrane asymmetry, most of the research concerning artificial models of the biological membrane relies on pure symmetric-lipid membrane models. Recently, techniques for producing asymmetric lipid bilayers along with computational simulations have provide compelling evidence that the lipid asymmetry does influence not only the dynamics of the lipids but also nano domains formation through domain registration. In lipid models recent effort have been seen toward the production of more stable asymmetric lipid bilayers, from a wide range of geometries which include supported lipid bilayers[45,46] and liposomes.[47,48]

1.3.1. Lipid Vesicles

Lipid vesicles or liposomes are one of the most widely used systems to mimic lipid bilayers. Liposomes are spontaneously formed after dispersion of lipids in water, making them easy to prepare.[49] Liposomes can be classified according to the size (small, large or giant) and lamellarity (uni- oligo-, and multilamellar vesicles).[50] The term "unilamellar" refers to a vesicle formed only by one lipid bilayer, which are the most commonly used on research. The size of liposomes can be controlled to form Small Unilamellar Vesicles (SUVs), Large Unilamellar Vesicles (LUVs), Giant Unilamellar Vesicles (GUVs) or Multilamellar Large Vesicles (MLVs) within the range of 100nm to several micrometres (*Figure 1.7*).

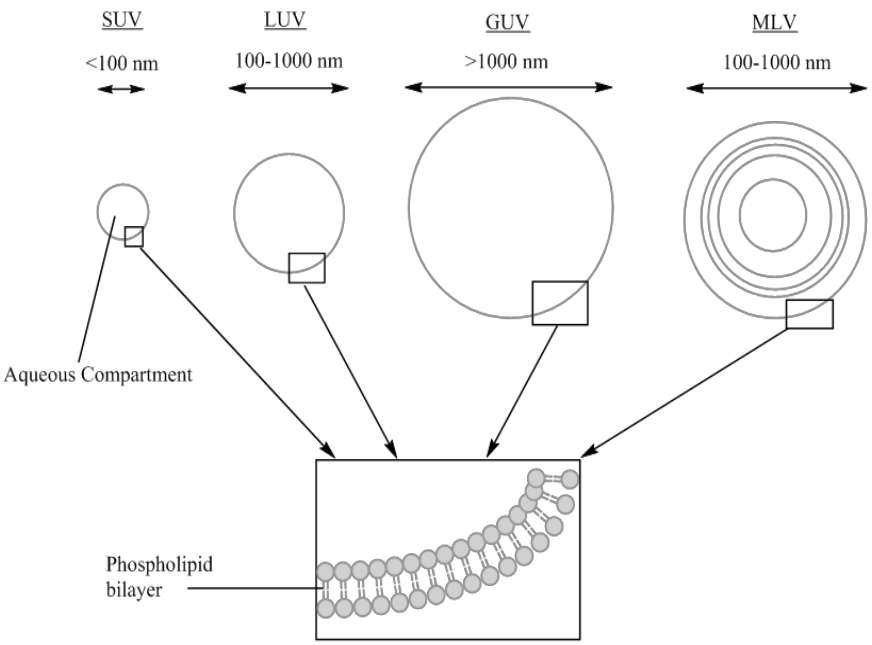

Figure 1.7. Schematic representation of the size distribution of liposomes.

- Small and Large Unilamellar Vesicles

In the recent years, several protocols of preparation of liposomes have been develop and optimized. Basically, the preparation can be divided in two main groups according to the starting materials, (a) from organic phase by transferring lipids from a solvent to an aqueous solution, and (b) from rehydration of a dried lipid film.[51] In this work, liposomes were prepared starting from a dried lipid film followed by a lipid vesicle resuspension to an aqueous solution as illustrated in *Figure 1.8*. The method involves solubilizing lipid molecules in an organic solvent, such chloroform, and posterior solvent evaporation. Phospholipid molecules self-assemble into a stack of bilayers on a substrate under solvent evaporation. On hydration, the dried bilayers separate from the substrate forming spherical liposomes.[52] This is obtained because phospholipids are poorly soluble in water unless they self-assemble into bilayers, excluding the hydrophobic tails from the bulk water phase. When exposed to water, lipid films tend to minimize the edge energy associated to the exposed hydrophobic tails by closing a spherical vesicle. The rate of rehydration affects the lamellarity of the liposomes. Usually faster hydration allow the formation of multilamellar vesicles.[51]

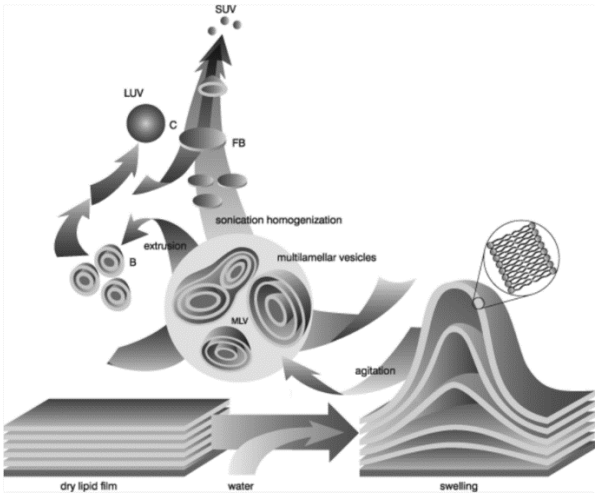

Figure 1.8. Mechanism of vesicle formation from dried lipid film to liposomes from a dried lipid film to resuspended liposomes. After addition of aqueous solution, MLVs are formed after mechanical agitation. In order to reduce lamellarity and size, MLVs are sonication or extruded to form SUVs/LUVs. Figure reproduced from reference.[53]

After resuspending liposomes in solution, a reduction on lamellarity and homogenization of size might be desirable. This can be important to a certain application of liposomes, for instance, multilamellar liposomes are less reactive in drug delivery and might aggregate or form multilayers when used to prepare supported lipid bilayers. The reduction of lamellarity can be obtained by subjecting liposomes to homogenization, sonication, extrusion or free-thaw cycles, which increase the control of the liposome size distribution. In this work, liposomes were prepared by extruding a solution of multilamellar vesicles through a polycarbonate membrane with specific pore dimensions (*Figure 1.9*).[52,54]

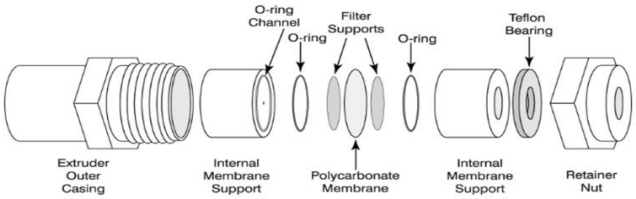

Figure 1.9. Apparatus used for liposomes extrusion. Obtained from Avanti Polar Lipids. Figure reproduced from reference.[55]

Due to its simple spheroid structure and relatively easy preparation, many applications of liposomes have emerged since their introduction in the early 1960s, including carriers for therapeutics in drug delivery and as artificial models of cell membranes to study physicochemical properties of lipids and proteins in a controlled manner. Also, due to good biocompatibility and biodegradability, lipid vesicles have been studied as carriers to medicine as platforms for drug delivery.[56] The closed volume of liposomes is suited for the encapsulation of hydrophilic drugs, particularly to those having poor solubility or with low absorption ability, which can be endocytosed by cells. The administration of liposomes-encapsulated drugs has certain advantages to the free administration of the active form of a drug with potential increase the therapeutic efficiency as the encapsulation of an active principle protects the therapeutic agent against enzymatic degradation and immunologic inactivation, which might lead to inactivation of the drug. In addition, in order to enhance their biological activity, liposomes can be functionalized with artificial, such PEGlated liposomes, or biological molecules , such antibodies or peptides, as shown in *Figure 1.10*.[57]

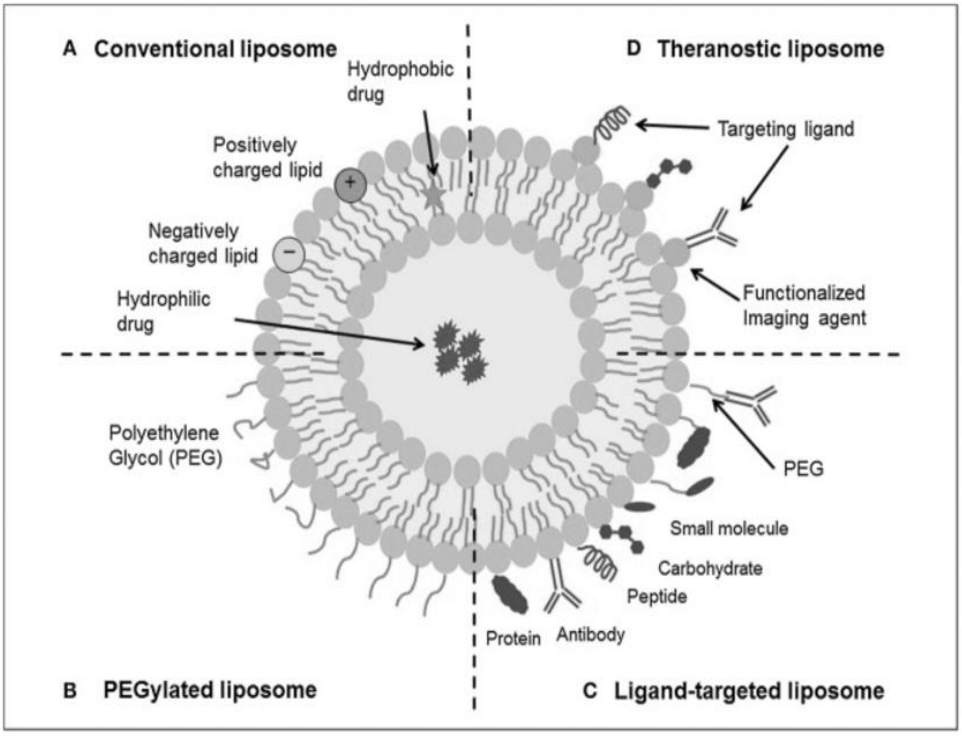

Figure 1.10. Schematic representation of liposomes in drug delivery systems. (A) conventional liposomes containing cationic/anionic lipid, (B) liposomes with PEGylation, (C) ligand-targeted liposomes, (D) Functionalized imaging liposomes. Figure reproduced from reference.[57]

Liposomes have shown they are effective for the delivery of various genetic material, such RNA, DNA and peptides to the cell.[58] Lipid nanocarriers can be used in gene therapy as DNA carriers for oligonucleotide delivery, which promotes uptake of poorly permeable species promoting endocytosis.[57] This has been particularly studied on the development of new messenger RNA (mRNA)-vaccines, which are based on RNA encapsulation. For example, the development of new chikungunya and zika viruses vaccines have recently used liposomes as carriers for mRNA.[59,60] In addition, the mRNA of SARS-Cov-2 have been used to the preparation of vaccines worldwide. In gene therapy, the encapsulation of DNA has particular interest in cancer therapy.[61] The use oligonucleotide cargos in gene delivery is explored in chapter 4.

- Proteoliposomes

As stated in the section 1.2.3, membrane proteins require a lipid environment to retain their structure and activity. Small and large lipid vesicles represent perhaps the simplest but very useful approach to unravel the function of membrane associated proteins. Proteoliposomes, or liposomes containing membrane proteins, have gained importance as biophysical tools to study lipid-protein interactions as they preserve the structure and/or functions of proteins in a native-like state. Different reproducible methods for the reconstitution of purified membrane proteins into lipid models have been proposed and the success of the reconstitution depends on many parameters, such the nature of the protein, type of lipids used, choice of solvent, detergent and others.[28,62] The reconstitution of membrane protein in liposomes to form proteoliposomes can be obtained following three different ways: Chemical reconstitution using organic solvents, direct incorporation into preformed liposomes by mechanical means, and detergent-mediated reconstitution (*Figure 1.11*).[63]

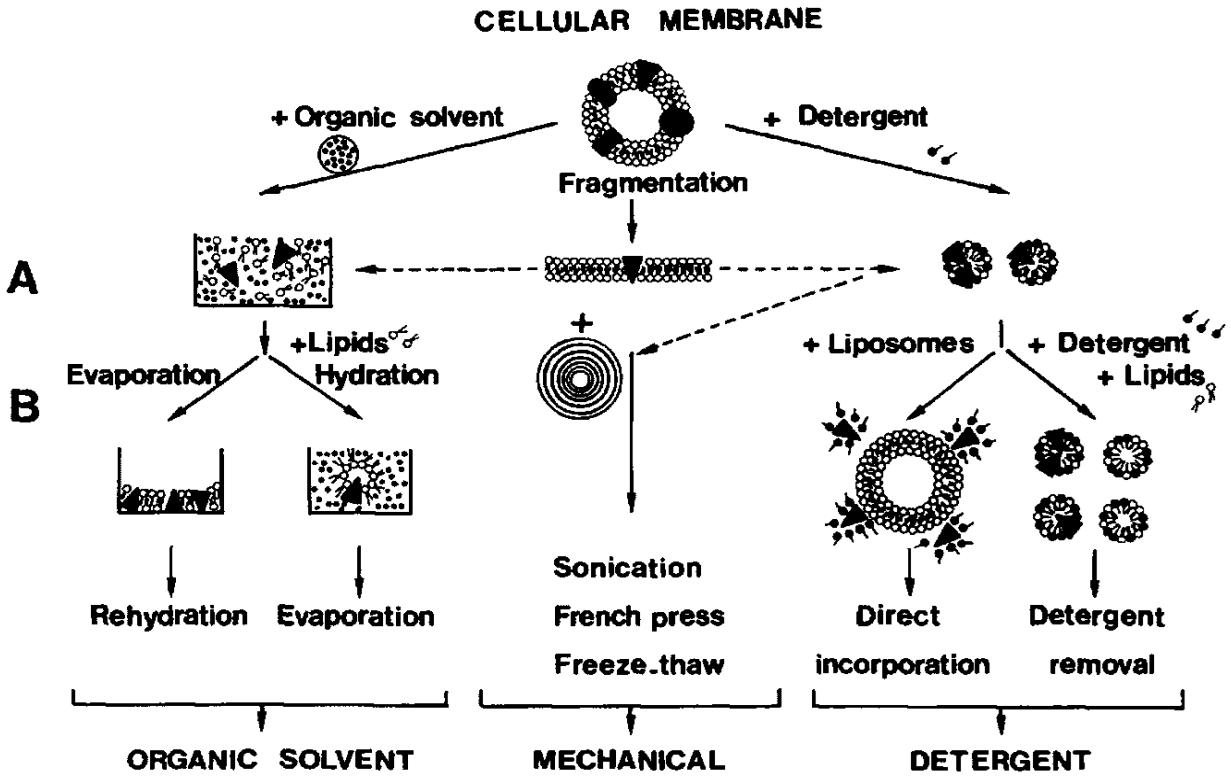

Figure 1.11. Schematic representation of different approaches for the reconstitution of functional membrane proteins into proteoliposomes. Figure reproduced from reference.[63]

Organic solvent-mediated reconstitution of membrane proteins has been used via direct evaporation of a lipids/proteins mixture. With this method, membrane proteins and lipids are mixed and solvent is evaporated. Then, proteoliposomes are prepared by resuspending the dried lipid-protein film in an aqueous media. Certain proteins were successful incorporated into liposomes, such cytochrome c oxidase[64], rhodopsin[65], bacteriorhodopsin[66]. However, the direct contact of membrane proteins to organic solvents might affect their functionality. Another simple approach to prepare proteoliposomes containing membrane proteins is via mechanical agitation or sonication of lipid in presence of membrane proteins. It is a rapid and solvent/detergent free method to produce proteoliposomes. However, a crucial drawback is that mechanical sonication can lead to denaturation of proteins.[63]

The most studied method of membrane protein incorporation is to use detergents mediate the reconstitution of proteins to proteoliposomes. With this method, lipids and membrane proteins can be solubilized in presence of a detergent or solubilized proteins can be mixed with preformed liposomes.[67] After adequate time, detergent is removed using dialysis, filtration or hydrophobic resins.[28] With the removal of detergent, lipid molecules tend to rearrange into bilayer structures due to the isolation of the hydrophobic cores from water molecules. Also, membrane proteins tend to accommodate within lipid molecules forming proteoliposomes. The nature of the detergent, molecular weight (CMC), concentration and rate of removal are parameters to be controlled and optimized during the process.[28,68–70] The properties of most common deterrents are presented in Table 1.

Table 1. Properties of common detergents used in proteoliposomes preparation. Adapted from[71].

Detergent	Category	Mw (Da)	CMC ($mmol.L^{-1}$)
Sodium dodecyl sulfate (SDS)	Ionic	288	7 – 10
Sodium cholate	Ionic	431	13 – 15
CHAPS	Zwitterionic	615	6
Triton X-100	Nonionic	647	0.2 – 0.9
n-Decyl-β-D-maltopyranoside	Nonionic	483	1.8
Octyl glucoside (OG)	Nonionic	292	23 – 25

The successful incorporation of protein, proteoliposomes size and homogeneity might be related to the choice of detergent. For example, the incorporation of bacteriorhodopsin (bR) was subjected to different protocols, which involved different detergents or lipids. For instance, Rigaud et al were pioneers in studying the implications of different surfactants, such Triton X-100, OG and SC, on bR reconstitution in purified egg-yolk phosphatidylcholine (egg-PC). They observed that Triton X-100 and OG mediated insertion of bR was successful with partial and total solubilization of liposomes, while SC successful only with complete solubilization of lipids. After reconstitution, the protein was fully functional as the proton pump activity was retained. Interestingly, the percentage of total inside-out oriented bR was higher for the partial solubilization of liposomes obtained with Triton X-100 and OG, 85% and 95%, respectively.[71] In addition, Wang et al reported that bR was successfully incorporated into proteoliposomes comprised of various charged lipids, such DMPG, DPPA, DOPS, DOTAP using OG as detergent. They reported that bR was more likely to take its natural orientation in presence of negatively charged lipids, while the inside-out orientation was obtained for neutral/positively charged liposomes.[72]

Despite the formation of lipid-protein mixture or detergent used, the surfactant must be removed to complete the formation of closed lipid bilayers with incorporated proteins. To achieve this, two common methods are effective, dialysis and detergent adsorb-beads. Dialysis removes excess of detergent against a detergent-free buffer. The detergent molecules passes though the dialysis chamber leaving the proteoliposomes. Dialysis is mostly used to remove detergents with higher CMC. Dialysis is a simple and cost-effective manner to remove surfactants. However, it can be time consuming and may leave traces of detergents in the lipid solution.[62]

Another efficient and widely diffused method is the use of adsorbent beads, such Bio-Beads SM-2. The method has certain advantages over dialysis. First the detergent-adsorbent beads are added directedly to the lipid-protein detergent solution, without the need of detergent-free buffer. In addition, adsorbent-beads can be applied to all types of detergents independently of CMC. Perhaps the most important advantage is that the rate of detergent removal can be controlled by varying the concentration of Bio-Beads added, providing better reproducibility.[62] In this thesis, adsorbent Bio-Beads were used for the removal of triton X-100 in chapters 4 and 5.

Thus, the varied protocols suggest that reconstitution of proteins to proteoliposomes are dependent on the combination of phospholipid and detergent used, which could be achieved by empirical experimentation. In this work, proteoliposomes were used to investigate the assembly of bacteriorhodopsin in MSLBs using detergent mediated process. This is discussed in more detail in chapter 3.

- Giant Unillamelar Vesicles

Another important class of lipid vesicle is Giant Unilamellar Vesicles (GUVs), which represent artificial liposomes with a diameter of > 1 μm. GUVs are usually obtained by resuspending a dried lipid film to a buffer solution. Originally introduced by Reeves and Dowben, GUVs were prepared by the gently hydration of dried lipid film.[73] In presence of an electric field, the rate of bilayer separation is increased yielding to unilamellar vesicles with size varying from 10 to 100 μm.[74] The main advantages of GUVs are the easy to prepared and manipulate and can be easily visualized by microscopy techniques. In particular, since the direct observation of coexisting gel/liquid phases for the first time[75], GUVs have been largely used to study the properties of lipid mixtures, such phase formation[76], lateral clustering[77] and lateral diffusivity[78]. In membrane studies, GUVs are a powerful tool for elucidating the structural aspects and lateral organization of lipids, particularly related to phase separation.[75] Due to its free-standing properties and membrane fluidity, GUVs have been largely used as a biomimic model, however analysis is often limited to fluorescence and imaging experiments.

In order to achieve more realistic model of membrane for study of lipid-lipid and lipid-protein interactions, the preparation of GUVs with desired transmembrane lipid asymmetry is challenging. Many effort has been made to induce transmembrane asymmetry in GUVs in chemically by depleting lipid molecules from the membranes, such lipid depletion via methyl-β-cyclodextrin (mβCD) lipid exchange[47,79], lipid hemifusion[80], or mechanically using microfluidic apparatus[81]. Chiantia *et al* reported the first preparation of GUVs with asymmetric lipid composition using mβCD to introduce SM to the outer leaflet of symmetric GUVs comprised of DOPC. They observed that the lateral diffusion of labelled SM in the outer leaflet decreased with the concentration of SM.[47] Differently, other methods free of mβCD were proposed. Hu *et al* used

microfluidics to assemble asymmetric GUVs in two independent steps where lipid monolayers were built at water-oil interface and transferred to lipid droplets to a second oil-water interface.[81] Most recently, Eniki *et al* promoted the exchange of lipids using hemifusion of GUVs to supported lipid bilayers in presence of Ca^{2+}, which lead to the formation of asymmetric GUVs, as confirmed by confocal microscopy.[80] The use of charged lipids also lead to the spontaneous formation of asymmetric GUVs. For instance, Steinkuhler *et al* reported asymmetric distribution of negatively charged PS in GUVs after electroformation.[82] However, the lipid asymmetry was nearly lost at higher temperatures, above room temperature, usually required to preparation with saturated lipids with higher melting temperatures, such sphingomyelin.[83]

In all, despite the lateral lipid mobility provided by GUVs, they generally preclude evaluation of impact of compositional asymmetry because of challenges in reliably building asymmetry in such structures,[84] a key feature in realistic membrane models for lipid-lipid or protein-membrane dynamics.[85] Also, the inner solution is usually filled with non-ionic solution such sucrose representing a deviation of the natural environment of lipid membranes. Other issues such long term stability and limitations to their geometry represent important drawbacks of this model system.[86] Overall, the use of liposomes as precursors to preparation of supported lipid bilayers, or in protein incorporation, or in therapeutics or in studying lipid dynamics and properties demonstrate the importance and ability of liposomes as a tool to biomimicry the plasma membrane environment. In this work, liposomes were used to build MSLBs with transversal asymmetry, delivering GSLs to the outer lipid leaflet and to study the incorporation of bR to MSLBs.

1.3.2. Droplet interface bilayers

Another interesting approach to obtain artificial lipid membranes are droplet interface bilayers (DIBs). They are aqueous microdroplets (10 – 100 μm diameter) immersed in an immiscible phase surrounded by a lipid monolayer. When droplets are brought together in pairs, a lipid bilayer is formed at the interface between the droplets.[87] DIB are flexible tools to analyse the effects of membrane lipid structure on bilayer transport since the droplet bilayer allows for direct observation of species transport across free standing bilayers.[88]

DIBs can be prepared in oil using solubilized lipid molecules or liposomes. by dissolving lipid molecules in an oil or incorporated within the droplets as vesicles.[89] In the first method, when a drop of water is add to the lipid-oil mixture, containing the phospholipids, they rearrange themselves forming a monolayer at the interface of the aqueous drop. This method allows the preparation of asymmetric lipid bilayers but it is limited to the incorporation of membrane proteins.[89] Another way of preparing DIBs is by introducing an aqueous solution of liposomes to an immiscible oil phase. With time, lipid vesicles will fuse at the boundary of the liquid drop forming a lipidic monolayer. The formed monolayer droplet can be mechanically manipulated with a micropipette within oil phase to assemble a lipid bilayer at the intersection between two or more droplets. With this method, the use of proteoliposomes allows the incorporation of membrane proteins to DIBs, such as mechanosentitive channel of large conductance (MscL)[90] and OmpG.[89]

DIBs have been used to study the electrical properties of lipid bilayers. Lipid bilayers can be pictured as a biological parallel plate capacitor therefore electrochemical measurement is a useful way to study their properties and to assess the area, thickness and surface potential of membranes.[91] While liposomes are not amenable to electrochemical study, electrochemical properties of the formed lipid membranes can be accurately determined by the insertion of electrodes into droplets which enable the application of a potential, as well as measurement of the ionic current flowing though embedded channels and pores (*Figure 1.12*).[92] Pore forming proteins For instance, the electrochemical properties of membrane protein MscL were well characterized using DIBs.[90,93,94] For instance, Haylock *et al.* studied the electrochemical properties of membrane protein MscL by monitoting the pore channel activatity using choronoamperometry. Reconstitute proteins were activated by the addition of MTSET. Using a series of DIBs, the observed that the electrochemical signal propagated though the network upon sequential channel activation.[90]

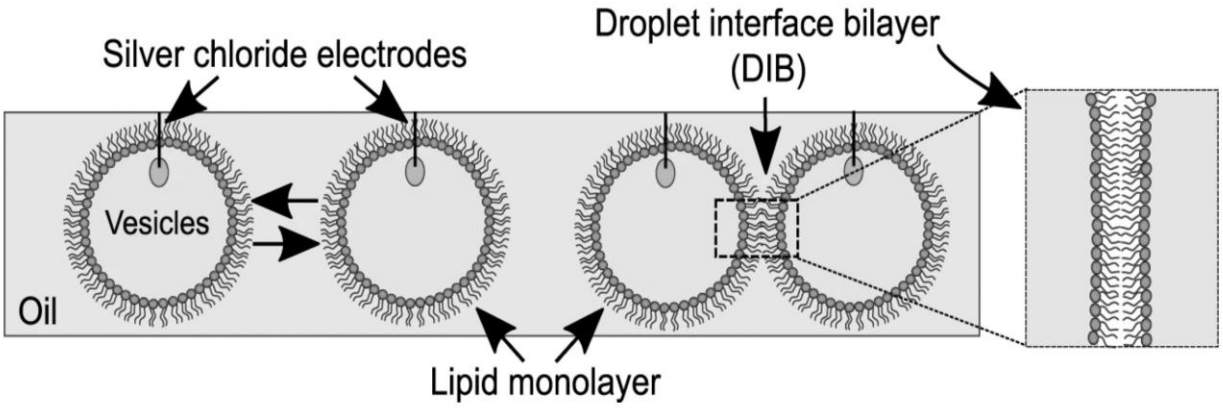

Figure 1.12. Assembly of droplet interface bilayers for electrochemical studies of membranes. Water droplets comprised of lipid vesicles are placed into a well of oil. The formed monolayers are manipulated to form a DIB. Figure reproduced from reference.[90]

Although DIBs are a versatile way of preparing lipid membranes containing membrane proteins, they rely on the intersection bilayer formed at the contact between two monolayer droplets. This reduces their application on more relevant studies over larger surfaces. The use of oil bath may also directly affect lipid diffusivity due to the higher viscosity of the surrounding media faced by the droplets. In addition, conditions such pH or salt concentration are difficult to readjust, which may limit the application of lipid droplets and their biomimicry.

1.3.3. Black lipid membranes

Planar lipid membranes offer the possibility to directly address optical, electrical and chemical properties of lipid membranes. One of the first models of planar membranes, Black lipid membranes (BLMs) were first introduced by Mueller *et al*. in the early 1960's and have greatly contributed to current understanding of lipid membranes.[95] Usually, BLMs are generated by painting lipid molecules dissolved in nonpolar organic solvent, such as n-decane, across a hydrophobic micrometre to millimetre pore between two solution chambers, as indicated in *Figure 13*a and *Figure 13*b.[96,97]

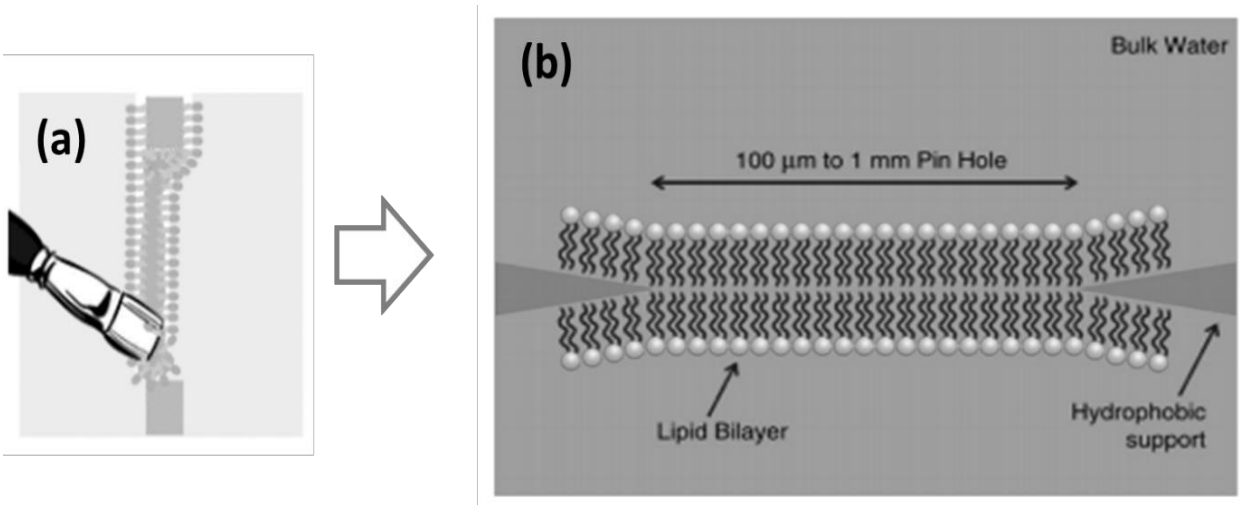

Figure 13. Schematic of a BLM free standing over a pore. (a) Process of fabrication of BLM involving depositing a lipid bilayer from organic solvent solution. Figure reproduced from.[97] (b) BLM spanned over aperture of a hydrophobic substrate. Figure reproduced from.[98]

The incorporation of proteins into BLMs can be obtained by exposing the preformed bilayer to liposomes containing protein of interest. The first report was described by Miller and Racker explored the ionophore properties of BLMs containing sarcoplasmic reticulum in BLMs with of diameter 1 mm made of 30%PS-70% PE and by studying the conductance increase in presence of Ca^{2+}.[99] This was also observed by Gomez-Lagunas *et al* when studying K^+ channels extract from yeast, in similar experimental conditions, e.g., lipid composition and BLM size.[100] Veatch *et al* reported the incorporation gramicidin A into BLMs comprised of DOPC by mixing purified peptides with lipids in chloroform. After solvent evaporation, the mix of DOPC/gramicidin A were solubilized in n-decane. The pore formation was monitor as the conductance of the bilayer increased with the surface density of peptide.[101] Recently, the introduction of horizontal BLMs have enabled they interrogation by optical microscopy combined with electrochemical measurements for studying ion channels[102] and ionophores.[103]

Overall, the surface tension required to span a bilayer across a millimetre pore affects the long term stability of membranes, often having a usable lifetime of less than 1h.[104] Strategies have been used to increase the stability of BLMs, such the use of hydrogel substrates[105] or reduction of pore size. Another inherent drawback of BLMs is the presence of residual organic solvent that may

affect the structure of the lipid bilayer and any reconstituted proteins, reducing their stability and possibly interfering in their properties. The direct transfer of lipid onto solid supported membranes may mitigate some of those limitations. Thus, freestanding BLMs are synthetic bilayers for studying fundamental electrochemical properties of lipid membrane and single-molecule studies of protein electrophysiology. However, the short lifetimes, poor mechanical stability along with the diffusivity in studying membrane diffusion, which is challenging or impracticable to be evaluated using BLMs, limiting their applications in studying lipid and protein diffusion.

1.3.3. Supported lipid bilayers

A very widely applied approach to form artificial bilayers is to form solid supported lipid bilayers, SLBs, by depositing a lipid bilayer onto a planar solid substrate (*Figure 1.14*). A typical SLB is spanned across a thin water layer, typically 2 to 5 nm, depending on the hydrophilicity of the substrate, which is sufficient to lubricate the lower leaflet.[98] However, limit their application to membrane protein functional investigation due to insufficient interfacial space requited to accommodate the extra membranous segments of proteins.

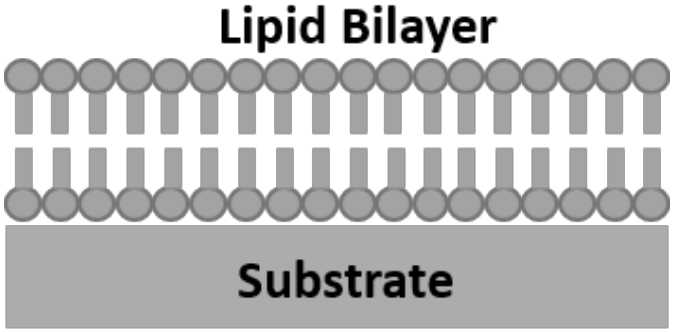

Figure 1.14. Schematic representation of a supported lipid bilayer to a solid substrate.

In contrast to BLMs, SLBs are more robust and depending on the fabrication method, a simple bilayer can be readily formed, avoiding multilayers. They are more easily studied by surface

sensitive methods, such atomic force microscopy, quartz crystal microbalance, photo-physical and spectroscopic methods, allowing deeper understanding of the mechanical properties of lipid membranes.[106,107] The substrate directedly influences the analytical method applied to investigate the lipid membrane. For instance, AFM requires atomically smooth surfaces, such mica, silica or flat gold. Surface Plasmon Resonance (SPR) required a noble metal thin layer, usually silver or gold. When prepared over transparent substrates, such silica, quartz, glass or PDMS, SLBs can be visualized by fluorescence microscopy techniques using fluorescent tagged lipids or with the addition of fluorescent dyes to the membranes, similarly to GUVs.[108] A drawback is that, SLBs tend show reduced lipid mobility due to substrate-membrane interactions affecting membrane fluidity and lipid diffusivity, usually limited within the range 0.3 – 4 $\mu m^2/s$.[109,110] In addition, frictional or electrostatic coupling of SLBs to the substrate may affect the morphology of lipid phase separation in comparison to free-standing membranes.[49,111]

Supported Lipid Bilayers are frequently prepared using Langmuir films deposition, vesicles fusion or a combination of the two methods (*Figure 1.15*). The use of Langmuir films (*Figure 1.15*a) permits a layer-by-layer preparation of lipid bilayers with different composition, or asymmetric composition. The lipid bilayers prepared by using Langmuir films are highly compact with great substrate coverage and low defects. However, the incorporation of membrane proteins is limited with this technique. The direct fusion of vesicles (*Figure 1.15*b), such GUVs or proteoliposomes, allows the preparation of SLBs without the use of additional equipment. With this method, a hydrophilic substrate, such glass is exposed to a solution containing lipid vesicles that disrupt at the solid-liquid interface forming the SLB. The preparation of SLBs containing membrane proteins can be achieved by this method using proteoliposomes. Although direct fusion of liposomes is a simple way to prepare SLBs, lipid bilayers are limited to the composition of the liposomes, hindering the preparation of asymmetric membranes.

A third method for preparing SLBs is the fusion of vesicles to pre-deposited lipid monolayers (*Figure 1.15*c). This method is a hybrid from both previous methods. First, a lipid layer is transferred to a hydrophilic substrate. Then, the substrate is exposed to a solution containing liposomes. The lipid bilayer is then prepared layer-by-layer, which allows the preparation of bilayer with asymmetric lipid membranes. The incorporation of membrane proteins into SLBs can

be obtained, similar to the fusion of proteoliposomes, although the self-orientation of protein in respect to the bilayer is relatively higher to SLBs formed with a pre-deposit lipid monolayer.[112]

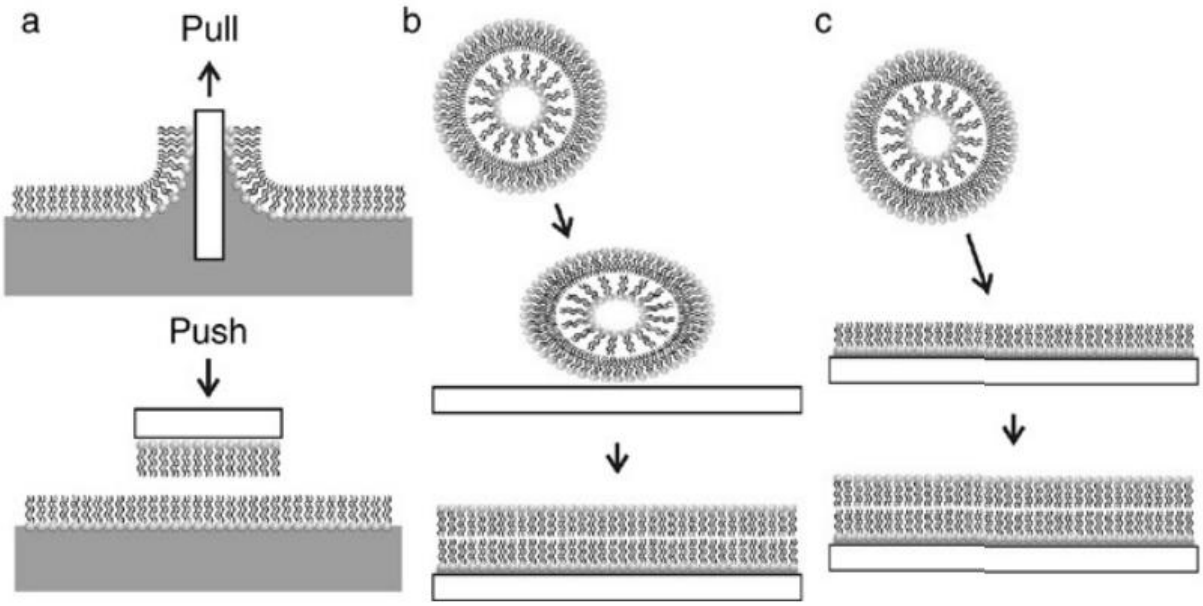

Figure 1.15. Schematic illustration of the main methods of preparation of supported lipid bilayers. a) The Langmuir-Blodgett/Langmuir- Schafer Method: deposition of an underlying lipid monolayer on the substrate using the Langmuir-Blodgett method followed by the formation of a second layer by horizontally dipping the substrate. b) Vesicle fusion method: the addition of unilamellar vesicles to a hydrophilic substrate and their spontaneous formation of a lipid bilayer c) Langmuir-Blodgett/Vesicle Fusion method: deposition of an underlying lipid monolayer on the substrate using the Langmuir Blodgett method followed by the addition of unilamellar vesicles which fuse and form the upper leaflet. Figure reproduced from reference.[113]

Although SLBs are relatively simple to prepare and easy to interrogate though different surface techniques, as described, the proximity of the lower lipid leaflet, to the substrate, which can vary from 1 to 2 nm, hinders the membrane fluidity interfering directedly in the properties of lipid bilayers.[112] Additionally, the interfacial separation may be too small to accommodate large integral proteins, which can lead to loss of mobility and functionality.[114] Thus, the underlying space poorly mimics the natural cellular space, which may affect molecules transfer across the bilayer.[115,116] In

order to overcome this issue, different approaches have been developed to reduce substrate-membrane interactions by decoupling the membrane from the substrate, by increasing the distance between the proximal leaflet to substrate.

An approach is using flexible polymer cushioned substrate to prevent direct contact of the bilayer with the solid support, resulting in more fluidic membranes (*Figure 1.16*a). Different polymers have been explored as cushion supports, such as cellulose[117], PEG[115], and S-layer proteins[118]. Although decoupling the membrane from substrate and in some cases, improving membrane diffusion, cushions also typically interact with lipid membranes, therefore limiting their use as artificial membranes. For example, Wang *et al* reported that lipid bilayers supported on PEG-cushion shown diffusivity of 5.5 $\mu m^2/s$ measured by single particle tracking (SPT), which was 10 fold faster than similar bilayer supported on bare glass[115]. Gyorvary *et al* shown that SOPC lipid bilayers containing ATP synthase spanned over cellulose sheets have lipid diffusion measured by Fluorescence Recovery After Photobleach (FRAP) of 2 $\mu m^2/s$, while ATP synthase shown no remarkable sign of lateral diffusion.[117] This is due to the fact that although the cushion might increase lipid diffusion compared to bare SLBs, the hydrophilic links are too short to accommodate membrane proteins. S-layer membranes have improved stability compared to BLMs, from 5 – 50h.[118] However, lateral diffusion of lipids is limited usually in the range of 0.5 – 3 $\mu m^2/s$.[119] Other issues were reported to loss of protein functionality of proteins when using polymer cushions may hinder their application in biomimic studies.[120]

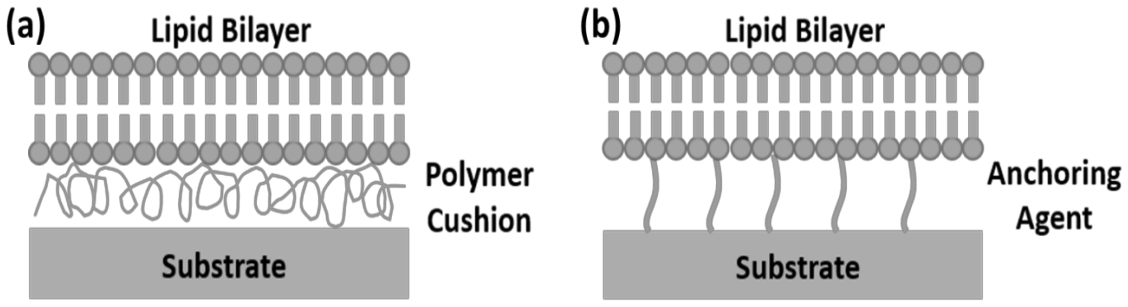

Figure 1.16. Schematic representation of cushioned supported lipid bilayers spanned over a polymer spacer and of tethered supported lipid bilayers.

Another strategy to reduce frictional interactions between lipid membranes and substrate are based on the use of anchor molecules to the lipid membrane, as observed in the *Figure 1.16*b. To do so, self-assembled monolayers (SAM) of thiols or conjugated lipids can be introduced to the lipid membrane. For example, Hughes et al demonstrated the use of thiol-POPC to form stable tethered-supported lipid bilayers comprised of DPPC and POPC on gold prepared by sequential Langmuir-Blodgett and Langmuir-Schaefer deposition.[121] Budvytyte *et al* proposed the use of a SAM mixture of WC14, FC16 and HC18 with β-mercaptoethanol to functionalize gold substrates for the fusion of DOPC vesicles. The highest diffusion coefficient of 4.0 $\mu m^2/s$ measured by FCS was obtained for the longest tether HC18, compared to approximately 2.0 $\mu m^2/s$ for shorter SAM, indicating that greater separation from substrate enhances the membrane fluidity, as expected.[122] Using a polymer-lipid spacer, Wagner and Tamm used DMPE conjugated to PEG to successfully decouple a POPC lipid bilayer from quartz substrate. They observed that the lipid diffusion coefficient was 0.8 – 1.2 $\mu m^2/s$. The mobility of peripheral proteins cytochrome b and annexin V was limited to 50%, with diffusion coefficient of 1 $\mu m^2/s$ and 0.3 $\mu m^2/s$, respectively.[120] In addition, the influence of frictional interaction with the substrate on the diffusion coefficient of molecules may depend on the distance of the bilayer to the substrate. Using native cell plasma membrane from HeLa cells, Wong *et al* demonstrated the effect of polymer length, represented by the molecular weight, on the diffusion of GPI-anchored proteins. They reported the diffusion of GPI-anchored protein in PEGylated DPPE was 0.01 – 0.1 $\mu m^2/s$ or immobile for short polymer PEG-1000. The diffusion coefficient increased to 1 – 5 $\mu m^2/s$ using longer PEG-5000.[123]

Overall, these reported observations indicate that the use of polymer cushions or tether improve the diffusion coefficient of molecules when compared to bare supported lipid bilayers. However, they rarely improve membrane diffusion in comparison to free standing bilayers, such GUVs, under similar conditions and frictional interactions are still present as observed in the reported diffusion values.[124] In order to avoid substrate interaction with lipid membranes, pore-suspended membranes were introduced as a method to decouple lipid membranes from substrate.

1.3.4. Pore suspended lipid bilayers

A relatively recent, alternative approach to improve membrane substrate interactions is to span the membrane over a pore. Pore suspended bilayers, also known as free-standing membranes, have been proposed to bridge the gap between solid supported lipid bilayers (SLBs) and BLMs.[125] This suspended format of the lipid bilayer over small pore, typically < 10 μm, offers the possibility of studying the properties of lipid bilayers away from the limitations imposed by membrane-substrate interactions, such as poor lipid diffusivity or protein denaturation, as shown in the schematic representation (*Figure 1.17*)

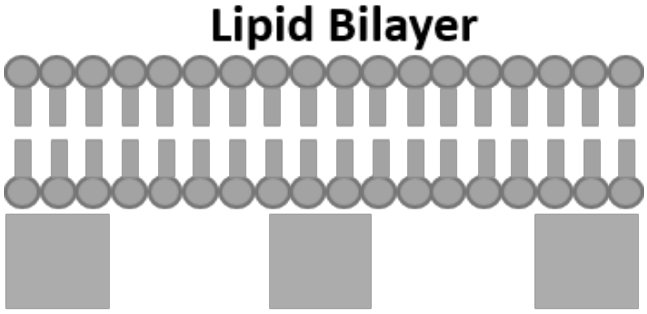

Figure 1.17. Schematic representation of pore-supported lipid bilayers.

Bilayers can be spanned directly over hydrophilic porous substrates as the interfacial water layer support the membrane in solid substrate contact. It makes a range of different materials have been used to assemble such pore supported bilayers, such porous silicon, alumina, silicon nitride or gold-coated silicon nitride[126]. Materials may be functionalized with molecules to increase hydrophilicity at pore rim improving affinity to the membrane. Gold-thiol chemistry is used to produce SAMs on the pore rims.[127,128] Silane chemistry can be applied on silicon and aluminium oxide surfaces.[129,86]

Similarly to SLBs, pore suspended lipid bilayer can be obtained from different methods, including, but not only, lipid transfer using Langmuir-Blodgett and or Langmuir-Schafer, vesicles fusion, or a combination of LB/VF. The most used method to prepare pore-suspended membranes remains the direct fusion of liposomes to the porous substrates. To obtain a pore-suspended membrane, liposomes with diameter greater than the aperture of the pores are required, limiting the use of SUVs and LUVs as they might disrupt inside the cavities rather than spanning across the pores.

To this purpose, GUVs are a valid alternative. For example, Heinemann and Schwille demonstrate a method to prepare free-standing membrane by direct fusion of GUVs to Si_3N_4 support containing 2.5 μm pores (*Figure 1.18*a). The lateral diffusion of lipids was monitored by FCS and lipid bilayers comprised of DOPC shown lipid diffusion of around 10 $\mu m^2/s$.[86] Using relatively smaller pores, Kocun *et al.* used a similar approach to prepare solvent-free pore spanning bilayers using GUV disruption onto porous silicon arrays with 1.2 μm of diameter of individual pores. They reported lipid diffusion coefficient measured by FRAP was 8 $\mu m^2/s$ DOPC bilayers. (*Figure 1.18*b) A drawback of this approach is that the bilayers formed after GUV fusion did not covered the full substrate but rather create patches of lipid bilayer of few micrometres.

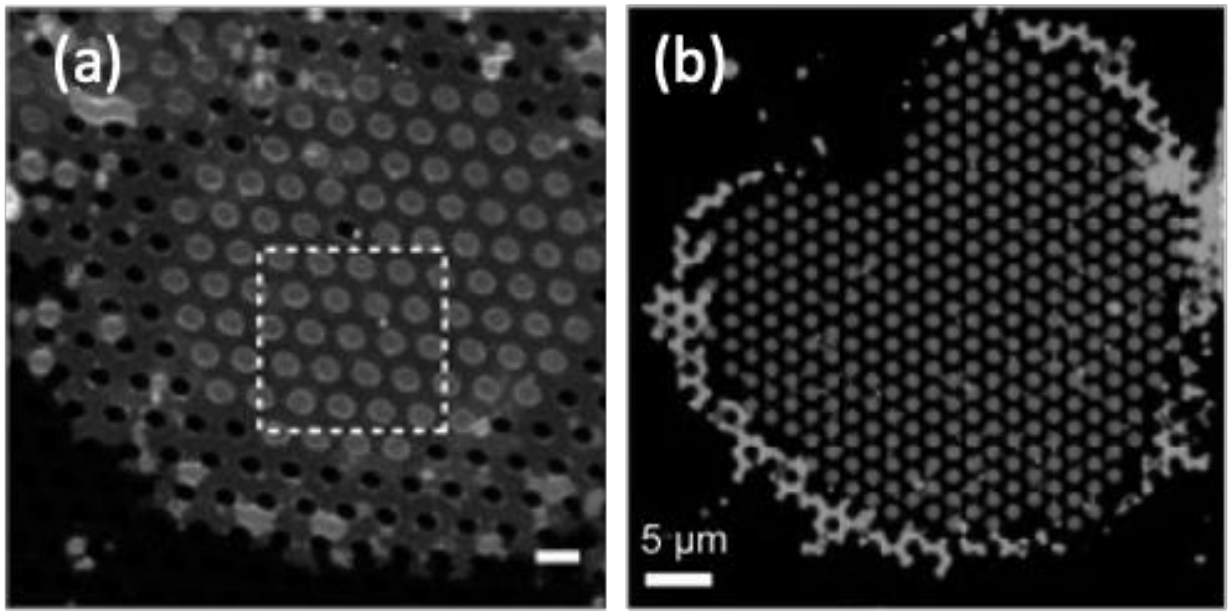

Figure 1.18. Pore-suspended lipid bilayers prepared by GUVs fusion over porous substrates. (a) Figure reproduced from.[86] (b) Figure reproduced from.[130]

Another method to prepare SLBs, Langmuir-Blodgett transfer provides the advantage of covering larger areas than lipid bilayer prepared by GUVs disruption. However, this method was not fully explored in the preparation of pore-suspended lipid membranes. Simon *et al* reported successful preparation of pore-suspended membranes obtained by Langmuir-Blodgett transfer. Lipid bilayers comprised of DOPC/DOPS (7:3 ratio) were spanned over 1 μm pored-sized silicon arrays.[131]

Although improving coverage of porous substrates, incorporation of proteins using LB methods is limited. In this work, the lipid bilayers were prepared over 1 cm^2 gold or PDMS microcavity arrays using Langmuir-Blodgett methods for the study of oligonucleotide delivery to MSLBs. The experimental protocol is described more detailed in chapter 5.

Lipid bilayers can be prepared using a combination of LB with liposome fusion, similar to SLBs. This is obtained by exposing a pre-transferred lipid monolayer to solution containing liposomes. The pre-deposit monolayer seals the pores preventing liposomes to disrupt at the interior of the cavities. However, few studies were conducted using this method. By eliminating the interaction of the bilayer with the underlying solid support while conserving relatively the stability of SLBs and allowing retention of lateral mobility, pore supported lipid bilayers permit the reconstitution of integral proteins with higher lateral mobility compared to SLBs. This was evidenced by Basit et al. that reported the incorporation of glycophorin A and $\alpha_{IIb}\beta_3$ using MSLBs. The reconstituted proteins exhibit high mobility with diffusion coefficient of 4 $\mu m^2/s$ and 3.2 $\mu m^2/s$, respectively.[132] Furthermore, Keyes's group have developed a microcavity array used using different materials, such PDMS, gold, of which lipid membranes have been used to address lateral mobility of lipids[37,132,133], build asymmetric lipid bilayers[37], and to evaluate passive permeability of therapeutics[133–135]. The use of LB combined with liposomes fusion opens the possibility of preparing asymmetric lipid bilayers as well as the incorporation of membrane proteins to pore supported lipid membranes. These two topics will be explored in the chapters 3 and 4. The diffusion coefficient of lipid molecules in pore supported lipid bilayers shown lateral usually matches the values reported for free suspended vesicles, such GUVs, and are in the range of 10 $\mu m^2/s$.[86,136] These values are 4 to 10 times higher than diffusion coefficients found in SLBs, evidencing a great advantage of pore-membranes over solid supported membranes.[137]

Other methods using chemical solvents were proposed. Recently, Watanabe *et al* reported stable pore-suspended membranes over 4 μm diameter using a microfluidic system of CYTOP over glass substrate. The lipid bilayer was prepared in 3 independent steps: first, the microtube was filled with aqueous solution. Then lipids dissolved in organic solvent were introduced in the chamber forming a monolayer. After a second organic solvent was introduced containing other lipids. Finally, the chamber was rinsed with water remove excess of lipid or solvent. The formation of the suspended lipid bilayer was demonstrated using FRAP technique without reporting diffusion

of lipids.[138] However, the use of harsh solvent limit the application of this method to the reconstitution of membrane proteins.

Overall, artificial membranes represent a more simplest platform than biological membranes, they provide good information about the lipid-lipid and lipid-protein interactions. Each system here presented has advantages and drawbacks. In this work, the use of a microarray was evaluated as sophisticated platforms to the preparation and characterization of asymmetric lipid bilayers along with the peripheral and integral assembly of proteins. The bilayers were prepared in a microfluidic environment by a hybrid LB/VF method without the need of harsh organic solvents.

1.4. Lateral diffusion and membrane fluidity

Lipid bilayers are complex in nature and its detailed organization of cellular membranes in biological cells remain to be revealed. Certain properties of cell membranes such lipid composition has been demonstrated to be heterogeneously distributed across the lipid leaflets. Also, lipids may form transient nanodomains that serve as platforms for membrane proteins to function. These properties may be reflected on certain membrane properties, such lipid diffusivity, which can be accessed by artificial ways. Membrane fluidity is important for several reasons as it ensures the dynamic environment required to enable functional components, such proteins and glycolipids to diffusion to their reaction sites and permits for aggregation and clustering processes involved in membrane signalling.[139] It has been shown that small deviations on the membrane fluidity of cells can affect cell's properties and lead to variations in several functions, including protein expression, exposure of cell membrane receptors and functional properties of the cell membrane.[18]

In biological membranes, the constituents such lipids, proteins or cholesterol can laterally diffuse within the lipid bilayer. The mobility of molecules in lipid membranes is determinant, for lipid/protein activity to interact with other molecules in the membrane or from the surrounding environment. For instance, processes that lead to cross-linking of receptors at cell membrane requires the presence of mobile receptors within the membrane.[140] Therefore, it is vital for artificial membrane models to encompass sufficient fluidity.

1.4.1. Theoretical models of diffusing constituents at lipid membranes

Membrane proteins can be integrated in lipid membranes or associated with the surface of cell membranes. In this context, lateral diffusion of proteins is important for cell activity.[141] Investigation of lipid/protein mobility in biological and artificial lipid models can provide information on membrane structure and dynamics. One of the key goals of this work is to accurately determine the diffusion coefficient of lipid molecules and transmembrane proteins, with emphasis on the peripheral binding of CTb, HA1 and membrane proteins such as bR and integrin $\alpha_5\beta_1$. We were particularly interested in the lateral assembly of proteins and their membrane receptors at lipid membrane. To this end, the change in the diffusion coefficient of proteins after receptor-binding determines the aggregation and local lipid environment. Throughout this work, we sought on obtaining the diffusion coefficient, commonly in $\mu m^2/s$, of molecules, or the distance a particle may travel due to its motion.

The diffusion of a molecule can be described as a random trajectory, or random walk. For example, a molecule in solution may diffuse randomly due to random shocks with water particles. For example, In 1827, Robert Brown observed that pollen grains inside water moved around randomly. His first thought was that the pollen was alive. Instead, the pollen grains moved around due to the collisions of water molecules with the grains. It was the first observation of what become called as Brownian motion, or random walk. The free Brownian motion as related to the movement of a molecule in a fluid is described by the Einstein relation (Eq 1), where $\langle \boldsymbol{r(t)^2} \rangle$ is the main square displacement (MSD) is proportional to the time t and the diffusion D, as shown in the Equation 1.1.

$$\langle r^2(t) \rangle = \langle (r(t) - r(0))^2 \rangle = 4Dt \qquad \text{(Equation 1.1)}$$

. In lipid models, especially free-standing bilayers, such GUVs, membrane constitutes can freely diffuse according to Brownian motion. The presence of lateral heterogeneities in the membrane may cause the diffusivity of its constitutes to be hindered, resulting in anomalous or sub-diffusion.

This phenomenon is a deviation from the Brownian or "random walk" diffusion of particles, where distance travelled by the molecules in not proportional to time, but to $4Dt^{\alpha}$ the exponent α varying from 0 to 1. According to Stokes-Einstein equation, the diffusion of a molecule in a liquid with low Reynolds number is described by the relation between the radius (r) as shown in Equation 1.2.

$$D = \frac{k_B.T}{6\pi\eta r} \qquad \text{(Equation 1.2)}$$

Where K_B is the Boltzmann constant, T is the temperature of the media, and η is the viscosity of the bulk solution. In lipid bilayer, molecules are treated as inclusions diffusing in a viscous media. However, the diffusion of particles in lipid membranes is 2D. Within a membrane, lipids move laterally through intermolecular gaps in the membrane. To explain the lateral diffusion of a molecules within a lipid membrane we used the Saffman-Delbrück model. This model describes the diffusivity (D_L) of molecules in a lipid bilayer as a cylindrical object diffusing within a thin layer of a viscous fluid surrounded by a less viscous fluid (Equation 1.3).

$$D_L = \frac{k_B T}{4\pi\mu h}\left(ln\left(\frac{\mu h}{\mu' r}\right) - \gamma\right) \qquad \text{(Equation 1.3)}$$

Where $\boldsymbol{D_L}$ is the lateral diffusion of the cylindrical inclusion of radius $\boldsymbol{r}$, $\boldsymbol{T}$ is the absolute temperature, $\boldsymbol{h}$ is the lipid membrane thickness, $\boldsymbol{\gamma}$ is Euler-Mascheroni constant (approx. 0.577), $\boldsymbol{\mu}$ and $\boldsymbol{\mu'}$ are the membrane viscosity and the bulk solution viscosity, respectively.

The Saffman-Delbrück model is widely used in the literature to describe the diffusion of proteins in lipid membranes. Various studies have shown that the model can be used to predict the diffusivity of membrane proteins.[142–145] The model infers a logarithm dependence of diffusion on radius of protein, which in practice means that the variance on protein radius has little effect on the diffusion coefficient, as shown in *Figure 1.19*.

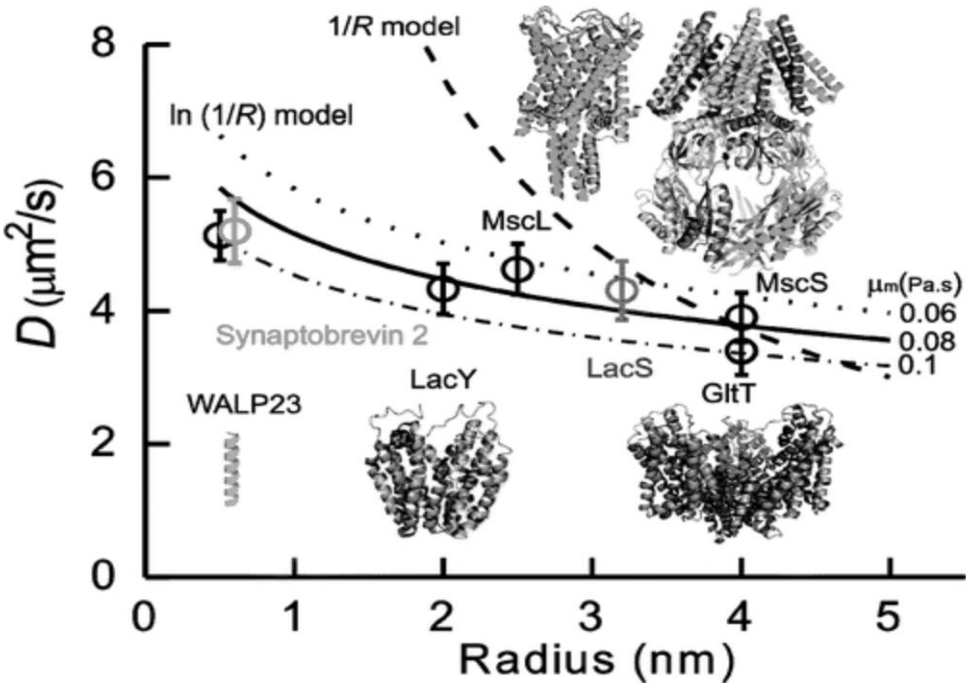

Figure 1.19. Size-dependent lateral diffusion of integral proteins in viscous thin lipid membranes. Solid lines represent the fit of data do Saffman-Delbrück model. The 1/R model was included for comparison. Figure adapted from.[145]

However, in spite of being widely used to describe protein diffusion, the Saffman-Delbrück model, the relation between protein size and diffusion remains in debate. For instance, Gambin *et al.* observed that the lateral mobility of proteins was strongly radius dependent. They proposed that the lateral diffusion of proteins was inversely related to radius r, or 1/R, and not logarithmic.[146] In addition, Ramandurai *et al.* pointed that the hydrophobic mismatch of proteins in lipid membranes may lead to deviations from the Saffman-Delbrück model.[145] It is therefore suggested that the Saffman-Delbrück model is applicable for particles with radius below a critical value, reported as 10 nm and 7 nm[147].

1.4.2. Factors influencing lipids and proteins diffusivity

Many factors can influence the mobility of lipids and proteins within membranes, such the lipidic composition of the membrane, lipid distribution, protein concentration and external factors.

- Membrane composition

The cell membrane is believed to be heterogeneously laterally organised. Saturated lipids and sterols are believed to form domains and also nanoscale structures within in the lipid membrane such as "rafts" The concept of the lipid raft was initially introduced due to explain the observation of insoluble fractions of lipid membranes from detergent extraction. DRMs have been shown to be mainly composed by sphingolipids and cholesterol along with proteins and glycolipids.[3,4] This lateral segregation is believed to serve as a platform for protein and lipids and may be required to certain cell functions.

In artificial membranes, the physico-chemical properties of membrane lipids, such length of fatty acid tails and degree of saturation of side chains, have been shown to impact the lateral packing of membranes and can result in the formation of distinct phases. Lipids have well defined transition phase temperature, which is dependent on the degree of saturation of the backbone hydrophobic tail. Unsaturated tails reduce lateral lipid packing due to the higher hydrophobic bulk volume of unsaturated fatty acids resulting in a more flexible membrane with lower melting point (T_m). This can lead to the formation of more fluidic phases with increased lipid mobility, also known as liquid disordered (L_d) domains (*Figure 1.20*a). The degree of unsaturation of lipids is related to the poorly packed membranes, it strongly indicates that the packing of membrane affects D.[148] In agreement, data obtained from molecular dynamics simulations have been reasonably successful in predicting the lateral diffusion coefficients.[149] On the other hand, due to greater van der Waals interactions along the length of the lipid tail, saturated fatty acids pack more tightly in membranes resulting in more rigid phases, or gel phases (L_β or S) as indicated in *Figure 1.20*b.

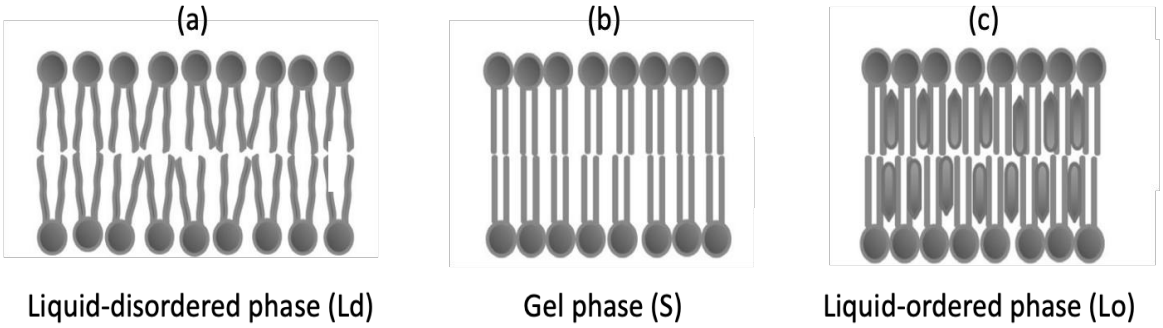

Figure 1.20. Representation of different lipid phases: (a) unsaturated lipid molecules Gel-phases formed by saturated lipid below Tm, (b), (c) liquid-ordered phase comprised of saturated lipid and cholesterol. Figure adapted from reference.[150]

In lipids models comprised of lipid with low and high melting point, cholesterol laterally segregates into ordered domains (L_o), containing preferentially with saturated phospholipids, as shown in *Figure 1.20*c. Bezlyepkina *et al*. suggested a phase diagram of ternary lipid mixtures of unsaturated DOPC, saturated SM (T_m DOPC ≈ -20 °C, T_m SM ≈ 45 °C) and cholesterol (*Figure 1.21*). In this diagram is possible to identify the different phases that would be formed at a certain concentration. For example, lipid bilayers comprised mostly of SM will form gel phases (blue area). The addition of cholesterol induces the formation of Lo + S (green area). By the mix of DOPC/SM two independent phases are obtained a L_d enriched in DOPC and a Lo enriched with SM (dark blue area). The addition of cholesterol causes the gradual formation of L_o phases as indicated in pink and red areas.

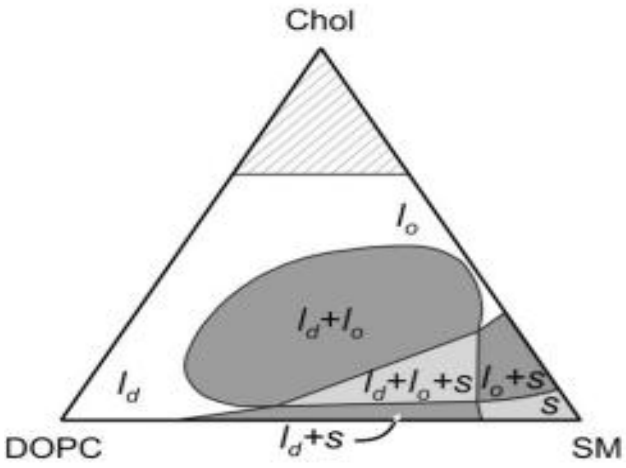

Figure 1.21. Estimate boundaries of one, two and three phase regions of DOPC, SM and Cholesterol. Figure adapted from reference.[151]

The impact of lipid phases in the diffusivity of membrane components have been studied using lipid models. For instance, Ariola *et al.* used an integrated fluorescence-dynamic assay of monophasic, biphasic and ternary composition of GUVs showed the influence of L_d and S phases on the diffusivity of fluorescently tagged bodipy-cholesterol (*Figure 1.22*).[152] They observe that the diffusion coefficient of cholesterol in monophasic lipid bilayers comprised of DOPC was 7.4 ± 0.3 $\mu m^2/s$ determined by FCS. In contrast, lipid bilayers comprised of SM showed diffusion coefficient of 0.35 $\mu m^2/s$. This difference is associated to the partition cholesterol to more viscous ordered phases enriched in SM. Sezgin *et al.* reported similar observations using GUVs comprised of DOPC/SM/Chol. The diffusion coefficient obtained by FCS was 10-fold for L_d in comparison to Lo domains, determined to be 5 $\mu m^2/s$ and 0.5 $\mu m^2/s$, respectively, indicating a higher fluidity for L_d portions of GUVs.[153]

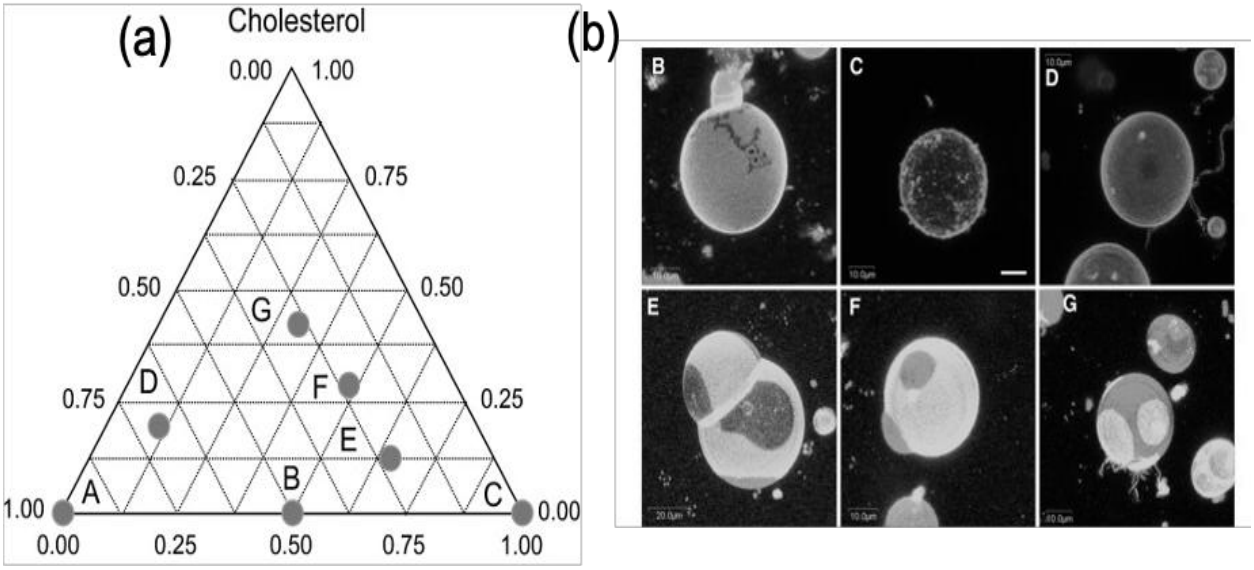

Figure 1.22. Formation of lipid phase domains in GUVs. (a) Ternary phase diagram of DOPC/SM/Chol at 23 °C. (b) Confocal images of GUVs of varied lipid compositions labelled with bodipy-Chol and Dil-C_{12}. Scale bar, 10 μm. Figure reproduced from reference.[152]

Other lipid models, such SLBs were equally used to explore the impact of lipid phases on the diffusion coefficient of particles. For instance, Woodward and Kelly used FCS to determine the diffusion coefficient of lipid in L_d and Lo phases on glass supported lipid bilayers. The diffusion of DPPE-TR was 4.9 $\mu m^2/s$ reported for lipid bilayers comprised of DPPC (L_d). The addition of DiPhyPC and cholesterol to DPPC caused the formation of L_d and L_o phases, which altered the diffusion of DPPE in Ld phase to 2.4 $\mu m^2/s$. [154] These observations indicate that the diffusion coefficient of molecules in Lo domains is significantly lower than the diffusion in Ld phases due to the enhanced lateral packing of lipids in Lo phases.

Along with domain formation, it has been suggested that membranes might rearrange the lipid membranes in a way that the special coincidence of domains at both leaflets. This interdigitation in believed to be implicated in nanodomains organization and to be involved in several events such signalling[155], proteins co-localization[156], immunological responses[157] and protein insertion to membrane[158]. The phase-segregation and co-localisation is usually studied by computation simulation using phenomenolical free energies. For instance, Reigada studied the effect of carbon tails of saturated lipids on domain registration (*Figure 1.23*). The lipid bilayers were comprised of

unsaturated DUPC, saturated DLPC or DSPC and cholesterol. He observed that bilayer containing short-tailed DLPC resulted in domain registration, while long-tailed DSPC results in anti-registration. However, the diffusion of PC lipids in ordered phases was observed to be higher in the anti-registration configuration, to be 5.1 $\mu m^2/s$, than in registration configuration, 4.3 $\mu m^2/s$. The diffusion of lipids in L_d phases was 8.8 $\mu m^2/s$ and 8.1 $\mu m^2/s$ for the membranes with DLPC and DSPS, respectively.[159]

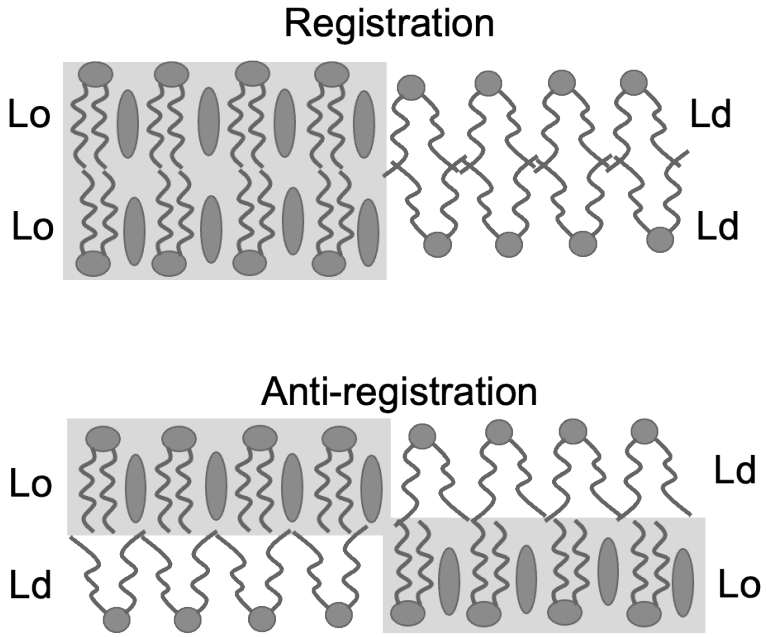

Figure 1.23. Schematic representation of ternary lipid membranes segregated in Ld and Lo domains containing saturated lipid (elongated), unsaturated lipids (shot) and cholesterol (grey disks). Two configurations can be obtained: phase registration (upper diagram) and anti-registration (bottom diagram).

- Transmembrane asymmetry

In addition to lateral segregation of lipids observed in lipid domains and plasma membranes, cell membranes were observed to have an asymmetric transmembrane composition, i.e., each leaflet has a different composition. This was firstly introduced in 1972 when the asymmetric composition of erythrocyte cells was revealed, indicating that lipid membranes were more complex than previously thought.[160] For example, many phospholipids, such as PC and SM are located predominantly in the extracellular lipid leaflet of cells. Amino phospholipids, such PI and PS, are

mostly present in the cytosolic lipid leaflet.[161,162] Other example are gangliosides, which reside at the extracellular leaflet of plasma membranes.[163,164]

The regulation of lipid asymmetry is carefully controlled in the living plasma membrane. Membrane proteins such ATPase regulate lipid sidedness of PS and PE in cytoplasm leaflet.[165] The functional roles for asymmetric phospholipid distribution have been suggested, for instance, structural and regulatory proteins such annexin[166], protein kinase C[167] and spectrin[168] are localized to the cytoplasmic leaflet due to their interaction with PS. In contrast, the disruption of lipid asymmetry exposes PS to the extracellular environment. This can generate, for example, a procoagulant surface on platelets which triggers macrophage recognition of apoptotic cells.[165] Therefore, transmembrane lipid asymmetry contributes to the cell complexity and has been a challenge to be consider as a key factor in more realistic biomimetic models.

The interdigitation between lipid leaflets is also believed to occur and be important in asymmetric membranes.[162] Perhaps the simplest method to study lipid asymmetry is using supported lipid bilayers in which experimental observation of interleaflet coupling has been observed. For example, Wan *et al*. showed that supported lipid bilayers exhibit more ordered domains in asymmetric lipid bilayers containing PC/PE/PS/chol in outer leaflet and PC/SM/chol in the inner leaflet than in symmetric lipid bilayers containing PC/SM/chol. They highlighted that PC/PE/PS/chol membranes are not able to segregate in lipid phases into their own, and phase separation was only observed in asymmetric bilayers.[169] The diffusion coefficient of the lipid membranes was reported in an independent study by Kiessling *et al.* Using SPT the diffusion coefficient of individual leaflets was obtained for L_o and L_d phases. The PC/SM/chol leaflet proximal leaflet to the substrate exhibited D of 0.20 $\mu m^2/s$ and 0.23 $\mu m^2/s$ for L_o and L_d, respectively. The distal leaflet comprised PC/PE/PS/chol shown diffusion coefficient of 0.18 $\mu m^2/s$ and 0.16 $\mu m^2/s$ for L_o and L_d. The reason for this difference is not clear. However, the interaction of the bilayer with the substrate might introduce inherent interactions that could affect the lipid mobility of asymmetric phases.[170] Also, using asymmetric GUVs prepared by lipid exchange with MβCD, Chiantia *et al*. showed that after exchange of SM from GUVs the lateral diffusion of lipids in the asymmetric lipid bilayer was reduced.[47] Interestingly, Chang and London observed that phase separation in LUVs show higher domain separation after SM exchange with

MβCD.[79] Therefore, it is clear that the transversal asymmetry of lipid bilayers and domain registration can alter the phase separation and the diffusion coefficient of lipid molecules.

However, lipids are dynamic and can diffuse from one layer to another, in a movement known as "flip-flop" or transversal diffusion. Although significantly slower than translational diffusion, flip-flop can be affected by temperature and membrane composition. Small molecules, such cholesterol, are expected to diffuse freely from one leaflet to the other.[171] Lipid phases may alter this dynamic process as it has been suggested more loosely packed phases (L_d) is enabling.[172] Many efforts have been made to quantify the rate of flip-flop in lipid models, indicating that the loss of lipid asymmetry in lipid systems depends mainly on the lipid phase (L_o, S or L_d) is expected to maintain several hours below the T_m of lipids as previously reported.[46,172,173] For instance, Kiessling *et al*. shouw that supported lipid bilayers lost their asymmetry over 15 hours in a uniform bilayer. Therefore, LB/VF bilayers could be used for 2 to 3 hours.[170] Using MSLBs, Robinson et al. explored the lateral assembly of Annexin V at asymmetric lipid bilayer contain DOPS. They reported that the no appreciable Annexin binding was observed over the first 21h when DOPS was asymmetrically distributed in the inner lipid leaflet.[37]

Other aspects may affect the diffusivity of lipid molecules and proteins in lipid membranes. For example, the inclusion of membrane proteins might represent an obstacle to lipid diffusivity, affecting the affect the diffusion of lipid. Ramadurai *et al*. studied the effect of membrane proteins on the diffusivity of lipids and proteins in GUVs. They observed that the mobility of lipids and proteins was reduced up to two fold with the increase of protein concentration.[145] In addition, Frick *et al*., shown a that the diffusion of proteins in plasma membranes was reduced when total protein content was increased.[174]

Overall, lipid asymmetry is an important physical property of membranes responsible for maintaining biological activities of cells. The dynamic environment of lipid membranes enables several intermolecular events to occur, such protein-protein, protein-lipid and lipid-lipid interactions. The understanding of the lateral asymmetry as well as lipid mobility and the factors affecting the membrane fluidity are key points to unravel the functionality of proteins and lipids in artificial lipid membranes.

1.4.3. Techniques used to measure the lateral diffusion of membrane constituents

In order to observe and quantify the motion of individual molecules, single molecule techniques have permitted understanding the two-dimensional (2D) movement of molecules within a lipid membrane but also the three-dimensional (3D) diffusivity of molecules in the cytoplasm as well as membrane bound molecules. A variety of experimental techniques have been employed to determine the diffusion coefficient of membrane constituents, therefore, making it a widely interrogated parameter of membrane dynamics and organization.[44] Over the years, different single molecule microscopy techniques have been employed to access the diffusivity of membrane constitutes, such Single Particle Tracking (SPT), Fluorescence Recovery After Photobleaching (FRAP) and Fluorescence Correlation Spectroscopy (FCS).

SPT is a single molecule technique that records the position of a fluorescent tracer molecule at certain time intervals. The molecule is imaged, and its trajectory is recorded as a series of time steps using a camera-based system. STP is performed by using an optical tag, such as gold nanoparticles[175] or with single fluorophores.[176] The mean square displacement is calculated based on the trajectory of the particle. In the case of random motion, SPT analysis can provide the diffusion coefficient of the particles and type of diffusion (*Figure 1.24*). However, the use of large particles could alter the mobility of molecule of interest.

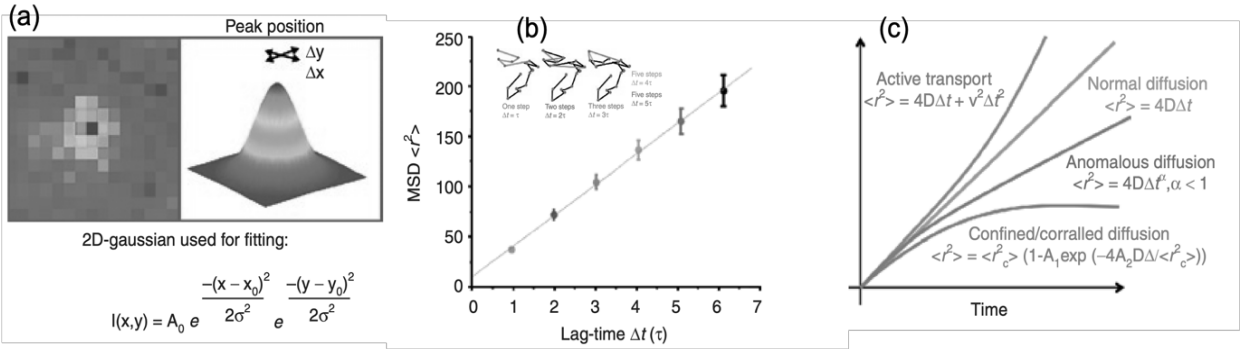

Figure 1.24. Tracking and mean-square displacement (MSD) obtained by SPT. (a) Single particle is present in the excitation volume with x and y coordinates. Central position of particle is obtained from 2D-Gaussian function. (b) MSD plots of trajectory showing the distances travelled by the particle. (c) Time dependence of MSD shows different types of diffusion confinement. Figure reproduced from reference.[177]

Another technique widely used to interrogate diffusional properties of molecules in lipid membranes, FRAP uses an intense laser beam focused on a region of interest relatively large (up to several μm^2) to photobleach fluorescence labelled molecules followed by the recovery of new fluorescent molecules into bleached area. The diffusivity of fluorescence molecules can be then calculated based on the time recovery of the of fluorescence signal of dye molecules into the pre-bleached area.[178] FRAP has been widely used to study membrane diffusion in lipid models as previously described in the section 1.3. However, the technique is limited in special and temporal resolution and high concentration of fluorophores.[179]

Finally, in the work described herein, we used the single molecule fluorescence techniques of FCS/FLCS to explore the diffusional characteristics of lipid membranes, reconstituted proteins and others in MSLBs. FCS/FLCS provides information about the diffusivity of fluorescent molecules based on the of the temporal fluctuations of fluorescence intensity of fluorophores diffusing into a femtoliter volume. The temporal intensity is autocorrelated providing local information (on the length-scale of the confocal volume) about parameters including the diffusion coefficient, particle concentration, flow rate, aggregates formations and triplet lifetimes.[180] Therefore, kinetics, medium viscosity and other insights can be resolved by FCS. Particularly, the confocal volume of FCS/FLCS, typically radii of 300 nm, is smaller than the aperture of microcavities, which correspond to approximately 2 μm, of which allows the interrogation of pore-supported lipid bilayer away of the interference of the substrate.

FCS/FLCS technique is discussed in more details in the section 1.5.3. However, it is important to highlight that FCS/FLCS provides some important advantages compared to SPT or FRAP. First, the femtoliter confocal volume of FCS/FLCS provides a significantly better special and temporal resolution and FRAP. This is particularly important to the dimension of cavities, which allow the interrogation of individual pores away from the hindered diffusion of rim supported bilayer. In addition, FCS/FLCS is a non-destructive to the fluorescent molecules which can be used to interrogate local molecule concentration and kinetic data.[44] Another aspect of FCS/FLCS is the low concentration of fluorophores required compared to FRAP. The introduction of exogenous molecules may affect the membrane fluidity. In addition, the difference of length in measurements may led to variances on the diffusion coefficients. Guo *et al.* reported a direct comparison between

FCS and FRAP when determining the diffusion coefficient of NBD-PE in POPC bilayers supported on glass, as shown in *Figure 1.25*. The diffusion values of tagged PE obtained from FCS and FRAP were 3.1 $\mu m^2/s$ and 1.0 $\mu m^2/s$, respectively.[179] They observe that this discrepancies in diffusion values may be related to difference in area of observation for the techniques. While FCS measures the diffusion on a diffraction-limited sport of approximately 500 nm, the region of interest obtained with FRAP is 5 to 6 μm. Therefore FRAP is more likely to measure defects or other artifacts which can led to a reduced apparent diffusion.[179]

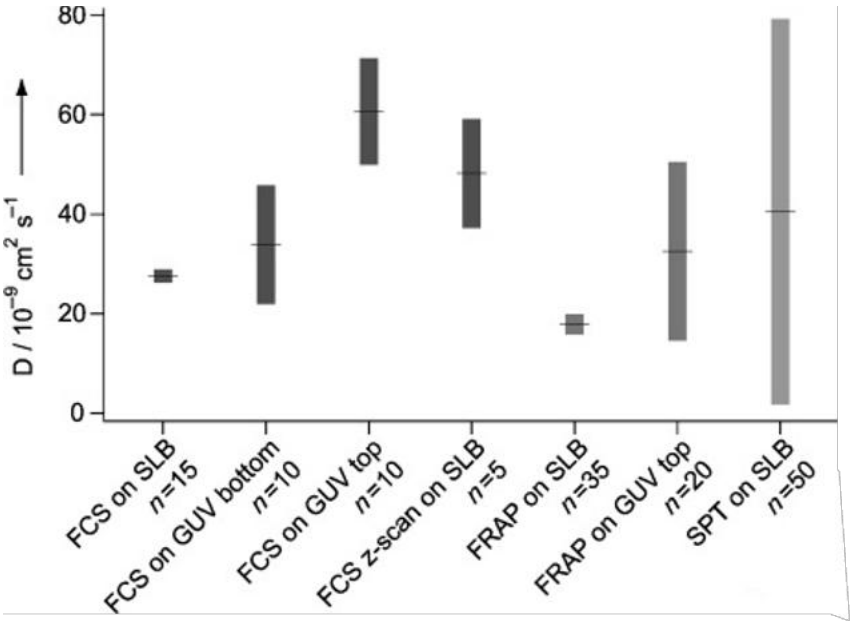

Figure 1.25. Comparison of the diffusion coefficient obtained from FCS, FRAP, and SPT on SLBs and GUVs comprised of POPC. The number of measurement is indicated by n. Figure reproduced from reference.[179]

A drawback of FCS/FLCS is that due to the low concentration of fluorophores required by the technique slower diffusing molecules might suffer from photobleaching, depending on their photostability. Therefore, an adequate mobility is a prerequisite to the successful application of FCS/FLCS measurements.

1.5. Background to Techniques used for preparation and characterization of Microcavity Supported Lipid Bilayers

Microcavity Supported lipid bilayers were prepared throughout this thesis using hybrid two-step method based on Langmuir-Blodgett followed by vesicle disruption. The membranes characterization was mainly conducted by Fluorescence and electrochemical technique. Here, the main techniques used to prepare and evaluate membrane formation and fluidity, protein binding and diffusivity as well as oligonucleotide delivery are reviewed.

1.5.1. Langmuir-Blodgett Lipid Transfer

The Langmuir-Blodgett (LB) methodology is based on the transfer of a monolayer film of amphiphilic molecules formed at a water/air interface to a solid substrate. Those molecules adsorbed at the water interface self-assembled into a monolayer, known as Langmuir film. Certain properties of the film, such molecular packing, density or arrangement can be varied by compressing the molecules between two barriers. Therefore, it allows the preparation of films with 2D lateral dimensional control, such interparticle distance, and can be used to build thin films of nanoparticles, silver nanowires, graphene, and others.

Phospholipids and other amphiphilic molecules re-orientate with the hydrophilic polar head group facing the water subphase while excluding the hydrophobic backbone carbon tails to air above the subphase. The accumulation of insoluble molecules to the water surface reduces the surface tension of water. It is possible to express the surface tension of a Langmuir film (Π) with the surface tension of water before monolayer (γ_o), which corresponds to 72.8 mN/m at 20 °C, and the surface tension with monolayer (γ), as shown in Equation 1.4.

$$\Pi = \gamma_0 - \gamma \qquad \text{(Equation 1.4)}$$

When compressed at constant temperature, the surface pressure of an ideal Langmuir films increases, similarly to an ideal gas compressed by a cylinder in a closed chamber. Consequently,

the relation between surface pressure and area of lipid monolayer compressed by the two barriers is an isotherm, in which the surface pressure is inversely proportional to the area of the compressed film at constant temperature. To measure the surface pressure of a subphase covered by a thin lipid film can be obtained using a Wilhemy plate. This method is based on the absolute measurement of the surface tension of the film on a plate, usually platinum or paper, partially immersed in the subphase. The variation on surface tension is converted to surface pressure using the dimensions of the plate.

Phospholipids and other amphiphilic molecules may present distinct regions of phases in the isotherm which can provide information about the monolayer at a given pressure. A typical isotherm that presents several phases formed under compression is displayed in *Figure 1.26*. The initial phase is called gas phase, due to the distance between the molecules that can diffuse freely at water/air interface, limiting their intermolecular interaction. Upon compression, the molecules intermolecular decreases and the molecules enter in a liquid-extended state (LE). Upon further compression the molecules enter in a liquid-condensed state (LC) as the intermolecular forces become stronger. With additional compression a compact ordered monolayer is formed known as solid phase (S). At this state, further compression will cause the monolayer collapse or the formation of a more stable 3D structures may occur, according to the nature of the amphiphilic molecule.

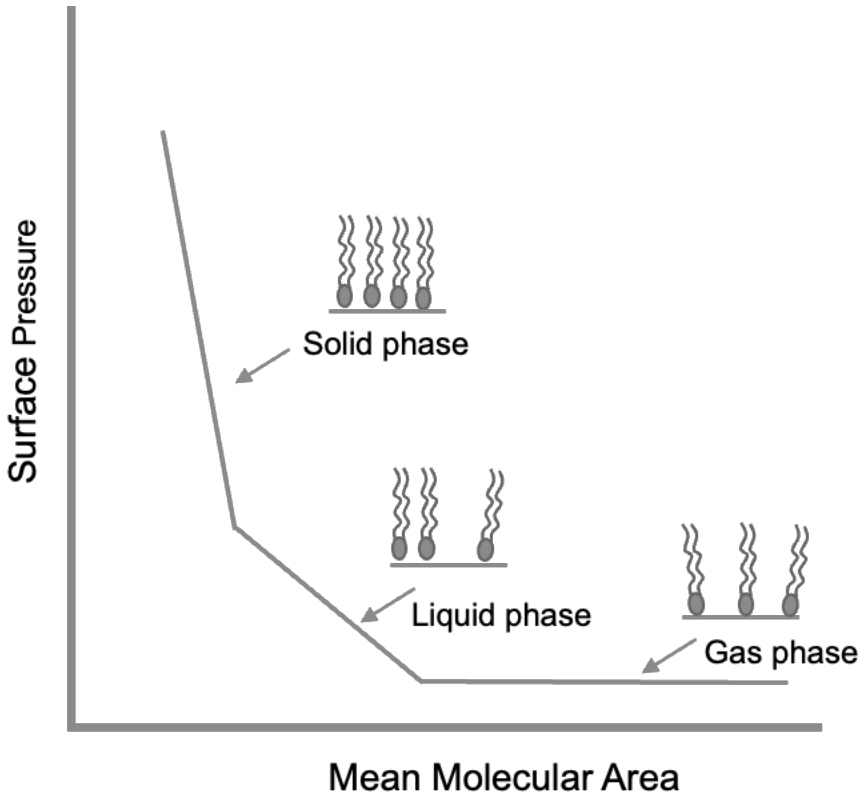

Figure 1.26 : Representation of a typical isotherm of amphiphilic molecules.

In order to form a Langmuir film and transfer it to a solid substrate, the amphiphilic material is dissolved in a volatile solvent and applied to the water subphase. The solvent should be insoluble in water and spread easily, preferentially with a positive spreading coefficient. After solvent evaporation, which could take several minutes, the monolayer film is compressed to an adequate surface pressure to avoid collapse of the film. Then, the monolayer can be vertically transferred to a hydrophilic substrate, as illustrate in *Figure 1.27*. To build a second lipid layer, the substrate can be dipped into solution vertically (LB/LB) or horizontally, known as Langmuir-Schaefer transfer (LS). These excellent combinations of LB/LB or LB/LS are two methods for creating asymmetric bilayers. The second method is a combination of the previous two methods where the monolayer is created using the LB and the upper layer is formed by liposome fusion.[181] This method allows the formation of asymmetric bilayer along with the incorporation of peripheral and transmembrane proteins. Additionally, this approach can be used to form complex artificial membranes within microfluidic systems were the exposure to air can be controlled by sealed devices.

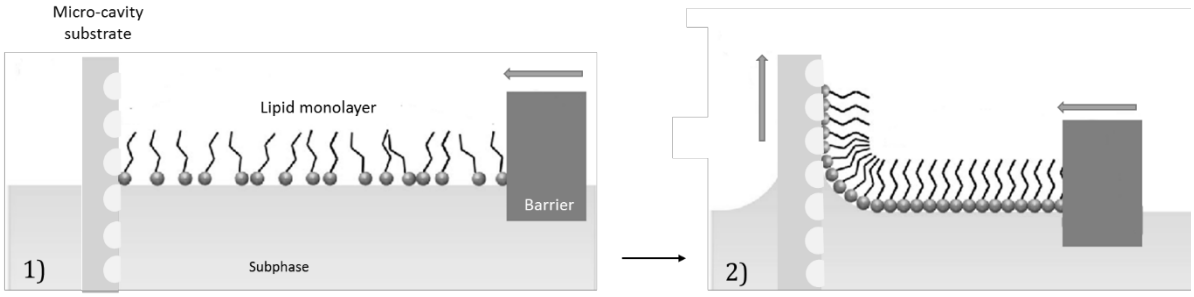

Figure 1.27. Schematic representation of lipid monolayer deposition to a microcavity array. (1) The lipid monolayer at gas phase is compressed. (2) at more ordered phase the substrate is pulled vertically while the barrier is compressing transferring the monolayer to the substrate.

1.5.2. Confocal Microscopy and Fluorescence Lifetime Imaging Microscopy

The introduction of the optical microscope in the seventeenth century has allowed scientist to observe micrometre sized particles and resolve features on this length scale therefore playing a central role in unrevealing the complex mysteries of biology, particularly to the discovery of several microorganisms, such bacteria, cells and organelles. Over the past three centuries, the introduction of new technologies has led to significantly advanced microscope designs improving dramatically image quality with minimal aberration. Although despite the advanced technologies in producing modern lens, glass-based microscopes are limited to a diffraction barrier, also called as diffraction limit of light. The theoretical description of the resolution of a microscope was introduced by Ernest Abbe in the late nineteenth century. According to Abbe, the resolution of a microscope, R_{Abbe}, or the ability of the optical instrument to distinguish between to specimens, is defined by the numerical aperture (NA) of the objective (Equation 1.5):

$$R_{Abbe} = \frac{0.61\lambda}{NA} \qquad \text{(Equation 1.5)}$$

Although the diffraction limit imposes an important constraint to optical microscopy, confocal microscopy has emerged as is one of the most used optical techniques applied to cell and biomimetic lipid bilayers imaging. The technique consists of exciting fluorophores with a collimated laser in a focal volume. In confocal microscopy a laser line coupled to an inverted microscope that excite fluorescently labelled molecules in a specific area from within a thin focal plane. The image is therefore formed by the emission intensity of fluorophores. The use of a pinhole allows confocal microscopy to exclude scattered or out-of-focus light from outside the focal plane resulting in a higher resolution image and lower background. The emitted photons collected e.g. by an avalanche detector are then converted to an electrical signal. A schematic diagram of confocal microscope is represented in *Figure 1.28*.

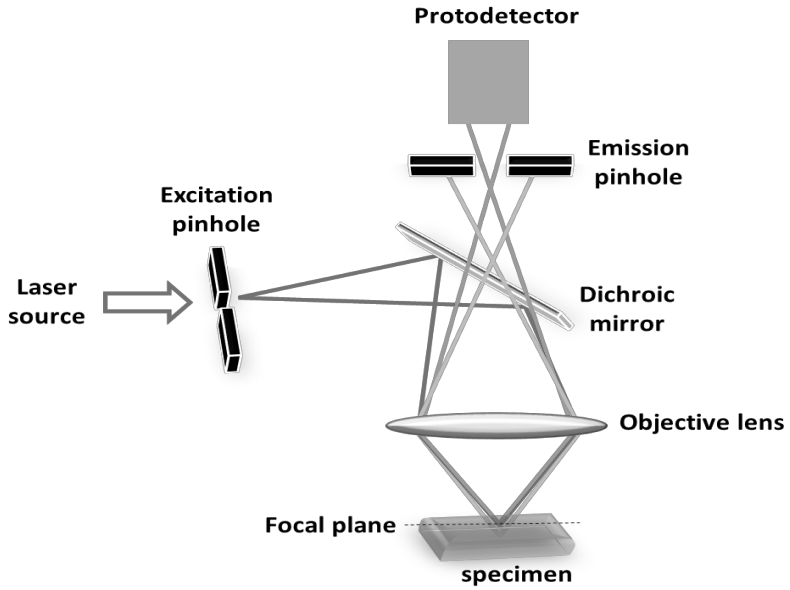

Figure 1.28. Schematic diagram of the components and optical setup in a laser scanning confocal microscope.

Confocal microscopy has been used to image fluorescence tagged supported and free-standing bilayers, as discussed in previous sections. To obtain more information about the local environment of molecules, the fluorescence collected from specimen can be also investigated by quantifying the fluorescence lifetime of the fluorophores. Fluorescence lifetime is a molecular photophysical property which provides an estimate of the average time a fluorophore persists in

excited state for before emitting a photon.[182] This can be quantified with the use of time correlated single photon counting (TCSPC) in order to determine the fluorescence lifetime of a fluorophore. This method used a time gate to measure the time passed between the excitation pulse and the emission a fluorescence photon. The synchronization of detected signals can be sorted into histogram of the fluorescence decay over time, from which the fluorescence lifetime can be determined (*Figure 1.29*).[183]

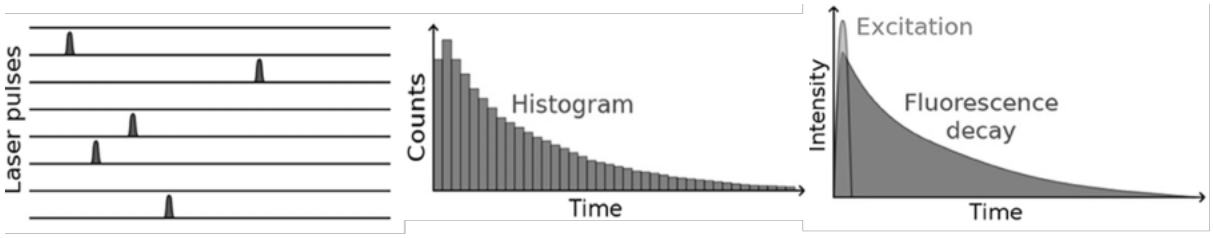

Figure 1.29. Schematic representation of TSCPC photon counting and probe lifetime. After repeatably exacting a fluorophore (left) the arriving photons are counted into a histogram (middle). The fluorescence lifetime is obtained from the calculated decay (right). Figure adapted from reference.[184]

Florescence Lifetime Imaging Microscopy (FLIM) is a technique that maps as images the lifetime decay of emitted photons from fluorescence molecules across a sample. In order to obtain a lifetime image, the lifetime of photons is related to individual pixels, which can generate a false-colour image. Based on the fluorescence lifetime of fluorophores, many properties can be inferred. For example, Stockl *et al*. studied lateral lipid segregation the influence using FLIM. They observed that the at different lipidic environments the lifetime of C6-NBD-PC changed, showing two lifetimes: one associated to liquid disordered phases (Ld) to be approximately 6.5 ns, and another related to liquid ordered phases around, which was higher than the previous at 12.1 ns (*Figure 1.30*).[183]

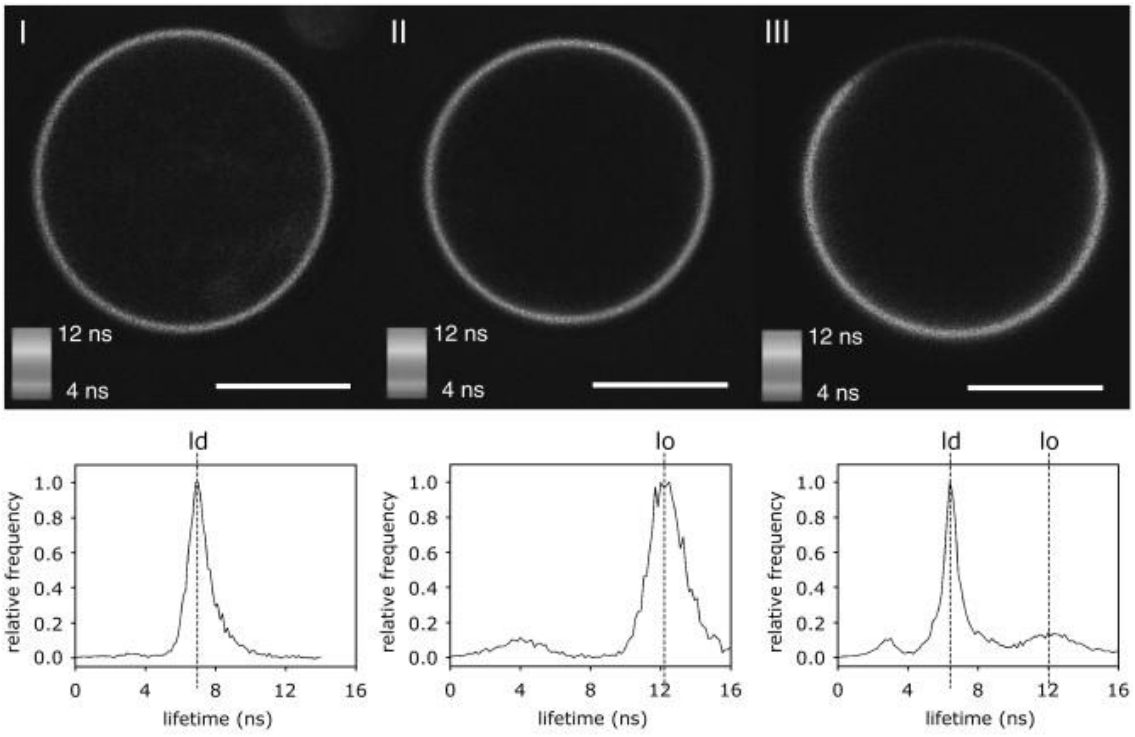

Figure 1.30. Fluorescence lifetime images of GUV comprised of combinations of DOPC/SM/Chol tagged withC6-NBD-PC. (I) pure DOPC. (II) DOPC/SM/Chol (1/1/8). (III) DOPC/SM/Chol (1/1/1). The lipid domains are observed based on the difference of lifetime of tagged lipid with different composition. The diagrams indicated the relative intensity of C6-NBD-PC lifetimes at each lipid concentration.[183]

1.5.3. Lipid bilayer characterisation by Fluorescence Lifetime Correlation Spectroscopy

As previously discussed in the section 1.4.1, FCS monitors the fluctuation in fluorescence signal from fluorophores as they diffuse through a focal volume of a confocal microscope. Under equilibrium conditions, the fluctuations are quantified by auto-correlating the intensity signal collected after exciting fluorescent molecules. When inside the confocal volume, the fluorescence fluctuations are described by a Poisson distribution, reflecting the probability that a given molecule residing in the focal volume at time t is still present after a time lag $t + \tau$. These fluctuations reflect the translational dynamics of the molecule. FCS is usually used in Chemistry and Biology to study the dynamic of biomolecular processes such as protein-protein interactions, surface binding and lipid dynamics in model and cell membranes.

The intensity fluctuations (F) of the fluorophore are generated as the molecule diffuses into and out of the confocal volume. Once inside the confocal volume fluorophore is excited by the light source and emitting photons. This in-and-out dynamic process is recorded over time. In order to obtain quantitative information about the molecular dynamics, the fluorescence intensity fluctuations are autocorrelated by comparing the intensity fluctuations at time t to the fluctuations at time (t + τ) with the average fluctuations denoted ⟨F⟩, such that Equation 1.6 and 1.7:

$$\delta F(t) = \langle F \rangle - F(t) \qquad \text{(Equation 1.6)}$$

$$\delta F(t + \tau) = \langle F \rangle - F(t + \tau) \qquad \text{(Equation 1.7)}$$

The autocorrelation decay is then obtained by the Equation 1.8.

$$G(t) = \frac{\langle \delta F(t)\, \delta F(t + \tau) \rangle}{\langle F \rangle^2} \qquad \text{(Equation 1.8)}$$

This allows to compare the signal at time t to the signal at time (t + τ), averaging the similarity of the signal throughout the time. This can be observed as for over shorter time intervals, fluorophores in the detection volume will travel short distances, not changing the intensity of the fluorescence signal. The signal shows a high degree of self-similarity, which is reflected as a high autocorrelation for small lag times. By increasing the time intervals, fluorescent molecules travel further distances, exiting and entering the confocal volume several times, leading to large changes in the fluorescence signal. Therefore, the degree of self-similarity of the signal is now low and the auto-correlation curve decays to zero at large lag times. The shape of the curve provides information on the time-scale diffusion processes by fitting to an adequate model. Faster moving molecules spend less time within the confocal volume so the autocorrelated curve decays to zero quicker than for slow diffusing molecules (*Figure 1.31*).

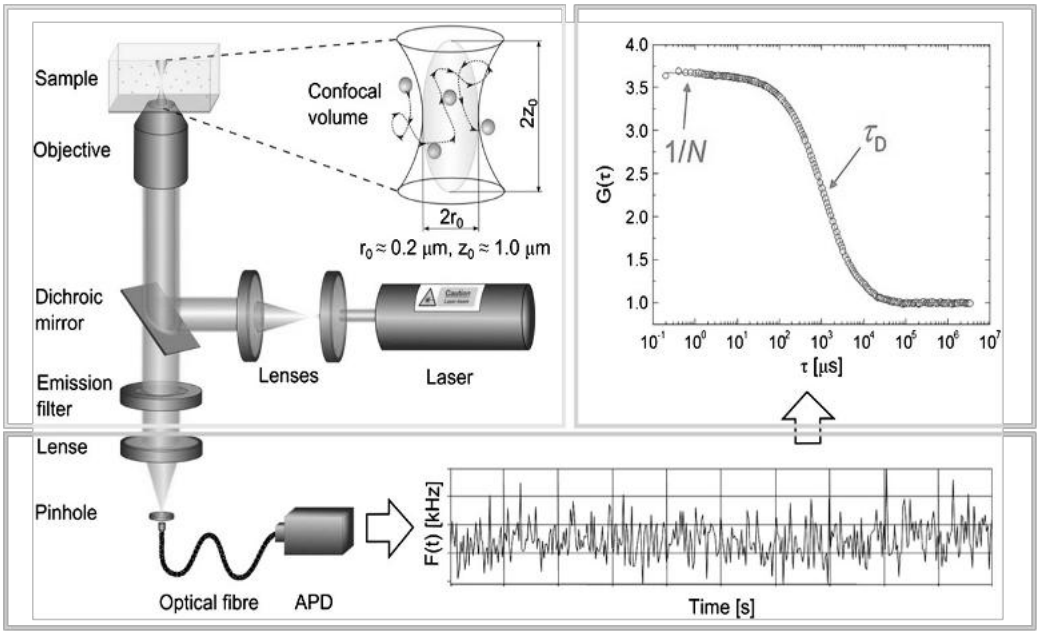

Figure 1.31. Schematic representation of a confocal apparatus adapted for FCS measurements. Detection of fluorescence fluctuations recorded over time and the autocorrelated function indicates the transit time τ_D and number of molecules (N) in the confocal volume. Figure adapted from reference. [185]

The two principal parameters that can be extracted from the autocorrelation curves are the concentration and the transit time of the fluorophores. The first is indicated by the amplitude of the auto correlation curves. At low concentration, the relative fluctuations of the intensity signal are higher, so the amplitude of the auto-correlation curve is high. At high concentration, the relative fluctuations are lower, therefore the amplitude of auto-correlation curve is lower, indicating that auto-correlation's amplitude is inversely proportional to the fluorophore concentration within the confocal volume (*Figure 1.32*).

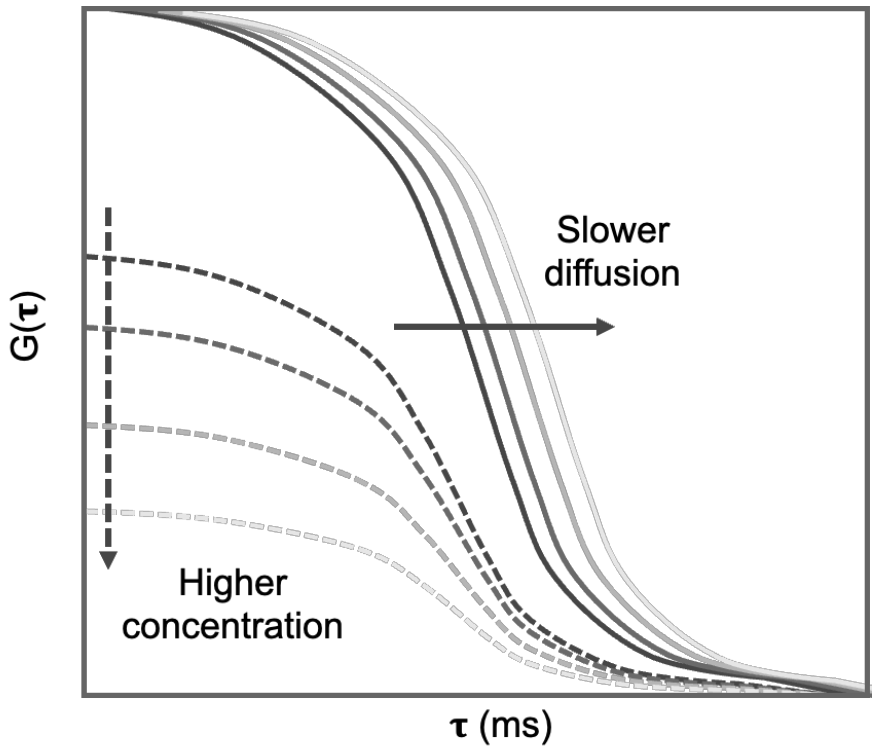

Figure 1.32. Relationship between concentration of molecules and time spent within the confocal volume. The dash curves indicate the effect concentration of molecules in the confocal volume on the amplitude of the autocorrelated curves. The solid curves indicate the dependence of transit time (τ) to the diffusivity of molecules.

The transit time (τ_D) is defined as the average time that a molecule requires to cross the confocal volume. In a 2-dimensional system, such a lipid bilayer, τ_D can be obtained by fitting the curve calculated defined by Eq. 6 to the following equation 1.9:

$$\boldsymbol{G}(\tau) = \mathbf{1} + \frac{\mathbf{1}}{\boldsymbol{N}} \frac{\mathbf{1}}{\mathbf{1} + (\frac{\tau}{\tau_{\boldsymbol{D}}})^{\boldsymbol{\alpha}}} \qquad \text{(Equation 1.9)}$$

Here, N is the number of molecules in the confocal volume, and α is the anomalous parameter related to deviation of the diffusional regime from Brownian motion, i.e., if the MSD does not

relate linearly to time, as illustrated in section 1.4.1. The fitted autocorrelation curve in *Figure 1.32* illustrates the amplitude of the autocorrelation curve (1/N) and the half-decay (τ_D). The diffusion time is calculated once the radius of the observation volume (ω) is known using the following Equation 1.10.

$$D = \frac{\omega^2}{4\tau_D} \qquad \text{(Equation 1.10)}$$

- Fluorescence Lifetime Correlation Spectroscopy

Since its introduction, FCS has been widely used to determine the diffusion co-efficient of molecules in 3D and 2D systems. However, conventional might FCS suffer from numerous issues. For instance, unwanted signal components, such distortions caused by scattered excitation light, detector thermal noise and afterpulsing may be incurred in the auto-correlation curves.[186] To overcome these issues, a variant of conventional FCS was proposed by Jorg Enderlein which is a fusion of FCS with Time-Correlated Single Photon Counting (TCSPC), called Fluorescence Lifetime Correlation Spectroscopy (FLCS), a modified method that uses picosecond time-resolved fluorescence detection to separate the different FCS contributions.[187] With this systems, a specimen is excited with a short laser pulse and the difference between the excitation pulse to the arrival of a emitted photon is synchronized and recorded by the TCSPC. By repeating this process several times, a statistically significant distribution of time differences is obtained and the lifetime of the contribution species can be determined.[188] In FLCS the TCSPC histogram is used to assign the luminescent lifetime of the probe, which occurs in a different timescale than the lifetime of unwanted components, the noise can be removed from the auto-correlation curve, therefore improving the accuracy of the diffusional data. For instance, FLCS can be used to avoid detector afterpulsing, providing a better data fitting (*Figure 1.33*).

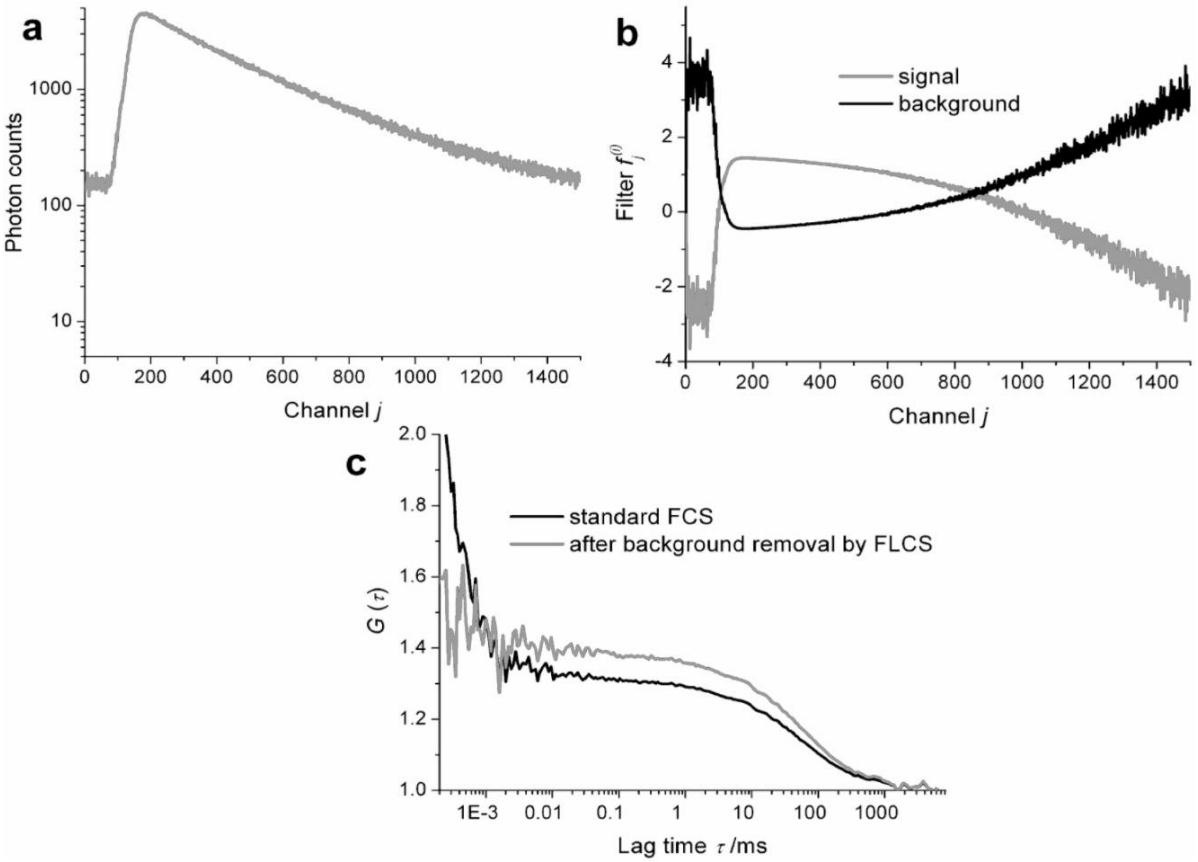

Figure 1.33. Comparison between classical FCS and FLCS auto-correlation curves after removing afterpulsing from detectors. a) TCSPC histogram of photon detection times. b) FLCS filters calculated for fluorescence signal (grey) and for uniform background (black). c) Autocorrelation function calculated without (black) and with FLCS filtering (gray). Figure reproduced from reference.[186]

In summary, FCS and FLCS are powerful single molecule methods that can be applied to study the properties of lipid bilayers, such the lateral mobility of lipids and to evaluate the binding and aggregation of proteins at the membrane surface. In this thesis FLCS technique was applied to determine the diffusion coefficient of fluorescently tagged lipids, peripheral proteins, membrane proteins and DNA within a variety of lipid bilayer compositions in MSLBs.

1.5.4. Electrochemical Impedance Spectroscopy

Electronic properties of biological membranes can be investigated by Electrochemical Impedance Spectroscopy (EIS). Those properties, such diffusion coefficients, adsorption mechanism, charge transfer resistances and capacitances, are relevant to the understanding of several phenomena in artificial models. The investigation of electrochemical impedance of lipid bilayers can reveal important information about reactions at the membrane level such diffusion reactions, e.g., passive/active permeation of the membrane,[126] capacitive-resistive behaviour to drugs or proteins,[134] and stability of the lipid film.

As an electrochemical technique, EIS relies on the fluctuations of the potential applied to a circuit (E) and electrical current (i). The relation between i, E and the natural resistance (R) against the electron flow of an electrical component is described by Ohm's Law, which defines the linear dependence to the voltage, current and the resistance and current across two points of a circuit (Equation 1.11).[189]

$$E = i\,R \qquad \text{(Equation 1.11)}$$

Even though, Ohm's law has been very important for the understanding of electrical properties of circuits and components, it is applied only when the current flows in one direction or Direct Current (DC) or to ideal resistors. When the electric charge changes the direction periodically in Alternated Current (AC) (Figure 1.34), Ohm's law has to be adapted to the oscillating current and voltage. Ideally an ideal resistor exhibits a resistance that is independent of applied AC. However, in most of the cases the resistance is dependent on the current flow frequency. Complex systems such supported lipid bilayers induce a phase separation to the applied AC. The phase shift (θ) between I and E reflects the impedance of the system.

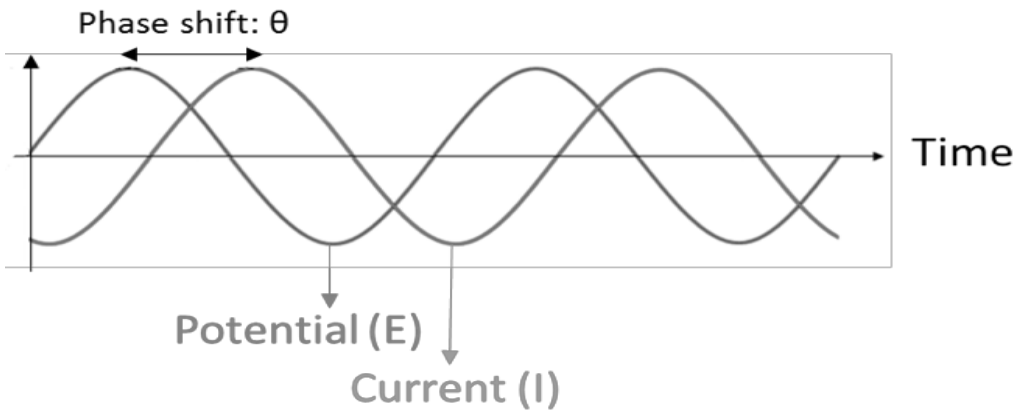

Figure 1.34. Phase separation (θ) between I and E to applied AC current voltage.

The phase shift of E and I is related to the impedance of the electrical components by the oscillating character of the applied E (Equation 1.12).

$$E_t = E_0 \, sin \, (\omega t) \qquad \text{(Equation 1.12)}$$

Where E_t is the potential applied at time t, E_0 is the amplitude of the signal and ω is the radial frequency. The response signal (Equation 1.13) is shifted by θ and has amplitude I_0.

$$I_t = I_0 \, sin \, (\omega t \, + \, \theta) \qquad \text{(Equation 1.13)}$$

Similar to Ohm's Law, the relation between E and I allow to calculate the impedance of the system (Equation 1.14).

$$Z = \frac{E_t}{I_t} = \frac{E_t = E_0 \, sin \, (\omega t)}{I_t = I_0 \, sin(\omega t \, + \, \theta)} = \, Z_0 \, \frac{sin(\omega t)}{sin(\omega t + \, \theta)} \qquad \text{(Equation 1.14)}$$

With the Euler's relationship, the impedance can be expressed as a complex function depending exclusively on the phase shift ($\boldsymbol{\theta}$) (Equation 1.15 and 1.16).

$$E_t = E_0\, e^{(j\omega t)} \qquad \text{(Equation 1.15)}$$

$$\mathrm{I_t} = \mathrm{I_0}\, \mathrm{e}^{(\mathrm{j}\omega \mathrm{t} - \theta)} \qquad \text{(Equation 1.16)}$$

If we then apply an AC potential, a relationship for the circuit impedance can be obtained as equation 1.17.

$$\mathrm{Z}(\omega) = \frac{\mathrm{E}}{\mathrm{I}} = \mathrm{Z_0}\, \mathrm{e}^{(\mathrm{j}\theta)} = \mathrm{Z_0}(\cos\theta + \mathrm{j}\sin\theta) \qquad \text{(Equation 1.17)}$$

The impedance data obtained from EIS can be represented in two different formats, a complex plane plot, or Nyquist plot, and phase/ frequency regime, or Bode plot. The Nyquist representation (Figure 1.35a) shows the real and imaginary components of the impedance (Z) at given frequency. The length of the vector |Z| gives the total impedance and the phase shit is represented by the angle between the vector |Z| and the real component axis. The Nyquist plot can be useful tool to interrogate immediate changes on the relative resistivity, induced for example by protein binding or molecular membrane permeation. The Bode plot (Figure 1.35b), however, plots the frequency in relation to the phase shift (θ) response.

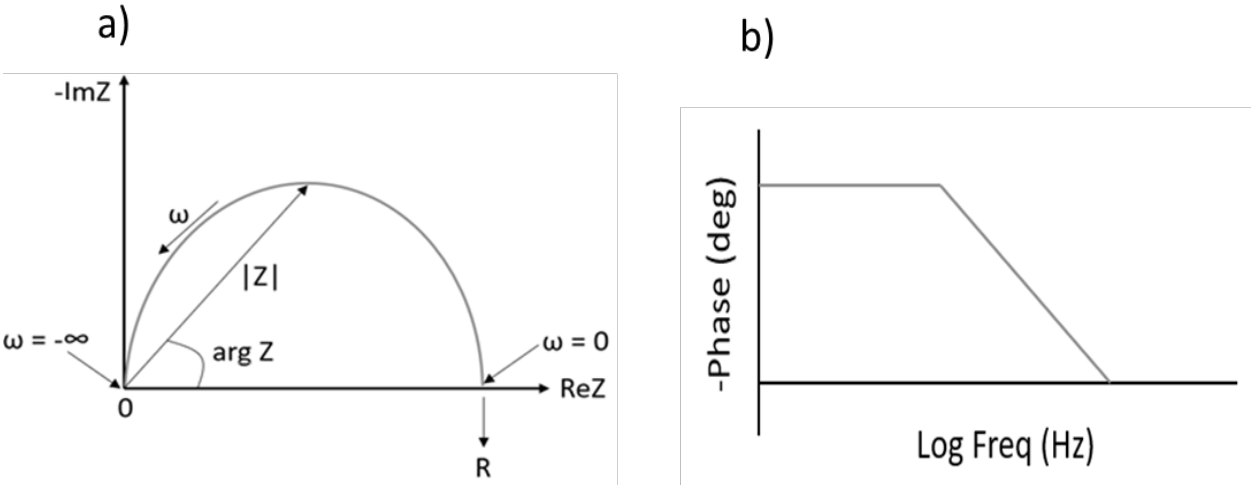

Figure 1.35. Schematic representation of a) Nyquist plot with – ImZ vs. ReZ, whereby frequencies range from $\omega = -\infty$ to $\omega = 0$. b) Bode plot representing the phase shift $\boldsymbol{\theta}$ versus the frequency ω applied.

In order to obtain quantitative information about the lipid bilayer resistivity and capacitance, the Nyquist and Bode plots have to be fitted to an equivalent circuit model (ECM). This is obtained by combining a series of electrical components, such resistances and capacitors. Lipid bilayers can be approximated as series of electrical components, such parallel plate capacitors and resistors, embedded in aqueous environment. The simplest model applied to supported lipid bilayers on planar electrodes in shown in Figure 1.36. Basically, the electrochemical properties of the bilayer are obtained by using a resistor in parallel to a capacitor.

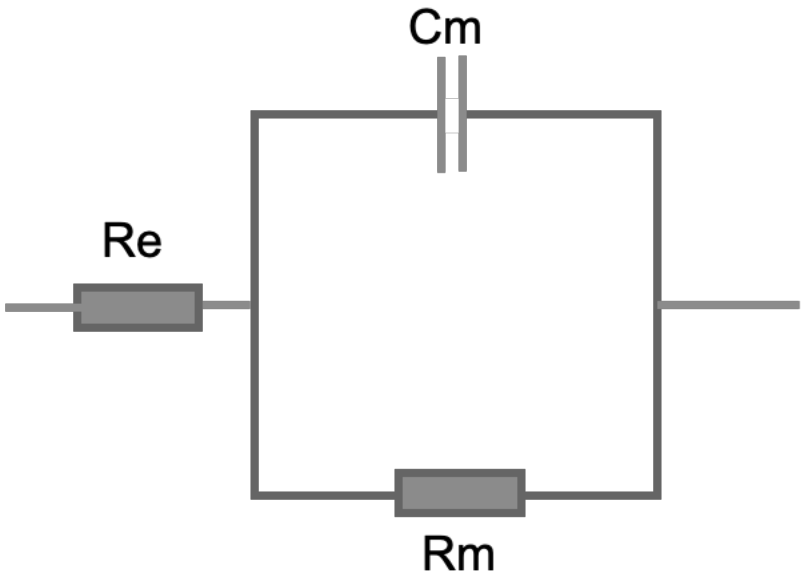

Figure 1.36. A typical equivalent circuit model (ECM) used for fitting EIS of SLBs.

An example of an ECM used for fitting the impedance data of a lipid bilayers spanned micro-cavity array if shown in Figure 1.37. It contains the solution resistance (R_{sol}) connected to complex circuit containing the resistor (R_{bl}) and a capacitor (CPE_{bl}) that corresponds to the electric and dielectric properties of the membrane spanned across the gold surface. There is an additional component for the microcavities array which contain the cavities resistance (R_{cav}) and also has a capacitor for the electronic double layer (CPE_{dl}) that is formed between the electrode and the surrounding electrolyte. The impedance spectra were fit to an equivalent circuit as described earlier previously.[126,134]

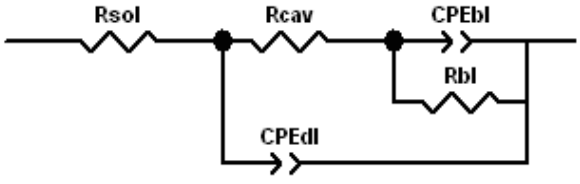

Figure 1.37. Equivalent circuit model (ECM) used to fit EIS data obtained for microcavity supported lipid bilayer.[126,134]

The constant phase elements (CPE) were used in the equivalent circuit to provide to account for the heterogeneity of the SLBs in microcavity array. The impedance of the CPE can be calculated using Equation 1.18:

$$Z_{CPE} = \frac{1}{Q(j\omega)^{\beta}} \qquad \text{(Equation 1.18)}$$

Where Q is the magnitude of the capacitance of the CPE, the exponent **β** varies from 0 to 1 and represents the CPE capacitive behaviour of the CPE, e.g., CPE may behave as ideal capacitor as closer to unit and **ω** is the angular frequency. An illustration of the electrochemical cell used in this work is displayed in Figure 1.38.

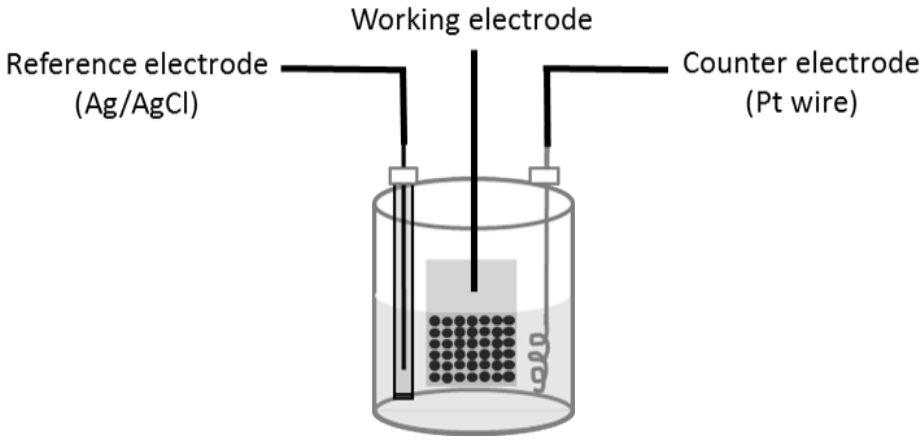

Figure 1.38. Schematic of the three-electrode cell used for EIS measurement of gold-MSLBs. The lipid bilayers were spanned following the protocol as previously described in chapter 2.

In summary, EIS is a very useful technique that can provide quantitative information about the electrochemical properties of a interfacial. For this reason, EIS is employed in this project for characterising the protein binding to lipid bilayers. This is discussed in more detail in the chapters 3 and 4. When prepared in gold, the arrays can work as an electrode permitting electrochemical

interrogation of membrane behavior.[126] Such stable microarray supported bilayers hold great potential as analytical devices for protein binding and detection.

1.6. Conclusion and scope of this thesis.

Cell membranes are complex and dynamic systems in which the development of model lipid membranes have a key role in elucidating the fundamental interactions between the cell membrane components including the distribution and behaviour of lipids and sterols themselves and As many proteins have specific receptors at cell membrane level, exploring their properties using more realistic in vitro models, that resolve the key components of the membrane from the complex cell environment can provide useful insights. into the role of the phospholipid membrane and its components as well as the receptor in protein association and binding.

In this thesis a versatile microcavity supported lipid bilayer to investigate the lipid dynamics, protein diffusion, interactions and aggregation, and DNA delivery. By using a microcavity array, we aimed to create supported lipid bilayers that mimic the lipid fluidity observed in free liposomes in a substrate like manner spanned over microcavity arrays. These Microcavity Supported Lipid Bilayers, or MSLBs, were prepared by a hybrid of Langmuir-Blodgett lipid transfer with liposomes fusion in a sealed microfluidic environment. The diffusivity of lipid membranes was investigated by FLCS and the impact of membrane asymmetry on lipid diffusivity was evaluated. Within this project, glycolipids were incorporated to MSBLs and its interaction to peripheral proteins, such Cholera Toxin and Hemagglutinin were investigated by FLCS and EIS. The binding of galectin-3 to integrin was evaluated in presence of glycolipids. The incorporation of an ion channel membrane protein was investigated using bacteriorhodopsin. A light activated proton gate was build and the impact of bR concentration, pH and frequency of activation were evaluated. Finally, MSLBs were tested as a novel oligonucleotide-bed to study gene delivery.

1.7. References

(1) Singer, S. J.; Nicolson, G. L. The Fluid Mosaic Model of the Structure of Cell Membranes. *Science* 1972, *175* (4023), 720–731.
(2) Fadeel, B.; Xue, D. The Ins and Outs of Phospholipid Asymmetry in the Plasma Membrane: Roles in Health and Disease. *Critical Reviews in Biochemistry and Molecular Biology* 2009, *44* (5), 264–277.
(3) Brown, D. A. Lipid Rafts, Detergent-Resistant Membranes, and Raft Targeting Signals. *Physiology (Bethesda)* 2006, *21*, 430–439.
(4) Schroeder, R. J.; Ahmed, S. N.; Zhu, Y.; London, E.; Brown, D. A. Cholesterol and Sphingolipid Enhance the Triton X-100 Insolubility of Glycosylphosphatidylinositol-Anchored Proteins by Promoting the Formation of Detergent-Insoluble Ordered Membrane Domains. *J. Biol. Chem.* 1998, *273* (2), 1150–1157.
(5) Khomami, B.; Niroomand, H.; Venkatesan, G. A. Lipid-Detergent Phase Transitions During Detergent-Mediated Liposome Solubilization.
(6) Bacia, K.; Schwille, P.; Kurzchalia, T. Sterol Structure Determines the Separation of Phases and the Curvature of the Liquid-Ordered Phase in Model Membranes. *PNAS* 2005, *102* (9), 3272–3277.
(7) Jacobson, K.; Papahadjopoulos, D. Phase Transitions and Phase Separations in Phospholipid Membranes Induced by Changes in Temperature, PH, and Concentration of Bivalent Cations. *Biochemistry* 1975, *14* (1), 152–161.
(8) Munro, S. Lipid Rafts: Elusive or Illusive? *Cell* 2003, *115* (4), 377–388.
(9) Ingólfsson, H. I.; Melo, M. N.; van Eerden, F. J.; Arnarez, C.; Lopez, C. A.; Wassenaar, T. A.; Periole, X.; de Vries, A. H.; Tieleman, D. P.; Marrink, S. J. Lipid Organization of the Plasma Membrane. *J. Am. Chem. Soc.* 2014, *136* (41), 14554–14559.
(10) Levental, I.; Levental, K.; Heberle, F. Lipid Rafts: Controversies Resolved, Mysteries Remain. *Trends Cell Biol* 2020, *30* (5), 341–353.
(11) Russell; Hertz; McMillan. *Biology The Dynamic Science*; Cengage: Canada, 2017; Vol. 4.
(12) Yu, R. K.; Tsai, Y.-T.; Ariga, T.; Yanagisawa, M. Structures, Biosynthesis, and Functions of Gangliosides—An Overview. *J Oleo Sci* 2011, *60* (10), 537–544.
(13) Gangliosides of the Vertebrate Nervous System. *Journal of Molecular Biology* 2016, *428* (16), 3325–3336.
(14) Marushchak, D.; Gretskaya, N.; Mikhalyov, I.; Johansson, L. B.-Å. Self-Aggregation – an Intrinsic Property of GM1 in Lipid Bilayers. *Molecular Membrane Biology* 2007, *24* (2), 102–112.
(15) Park, W.-J.; Park, J.-W. The Role of Sphingolipids in Endoplasmic Reticulum Stress. *FEBS Letters* 2020, *594* (22), 3632–3651.
(16) Todeschini, A. R.; Hakomori, S. Functional Role of Glycosphingolipids and Gangliosides in Control of Cell Adhesion, Motility, and Growth, through Glycosynaptic Microdomains. *Biochim Biophys Acta* 2008, *1780* (3), 421–433.
(17) Yuan, C.; Furlong, J.; Burgos, P.; Johnston, L. J. The Size of Lipid Rafts: An Atomic Force Microscopy Study of Ganglioside GM1 Domains in Sphingomyelin/DOPC/Cholesterol Membranes. *Biophysical journal* 2002, *82* (5), 2526–2535.
(18) Sameni, S.; Malacrida, L.; Tan, Z.; Digman, M. A. Alteration in Fluidity of Cell Plasma Membrane in Huntington Disease Revealed by Spectral Phasor Analysis. *Sci Rep* 2018, *8*.
(19) Ackerman, G. A.; Wolken, K. W.; Gelder, F. B. Surface Distribution of Monosialoganglioside GM1 on Human Blood Cells and the Effect of Exogenous GM1 and Neuraminidase on Cholera Toxin Surface Labeling. A Quantitative Immunocytochemical Study. *J. Histochem. Cytochem.* 1980, *28* (10), 1100–1112.
(20) Kitov, P. I.; Sadowska, J. M.; Mulvey, G.; Armstrong, G. D.; Ling, H.; Pannu, N. S.; Read, R. J.; Bundle, D. R. Shiga-like Toxins Are Neutralized by Tailored Multivalent Carbohydrate Ligands. *Nature* 2000, *403* (6770), 669–672.

(21) Basu, I.; Mukhopadhyay, C. Insights into Binding of Cholera Toxin to GM1 Containing Membrane. *Langmuir* 2014, *30* (50), 15244–15252.
(22) Reig, N.; van der Goot, F. G. About Lipids and Toxins. *FEBS letters* 2006, *580* (23), 5572–5579.
(23) Rustmeier, N. H.; Strebl, M.; Stehle, T. The Symmetry of Viral Sialic Acid Binding Sites–Implications for Antiviral Strategies. *Viruses* 2019, *11* (10), 947.
(24) Suzuki, Y. Sialobiology of Influenza: Molecular Mechanism of Host Range Variation of Influenza Viruses. *Biological and Pharmaceutical Bulletin* 2005, *28* (3), 399–408.
(25) Zhang, J.; Li, Q.; Wu, Y.; Wang, D.; Xu, L.; Zhang, Y.; Wang, S.; Wang, T.; Liu, F.; Zaky, M. Y.; Hou, S.; Liu, S.; Zou, K.; Lei, H.; Zou, L.; Zhang, Y.; Liu, H. Cholesterol Content in Cell Membrane Maintains Surface Levels of ErbB2 and Confers a Therapeutic Vulnerability in ErbB2-Positive Breast Cancer. *Cell Commun Signal* 2019, *17*.
(26) The Role of Cholesterol in Membrane Fusion. *Chemistry and Physics of Lipids* 2016, *199*, 136–143.
(27) The Influence of Cholesterol on Phospholipid Membrane Curvature and Bending Elasticity. *Biophysical Journal* 1997, *73* (1), 267–276.
(28) Ciancaglini, P.; Simão, A. M. S.; Bolean, M.; Millán, J. L.; Rigos, C. F.; Yoneda, J. S.; Colhone, M. C.; Stabeli, R. G. Proteoliposomes in Nanobiotechnology. *Biophys Rev* 2012, *4* (1), 67–81.
(29) Steck, T. L. THE ORGANIZATION OF PROTEINS IN THE HUMAN RED BLOOD CELL MEMBRANE. *J Cell Biol* 1974, *62* (1), 1–19.
(30) Lodish, H.; Berkman, A.; Zipursky, S. *Molecular Cell Biology*, Fourth.; W.H. Freeman: New York, 2000.
(31) Lee, A. G. How Lipids Affect the Activities of Integral Membrane Proteins. *Biochimica et Biophysica Acta (BBA) - Biomembranes* 2004, *1666* (1), 62–87.
(32) Contreras, F.-X.; Ernst, A. M.; Wieland, F.; Brügger, B. Specificity of Intramembrane Protein–Lipid Interactions. *Cold Spring Harb Perspect Biol* 2011, *3* (6).
(33) van Klompenburg, W.; Nilsson, I.; von Heijne, G.; de Kruijff, B. Anionic Phospholipids Are Determinants of Membrane Protein Topology. *EMBO J* 1997, *16* (14), 4261–4266.
(34) Bogdanov, M.; Heacock, P. N.; Dowhan, W. A Polytopic Membrane Protein Displays a Reversible Topology Dependent on Membrane Lipid Composition. *EMBO J* 2002, *21* (9), 2107–2116.
(35) Powl, A. M.; East, J. M.; Lee, A. G. Importance of Direct Interactions with Lipids for the Function of the Mechanosensitive Channel MscL. *Biochemistry* 2008, *47* (46), 12175–12184.
(36) Powl, A. M.; East, J. M.; Lee, A. G. Anionic Phospholipids Affect the Rate and Extent of Flux through the Mechanosensitive Channel of Large Conductance MscL. *Biochemistry* 2008, *47* (14), 4317–4328.
(37) Robinson, J.; Berselli, G. B.; Ryadnov, M. G.; Keyes, T. E. Annexin V Drives Stabilization of Damaged Asymmetric Phospholipid Bilayers. *Langmuir* 2020, *36* (19), 5454–5465.
(38) Swairjo, M. A.; Concha, N. O.; Kaetzel, M. A.; Dedman, J. R.; Seaton, B. A. Ca 2+ -Bridging Mechanism and Phospholipid Head Group Recognition in the Membrane-Binding Protein Annexin V. *Nature Structural Biology* 1995, *2* (11), 968–974.
(39) Myers, V. B.; Haydon, D. A. Ion Transfer across Lipid Membranes in the Presence of Gramicidin A: II. The Ion Selectivity. *Biochimica et Biophysica Acta (BBA) - Biomembranes* 1972, *274* (2), 313–322.
(40) Tawfik, H.; Puza, S.; Seemann, R.; Fleury, J.-B. Transport Properties of Gramicidin A Ion Channel in a Free-Standing Lipid Bilayer Filled With Oil Inclusions. *Front. Cell Dev. Biol.* 2020, *8*.
(41) Wolf, A. A.; Jobling, M. G.; Saslowsky, D. E.; Kern, E.; Drake, K. R.; Kenworthy, A. K.; Holmes, R. K.; Lencer, W. I. Attenuated Endocytosis and Toxicity of a Mutant Cholera Toxin with Decreased Ability To Cluster Ganglioside GM1 Molecules. *Infect. Immun.* 2008, *76* (4), 1476–1484.
(42) A, R. W.; B, J. S.; C, A. N. P.; B, A. P. S.; D, L. C.; B, B. I. S. *Evidence for Cholera Aggregation on GM1-Decorated Lipid Bilayers*.
(43) Cebecauer, M.; Hof, M.; Amaro, M. Impact of GM 1 on Membrane-Mediated Aggregation/Oligomerization of β -Amyloid: Unifying View. *Biophysical Journal* 2017.

(44) Macháň, R.; Hof, M. Lipid Diffusion in Planar Membranes Investigated by Fluorescence Correlation Spectroscopy. *Biochimica et Biophysica Acta (BBA) - Biomembranes* 2010, *1798* (7), 1377–1391.
(45) Reich, C.; Horton, M. R.; Krause, B.; Gast, A. P.; Rädler, J. O.; Nickel, B. Asymmetric Structural Features in Single Supported Lipid Bilayers Containing Cholesterol and GM1 Resolved with Synchrotron X-Ray Reflectivity. *Biophysical Journal* 2008, *95* (2), 657–668.
(46) Visco, I.; Chiantia, S.; Schwille, P. Asymmetric Supported Lipid Bilayer Formation via Methyl-β-Cyclodextrin Mediated Lipid Exchange: Influence of Asymmetry on Lipid Dynamics and Phase Behavior. *Langmuir* 2014, *30* (25), 7475–7484.
(47) Chiantia, S.; Schwille, P.; Klymchenko, A. S.; London, E. Asymmetric GUVs Prepared by MβCD-Mediated Lipid Exchange: An FCS Study. *Biophys J* 2011, *100* (1), L1–L3.
(48) Cheng, H.-T.; Megha, null; London, E. Preparation and Properties of Asymmetric Vesicles That Mimic Cell Membranes: Effect upon Lipid Raft Formation and Transmembrane Helix Orientation. *J. Biol. Chem.* 2009, *284* (10), 6079–6092.
(49) Czogalla, A.; Grzybek, M.; Jones, W.; Coskun, Ü. Validity and Applicability of Membrane Model Systems for Studying Interactions of Peripheral Membrane Proteins with Lipids. *Biochimica et Biophysica Acta (BBA) - Molecular and Cell Biology of Lipids* 2014, *1841* (8), 1049–1059.
(50) Bozzuto, G.; Molinari, A. Liposomes as Nanomedical Devices. *Int J Nanomedicine* 2015, *10*, 975–999.
(51) Patil, Y. P.; Jadhav, S. Novel Methods for Liposome Preparation. *Chemistry and Physics of Lipids* 2014, *177*, 8–18.
(52) Akbarzadeh, A.; Rezaei-Sadabady, R.; Davaran, S.; Joo, S. W.; Zarghami, N.; Hanifehpour, Y.; Samiei, M.; Kouhi, M.; Nejati-Koshki, K. Liposome: Classification, Preparation, and Applications. *Nanoscale Res Lett* 2013, *8* (1), 102.
(53) Lasic, D. D. The Mechanism of Vesicle Formation. *Biochem J* 1988, *256* (1), 1–11.
(54) Hope, M. J.; Bally, M. B.; Webb, G.; Cullis, P. R. Production of Large Unilamellar Vesicles by a Rapid Extrusion Procedure. Characterization of Size Distribution, Trapped Volume and Ability to Maintain a Membrane Potential. *Biochimica et Biophysica Acta (BBA) - Biomembranes* 1985, *812* (1), 55–65.
(55) Equipment https://avantilipids.com/ (accessed 2019 -05 -12).
(56) Patra, J. K.; Das, G.; Fraceto, L. F.; Campos, E. V. R.; Rodriguez-Torres, M. del P.; Acosta-Torres, L. S.; Diaz-Torres, L. A.; Grillo, R.; Swamy, M. K.; Sharma, S.; Habtemariam, S.; Shin, H.-S. Nano Based Drug Delivery Systems: Recent Developments and Future Prospects. *Journal of Nanobiotechnology* 2018, *16* (1), 71.
(57) Sercombe, L.; Veerati, T.; Moheimani, F.; Wu, S. Y.; Sood, A. K.; Hua, S. Advances and Challenges of Liposome Assisted Drug Delivery. *Front Pharmacol* 2015, *6*.
(58) Tros de Ilarduya, C.; Sun, Y.; Düzgüneş, N. Gene Delivery by Lipoplexes and Polyplexes. *Eur J Pharm Sci* 2010, *40* (3), 159–170.
(59) Abeyratne, E.; Tharmarajah, K.; Freitas, J. R.; Mostafavi, H.; Mahalingam, S.; Zaid, A.; Zaman, M.; Taylor, A. Liposomal Delivery of the RNA Genome of a Live-Attenuated Chikungunya Virus Vaccine Candidate Provides Local, but Not Systemic Protection After One Dose. *Front Immunol* 2020, *11*, 304.
(60) Richner, J. M.; Himansu, S.; Dowd, K. A.; Butler, S. L.; Salazar, V.; Fox, J. M.; Julander, J. G.; Tang, W. W.; Shresta, S.; Pierson, T. C.; Ciaramella, G.; Diamond, M. S. Modified MRNA Vaccines Protect against Zika Virus Infection. *Cell* 2017, *168* (6), 1114-1125.e10.
(61) Cai, X.; Jiang, Y.; Lin, M.; Zhang, J.; Guo, H.; Yang, F.; Leung, W.; Xu, C. Ultrasound-Responsive Materials for Drug/Gene Delivery. *Front Pharmacol* 2020, *10*.
(62) Rigaud, J.-L.; Lévy, D. Reconstitution of Membrane Proteins into Liposomes. In *Methods in Enzymology*; Liposomes, Part B; Academic Press, 2003; Vol. 372, pp 65–86.

(63) Rigaud, J.-L.; Pitard, B.; Levy, D. Reconstitution of Membrane Proteins into Liposomes: Application to Energy-Transducing Membrane Proteins. *Biochimica et Biophysica Acta (BBA) - Bioenergetics* 1995, *1231* (3), 223–246.
(64) Darszon, A.; Vandenberg, C. A.; Schönfeld, M.; Ellisman, M. H.; Spitzer, N. C.; Montal, M. Reassembly of Protein-Lipid Complexes into Large Bilayer Vesicles: Perspectives for Membrane Reconstitution. *Proc Natl Acad Sci U S A* 1980, *77* (1), 239–243.
(65) Darszon, A.; Vandenberg, C. A.; Ellisman, M. H.; Montal, M. Incorporation of Membrane Proteins into Large Single Bilayer Vesicles. Application to Rhodopsin. *Journal of Cell Biology* 1979, *81* (2), 446–452.
(66) Rigaud, J. L.; Bluzat, A.; Buschlen, S. Incorporation of Bacteriorhodopsin into Large Unilamellar Liposomes by Reverse Phase Evaporation. *Biochemical and Biophysical Research Communications* 1983, *111* (2), 373–382.
(67) Sejwal, K.; Chami, M.; Baumgartner, P.; Kowal, J.; Müller, S. A.; Stahlberg, H. Proteoliposomes – a System to Study Membrane Proteins under Buffer Gradients by Cryo-EM. *Nanotechnology Reviews* 2017, *6* (1), 57–74.
(68) Camolezi, F. L.; Daghastanli, K. R. P.; Magalhães, P. P.; Pizauro, J. M.; Ciancaglini, P. Construction of an Alkaline Phosphatase–Liposome System: A Tool for Biomineralization Study. *The International Journal of Biochemistry & Cell Biology* 2002, *34* (9), 1091–1101.
(69) Simão, A. M. S.; Yadav, M. C.; Narisawa, S.; Bolean, M.; Pizauro, J. M.; Hoylaerts, M. F.; Ciancaglini, P.; Millán, J. L. Proteoliposomes Harboring Alkaline Phosphatase and Nucleotide Pyrophosphatase as Matrix Vesicle Biomimetics. *J Biol Chem* 2010, *285* (10), 7598–7609.
(70) Rigos, C. F.; de Lima Santos, H.; Yoneda, J. S.; Montich, G.; Maggio, B.; Ciancaglini, P. Cytoplasmatic Domain of Na,K-ATPase α-Subunit Is Responsible for the Aggregation of the Enzyme in Proteoliposomes. *Biophysical Chemistry* 2010, *146* (1), 36–41.
(71) Paternostre, M. T.; Roux, M.; Rigaud, J. L. Mechanisms of Membrane Protein Insertion into Liposomes during Reconstitution Procedures Involving the Use of Detergents. 1. Solubilization of Large Unilamellar Liposomes (Prepared by Reverse-Phase Evaporation) by Triton X-100, Octyl Glucoside, and Sodium Cholate. *Biochemistry* 1988, *27* (8), 2668–2677.
(72) Wang, Z.; Bai, J.; Xu, Y. The Effect of Charged Lipids on Bacteriorhodopsin Membrane Reconstitution and Its Photochemical Activities. *Biochemical and Biophysical Research Communications* 2008, *371* (4), 814–817.
(73) Reeves, J. P.; Dowben, R. M. Formation and Properties of Thin-Walled Phospholipid Vesicles. *Journal of Cellular Physiology* 1969, *73* (1), 49–60.
(74) Morales-Penningston, N. F.; Wu, J.; Farkas, E. R.; Goh, S. L.; Konyakhina, T. M.; Zheng, J. Y.; Webb, W. W.; Feigenson, G. W. GUV Preparation and Imaging: Minimizing Artifacts. *Biochim Biophys Acta* 2010, *1798* (7), 1324–1332.
(75) Korlach, J.; Schwille, P.; Webb, W. W.; Feigenson, G. W. Characterization of Lipid Bilayer Phases by Confocal Microscopy and Fluorescence Correlation Spectroscopy. *PNAS* 1999, *96* (15), 8461–8466.
(76) Bagatolli, L. A.; Gratton, E. Two-Photon Fluorescence Microscopy Observation of Shape Changes at the Phase Transition in Phospholipid Giant Unilamellar Vesicles. *Biophysical Journal* 1999, *77* (4), 2090–2101.
(77) Gaul, V.; Lopez, S. G.; Lentz, B. R.; Moran, N.; Forster, R. J.; Keyes, T. E. The Lateral Diffusion and Fibrinogen Induced Clustering of Platelet Integrin AIIbβ3 Reconstituted into Physiologically Mimetic GUVs. *Integrative Biology* 2015, *7* (4), 402–411.
(78) Kahya, N.; Scherfeld, D.; Bacia, K.; Schwille, P. Lipid Domain Formation and Dynamics in Giant Unilamellar Vesicles Explored by Fluorescence Correlation Spectroscopy. *Journal of Structural Biology* 2004, *147* (1), 77–89.
(79) Cheng, H.-T.; London, E. Preparation and Properties of Asymmetric Large Unilamellar Vesicles: Interleaflet Coupling in Asymmetric Vesicles Is Dependent on Temperature but Not Curvature. *Biophys J* 2011, *100* (11), 2671–2678.

(80) Enoki, T. A.; Feigenson, G. W. Asymmetric Bilayers by Hemifusion: Method and Leaflet Behaviors. *Biophysical Journal* 2019, *117* (6), 1037–1050.
(81) Hu, P. C.; Li, S.; Malmstadt, N. Microfluidic Fabrication of Asymmetric Giant Lipid Vesicles. *ACS Appl Mater Interfaces* 2011, *3* (5), 1434–1440.
(82) Steinkühler, J.; De Tillieux, P.; Knorr, R. L.; Lipowsky, R.; Dimova, R. Charged Giant Unilamellar Vesicles Prepared by Electroformation Exhibit Nanotubes and Transbilayer Lipid Asymmetry. *Scientific Reports* 2018, *8* (1), 11838.
(83) Sot, J.; Ibarguren, M.; Busto, J. V.; Montes, L.-R.; Goñi, F. M.; Alonso, A. Cholesterol Displacement by Ceramide in Sphingomyelin-Containing Liquid-Ordered Domains, and Generation of Gel Regions in Giant Lipidic Vesicles. *FEBS Letters* 2008, *582* (21), 3230–3236.
(84) Peyret, A.; Ibarboure, E.; Meins, J.-F. L.; Lecommandoux, S. Asymmetric Hybrid Polymer–Lipid Giant Vesicles as Cell Membrane Mimics. *Advanced Science* 2018, *5* (1), 1700453.
(85) Marquardt, D.; Geier, B.; Pabst, G. Asymmetric Lipid Membranes: Towards More Realistic Model Systems. *Membranes* 2015, *5* (2), 180–196.
(86) Heinemann, F.; Schwille, P. Preparation of Micrometer-Sized Free-Standing Membranes. *ChemPhysChem* 2011, *12* (14), 2568–2571.
(87) J. Booth, M.; Schild, V. R.; G. Downs, F.; Bayley, H. Functional Aqueous Droplet Networks. *Molecular BioSystems* 2017, *13* (9), 1658–1691.
(88) Lee, S. Good to the Last Drop: Interfacial Droplet Chemistry, from Crystals to Biological Membranes. *Acc. Chem. Res.* 2018, *51* (10), 2524–2534.
(89) Hwang, W. L.; Chen, M.; Cronin, B.; Holden, M. A.; Bayley, H. Asymmetric Droplet Interface Bilayers. *J. Am. Chem. Soc.* 2008, *130* (18), 5878–5879.
(90) Haylock, S.; Friddin, M. S.; Hindley, J. W.; Rodriguez, E.; Charalambous, K.; Booth, P. J.; Barter, L. M. C.; Ces, O. Membrane Protein Mediated Bilayer Communication in Networks of Droplet Interface Bilayers. *Communications Chemistry* 2020, *3* (1), 1–8.
(91) Gross, L. C. M.; Heron, A. J.; Baca, S. C.; Wallace, M. I. Determining Membrane Capacitance by Dynamic Control of Droplet Interface Bilayer Area. *Langmuir* 2011, *27* (23), 14335–14342.
(92) Bayley, H.; Cronin, B.; Heron, A.; Holden, M. A.; Hwang, W.; Syeda, R.; Thompson, J.; Wallace, M. Droplet Interface Bilayers. *Mol Biosyst* 2008, *4* (12), 1191–1208.
(93) Barriga, H. M. G.; Booth, P.; Haylock, S.; Bazin, R.; Templer, R. H.; Ces, O. Droplet Interface Bilayer Reconstitution and Activity Measurement of the Mechanosensitive Channel of Large Conductance from Escherichia Coli. *Journal of The Royal Society Interface* 2014, *11* (98), 20140404.
(94) Rosholm, K. R.; Baker, M. A. B.; Ridone, P.; Nakayama, Y.; Rohde, P. R.; Cuello, L. G.; Lee, L. K.; Martinac, B. Activation of the Mechanosensitive Ion Channel MscL by Mechanical Stimulation of Supported Droplet-Hydrogel Bilayers. *Scientific Reports* 2017, *7* (1), 45180.
(95) Mueller, P.; Rudin, D. O.; Tien, H. T.; Wescott, W. C. Reconstitution of Cell Membrane Structure in Vitro and Its Transformation into an Excitable System. *Nature* 1962, *194*, 979–980.
(96) Winterhalter, M. Black Lipid Membranes. *Current Opinion in Colloid & Interface Science* 2000, *5* (3), 250–255.
(97) Demarche, S.; Sugihara, K.; Zambelli, T.; Tiefenauer, L.; Vörös, J. Techniques for Recording Reconstituted Ion Channels. *Analyst* 2011, *136* (6), 1077–1089.
(98) Castellana, E. T.; Cremer, P. S. Solid Supported Lipid Bilayers: From Biophysical Studies to Sensor Design. *Surface Science Reports* 2006, *61* (10), 429–444.
(99) Miller, C.; Racker, E. Ca++-Induced Fusion of Fragmented Sarcoplasmic Reticulum with Artificial Planar Bilayers. *J Membr Biol* 1976, *30* (3), 283–300.
(100) Gómez-Lagunas, F.; Peña, A.; Liévano, A.; Darszon, A. Incorporation of Ionic Channels from Yeast Plasma Membranes into Black Lipid Membranes. *Biophysical Journal* 1989, *56* (1), 115–119.
(101) Veatch, W. R.; Mathies, R.; Eisenberg, M.; Stryer, L. Simultaneous Fluorescence and Conductance Studies of Planar Bilayer Membranes Containing a Highly Active and Fluorescent Analog of Gramicidin A. *Journal of Molecular Biology* 1975, *99* (1), 75–92.

(102) Ide, T.; Takeuchi, Y.; Yanagida, T. Development of an Experimental Apparatus for Simultaneous Observation of Optical and Electrical Signals from Single Ion Channels. *Single Molecules* 2002, *3* (1), 33–42.
(103) Tsemperouli, M.; Amstad, E.; Sakai, N.; Matile, S.; Sugihara, K. Black Lipid Membranes: Challenges in Simultaneous Quantitative Characterization by Electrophysiology and Fluorescence Microscopy. *Langmuir* 2019, *35* (26), 8748–8757.
(104) Khan, M.; Dosoky, N.; Williams, J. Engineering Lipid Bilayer Membranes for Protein Studies. *International Journal of Molecular Sciences* 2013, *14* (11), 21561–21597.
(105) Mech-Dorosz, A.; Heiskanen, A.; Bäckström, S.; Perry, M.; Muhammad, H. B.; Hélix-Nielsen, C.; Emnéus, J. A Reusable Device for Electrochemical Applications of Hydrogel Supported Black Lipid Membranes. *Biomed Microdevices* 2015, *17* (1), 21.
(106) Lv, Z.; Banerjee, S.; Zagorski, K.; Lyubchenko, Y. L. Supported Lipid Bilayers for Atomic Force Microscopy Studies. *Methods Mol Biol* 2018, *1814*, 129–143.
(107) Melby, E. S.; Mensch, A. C.; Lohse, S. E.; Hu, D.; Orr, G.; Murphy, C. J.; Hamers, R. J.; Pedersen, J. A. Formation of Supported Lipid Bilayers Containing Phase-Segregated Domains and Their Interaction with Gold Nanoparticles. *Environ. Sci.: Nano* 2016, *3* (1), 45–55.
(108) Rascol, E.; Devoisselle, J.-M.; Chopineau, J. The Relevance of Membrane Models to Understand Nanoparticles–Cell Membrane Interactions. *Nanoscale* 2016, *8* (9), 4780–4798.
(109) Dertinger, T.; von der Hocht, I.; Benda, A.; Hof, M.; Enderlein, J. Surface Sticking and Lateral Diffusion of Lipids in Supported Bilayers. *Langmuir* 2006, *22* (22), 9339–9344.
(110) Zhang, L.; Granick, S. Lipid Diffusion Compared in Outer and Inner Leaflets of Planar Supported Bilayers. *J. Chem. Phys.* 2005, *123* (21), 211104.
(111) Stottrup, B. L.; Veatch, S. L.; Keller, S. L. Nonequilibrium Behavior in Supported Lipid Membranes Containing Cholesterol. *Biophys J* 2004, *86* (5), 2942–2950.
(112) Kiessling, V.; Tamm, L. K. Measuring Distances in Supported Bilayers by Fluorescence Interference-Contrast Microscopy: Polymer Supports and SNARE Proteins. *Biophys J* 2003, *84* (1), 408–418.
(113) Castellana, E. T.; Cremer, P. S. Solid Supported Lipid Bilayers: From Biophysical Studies to Sensor Design. *Surface Science Reports* 2006, *61* (10), 429–444.
(114) Salafsky, J.; Groves, J. T.; Boxer, S. G. Architecture and Function of Membrane Proteins in Planar Supported Bilayers: A Study with Photosynthetic Reaction Centers. *Biochemistry* 1996, *35* (47), 14773–14781.
(115) Wang, T.; Ingram, C.; Weisshaar, J. C. Model Lipid Bilayer with Facile Diffusion of Lipids and Integral Membrane Proteins. *Langmuir* 2010, *26* (13), 11157–11164.
(116) Wang, T.; Smith, E. A.; Chapman, E. R.; Weisshaar, J. C. Lipid Mixing and Content Release in Single-Vesicle, SNARE-Driven Fusion Assay with 1–5 Ms Resolution. *Biophys J* 2009, *96* (10), 4122–4131.
(117) Tutus, M.; Rossetti, F. F.; Schneck, E.; Fragneto, G.; Förster, F.; Richter, R.; Nawroth, T.; Tanaka, M. Orientation-Selective Incorporation of Transmembrane F0F1 ATP Synthase Complex from Micrococcus Luteus in Polymer-Supported Membranes. *Macromolecular Bioscience* 2008, *8* (11), 1034–1043.
(118) Schuster, B.; Pum, D.; Sleytr, U. B. S-Layer Stabilized Lipid Membranes (Review). *Biointerphases* 2008, *3* (2), FA3.
(119) Györvary, E.; Wetzer, B.; Sleytr, U. B.; Sinner, A.; Offenhäusser, A.; Knoll, W. Lateral Diffusion of Lipids in Silane-, Dextran-, and S-Layer-Supported Mono- and Bilayers. *Langmuir* 1999, *15* (4), 1337–1347.
(120) Wagner, M. L.; Tamm, L. K. Tethered Polymer-Supported Planar Lipid Bilayers for Reconstitution of Integral Membrane Proteins: Silane-Polyethyleneglycol-Lipid as a Cushion and Covalent Linker. *Biophys J* 2000, *79* (3), 1400–1414.

(121) Hughes, A. V.; Holt, S. A.; Daulton, E.; Soliakov, A.; Charlton, T. R.; Roser, S. J.; Lakey, J. H. High Coverage Fluid-Phase Floating Lipid Bilayers Supported by ω-Thiolipid Self-Assembled Monolayers. *Journal of The Royal Society Interface* 2014, *11* (98), 20140447.
(122) Budvytyte, R.; Valincius, G.; Niaura, G.; Voiciuk, V.; Mickevicius, M.; Chapman, H.; Goh, H.-Z.; Shekhar, P.; Heinrich, F.; Shenoy, S.; Lösche, M.; Vanderah, D. J. Structure and Properties of Tethered Bilayer Lipid Membranes with Unsaturated Anchor Molecules. *Langmuir* 2013, *29* (27), 8645–8656.
(123) Wong, W. C.; Juo, J.-Y.; Lin, C.-H.; Liao, Y.-H.; Cheng, C.-Y.; Hsieh, C.-L. Characterization of Single-Protein Dynamics in Polymer-Cushioned Lipid Bilayers Derived from Cell Plasma Membranes. *J. Phys. Chem. B* 2019, *123* (30), 6492–6504.
(124) Przybylo, M.; Sýkora, J.; Humpolíčková, J.; Benda, A.; Zan, A.; Hof, M. Lipid Diffusion in Giant Unilamellar Vesicles Is More than 2 Times Faster than in Supported Phospholipid Bilayers under Identical Conditions. *Langmuir* 2006, *22* (22), 9096–9099.
(125) Simon, A.; Girard-Egrot, A.; Sauter, F.; Pudda, C.; Picollet D'Hahan, N.; Blum, L.; Chatelain, F.; Fuchs, A. Formation and Stability of a Suspended Biomimetic Lipid Bilayer on Silicon Submicrometer-Sized Pores. *Journal of Colloid and Interface Science* 2007, *308* (2), 337–343.
(126) Maher, S.; Basit, H.; Forster, R. J.; Keyes, T. E. Micron Dimensioned Cavity Array Supported Lipid Bilayers for the Electrochemical Investigation of Ionophore Activity. *Bioelectrochemistry* 2016, *112*, 16–23.
(127) Mey, I.; Stephan, M.; Schmitt, E. K.; Müller, M. M.; Ben Amar, M.; Steinem, C.; Janshoff, A. Local Membrane Mechanics of Pore-Spanning Bilayers. *J. Am. Chem. Soc.* 2009, *131* (20), 7031–7039.
(128) Steltenkamp, S.; Müller, M. M.; Deserno, M.; Hennesthal, C.; Steinem, C.; Janshoff, A. Mechanical Properties of Pore-Spanning Lipid Bilayers Probed by Atomic Force Microscopy. *Biophys J* 2006, *91* (1), 217–226.
(129) Lazzara, T. D.; Carnarius, C.; Kocun, M.; Janshoff, A.; Steinem, C. Separating Attoliter-Sized Compartments Using Fluid Pore-Spanning Lipid Bilayers. *ACS Nano* 2011, *5* (9), 6935–6944.
(130) Kocun, M.; Lazzara, T. D.; Steinem, C.; Janshoff, A. Preparation of Solvent-Free, Pore-Spanning Lipid Bilayers: Modeling the Low Tension of Plasma Membranes. *Langmuir* 2011, *27* (12), 7672–7680.
(131) Simon, A.; Gounou, C.; Tan, S.; Tiefenauer, L.; Di Berardino, M.; Brisson, A. R. Free-Standing Lipid Films Stabilized by Annexin-A5. *Biochimica et Biophysica Acta (BBA) - Biomembranes* 2013, *1828* (11), 2739–2744.
(132) Basit, H.; Gaul, V.; Maher, S.; Forster, R. J.; Keyes, T. E. Aqueous-Filled Polymer Microcavity Arrays: Versatile & Stable Lipid Bilayer Platforms Offering High Lateral Mobility to Incorporated Membrane Proteins. *The Analyst* 2015, *140* (9), 3012–3018.
(133) Ramadurai, S.; Sarangi, N. K.; Maher, S.; MacConnell, N.; Bond, A. M.; McDaid, D.; Flynn, D.; Keyes, T. E. Microcavity-Supported Lipid Bilayers; Evaluation of Drug-Lipid Membrane Interactions by Electrochemical Impedance and Fluorescence Correlation Spectroscopy. *Langmuir* 2019, *35* (24), 8095–8109.
(134) Basit, H.; Maher, S.; Forster, R. J.; Keyes, T. E. Electrochemically Triggered Release of Reagent to the Proximal Leaflet of a Microcavity Supported Lipid Bilayer. *Langmuir* 2017, *33* (27), 6691–6700.
(135) Sarangi, N. K.; Stalcup, A.; Keyes, T. E. The Impact of Membrane Composition and Co-Drug Synergistic Effects on Vancomycin Association with Model Membranes from Electrochemical Impedance Spectroscopy. *ChemElectroChem* 2020, *7* (22), 4507–4507.
(136) Mey, I.; Steinem, C.; Janshoff, A. Biomimetic Functionalization of Porous Substrates: Towards Model Systems for Cellular Membranes. *J. Mater. Chem.* 2012, *22* (37), 19348–19356.
(137) Sonnleitner, A.; Schutz, G. J.; Schmidt, T. Free Brownian Motion of Individual Lipid Molecules in Biomembranes. *Biophysical Journal* 1999, *77* (5), 2638.

(138) Watanabe, R.; Soga, N.; Yamanaka, T.; Noji, H. High-Throughput Formation of Lipid Bilayer Membrane Arrays with an Asymmetric Lipid Composition. *Scientific Reports* 2014, *4* (1), 7076.
(139) Sunshine, H.; Iruela-Arispe, M. L. Membrane Lipids and Cell Signaling. *Curr Opin Lipidol* 2017, *28* (5), 408–413.
(140) Irannejad, R.; von Zastrow, M. GPCR Signaling along the Endocytic Pathway. *Current Opinion in Cell Biology* 2014, *27*, 109–116.
(141) Axelrod, D. Lateral Motion of Membrane Proteins and Biological Function. *J. Membrain Biol.* 1983, *75* (1), 1–10.
(142) Petrov, E. P.; Schwille, P. Translational Diffusion in Lipid Membranes beyond the Saffman-Delbrück Approximation. *Biophysical Journal* 2008, *94* (5), L41–L43.
(143) Hughes, B. D.; Pailthorpe, B. A.; White, L. R. The translational and rotational drag on a cylinder moving in a membrane. *Journal of Fluid Mechanics* 1981, *110*, 349–372.
(144) Daniels, D. R.; Turner, M. S. Diffusion on Membrane Tubes: A Highly Discriminatory Test of the Saffman−Delbruck Theory. *Langmuir* 2007, *23* (12), 6667–6670.
(145) Ramadurai, S.; Holt, A.; Krasnikov, V.; van den Bogaart, G.; Killian, J. A.; Poolman, B. Lateral Diffusion of Membrane Proteins. *Journal of the American Chemical Society* 2009, *131* (35), 12650–12656.
(146) Gambin, Y.; Lopez-Esparza, R.; Reffay, M.; Sierecki, E.; Gov, N. S.; Genest, M.; Hodges, R. S.; Urbach, W. Lateral Mobility of Proteins in Liquid Membranes Revisited. *PNAS* 2006, *103* (7), 2098–2102.
(147) Guigas, G.; Weiss, M. Size-Dependent Diffusion of Membrane Inclusions. *Biophysical Journal* 2006, *91* (7), 2393–2398.
(148) Lindblom, G.; Orädd, G. Lipid Lateral Diffusion and Membrane Heterogeneity. *Biochimica et Biophysica Acta (BBA) - Biomembranes* 2009, *1788* (1), 234–244.
(149) Vaz, W. L. C.; Clegg, R. M.; Hallmann, D. Translational Diffusion of Lipids in Liquid Crystalline Phase Phosphatidylcholine Multibilayers. A Comparison of Experiment with Theory. *Biochemistry* 1985, *24* (3), 781–786.
(150) Zalba, S.; ten Hagen, T. L. M. Cell Membrane Modulation as Adjuvant in Cancer Therapy. *Cancer Treatment Reviews* 2017, *52*, 48–57.
(151) Bezlyepkina, N.; Gracià, R. S.; Shchelokovskyy, P.; Lipowsky, R.; Dimova, R. Phase Diagram and Tie-Line Determination for the Ternary Mixture DOPC/ESM/Cholesterol. *Biophys. J.* 2013, *104* (7), 1456–1464.
(152) Ariola, F. S.; Li, Z.; Cornejo, C.; Bittman, R.; Heikal, A. A. Membrane Fluidity and Lipid Order in Ternary Giant Unilamellar Vesicles Using a New Bodipy-Cholesterol Derivative. *Biophysical Journal* 2009, *96* (7), 2696–2708.
(153) Sezgin, E.; Levental, I.; Grzybek, M.; Schwarzmann, G.; Mueller, V.; Honigmann, A.; Belov, V. N.; Eggeling, C.; Coskun, Ü.; Simons, K.; Schwille, P. Partitioning, Diffusion, and Ligand Binding of Raft Lipid Analogs in Model and Cellular Plasma Membranes. *Biochimica et Biophysica Acta (BBA) - Biomembranes* 2012, *1818* (7), 1777–1784.
(154) Woodward, X.; Kelly, C. V. Single-Lipid Dynamics in Phase-Separated Supported Lipid Bilayers. *Chemistry and Physics of Lipids* 2020, *233*, 104991.
(155) Simons, K.; Toomre, D. Lipid Rafts and Signal Transduction. *Nature Reviews Molecular Cell Biology* 2000, *1* (1), 31–39.
(156) Suzuki, K. G. N.; Fujiwara, T. K.; Edidin, M.; Kusumi, A. Dynamic Recruitment of Phospholipase Cγ at Transiently Immobilized GPI-Anchored Receptor Clusters Induces IP3–Ca2+ Signaling: Single-Molecule Tracking Study 2. *J Cell Biol* 2007, *177* (4), 731–742.
(157) Chiantia, S.; London, E. Acyl Chain Length and Saturation Modulate Interleaflet Coupling in Asymmetric Bilayers: Effects on Dynamics and Structural Order. *Biophys J* 2012, *103* (11), 2311–2319.
(158) Janmey, P. A.; Kinnunen, P. K. J. Biophysical Properties of Lipids and Dynamic Membranes. *Trends in Cell Biology* 2006, *16* (10), 538–546.

(159) Reigada, R. Alteration of Interleaflet Coupling Due to Compounds Displaying Rapid Translocation in Lipid Membranes. *Scientific Reports* 2016, *6* (1), 32934.
(160) Verkleij, A. J.; Zwaal, R. F. A.; Roelofsen, B.; Comfurius, P.; Kastelijn, D.; van Deenen, L. L. M. The Asymmetric Distribution of Phospholipids in the Human Red Cell Membrane. A Combined Study Using Phospholipases and Freeze-Etch Electron Microscopy. *Biochimica et Biophysica Acta (BBA) - Biomembranes* 1973, *323* (2), 178–193.
(161) Bretscher, M. S. Asymmetrical Lipid Bilayer Structure for Biological Membranes. *Nature New Biol.* 1972, *236* (61), 11–12.
(162) Fujimoto, T.; Parmryd, I. Interleaflet Coupling, Pinning, and Leaflet Asymmetry—Major Players in Plasma Membrane Nanodomain Formation. *Front. Cell Dev. Biol.* 2017, *4*.
(163) Mikhalyov, I.; Samsonov, A. Lipid Raft Detecting in Membranes of Live Erythrocytes. *Biochimica et Biophysica Acta (BBA) - Biomembranes* 2011, *1808* (7), 1930–1939.
(164) Panasiewicz, M.; Domek, H.; Hoser, G.; Kawalec, M.; Pacuszka, T. Structure of the Ceramide Moiety of GM1 Ganglioside Determines Its Occurrence in Different Detergent-Resistant Membrane Domains in HL-60 Cells. *Biochemistry* 2003, *42* (21), 6608–6619.
(165) Manno, S.; Takakuwa, Y.; Mohandas, N. Identification of a Functional Role for Lipid Asymmetry in Biological Membranes: Phosphatidylserine-Skeletal Protein Interactions Modulate Membrane Stability. *Proc Natl Acad Sci U S A* 2002, *99* (4), 1943–1948.
(166) Meers, P.; Mealy, T. Calcium-Dependent Annexin V Binding to Phospholipids: Stoichiometry, Specificity, and the Role of Negative Charge. *Biochemistry* 1993, *32* (43), 11711–11721.
(167) Govekar, R. B.; Zingde, S. M. Protein Kinase C Isoforms in Human Erythrocytes. *Ann Hematol* 2001, *80* (9), 531–534.
(168) O'Toole, P. J.; Wolfe, C.; Ladha, S.; Cherry, R. J. Rapid Diffusion of Spectrin Bound to a Lipid Surface. *Biochimica et Biophysica Acta (BBA) - Biomembranes* 1999, *1419* (1), 64–70.
(169) Wan, C.; Kiessling, V.; Tamm, L. K. Coupling of Cholesterol-Rich Lipid Phases in Asymmetric Bilayers. *Biochemistry* 2008, *47* (7), 2190–2198.
(170) Kiessling, V.; Crane, J. M.; Tamm, L. K. Transbilayer Effects of Raft-Like Lipid Domains in Asymmetric Planar Bilayers Measured by Single Molecule Tracking. *Biophys J* 2006, *91* (9), 3313–3326.
(171) Bennett, W. F. D.; MacCallum, J. L.; Hinner, M. J.; Marrink, S. J.; Tieleman, D. P. Molecular View of Cholesterol Flip-Flop and Chemical Potential in Different Membrane Environments. *J. Am. Chem. Soc.* 2009, *131* (35), 12714–12720.
(172) van Meer, G. Dynamic Transbilayer Lipid Asymmetry. *Cold Spring Harbor Perspectives in Biology* 2011, *3* (5), a004671–a004671.
(173) Crane, J. M.; Kiessling, V.; Tamm, L. K. Measuring Lipid Asymmetry in Planar Supported Bilayers by Fluorescence Interference Contrast Microscopy. *Langmuir* 2005, *21* (4), 1377–1388.
(174) Frick, M.; Schmidt, K.; Nichols, B. J. Modulation of Lateral Diffusion in the Plasma Membrane by Protein Density. *Current Biology* 2007, *17* (5), 462–467.
(175) Chen, Y.; Lagerholm, B. C.; Yang, B.; Jacobson, K. Methods to Measure the Lateral Diffusion of Membrane Lipids and Proteins. *Methods* 2006, *39* (2), 147–153.
(176) Shen, H.; Tauzin, L. J.; Baiyasi, R.; Wang, W.; Moringo, N.; Shuang, B.; Landes, C. F. Single Particle Tracking: From Theory to Biophysical Applications. *Chem. Rev.* 2017, *117* (11), 7331–7376.
(177) Ruthardt, N.; Lamb, D. C.; Bräuchle, C. Single-Particle Tracking as a Quantitative Microscopy-Based Approach to Unravel Cell Entry Mechanisms of Viruses and Pharmaceutical Nanoparticles. *Mol Ther* 2011, *19* (7), 1199–1211.
(178) Sprague, B. L.; Pego, R. L.; Stavreva, D. A.; McNally, J. G. Analysis of Binding Reactions by Fluorescence Recovery after Photobleaching. *Biophys J* 2004, *86* (6), 3473–3495.
(179) Guo, L.; Har, J. Y.; Sankaran, J.; Hong, Y.; Kannan, B.; Wohland, T. Molecular Diffusion Measurement in Lipid Bilayers over Wide Concentration Ranges: A Comparative Study. *ChemPhysChem* 2008, *9* (5), 721–728.

(180) Schwille, P.; Haupts, U.; Maiti, S.; Webb, W. W. Molecular Dynamics in Living Cells Observed by Fluorescence Correlation Spectroscopy with One- and Two-Photon Excitation. *Biophys J* 1999, *77* (4), 2251–2265.
(181) Kalb, E.; Frey, S.; Tamm, L. K. Formation of Supported Planar Bilayers by Fusion of Vesicles to Supported Phospholipid Monolayers. *Biochimica et Biophysica Acta (BBA) - Biomembranes* 1992, *1103* (2), 307–316.
(182) Sankaran, J.; Wohland, T. Fluorescence Strategies for Mapping Cell Membrane Dynamics and Structures. *APL Bioengineering* 2020, *4* (2), 020901.
(183) Stöckl, M.; Plazzo, A. P.; Korte, T.; Herrmann, A. Detection of Lipid Domains in Model and Cell Membranes by Fluorescence Lifetime Imaging Microscopy of Fluorescent Lipid Analogues. *J Biol Chem* 2008, *283* (45), 30828–30837.
(184) Hirvonen, L. M.; Suhling, K. Fast Timing Techniques in FLIM Applications. *Front. Phys.* 2020, *8*.
(185) Koynov, K.; Butt, H.-J. Fluorescence Correlation Spectroscopy in Colloid and Interface Science. *Current Opinion in Colloid & Interface Science* 2012, *17* (6), 377–387.
(186) Kapusta, P.; Macháň, R.; Benda, A.; Hof, M. Fluorescence Lifetime Correlation Spectroscopy (FLCS): Concepts, Applications and Outlook. *International Journal of Molecular Sciences* 2012, *13* (12), 12890–12910.
(187) Böhmer, M.; Wahl, M.; Rahn, H.-J.; Erdmann, R.; Enderlein, J. Time-Resolved Fluorescence Correlation Spectroscopy. *Chemical Physics Letters* 2002, *353* (5–6), 439–445.
(188) Walsh, A. J.; Sharick, J. T.; Skala, M. C.; Beier, H. T. Temporal Binning of Time-Correlated Single Photon Counting Data Improves Exponential Decay Fits and Imaging Speed. *Biomedical Optics Express* 2016, *7* (4), 1385.
(189) Tenny, K. M.; Keenaghan, M. Ohm's Law. In *StatPearls*; StatPearls Publishing: Treasure Island (FL), 2019.
(190) Joubert, J. R.; Smith, K. A.; Johnson, E.; Keogh, J. P.; Wysocki, V. H.; Gale, B. K.; Conboy, J. C.; Saavedra, S. S. Stable, Ligand-Doped, Poly(Bis-SorbPC) Lipid Bilayer Arrays for Protein Binding and Detection. *ACS Appl. Mater. Interfaces* 2009, *1* (6), 1310–1315.

Chapter 2: Microcavity Supported Lipid Membranes: Versatile Platforms for Building Asymmetric lipid bilayers and for Protein Recognition

Published in *ACS Applied Bio Mat*, 2019, 2, 3404-3417.

Guilherme B. Berselli, Nirod Kumar Sarangi, Sivaramakrishnan Ramadurai, Paul V. Murphy, Tia E. Keyes.

Within this work I was the first author and contributor to the experimental design, execution, analyses and preparation of the manuscript. I specifically contributed towards the following sections: preparation and characterization of LUVs, PDMS microcavity arrays preparation and characterization, and FLCS studies. EIS studies were carried out by Dr. N. Sarangi. Dr. S. Ramandurai assisted in FLCS execution and data analysis. Supporting information associated with this chapter can be found in Appendix A.

2.1. Abstract

Microcavity supported lipid bilayers (MSLB) are contact-free membranes suspended across aqueous-filled pores that maintain the lipid bilayer in a highly fluidic state, free from frictional interactions with substrate. Such platforms offer the prospect of liposome-like fluidity with the compositional versatility and addressability of supported lipid bilayers and thus offer significant opportunity for modelling membrane asymmetry, protein-membrane and aggregation interactions at the membrane interface. Herein, we evaluate their performance in this regard, by studying the effect of transmembrane lipid asymmetry on lipid diffusivity, membrane viscosity and cholera toxin- ganglioside recognition across 6 symmetric and asymmetric membranes including binary compositions containing both fluid and gel phase, and ternary phase liquid ordered and disordered separated membrane compositions. Fluorescence lifetime correlation spectroscopy (FLCS) was used to determine the lateral mobility of lipid and protein, and electrochemical impedance spectroscopy (EIS) enabled detection of protein-membrane assembly over the nanomolar range. Transmembrane leaflet asymmetry was observed to have profound impact on membrane electrochemical resistance where the resistance of a ternary symmetric phase separated bilayer was found to be at least 2.6 times higher than the asymmetric bilayer with analogous composition at the distal leaflet but where the lower leaflet comprised only DOPC. Similarly, the diffusion coefficient for MSLBs was observed to be 2.5 fold faster for asymmetric MSLBs where the lower leaflet is DOPC alone. Our results demonstrate that interplay of lipid packing across both membrane leaflets and concentration of GM1 both affect the extent of cholera toxin aggregation and consequent diffusion of the cholera-GM1 aggregates. Given that true biomembranes are both fluidic and asymmetric MSLBs offer the opportunity for building greater biomimecry into biophysical models and the approach described demonstrates the value of MSLBs in studying aggregation and membrane associated multivalent interactions prevalent in many carbohydrates mediated processes.

2.2. Introduction

Artificial lipid membranes are indispensable tools for evaluating biophysical processes, such as membrane permeation, protein recognition and aggregation, under conditions of controlled lipid composition.[1] They can provide a means to disentangle insights into unit membrane processes

from the confounding complexity of the cell.[2] A good artificial model will have controllable lipid composition, good stability and critically, will maintain high membrane lateral fluidity.[3–5] Also, ideally, in the interests of biomimicry, the membrane should be asymmetric. The plasma membrane is naturally asymmetric, the lipid composition of the mammalian membrane for instance, contains predominantly phosphatidylcholine and other choline derivatives, glycolipids and sphingomyelin at the exterior leaflet, whereas the cytoplasmic leaflet contains DOPE, negatively charged lipids such as phosphatidylserine (PS) and other aminolipids. Cholesterol is contained within and is mobile across both leaflets.

The asymmetry is thought to lead to significant differences in phase behavior and diffusivity of each leaflet of the plasma membrane. In particularly the predominance of SM at the outer leaflet leads to coexistence of Lo and Ld and gel phases, whereas model distal leaflets have shown no evidence of such domain formation. Thuso it is likely that there is a significant disparity in the fluidity of each of the plasma membrane leaflets. Furthermore, transmembrane lipid asymmetry and inter-leaflet coupling have been reported to play a crucial role in plasma membrane function and organization, where evidence suggests that inter-leaflet coupling and domain registration lead each leaflet to be profoundly influenced by the composition of its neighbour.[6,7] This effect has been predicted widely in computational simulations, but experimental investigations into the influence of asymmetry/symmetry of lipid membranes on lipid-leaflet coupling and mobility are relatively uncommon.[8–11] Presumably, because of challenges in building model systems at which asymmetry and lateral fluidity can be simultaneously accomplished.[8,12,13]

Liposomes and supported lipid bilayers (SLBs) are some of the most widely applied artificial cell membrane models. However, they respectively preclude reliable attainment of controlled asymmetric composition and optimal fluidity.[6,14] In the latter case, asymmetric supported lipid bilayers (aSLBs) are readily accessible using controlled lipid deposition techniques to assemble, independently, two lipid monolayers[9] or by lipid translocation using chemical or mechanical lipid redistribution after vesicle fusion to a planar substrate.[10,15,16] However, frictional interactions between the lower (proximal) leaflet and the substrate hinder lateral diffusion in these and related tethered or cushioned, structures. Therefore, lipid and reconstituted protein mobility in asymmetric cell membrane models have not been widely explored using such models.

An alternative approach to emerge in recent years are porous-supported membrane structures where the lipid membrane is supported in part over air or fluid.[1,17–23] In the former case, stable bilayers typically require nano-pore dimensions but where aqueous filled supports are used, the bilayer can be suspended over pores of multiple microns. Recently, we demonstrated that lipid bilayers supported above aqueous filled micron-sized spherical pore arrays in gold and in poly(dimethylsiloxane) (PDMS) are stable and produce highly fluidic bilayers simulating the behavior of liposome. The micron dimensioned pores are attractive as they are amenable to microscopy, enabling single pores to be individually interrogated. Across arrays, this can lead to robust statistical reliability of results. When prepared in gold, the arrays can work as an electrode permitting electrochemical interrogation of membrane behavior.[24] Such stable microarray supported bilayers hold great potential as analytical devices for protein binding and detection.[25]

Using MSLBs, herein, we examine the impact of lipid composition and asymmetry on cholera toxin-GM1 recognition and aggregation using Fluorescence Lifetime Correlation Spectroscopy (FLCS) and Electrochemical Impedance Spectroscopy (EIS). Cholera Toxin recognizes, specifically, the monosialosyl ganglioside GM1 at the plasma membrane of the gut epithelia through its subunit b (CTb). This membrane localized recognition is the first step in a process that permits the toxin to gain access to the endoplasmic reticulum. CTb-GM1 association is a multivalent process that has been studied at a variety of membrane models and has been applied to evaluate new lipid-protein platform models for protein detection.[25–30] In complex and phase separated lipid compositions and at the cell membrane, a number of studies have demonstrated that CTb associates at the liquid ordered (L_o) phase, and that CTb stabilizes raft domains via a lipid-crosslinking.[31–33] However, to date, the impact, of lipid membrane asymmetry on CTb-GM1 association has not been considered in detail, although in true biological membranes, as described, the bilayers would be highly asymmetric.

Using microfluidic MLSBs we demonstrated a simple method to build transversally asymmetric lipid bilayer compositions using a hybrid Langmuir Blodgett-Vesicle Fusion (LB-VF) lipid assembly[22,24] and examined the lateral diffusion of labeled lipid marker within different asymmetric and symmetric lipid systems evaluating the impact of lipid bilayer asymmetric

compositions on CTb- glycosphingolipid(GSL) binding and mobility. The relatively high fluidity of the asymmetric bilayer compositions enabled us to study diffusion of cholera toxin aggregates at phase separated bilayers rendered impossible at symmetric compositions due to slow diffusion/photobleaching of the labels. The observations reflect the influence of lipid complex composition on the lateral aggregation of CTb at GM1 containing bilayers. Our results demonstrate the utility of microfluidic cavity array supported bilayers as a versatile platform for the assembly and study of asymmetric lipid compositions and for evaluation of biologically important multivalent binding systems and protein aggregation at ligand containing membranes.

2.3. Experimental Section

2.3.1. Materials

1,2-dioleoyl-*sn*-glycero-3-phosphocholine (DOPC), porcine brain N-(octadecanoyl)-sphing-4-enine-1-phosphocholine (SM), cholesterol and ganglioside GM1 were purchased with maximum degree of purity (> 99%) from Avanti Polar Lipids (Alabama, USA) and used without further purification. 1,2-dioleoyl-*sn*-glycero-3-phosphoethanolamine labeled Atto655 (DOPE-A655) was purchase from ATTO-TEC GmbH (Siegen, Germany). Conjugated B subunit cholera toxin labeled Alexa 555 (CTb-A555) was purchased from Invitrogen (Thermo Fisher). Free unlabelled B subunit cholera toxin (CTb) and phosphate buffer saline (PBS) tablets were purchased from Sigma-Aldrich (Wicklow, Ireland). Aqueous solutions were prepared using Milli-Q water (Millipore Corp., Bedford, USA). Polydimethylsiloxane silicon elastomer (PDMS) was purchased from Dow Corning GmbH (Wiesbaden, Germany) and mixed following supplier instructions. Silicon wafers coated with a 100 nm layer of gold on a 50 Å layer of titanium were obtained from AMS Biotechnology Inc. The monodisperse polystyrene latex sphere with a diameter of 1 μm was obtained from Bangs Laboratories Inc. The commercial cyanide free gold plating solution (TG-25 RTU) was obtained from Technic Inc. All other HPLC grade reagents were obtained from Sigma-Aldrich and used as obtained.

2.3.2. Gold and PDMS microcavity array preparation

The lipid bilayers were suspended across buffer-filled PDMS or gold microcavity arrays prepared according to protocols previously described by our group.[22] Briefly, for FCS, the microcavity array

was prepared by drop casting 50 µL of ethanol containing 0.1% of 4.61 µm polystyrene spheres (Bangs Laboratories) onto a 1 cm x 1 cm hand cleaved mica sheet. After ethanol evaporation, PDMS was poured onto the PS spheres array and cured at 90 °C for 1h. The microcavities array is then formed after removing the inserted PS spheres by sonicating the PDMS substrate in tetrahydrofuran (THF) for 15 min. The substrates were then left to dry overnight. Prior to lipid bilayer formation, the substrates were plasma cleaned using oxygen plasma for 5 min and microcavities were buffer filled before to lipid monolayer deposition by sonicating PDMS substrate in PBS buffer (pH 7.4) for 1h. As previously reported, this step is important to increase the hydrophilicity of the substrate.[22]

For electrochemical studies, lipid bilayers were suspended across gold microcavity arrays prepared by microsphere lithography and selectively modified with a self-assembled monolayer (SAM) of 1 mM 6-Mercapto-1-hexanol (MH) as described previously.[24,34] The detailed description for the preparation of microcavity array and MSLBs are presented in the supplementary information (Fig. S1 and S2).

2.3.3. Preparation of Large Unilamellar Vesicles (LUVs)

In this work, liposome fusion was used to form the distal lipid leaflet on MSLB's. To prepare the liposomes, stock solutions of all vesicle components such as DOPC, brain sphingomyelin (SM) and cholesterol (Chol) 50 mg/ml each, and GM1 (1 mg/ml) were prepared in chloroform and stored in sealed glass vials at -20°C. For fluorescence studies, unlabeled lipids and fluorescently labeled phospholipid DOPE-A655 were mixed in a ratio of 50000:1 mol/mol. For electrochemical measurements, as EIS is label-free, the probe was not included during the preparation of MSLBs. Aliquots of the appropriate amounts of the stock solutions were mixed in clean amber glass vials and the chloroform was removed under a gentle stream of nitrogen to form a thin layer lipid coating on glass vials. To ensure complete removal of residual chloroform, the lipids thin films were placed under vacuum for at least 3 h and then the lipids were rehydrated in 1 ml of PBS buffer and vortexed vigorously for 60 s. A mini-extruder (Avanti Polar Lipids) was used to extrude the multilamellar vesicles suspension through a polycarbonate membrane (0.1 µm pore size). The resulting large unilamellar vesicles (LUV) (approximately 100 nm diameter) solution was diluted

to 0.25 mg/ml. Liposomes composed of SM were extruded at 45°C, above the SM transition temperature, to guarantee that vesicles are in the fluidic state.

2.3.4. Microcavity Supported Lipid Bilayers (MSLB) preparation

To assemble suspended asymmetric/symmetric lipid bilayer membranes across pre-buffer filled microcavity arrays of both PDMS and gold substrates, a hybrid two-step method, Langmuir-Blodgett lipid transfer followed by vesicle fusion (LB-VF) method was employed.[22] Briefly, a spanned lipid monolayer is first deposited onto the microcavity substrate by LB transfer (LB trough; KSV Nima Model 102M) with Milli-Q water as the subphase. Lipid solution (50 µL, 1 mg/ml in chloroform) was added dropwise gently over 2-3 min on the subphase of LB trough and allowed solvent to evaporate for 15 min. Prior to the preparation of proximal leaflet monolayer using LB method, multiple compression-expansion cycles were followed before the collapse surface pressure and subsequently the monolayers were transferred at a highly condensed surface pressure of 32 mNm^{-1} by the vertical withdrawal of submerged substrate at a speed of 15 mm/min (Fig. S3). To form supported lipid bilayer, the monolayer-coated gold substrate was dipped in LUV solution for 30 min for fusion and then washed with PBS buffer and stored in PBS until further use. Prior to liposome fusion on to the monolayer coated PDMS thin chamber, the substrate was sealed to a cover glass with rapid adhesive glue (Araldite). The microfluidic device was formed after insertion of two silicon tubes to the sealed chamber containing the microcavity array by punching two holes through the PDMS into cavity chamber (see SI). To remove residual/unreacted liposomes, the microfluidic device was purged with 1 ml of PBS buffer (pH 7.4). Care was taken to ensure that at no stage during the preparation or measurements the bilayer was exposed to air. In this work, the proximal leaflet refers to the LB deposited lipid leaflet next to the substrate and the distal leaflet is the outer lipid layer facing toward the bulk solution.

2.3.5. Electrochemical impedance spectroscopy (EIS)

Electrochemical impedance measurements were performed on a CHI 760B bipotentiostat (CH Instruments Inc., Austin, TX) in a three-electrode cell consisting of a Ag/AgCl (1 M KCl) reference electrode, platinum coiled wire as a counter electrode and the gold substrate with microcavity array served as the working electrode. 1 mM $[Fe(CN)_6]^{3-/4-}$ was used as an internal redox probe in 0.1 M KCl electrolyte solution in PBS buffer. Impedance measurements are performed in the presence

of 1 mM $K_3[Fe(CN)_6]$/ $K_4[Fe(CN)_6]$ (1:1 mol/mol) mixture, as a redox probe dissolved in PBS buffer containing additional 0.1 M KCl as supporting electrolyte. EIS data were measured using a 3-electrode cell described above. The electrodes were characterized by EIS measurements with $[Fe(CN)_6]^{3-/4-}$ as internal redox probe to follow each step of the fabrication.

The EIS recording was performed in the frequency region between 10^4 and 0.01 Hz with a bias potential of 0.26 V vs Ag/AgCl. The impedance spectra were fit to an equivalent circuit as described earlier previously [24] and the same has been shown in Figure 3b. In the circuit, $\boldsymbol{R_S}$ is the solution resistance, $\boldsymbol{R_M}$ and $\boldsymbol{CPE_M}$ represents the resistance and constant phase element of the membrane and $\boldsymbol{R_C}$ and $\boldsymbol{CPE_C}$ represents the cavity resistance and constant phase element of the gold substrate. The constant phase elements (CPE) were used in the equivalent circuit to provide to account for the heterogeneity of the SLBs in microcavity array. The impedance of the CPE can be calculated using Eq. (1);

$$Z_{CPE} = \frac{1}{Q(j\omega)^{\beta}} \tag{1}$$

where Q and the exponent $\boldsymbol{\beta}$ represent respectively the CPE and an empirical constant related to the frequency dispersion. The experiments were conducted in triplicates.

2.3.6. Fluorescence Lifetime Correlation Spectroscopy (FLCS)

Single point FLCS was used to assess both the lipid membrane fluidity as well as the change in CTb binding to GM1. FLCS measurements were performed on a MicroTime 200 lifetime (PicoQuant GmbH, Berlin, Germany) using a water immersion objective (NA 1.2 UPlanSApo 60 x 1.2 CC1.48, Olympus). The detection unit comprises of two single photon avalanche diode (SPAD) from PicoQuant. Labeled lipid membrane marker DOPE-A655 was excited with 640 nm LDH-P-C-640B (PicoQuant) and CTb-A555 was excited with 532 nm PicoTA laser from Toptica (PicoQuant). To exclude scattered or reflected laser light emitted fluorescence was collected through a HG670lp AHF/Chroma or HQ550lp AHF/Chroma band pass filter for 640 or 532 nm laser respectively. A 50 μm pinhole was used to eliminate photons from outside the confocal volume. Before FCLS measurement, backscattered images of the substrate were taken using an

OD3 density filter to ensure the optimal positioning of the focus to the centre of the microcavity. Then, the bilayer position was determined by z-scanning until the point of maximal fluorescence intensity of DOPE-A655 was found. At this point, the fluctuating fluorescence intensity of labeled lipid marker or CTb-A555 were measured for 30 to 60 seconds per cavity, and replicate data from 20 to 30 cavities were measured per sample. To assess simultaneously the diffusion time (ms) and the fluorescence lifetime (ns) the emitted photons were analyzed by a time-correlated single photon counting system (TCSPC) (PicoHarp 300 from Picoquant).[35] The fluorescence fluctuations obtained are then correlated with a normalized autocorrelation function (Equation 2):

$$G(\tau) = \frac{\langle \delta F(t).\, \delta F(t+\tau) \rangle}{\langle F(t) \rangle^2} \tag{2}$$

The auto-correlation curves obtained from the fluorescence fluctuations were fitted to a 2-D model (Equation 3) using the software SymphoTime (SPT64) version 2.2 (PicoQuant).

$$G(\tau) = \frac{1}{N(1-T)}\left[1 - T + Te^{\left(-\frac{\tau}{\tau_T}\right)}\right]\left[1 + \left(\frac{\tau}{\tau_D}\right)^{\alpha}\right]^{-1} \tag{3}$$

Some of the autocorrelation data were fitted using 2D diffusion model for two diffusing moieties by adding a second component to equation 3, (equation 4).

$$G(\tau) = \frac{1}{N(1-T)}\left[1 - T + Te^{\left(-\frac{\tau}{\tau_T}\right)}\right]\left[1 + \left(\frac{\tau}{\tau_{D1}}\right)^{\alpha 1}\right]^{-1}\left[1 + \left(\frac{\tau}{\tau_{D2}}\right)^{\alpha 2}\right]^{-1} \tag{4}$$

Here, ρ represents the amplitude at G(τ) and is defined as the inverse of number of molecules (1/N), T corresponds to the fraction of molecules at triplet "dark" state, τ_{trip} is the triple state time and α is the anomalous parameter; τ_D is the diffusion time of the molecules and τ_T is the decay time for the triplet state. The diffusion coefficient is related to the correlation time τ_D by the relation $D = \omega^2/4\tau_D$, where ω is the $1/e^2$ radius of the confocal volume i.e. the waist of the exciting laser beam. ω was measured for each excitation using a reference solution of free dye for which the

diffusion coefficient is known. The ω was determined by calibration using reference dyes; Atto 655 (Atto TEC, GmbH) for 640nm laser and Rhodamine 6G for 532 nm laser at 20°C in water. Detailed description of the experimental set up can be found in figure S4. The experiments were conducted in triplicates.

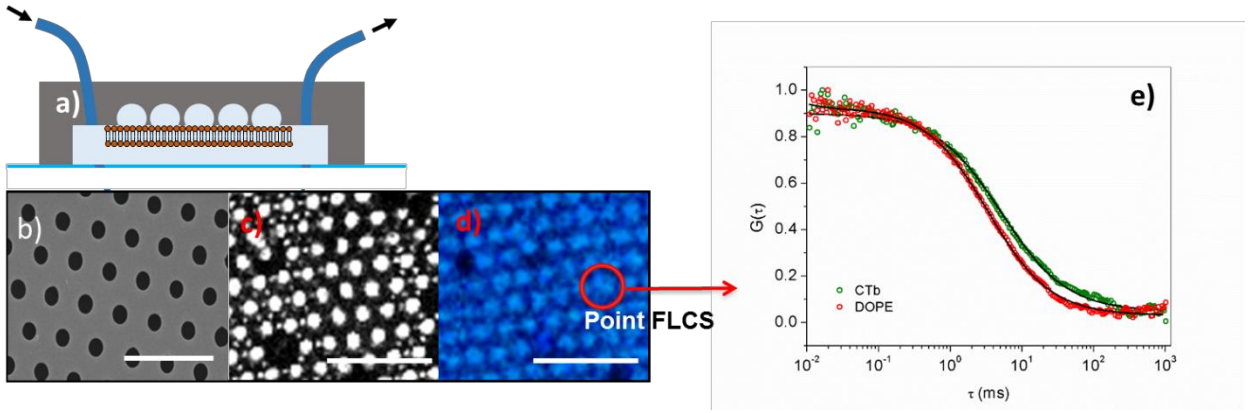

Figure 1. a) Schematic of the microfluidic platform made of PDMS. b) SEM image of cured PDMS microcavity array before buffer spanning a lipid bilayer made by pouring the polymer to 4.6 µm diameter polystyrene spheres before assembling the microfluidic device. c) reflectance image obtained using a OD3 density filter after lipid bilayer deposition. d) Fluorescence lifetime image of labeled DOPE-A655 of an asymmetric DOPC (proximal leaflet) // DOPC/GM1 (1 mol%) (distal leaflet) lipid bilayer. The scale bar is 10µm. e) Typical FLCS autocorrelation data of labeled DOPE (red) and CTb (green) over a microcavity. Solid lines represent the 2D fitting to equation (3).

Due to the suspended character of planar MSLBs, where both leaflets are in contact with bulk aqueous phase, we can assume the Saffman-Delbruck model (Equation 5) applies and thus use it to estimate the membrane viscosity from lateral diffusion values obtained for labeled DOPE-A655:

$$D = \frac{KT}{4\pi\mu h}\left(\ln\left(\frac{\mu h}{\mu' r}\right) - \gamma\right) \qquad (5)$$

Where $\boldsymbol{D}$ is the lateral diffusion obtained from FLCS, $\boldsymbol{K}$ is Boltzmann constant, $\boldsymbol{T}$ is the absolute temperature, $\boldsymbol{r}$ is the radius of the cylindrical membrane inclusion, $\boldsymbol{h}$ is the membrane thickness, $\boldsymbol{\gamma}$ is Euler-Mascheroni constant (approx. 0.577), $\boldsymbol{\mu}$ and $\boldsymbol{\mu'}$ are the membrane viscosity and the bulk

solution viscosity, respectively. The parameters used to estimate the membrane $\boldsymbol{\mu}$ were: radius of the inclusion $\boldsymbol{r}$ = 0.1 nm, membrane height $\boldsymbol{h}$ = 3.8 nm and the viscosity of the surrounding media $\boldsymbol{\mu'}$ = 0.001 Pa.s.

2.4. Results and Discussion

2.4.1. Preparation of transversally asymmetric microcavity supported lipid bilayers

The eukaryotic cell membrane has a transversally asymmetric lipid distribution and this characteristic has important biophysical consequences in natural systems.[5] A key advantage of the microcavity supported lipid membrane is that it is readily amenable to the preparation of asymmetric lipid bilayer compositions in a manner similar to supported lipid membranes but with the key difference that the MSLBs retains the fluidity of a liposome membrane. To investigate the influence of transmembrane asymmetry on lipid diffusivity, the MSLBs were prepared using a hybrid Langmuir Blodgett-vesicle fusion method, so that the proximal leaflet (array substrate side) comprised of DOPC while the distal leaflet comprised of either DOPC, DOPC:SM (1:1) or DOPC:SM:Chol (2:2:1). Note that 1% (mol:mol) GM1 was added in each case only to the distal leaflet as a receptor to CTb. The labeled lipid DOPE-A655 used as a fluorescent marker at 0.01 mol% was inserted only into the distal leaflet. A schematic representation of the MSLB's on buffer filled microcavities and the microcavity array are shown in Figure 1a and 1b, respectively.

A number of studies at SLBs indicate that lipid asymmetry is maintained for many hours.[9–11] As the asymmetric bilayers are not at equilibrium, to confirm that asymmetry was maintained during our experimental windows we evaluated the diffusion coefficient of the outer leaflet over 48 hours following assembly and found that negligible change had occurred. Because of the large difference between diffusivity of the DOPC and mixed composition monolayers if significant mixing/flip-flop were occurring over this time-scale we would expect to see increasing diffusion coefficient or biphasic behavior if the probe were flip-flopping. Nonetheless, to mitigate against any loss of asymmetry, measurements were completed in the present studies immediately following bilayer preparation and were completed within 3 to 4 hours). It is expected, however, that in cholesterol-containing asymmetric compositions, cholesterol can flip-flop to the proximal leaflet rapidly.[36]

We note that we do not observe, over the experimental time scale used herein (2 to 3 hours), changes to bilayer fluidity.

Confocal imaging of DOPE-A655 labeled MSLB's confirm continuous lipid bilayer spanning the PDMS microcavities are formed for all lipid compositions (Figure 1c and 1d). Occasionally unfilled cavities occur but these are easily distinguished as "dark spots" caused by the absence of lipid membrane at pores that have failed to fill with water and where consequently bilayers tend to be unstable at the air interface across such large pores. Without the lipid marker DOPE-A655 present in the bilayers, no background fluorescence was observed from the PDMS platform or bilayers (see SI). To avoid contributions from diffusion of lipid bilayer over the flat regions of array, all measurements are performed at a buffer encapsulated cavity by focusing first with the reflectance image on a single aqueous filled pore before Z-scanning to focus on the bilayer and acquiring the FLCS autocorrelation function (ACF). Representative FLCS data from a cavity spanned DOPC membrane labeled with DOPE-A655 is shown in Figure 1e (open symbol). The lateral diffusion is calculated after fitting the obtained ACF with equation 3 (solid line, Figure 1e).

2.4.2. Transmembrane lipid symmetry affects the lipid membrane fluidity and viscosity

The diffusivity of DOPE-A655 at MSLBs with different asymmetric and symmetric MSLBs were extracted (Table 1) and plotted against lipid composition (Figure 2). The lateral diffusion coefficient obtained for a DOPC lipid bilayer was approximately 10 $\mu m^2 s^{-1}$, which is consistent with previously reported values for DOPC MSLBs as well as for reported free-standing DOPC bilayers.[22,37]

As expected, the composition of the bilayer, has a profound effect on diffusivity. For instance, upon addition of SM to the distal layer of the MSLBs so that it comprises 1:1 mol/mol DOPC:SM, where the proximal leaflet is DOPC alone, DOPE-A655 lateral diffusion in the distal leaflet reduces to 5.37 ± 0.75 $\mu m^2 s^{-1}$. The reduced fluidity of the bilayer is attributed to the presence of enriched SM gel-phases that increase the distal layer viscosity. Indeed, reports of diffusion of analogous compositions in symmetric silicate-supported SLBs show that diffusion is suppressed.[38]

The inclusion of cholesterol (Chol) in the asymmetric MSLBs so that the distal leaflet comprises DOPC/SM/Chol (2:2:1) mol/mol/mol) increases DOPE-A655 diffusion to 8.66 ± 2.53 $\mu m^2 s^{-1}$ as compared to the diffusivity values of DOPC:SM(1:1)/DOPC bilayer. This is consistent with numerous previous reports[39], including that of Yokota and Ogino who demonstrated that introduction of Chol into DOPC/SM (1:1) transitions the membrane from co-existing gel and fluid phases in SLBs to mixed phases of liquid disordered (L_d) domains rich in DOPC and micron-sized liquid ordered (L_o) domains rich in SM and cholesterol.[38] The formation of L_o domains are thought to be promoted by hydrogen bonding interactions between SM tails and cholesterol[40–42] and the increase in fluidity reported is attributed to the preferential partitioning of labeled DOPE to L_d phase.[40]

Table 2. Diffusion coefficient of labeled DOPE at the distal layer of MSLBs and calculated membrane viscosity for different lipid compositions using Saffman-Delbruck model. The viscosity values obtained from DOPE diffusion lie within ranges previously reported for lipid bilayers at 20 °C.

Lipid composition	DOPE diffusion ($\mu m^2 s^{-1}$)	calculated μ (Pa.s)
Sym DOPC + GM1 (1 mol%)	10.0 ± 0.84	0.05 ± 0.006
Asym DOPC/SM/Chol (2:2:1) + GM1 (1 mol%)	8.66 ± 2.53	0.06 ± 0.01
Asym DOPC/SM (1:1) + GM1 (1 mol%)	5.37 ± 0.75	0.10 ± 0.005
Sym DOPC/SM/Chol (2:2:1) + GM1 (1 mol%)	3.34 ± 0.67	0.15 ± 0.003
Sym DOPC/SM (1:1) + GM1 (1 mol%)	1.52 ± 0.69	0.40 ± 0.003

To compare the fluidity of asymmetric and symmetric bilayers, we prepared symmetric MSLBs using the LB-VF method but where both LB and LUVs had the same composition, but for 1% mol/mol GM1 in the LUV. Lateral mobility of labeled DOPE obtained at the symmetric lipid bilayers are presented in Figure 2 (open spheres).

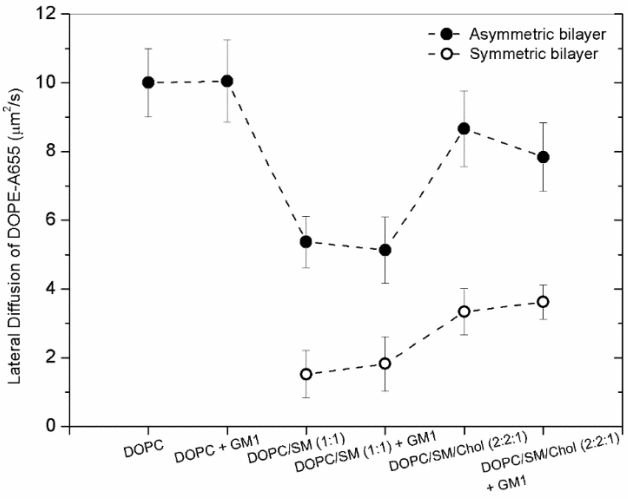

Figure 2. Lateral diffusion of labeled DOPE at asymmetric (closed spheres) and symmetric (open spheres) lipid bilayers. For the asymmetric bilayers, the proximal leaflet is comprised of DOPC. The GSL GM1 was introduced only in the distal leaflet during LUV preparation across all compositions. In each case, the mean diffusivity values presented herein are averages from 40 to 50 points (cavities) obtained across three independent bilayers. The experiments were performed at 20 ± 0.5 °C.

In all cases, it is the distal leaflet that is fluorescently labeled. The composition of the lower leaflet dramatically impacts diffusion of the upper leaflet. In symmetric lipid bilayers composed of DOPC/SM (1:1 mol/mol) the lateral diffusion coefficient of DOPE-A655 labeled at the distal leaflet is 1.52± 0.69 $\mu m^2 s^{-1}$, showing diffusion is significantly slowed compared with its asymmetric analogue (5.37 ± 0.75 $\mu m^2 s^{-1}$). This distinction indicates the integrity of the lipid distribution in the asymmetric bilayers and reflects the impact of inter-leaflet coupling in dictating membrane diffusion.

In the presence of cholesterol, i.e., in MSLBs with symmetric composition of DOPC/SM/Chol (2:2:1) in each leaflet, the lateral mobility of DOPE-A655 was measured as 3.34 ± 0.67 $\mu m^2 s^{-1}$ which is approximately 2.5 times slower than the asymmetric analogue (8.66 ± 2.53 $\mu m^2 s^{-1}$). Notably, inclusion of 1 mol% GM1 at the distal leaflet does not measurably alter DOPE-A655 diffusion coefficient irrespective of the membrane composition or symmetry. Overall, our data indicate that it is possible to build stable asymmetric microcavity supported lipid bilayers and that the implicit fluidity of the MSLBs enables the facile study of diffusion as a function of different lipid composition. The data reflect the profound impact of leaflet asymmetry on membrane fluidity

at both gel phase containing and in phase-separated lipid compositions. The magnitude of the change in fluidity between asymmetric and symmetric bilayers ($\Delta D = D_{asym}-D_{sym}$) is greater for binary fluid-gel phase membrane $\Delta D=3.6\ \mu m^2 s^{-1}$ than for fluid-fluid phase separated ternary membrane ($\Delta D = 2.6\ \mu m^2 s^{-1}$).

The decreased fluidity observed in symmetric bilayers is in agreement with computational predictions and with previous observations on liposomes where comparable differences in lipid lateral diffusion at symmetric and asymmetric were observed at similar temperatures.[43,8] For supported lipid bilayer systems based on solid substrate-supports, confounding surface-membrane frictional interactions complicate the interpretation of membrane viscosity as both inter-leaflet and substrate friction contribute to the measured viscosity.[44]

The obtained viscosity values for the asymmetric and symmetric lipid bilayers are displayed in Table 1. We assume that the lipid bilayers spanned across the microcavity are planar. Although reported membrane viscosity values vary due to varying experimental conditions, such as lipid composition, temperature and bilayer model,[45] the viscosity values obtained herein lie within the range of previously literature reports, between 0.02 and 0.5 Pa.s.[46] The membrane viscosity calculated for DOPC with GM1 (1 mol%) present in the distal leaflet is comparable to previous data reported for DOPC lipid membranes.[47] The viscosity calculated for the asymmetric lipid bilayers comprised of DOPC//DOPC/SM (1:1) 0.1 Pa.s are decreased as expected but also lie within membrane viscosity ranges reported previously.[48] On the addition of cholesterol, the membrane viscosity decreases to 0.06 Pa.s which is anticipated since cholesterol increases membrane fluidity in lipid bilayers containing sphingomyelin. As expected from the FLCS data, lipid leaflet asymmetry exerts a profound influence on the membrane viscosity where the viscosity of the DOPC/SM(1:1) with 1% GM1 at 0.4 Pa.s is 4 times more viscous when the lower leaflet is of the same composition, compared with a DOPC only lower leaflet. The effect is less pronounced in the cholesterol-containing bilayer where the viscosity in the symmetric composition is 2.5 greater than the asymmetric layer. This indicates, again that there is significant frictional or inter-leaflet coupling transmitted through the membrane.

2.4.3. Protein assembly, detection and dynamics using highly versatile MSLBs

Next, we assessed the suitability of MSLBs as a platform to study GSL-protein interactions, by modeling the GM1-cholera toxin interaction. GSLs are important receptors for lectin-binding that reside in cells exclusively at exofacial leaflet of mammalian membranes where they can participate in remodeling and crosslinking of domains on receptor binding.[25] Fluidity is important in artificial platforms that model such behaviors as lateral diffusion of the participating players are required for remodeling. We examined here, the impact of GSL-toxin recognition on lipid membrane impedance and fluidity as a function of membrane trans-leaflet composition.

2.4.4. The impact of GSL-protein recognition on electrochemical properties of the MSLB

The gold MSLBs were prepared from gold arrays (Figure 3a) that were selectively modified at the top surface with a 6-Mercapto-1-hexanol (MH) self-assembled monolayers using the PS sphere templates as a mask as described previously.[49] A schematic representation of the MSLBs on gold substrate is shown in Figure 3b. The EIS data was fitted to a heuristic model circuit (Figure 3c) of the MSLB described previously[24], where solution resistance is $\boldsymbol{R_s}$, the membrane charge transfer resistance and double capacitance are represented by $\boldsymbol{R_M}$ and $\boldsymbol{CPE_M}$ and the cavity resistance and capacitance by $\boldsymbol{R_C}$ and $\boldsymbol{CPE_C}$. As shown in Figure 3d, before PS templating sphere removal, there is a finite resistance (R_{SAM+PS}=1317Ω, data not shown) which decreases to 440Ω (R_{SAM}) upon PS removal (grey symbol) indicating increased access of redox probe to the cavity, but the resistance is considerably greater than the unmodified electrodes, confirming, consistent with previous measurements, that the gold of the cavities are exposed whilst the SAM remains intact at the top interface. The cavities are filled with PBS buffer and the substrate was always kept in contact with PBS buffer for further use in bilayer fabrication.

EIS provides complementary insights to the FLCS studies, by interrogating the electrical properties of the bilayer membranes in terms of capacitive and resistive changes. These parameters, in turn, reflect changes to aqueous/ionic permeability in response to CTb surface binding and aggregation to GM1. Figure 3c shows representative EIS plots before and after CTb exposure to the asymmetric SLBs comprised of DOPC in the proximal and DOPC/SM/Chol (2:2:1) with additional 1 mol% GM1 in the distal leaflet of the bilayer. The complex impedance (Nyquist plot) is presented as the sum of the real, Z', and the imaginary, $-Z''$ components that originate mainly from the resistance and capacitance respectively of the measured electrochemical system.

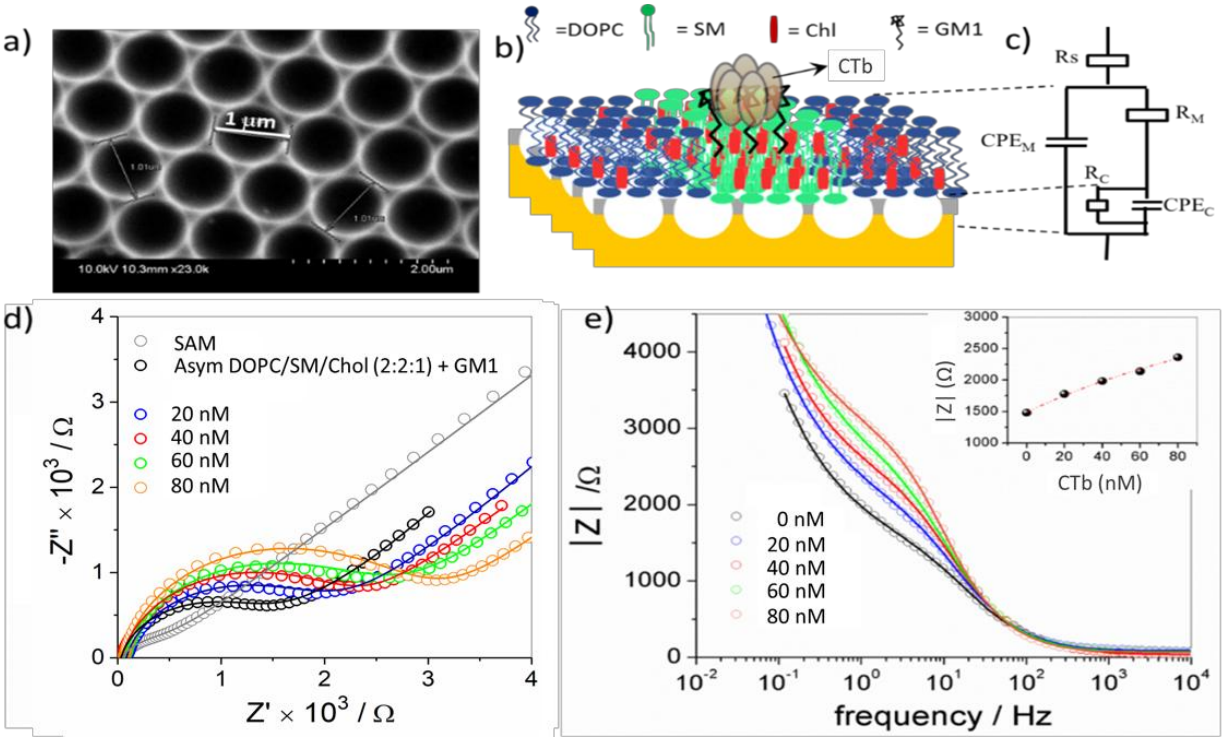

Figure 3. (a) SEM image of hemisphere micro cavity array made from electrochemical deposition through templates assembled from ~ 1µm diameter polystyrene spheres on gold substrates. The electrodeposition potential was -0.60 V vs Ag/AgCl. (b) Schematic representation of microcavity array based SLBs with CTb binding. (c) Represents the equivalent circuit model used to fit EIS data; where R_S: electrolyte solution resistane, R_M and CPE_M represent the membrane resistance and constant phase element, and R_C and CPE_C represent the resistance and constant phase element of cavity array. (d) Nyquist plot of electrodeposited gold electrode modified with 6-Mercapto-1-hexanol with (open gray: SAM of 6-Mercapto-1-hexanol). Open black symbols show the EIS data of the cavity modified with asymmetric bilayers composed of proximal leaflet, DOPC and distal leaflet, DOPC/SM/Chol (2:2:1) with GM1 (1 mol%) and EIS spectra with different CTb concentration (blue: 20 nM, red: 40 nM, green, 60 nM, orange, 80 nM). (e) Magnitude of total impedance before and after CTb reconstitution. Inset shows total impedance at a fixed frequency (4 Hz) as a function of the CTb concentration. All the EIS spectra recorded in the presence of 1 mM $Fe(CN)_6^{3-/4-}$ and 0.1 M KCl at the potential of +0.26 V vs. Ag/AgCl/sat.KCl and frequency range of 10^4 to 0.01 Hz using a three-electrode setup consisting of a platinum counter, Ag/AgCl reference, and the microcavity array as working electrode.

The Nyquist plot for the gold microcavity electrode selectively modified with 6-Mercapto-1-hexanol monolayer appears as a semicircle near the origin, at high frequencies, corresponding to heterogeneous electron transfer limited process, whereas the linear portion of the plot, at lower frequencies, represents the diffusion-controlled electron transfer process (Figure 3d, light grey). The assembly of the bilayer yields similar impedance curves but decreasing double layer capacitance due to retardation of the interfacial electron transfer rates compared to a bare or selectively modified metal electrode. This is reflected in the increase in semicircle diameter (black open symbol) in Figure 3d. Exposing the GM1 containing bilayer to increasing concentrations of CTb increases the semicircle diameter systematically and the data can be fit adequately by the Randles circuit as shown in Figure 3c. Since the membrane is a perfect resistance-capacitance element, the resistance is directly, and the capacitance inversely, proportional to the thickness of the dielectric layer. The parameter $\boldsymbol{\beta}$ of CPE_M in Eq.(1) is close to unity and hence a constant phase element, $\boldsymbol{CPE_M}$ could be used as a good representation of the electrode capacitance. From the fitting, the absolute resistance and capacitance of the asymmetric DOPC//DOPC/SM/Chol (2:2:1) with GM1 (1 mol%) at the outer leaflet, was found to be ~1.5 ± 0.06 kΩ.cm^2 and 1.4 ± 0.01 μF/cm^2 respectively which is in line with previous reports.[50,51] The relative change in resistance and capacitance values before and after toxin addition extracted from the fit are summarized in Table 2. We compare relative change rather than absolute C and R values as initial resistance values vary modestly from substrate to substrate for identical bilayer compositions due to small variations in the uniformity of cavity packing and electrode dimensions. We compared data across several replicate substrates and report the average relative changes in bilayer resistance and capacitance.

Table 2. Resistance and capacitance data for MSLBs at a fixed concentration (40 nM) of CTb. Results presented reflect the change (Δ) recorded following CTb addition, relative to bilayer prior to CTb addition. Asym indicates a bilayer that has a DOPC-only proximal leaflet, Sym indicates the bilayer is symmetric composition but for GM1 which in all compositions is only present at the outer leaflet.

Lipid composition	ΔR (kΩ.cm^2)	ΔC (μF/cm^2)
Sym DOPC + GM1 (1 mol%)	0.22 ± 0.01	-0.90 ± 0.15
Asym DOPC/SM/Chol (2:2:1) + GM1 (1 mol%)	0.87 ± 0.02	-0.80 ± 0.23
Sym DOPC/SM/Chol (2:2:1) + GM1 (1 mol%)	2.68 ± 0.13	-0.82 ± 0.24

As shown in Table 3, increasing CTb concentration in the solution in contact with the bilayer leads to a systematic increase in membrane resistance. The change in resistance is defined as $\Delta R = \Delta R_{CTb} - \Delta R_0$, where ΔR_{CTb} and ΔR_0 is the membrane resistance in the presence and in the absence of toxin respectively. Conversely, the capacitance ($\Delta C = \Delta C_{CTb} - \Delta C_0$) decreases systemically with increasing CTb concentration. Figure 3e represents the total impedance of the MSLBs as a function of increased concentration of CTb. At a fixed frequency of 4 Hz, the impedance rises with increasing CTb concentration (inset Figure 3e).

Table 3. Effect of CTb on the resistance and capacitance of asymmetric DOPC/SM/Chol (2:2:1) + GM1 (1 mol%) bilayer at increasing concentration. Results indicate change (Δ) recorded following CTb addition, relative to bilayer prior to CTb interaction.

[CTb] / nM	Asym DOPC/SM/Chol (2:2:1) + GM1 (1 mol%)	
	ΔR ($k\Omega cm^2$)	ΔC ($\mu F/cm^2$)
0	0	0
20	0.42 ± 0.01	-0.4 ± 0.11
40	0.87 ± 0.02	-0.8 ± 0.23
60	0.96 ± 0.02	-1.7 ± 0.34
80	1.31 ± 0.015	-3.4 ± 0.42

In order to confirm CTb recognition by GM1 is specific, we carried out control experiments to evaluate impedance changes on exposure of CTb to DOPC and ternary DOPC/SM/Chol bilayer membranes in the absence of GM1. In contrast to the DOPC containing GM1 bilayers, no significant changes to film resistance or capacitance was observed on exposure to CTb across any of the toxin concentrations explored in the absence of GM1 in the distal leaflet (Table S1 and Figures S5a). These results confirm that the presence of GM1 in the distal leaflet is necessary for CTb binding.

Conversely, for the symmetric ternary bilayer composed of DOPC/SM/Chol (2:2:1) with GM1 (1 mol%) at the distal leaflet, upon addition of 40 nM CTb, the relative change in resistance and capacitance was found to be 2.68±0.13 $k\Omega cm^2$ and -0.6±0.24 $\mu F cm^{-2}$ respectively (Table 2). Note that, the magnitude of change in absolute resistance for symmetric DOPC/SM/Chol (2:2:1) with GM1 (1 mol%) composition (~4.01 $k\Omega cm^2$) is higher than the asymmetric DOPC//DOPC/SM/Chol (2:2:1) with GM1 (1 mol%) composition (1.5 $k\Omega cm^2$). Interestingly, when there is no GM1 present for symmetric ternary bilayer (DOPC/SM/Chol), the resistance of

the membrane was found to be 3.16±0.05 kΩcm^2 in the absence of toxin, increasing in the presence of CTb to 3.82 ±0.05 kΩcm^2 (Figure S5b). This contrasted with the DOPC-only bilayer where in the absence of GM1, CTb elicited no change to membrane impedance (Figure S5a). The change suggests that CTb is associating with the membrane when SM is present but GM1 is not. These results are further supported by FLCS studies, below, that show retardation of toxin diffusivity when exposed to SM containing bilayers in the absence of GM1 (Figure S5c, Table S1).

As Tables 2 and 3 show, reflect the large increases in bilayer resistance and decreases to capacitance that accompany exposure to CTb at both DOPC and ternary bilayer membranes in the presence of GM1. The magnitude of the changes is much greater than observed for the SM containing bilayers and are consistent with the formation of a resistive layer of toxin at the membrane interface that leads to an increase in film thickness reflected in the capacitance decrease. Resistance is notably greatest when both leaflets comprise domain forming lipids. That much lower resistance values are observed for the asymmetric systems again, confirms the asymmetry of the bilayers achieved at the MSLBs[52–55]. The greater resistance of domain forming bilayers is likey attributed to organization/tight packing of lipid bilayers propagated longitudinally along both leaflets.

2.4.5. Lateral mobility of the CTb-GM1 complex is dependent on transmembrane composition

Labeled CTb-A555 was used to directly monitor the protein diffusion by FLCS on exposure to GM1-containing membrane binding. The labelled toxin, dissolved in PBS buffer (pH 7.4) at 4 nM was injected into the MSLB contacting solution in the microfluidic device and incubated for 30 min to ensure equilibrium is reached.[30,56] Figures 4 a and b shows the reflectance and fluorescence images respectively obtained following CTb incubation at a DOPC MSLB containing 1mol% GM1 at the distal interface. The corresponding FLCS data is shown in Table 4.

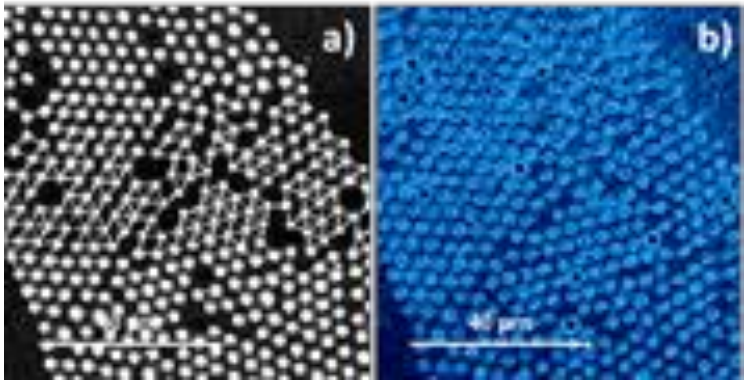

Figure 4. Representative confocal microscopy images obtained for labeled CTb-A555 of asymmetric DOPC + GM1 (1 mol%) lipid bilayer. (a) shows the reflectance image using OD3 filter before inserting labeled CTb. (b) shows the fluorescence lifetime image after incubating the lipid bilayer with 4 nm labelled CTb for 30min. The scale bar is 40 μm.

As the DOPC + GM1 (1 mol% at the outer leaflet) MSLB shown in Figure 4 is otherwise unlabeled we can conclude from imaging that the intense emission localized at the membrane following CTb incubation is due to toxin associating with the GM1-containing bilayer. The FLCS ACF fit to a single component 2D diffusion model diffusion coefficient for the toxin at the was determined as $5.65 \pm 0.75\ \mu m^2 s^{-1}$. This value is consistent with values reported for CTb assembly at GM1/DOPC GUVs where diffusion coefficient of GM1-bound CTb was similarly determined as to be approximately half that of the lipid marker.[57] As expected, the diffusion coefficient for MSLB membrane-bound CTb is significantly higher than values reported from SLBs with similar lipid bilayer composition. For instance, the lateral diffusion coefficient obtained for labeled CTb in supported lipid bilayers on silica substrate containing GM1 (0.1 mol%) was reported as $0.12 \pm 0.03\ \mu m^2 s^{-1}$, measured by FRAP [58] and using STED/FCS, Honigmann *et al.* reported the lateral diffusion of CTb as $0.14 \pm 0.01\ \mu m^2 s^{-1}$ for glass supported lipid bilayers.[59] The data reported here reflect the advantagous fluidity of the MSLBs compared to SLBs.

In asymmetric MSLBs comprised of DOPC/SM (1:1) + GM1 (1 mol%) at the distal leaflet and DOPC at the proximal, the ACF obtained for labeled CTb showed two diffusing populations. Fitting to a two-component model, equation 4, the populations contributed equally to the CTb fit with diffusion coefficients determined as $1.47 \pm 0.40\ \mu m^2.s^{-1}$ and $0.03 \pm 0.02\ \mu m^2.s^{-1}$. Recalling that lipid marker diffusion for the DOPC/SM (1:1 mol/mol) + GM1 (1 mol%) composition was determined as $5.13 \pm 0.96\ \mu m^2.s^{-1}$, the diffusion coefficient of the fast component for CTb diffusion

is five times slower than the lipid marker, rather than the half expected. The binary composition is expected to have co-existent liquid disordered and gel phases. The fast and slow diffusing components may be due to the toxin associated with GM1 localized in each phase.[60] However, given that the diffusion value is so much lower than the lipid marker for this composition and that the GM1 is expected to localize most strongly with the sphingomyelin (promoted through H-bonding) containing phase, it is more likely that the two populations reflect diffusion of CTb both at the gel phase but associated with different numbers of GM1. For the symmetric DOPC/SM bilayer (GM1 1 mol% in the distal leaflet) the lateral diffusion of CTb-GM1 complex is dramatically reduced and only a single diffusing population is evident. Indeed, diffusion is so slow that the intensity time trace shows strong photobleaching. This supports the argument that diffusion is due to two populations with different numbers of GM1 bound as only the gel phase would be expected to be so strongly affected by transverse lipid symmetry suggesting that the GM1-CTb complexes are confined to the sphingomyelin rich gel phase.

Next, we studied CTb binding at asymmetric phase-separated lipid bilayers where the distal lipid leaflet was composed of a DOPC/SM/Chol (2:2:1) + GM1 (1 mol%) and proximal DOPC only. The diffusivity of CTb fit well to a single component model and was determined as 3.26 ± 0.73 $\mu m^2 s^{-1}$. As for the DOPC bilayer, the ternary bilayer the CTb diffusion coefficient was roughly half that of the diffusion coefficient of labeled lipid in the same composition. In the symmetric composition; both leaflets comprised of DOPC/SM/cholesterol (2:2:1) with GM1 (1 mol%) at the distal leaflet, the diffusivity of CTb (4nM) bound to GM1 is two orders of magnitude lower than the asymmetric lipid bilayer of the same composition. This dramatic impedance of diffusion suggests strongly that CTb-GM1 association occurs preferentially at the Lo phase, consistent with previous observations.[61–63] But the data may also suggest that both leaflets must have domain forming compositions for such phases to form, i.e. that domains are transmitted through both leaflets. Similar results of the influence of lipid composition on lateral CTb dynamics were noted by Burns *et al*. Using FCS, they showed that the lateral diffusion of labeled CTb-Alexa 488 was 0.040 $\mu m^2 s^{-1}$ after binding to GM1 in domain forming membranes in SLBs.[62]

Table 4. Effect of lipid composition on the lateral diffusion of CTb in symmetric and asymmetric MSLBs lipid compositions. GM1 at 1 mol% was present only in the distal lipid leaflet. The experiments were performed at 20 ± 0.5 °C.

Lipid composition	CTb lateral diffusion ($\mu m^2 s^{-1}$)
Sym DOPC + GM1	5.6 ± 0.7
Asym DOPC/SM/Chol (2:2:1) + GM1	3.3 ± 0.7
Asym DOPC/SM (1:1) + GM1	1.47 ± 0.40; 0.03 ± 0.02
Sym DOPC/SM/Chol (2:2:1) + GM1	0.61 ± 0.12
Sym DOPC/SM (1:1) + GM1	0.05 ± 0.08

To determine if non-specific CTb adsorption at the membrane in the absence of GM1 occurs, control experiments were performed by FLCS and confocal fluorescence imaging. After extensive incubation of CTb at DOPC-only membranes, consistent with the EIS experiments, there was no evidence of CTb binding at the membrane. In contrast however, CTb (4nM) was observed to adsorb at SM-containing bilayer in the absence of GM1. At a DOPC/SM (1:1) binary membrane, imaging emission from bound labelled CTb and FLCS revealed a diffusion coefficient of 4.6 ± 1.8 $\mu m^2 s^{-1}$ and 3.1 ± 1.5 $\mu m^2 s^{-1}$ for CTb at the asymmetric and symmetric SM-containing bilayers respectively. On incubation at a ternary symmetric DOPC/SM/Chol (2:2:1) bilayer CTb was also found to association and exhibited diffusivity of 1.50 ± 0.20 $\mu m^2 s^{-1}$ (See Supplementary Information, Figure S5 and Table S1). Notably, the diffusion values are roughly half that observed for the toxin when GM1 is present, and correspond more closely with the diffusion values of the lipid label. Analogous behavior is evident at the ternary compositions in absence of GM1, but our data that whereas SM must be present, cholesterol does not need to be present for CTb adsorption to occur The mechanism behind CTb interaction at SM containing bilayers is unknown but given the correlation between the diffusion rates of bound CTb and lipid, it is likely mediated by a direct single SM-CTb interaction. Given the propensity of SM to H-bond, perhaps this plays a role. To our knowledge, there are no previous reports of CTb association with sphingolipid although, SM interaction with other AB toxins has been proposed noted.[28,64]

From FLIM the average lifetime of the CTb-A555 on GM1 binding was also collected. The toxin bound A555 probe exhibits dual exponential fluorescence decay kinetics in all cases. In PBS (pH 7.4) buffer, away from membrane, τ1 was determined as 1.90 ns and τ2 as 0.54 ns (amplitude of 10% and 90% respectively), which is similar to previous data obtained for bioconjugated Alexa 555 dye.[65] On association with the GM1 at the lipid membrane the fluorescent lifetime, particularly of the longer lived, lower amplitude component was significantly extended as shown in Table S2. For example, in DOPC bilayers with 1% GM1 at the distal leaflet, τ1 was determined as 3.1 ns and τ2 as 0.6 ns (amplitude of 20% and 80% respectively, Figure S6 and Table S2). There was a modest dependence of the long component on the bilayer composition, (supplemental materials) wherein ternary composition τ1 it was slightly shorter but the substantial extension to fluorescent lifetime in all cases on GSL binding, is a useful marker for GM1 association.

2.4.6. CTb concentration affects its lateral diffusion on lipid bilayers due to toxin clustering

CTb/GM1 complexes have been demonstrated to diffuse very slowly within the plasma membrane of live cells compared to other protein-lipid complexes including the Shiga toxin complex.[57] The restricted lateral diffusion of CTb/GM1 complexes has been attributed to interaction with actin and also seems to be associated with ATP-dependent processes, that affects the cytoskeletal structure.[66] However, contributions from cross-linking of lipid domains due to multivalent binding of CTb, or due to aggregation of CTb after binding to GM1 may also contribute to the anomalously low mobility of CTb/GM1 complex. As, using Atomic force microscopy (AFM), Wang et al. demonstrated the presence of CTb aggregates on POPC-GM1 bilayer. To date however, there have been no reports on the effect of cholera-cholera aggregation following GM1 association on the lateral diffusion of the resulting aggregates in membranes.[67,68]

To this end, we performed FLCS measurements to interrogate the diffusion of CTb/GM1 as a function of membrane composition. We first monitored the change in lateral mobility of CTb-A555 as a function of increasing concentration of unlabelled CTb at membranes containing static concentrations of GM1. Next, we addressed how membrane fluidity influences CTb binding. This is of interest because previous studies have shown that CTb intoxication occurs mostly at lipid raft or L_o domains whereas depletion of cholesterol has been shown to enhance CTb/GM1 binding.[66,69]

For the mixed bilayers, we used the asymmetric MSLB's to enable these studies, because their enhanced fluidity, ensured diffusion of even aggregated CTb was fast enough to be measurable, and examined two lipid compositions, DOPC alone and DOPC/SM, both containing GM1 in the distal leaflet. To understand if the aggregation is driven by GM1 concentration, we also compared two receptor densities (1 mol% and 5 mol% GM1) at both lipid compositions.

The diffusion coefficient of labeled CTb-A555 (4 nM) was first measured following its incubation for 30 min at room temperature at the aforementioned lipid bilayers. Because of the need for low luminophore levels in FLCS unlabeled CTb concentration was then increased systematically whilst holding the concentration of labeled toxin CTb-A555 constant at 4nM. Following each addition of unlabeled CTb, a minimum of 30 min incubation was allowed. We confirmed separately that beyond 30 minutes no further change to CTb-A555 diffusivity occurred. Figures 5a and 5b show representative ACF curves for CTb-A555 as a function of CTb concentration at the DOPC MSLB containing GM1 1 mol% and 5 mol% respectively. The diffusivity of CTb-A555 at 4 nM fit to a single component model and exhibited Brownian diffusion with a diffusion coefficient of 5 μm2s-1 at 1 mol% GM1. Above 4nM CTb, aggregation of the toxin was evident from the ACFs with concurrent fast and slow component to the fit caused by photobleach of labelled CTb (Figure 5c and 5d). The slow component, on time scale of our experiments were essentially immobile. The diffusivity of the mobile CTb component is plotted versus CTb concentration in Figure 6.

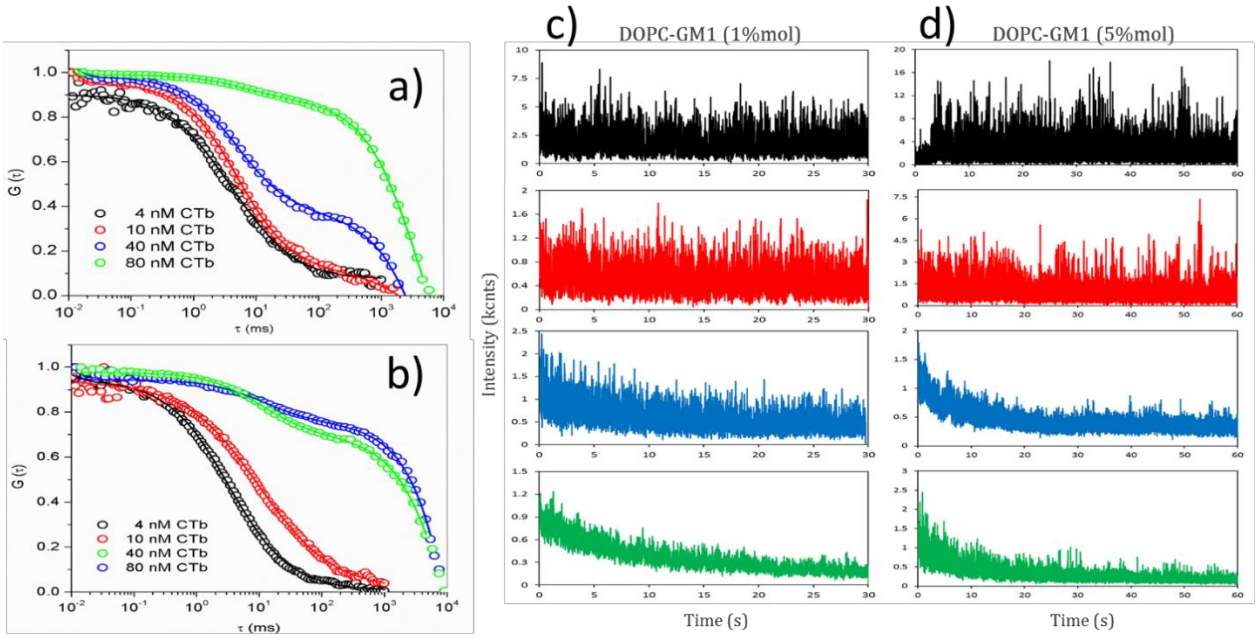

Figure 5. ACF and fluorescence intensity decay of CTb to an asymmetric DOPC lipid bilayer containing a) 1 and b) 5 mol% GM1 at distal leaflet at 20 °C. ACF curves in both panel at varied CTb concentrations are represented by 4 nM (black), 10 nM (red), 40 nM (blue) and 80 nM (green). Solid lines are the fitted data. CTb concentration of 10 nM, 40 nM and 80 nM were fitted with 2 diffusing components. The % contribution of the slow population (aggregates) to the ACF increases with GM1 concentration and CTb concentration. c) and d) represent the fluorescence intensity decay of labeled CTb-A555 at different unlabelled CTb concentration. Photobleaching induced by CTb aggregates can be observed at 40 nM (blue) and 80 nM (green) for both GM1 concentrations.

At DOPC MSLBs with 5 mol% GM1 at the distal leaflet, at 4 nM CTb, notably, D was considerably higher than for 1% GM1 at 8 $\mu m^2 s^{-1}$. Also, in contrast, at the 5 mol% GM1/DOPC membrane, the CTb diffusion remained single-component (Figure 6b) up to a CTb concentration of 10 nM indicating that the valency of GM1-CTb binding depends inversely on GM1 concentration. At CTb concentrations greater than 10 nM, the ACF data again confirmed to a two-component fit and with decreasing diffusion coefficient in the fast component and increasing $\%P_{im}$ content. Although we were unable to estimate the diffusivity value for the immobile fraction because of photobleaching we were able to estimate its relative % contribution the signal and observed that it increased systematically from 0% at 4nM CTb to over 90% at 80 nM CTb for both

GM1 concentrations. This very slow component is likely to be the crosslinked aggregates of CTb with multiple GM1 anchors. Estimation of diffusivity could be made for the fast diffusing fraction in the two-component fit (Figure 6) and this fraction is taken to be GM1 associated with varying number of GM1 anchors. The data shows that at simple DOPC bilayers the extent of CTb-GM1 aggregation depends directly on CTb concentration. And, that at lower concentrations of CTb the number of GM1 associating with the CTb is inversely dependent on the GM1 content in the membrane. Our observations are consistent with previous reports, where increasing in GM1 content was observed to inhibit CTb binding.[70–75] However, at higher CTb concentrations, irrespective of GM1 concentration, the fast diffusing component is the same and extensive aggregation of the CTb has occurred.

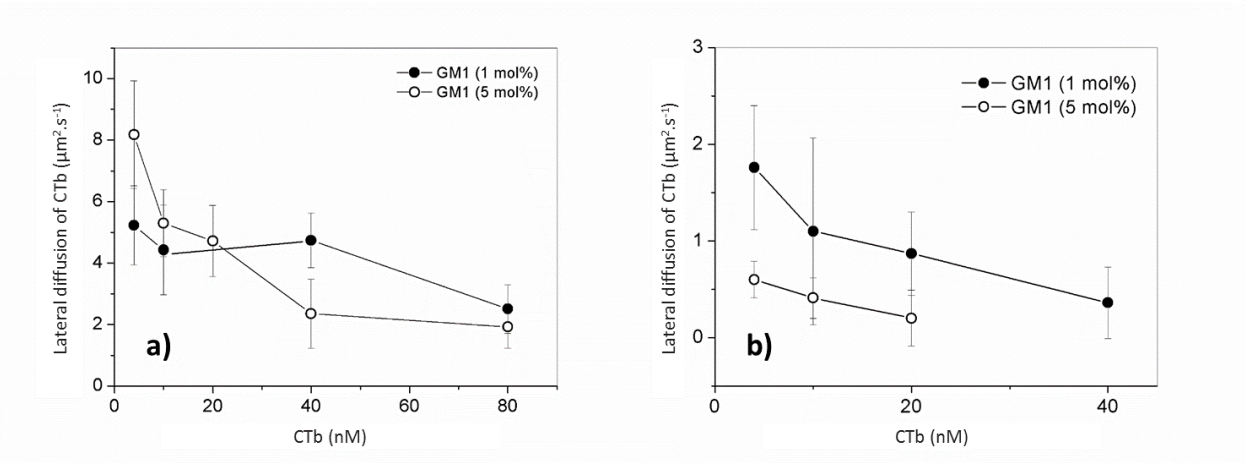

Figure 6 – Diffusion of the fast component of CTb-A555 in presence of increasing concentrations of CTb for lipid bilayers containing 1 mol% (filled circles) and 5 mol% of GM1 (open circles) in the distal leaflet. (a) DOPC and (b) asymmetric DOPC/SM (1:1) mol/mol.

To further confirm that GM1-CTb clustering is occurring, GM1 diffusion was examined at a DOPC bilayer containing GM1 (1 mol %) at the distal leaflet containing 0.01% mol GM1 Bodipy-FL 488. Figure 7 shows the ACF of labeled GM1 before and after incubation with CTb (80 nM). The lateral diffusion of labeled GM1-488 in the distal leaflet in the absence of toxin was measured as 11.45 ± 3.55 $\mu m^2.s^{-1}$ (red symbols). Following incubation with unlabelled CTb (80 nM) the diffusion of GM1-488 became complex (green symbols) comprising a mobile and a slow-diffusing

fraction. This behavior mirrors the diffusive behavior of the labeled CTb aggregation under the same conditions confirming the GM1 is participating in a GM1-CTb network.

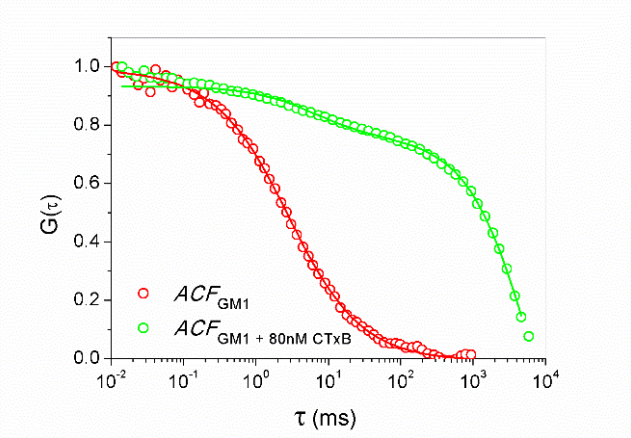

Figure 7. Autocorrelation functions (ACF) of labelled GM1-488 in asymmetric DOPC/DOPC + GM1 (1 mol %) lipid membrane prior (red) and after incubation with 80 nM of unlabelled CTb (green). The shift to right represents the increasing of slow diffusing population, similarly to the labelled CTb scenario indicating that aggregation of CTb is dependent on protein concentration.

2.4.7. Effect of sphingomyelin on CTb binding within asymmetric lipid bilayers containing GM1

Concentration-dependent in-vitro studies of CTb binding due to GM1 clustering have focused on highly fluidic membranes comprised of DOPC and/or POPC.[67] To provide insight into the aggregation of CTb in SM containing membranes, we examined DOPC/SM (1:1) mixed lipid composition in the distal leaflet containing 1 mol% and 5 mol% of GM1 with DOPC in the proximal leaflet. The estimated diffusivity values for the toxin and the $\%P_{im}$ extracted from the fit to the ACF data are presented in Figure 8a and 8b and in Table S4. Initially, at 1 mol% GM1, the CTb response is strongly influenced by the presence of SM where even at 4 nm CTb concentration, a slow diffusing component and immobile/slow fraction constitute 50% of the population (Figure 8c), which is in agreement with previous studies reported by Schwille[57] and Kraut[76] showing that SM leads to immobilization of CTb. The CTb becomes completely immobile in the presence of 40 nM of unlabeled CTb, seen by the evolution of the ACF and fluorescence intensity of CTb-A555 (Figures 8 a and c). Similarly, for 5 mol % GM1, the fluorescence intensity fluctuations of CTb

are affected by photobleaching (Figure 8b and Figure 8d). However, the % of immobile fraction increases with CTb concentration and is similarly evident even at 4 nM of CTb-A555, indicating that GM1 incorporates preferentially to SM to enriched gel domains and this can enhance CTb cross-linking of lipid domains. [77] Together with the non-selective adsorption of CTb at SM containing GM1-free bilayers this behavior may indicate that CTb clustering occurs in a cooperative manner with SM enriched domains and can be related to induced clustering of SM caused by CTb. Interestingly, unlike the DOPC-only bilayer higher GM1 concentration in the distal leaflet appear to enhance GM1 binding; the lateral diffusion of CTb-A555 (4 nM) was found to be 0.6 ± 0.19 $\mu m^2 s^{-1}$ for 5 mol% GM1, which is approximately a 66% lower than diffusivity for the same bilayer at 1 mol% GM1 containing membrane (Figure 5b, Table S4).

Many authors report the bound CTb lateral diffusion as far slower than lipid markers in L_d or L_o regions in cells or GUVs.[57,74,78] Similarly our results obtained for symmetric lipid bilayers in particular, at MSLBs show immobility of CTb-GM1, suggesting extensive aggregation. Although asymmetric lipid bilayers also showed limited mobility which was rapidly diminished with increasing of CTb at the nanomolar range, we can propose that domain registry along with CTb and GM1 concentration contributes to the highly reduced CTb diffusion in cells and GUVs. Our data also indicate lipid diffusivity of DOPE-A655 was also altered by CTb binding but only for SM membranes (Table S4). This lateral mobility effect could be due to a lateral ordering of the lipid membrane dependently on CTb concentration as previously reported.[79] However, to the best of our knowledge, this is the first time that this effect is observed in an asymmetric lipid bilayer formed by a purely disordered DOPC lipid leaflet and a gel phase of DOPC containing SM lipid leaflet.

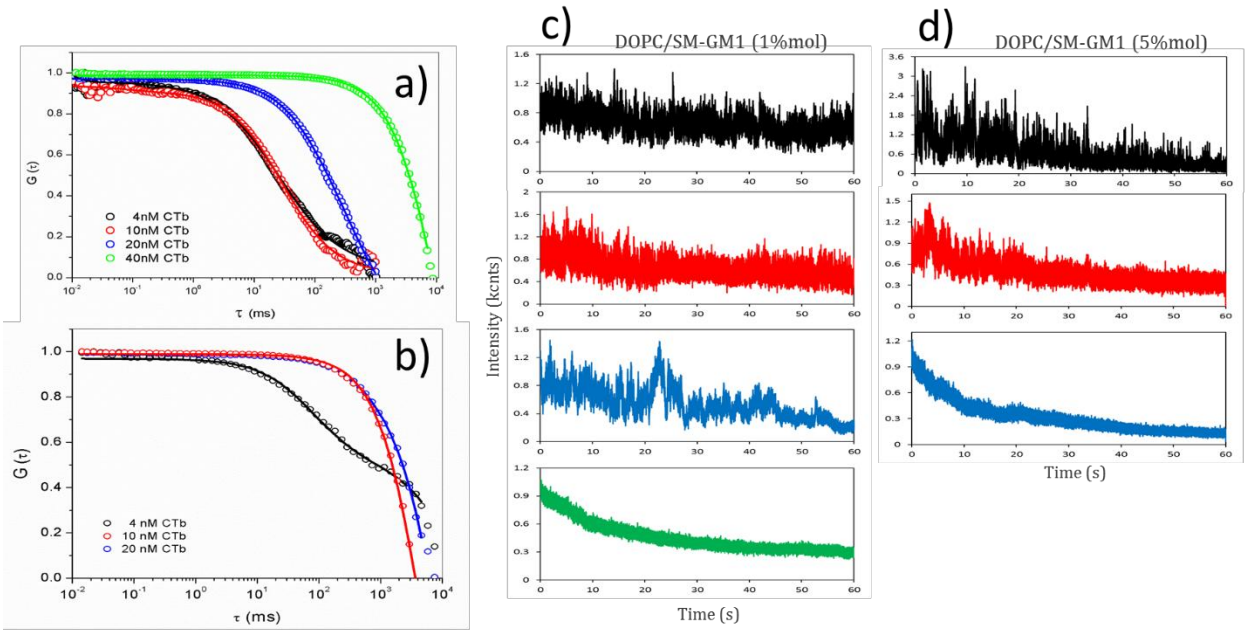

Figure 8. ACF and fluorescence intensity decay of CTb at an asymmetric lipid bilayer comprised of DOPC/SM (1:1 mol/mol) with GM1 (1 mol%), GM1 (5 mol%) studied by FLCS at 20 °C. a) and b) ACF curves obtained for 1 mol% and 5 mol% of GM1 respectively at 4 nM (black), 10 nM (red), 20 nM (blue) and 40 nM (green) of CTb with row data (dots) and fitting (solid line). CTb concentrations of 10 nM, 20 nM and 40 nM were fitted with 2 diffusing components. The % of slow diffusing population (aggregates) increases with GM1 concentration. c) and d) represent the fluorescence intensity decay of labeled CTb-A555 at different wild type CTb concentration. Strong photobleaching induced by CTb aggregates is observed at 20nM (blue) and 40nM (green) for both GM1 concentrations.

2.5. Conclusions

The use of microcavity supported lipid bilayers as a platform to build transversally asymmetric lipid bilayer compositions and as a means to detect and study peripheral protein-membrane recognition at nanomolar range using EIS and FLCS at symmetric and asymmetric lipid bilayer compositions is reported. Six membrane compositions were prepared using a combined Langmuir Blodgett vesicle fusion method; Three symmetric bilayers: DOPC alone, a binary membrane contianing 1: 1 Sphingomyelin and DOPC as a model of mixed gel and L_d phase and a ternary phase separated DOPC:SM:Chol membrane containing fluid-fluid coexisting phases. Analogous asymmetric membranes in which the lower leaflet comprised DOPC were also prepared. in which

DOPC comprised the lower leaflet and binary or ternary mixtures comprised the distal leaflets were successfully prepared at MSLBs. Fluorescence correlation spectroscopy demonstrated that transmembrane asymmetry has a profound influence on membrane fluidity. Where the gel phase and ternary compositions showed 2.5 to 3.5 times lower diffusion coefficient compared to their asymmetric analogues with a DOPC proximal leaflet. The high fluidity of the asymmetric MSLBs enabled FLCS interogation into the effect of CTb binding on GM1-CTb aggregation, which was evaluated as a function of CTb concentration.. Following CTb administration two populations were found to contribute to the diffusion model.The % contribution of the slow diffusing fraction scaled with CTb concentration, suggesting it is CTb led -crosslinked aggregates, while the fast component % diminished and slowed with CTb concentration. This component was attributed to single CTb units anchored to 1, 2 or 3 GM1 units at the membrane, based on simple Saffman Delbruch estimations of radii.

Notably, the data indicate that SM binds non-specifically to CTb perhaps contributing in a cooperative capacity to CTb GM1 binding at the membrane. Gangliosides such as GM1 participate in a wide range of recognition and signalling processes at the cell membrane where signalling in many cases is driven by oligomerization or 2-dimensoinal network formation at the cell membrane. Modelling of such processes at artificial membrane requires capability to build transversally asymmetric bilayers but also fluidity is crucial to enable bilayer organisation. We demonstrate here that MSLBs are a versatile platform for evaluation of GSL-protein interactions at the lipid membrane that encompass these demands and permit multimodal detection methodologies in a single platform approach.

2.6. Supporting Material

Supporting Material data associated with this chapter can be found in Appendix A.

2.7. References

(1) Schuster, B. S-Layer Protein-Based Biosensors. *Biosensors (Basel)* 2018, *8* (2).
(2) Siontorou, C. G.; Nikoleli, G.-P.; Nikolelis, D. P.; Karapetis, S. K. Artificial Lipid Membranes: Past, Present, and Future. *Membranes* 2017, *7* (3), 38.
(3) Espinosa, G.; López-Montero, I.; Monroy, F.; Langevin, D. Shear Rheology of Lipid Monolayers and Insights on Membrane Fluidity. *PNAS* 2011, *108* (15), 6008–6013.
(4) Engelman, D. M. Membranes Are More Mosaic than Fluid. *Nature* 2005, *438*, 578–580.
(5) Daleke, D. L. Regulation of Transbilayer Plasma Membrane Phospholipid Asymmetry. *J. Lipid Res.* 2003, *44* (2), 233–242.
(6) Marquardt, D.; Geier, B.; Pabst, G. Asymmetric Lipid Membranes: Towards More Realistic Model Systems. *Membranes* 2015, *5* (2), 180–196.
(7) Kiessling, V.; Wan, C.; Tamm, L. K. Domain Coupling in Asymmetric Lipid Bilayers. *Biochimica et Biophysica Acta (BBA) - Biomembranes* 2009, *1788* (1), 64–71.
(8) Perlmutter, J. D.; Sachs, J. N. Interleaflet Interaction and Asymmetry in Phase Separated Lipid Bilayers: Molecular Dynamics Simulations. *J. Am. Chem. Soc.* 2011, *133* (17), 6563–6577.
(9) Crane, J. M.; Kiessling, V.; Tamm, L. K. Measuring Lipid Asymmetry in Planar Supported Bilayers by Fluorescence Interference Contrast Microscopy. *Langmuir* 2005, *21* (4), 1377–1388.
(10) Visco, I.; Chiantia, S.; Schwille, P. Asymmetric Supported Lipid Bilayer Formation via Methyl-β-Cyclodextrin Mediated Lipid Exchange: Influence of Asymmetry on Lipid Dynamics and Phase Behavior. *Langmuir* 2014, *30* (25), 7475–7484.
(11) van Meer, G. Dynamic Transbilayer Lipid Asymmetry. *Cold Spring Harbor Perspectives in Biology* 2011, *3* (5), a004671–a004671.
(12) Peyret, A.; Ibarboure, E.; Meins, J.-F. L.; Lecommandoux, S. Asymmetric Hybrid Polymer–Lipid Giant Vesicles as Cell Membrane Mimics. *Advanced Science* 2018, *5* (1), 1700453.
(13) Hwang, W. L.; Chen, M.; Cronin, B.; Holden, M. A.; Bayley, H. Asymmetric Droplet Interface Bilayers. *J. Am. Chem. Soc.* 2008, *130* (18), 5878–5879.
(14) Raggers, R. J.; Pomorski, T.; Holthuis, J. C.; Kälin, N.; van Meer, G. Lipid Traffic: The ABC of Transbilayer Movement. *Traffic* 2000, *1* (3), 226–234.
(15) Chiantia, S.; London, E. Acyl Chain Length and Saturation Modulate Interleaflet Coupling in Asymmetric Bilayers: Effects on Dynamics and Structural Order. *Biophys J* 2012, *103* (11), 2311–2319.
(16) Przybylo, M.; Sýkora, J.; Humpolíčková, J.; Benda, A.; Zan, A.; Hof, M. Lipid Diffusion in Giant Unilamellar Vesicles Is More than 2 Times Faster than in Supported Phospholipid Bilayers under Identical Conditions. *Langmuir* 2006, *22* (22), 9096–9099.
(17) Steltenkamp, S.; Müller, M. M.; Deserno, M.; Hennesthal, C.; Steinem, C.; Janshoff, A. Mechanical Properties of Pore-Spanning Lipid Bilayers Probed by Atomic Force Microscopy. *Biophys J* 2006, *91* (1), 217–226.
(18) Hennesthal, C.; Steinem, C. Pore-Spanning Lipid Bilayers Visualized by Scanning Force Microscopy. *J. Am. Chem. Soc.* 2000, *122* (33), 8085–8086.
(19) Schuster, B.; Weigert, S.; Pum, D.; Sára, M.; Sleytr, U. B. New Method for Generating Tetraether Lipid Membranes on Porous Supports. *Langmuir* 2003, *19* (6), 2392–2397.
(20) Schuster, B.; Sleytr, U. B. S-Layer-Supported Lipid Membranes. *Reviews in Molecular Biotechnology* 2000, *74* (3), 233–254.
(21) Harishchandra, R. K.; Neumann, B. M.; Gericke, A.; Ross, A. H. Biophysical Methods for the Characterization of PTEN/Lipid Bilayer Interactions. *Methods* 2015, *0*, 125–135.
(22) Basit, H.; Gaul, V.; Maher, S.; Forster, R. J.; Keyes, T. E. Aqueous-Filled Polymer Microcavity Arrays: Versatile & Stable Lipid Bilayer Platforms Offering High Lateral Mobility to Incorporated Membrane Proteins. *The Analyst* 2015, *140* (9), 3012–3018.

(23) Ogier, S. D.; Bushby, R. J.; Cheng, Y.; Evans, S. D.; Evans, S. W.; Jenkins, A. T. A.; Knowles, P. F.; Miles, R. E. Suspended Planar Phospholipid Bilayers on Micromachined Supports. *Langmuir* 2000, *16* (13), 5696–5701.
(24) Maher, S.; Basit, H.; Forster, R. J.; Keyes, T. E. Micron Dimensioned Cavity Array Supported Lipid Bilayers for the Electrochemical Investigation of Ionophore Activity. *Bioelectrochemistry* 2016, *112*, 16–23.
(25) Joubert, J. R.; Smith, K. A.; Johnson, E.; Keogh, J. P.; Wysocki, V. H.; Gale, B. K.; Conboy, J. C.; Saavedra, S. S. Stable, Ligand-Doped, Poly(Bis-SorbPC) Lipid Bilayer Arrays for Protein Binding and Detection. *ACS Appl. Mater. Interfaces* 2009, *1* (6), 1310–1315.
(26) Jobling, M. G.; Yang, Z.; Kam, W. R.; Lencer, W. I.; Holmes, R. K. A Single Native Ganglioside GM1-Binding Site Is Sufficient for Cholera Toxin To Bind to Cells and Complete the Intoxication Pathway. *mBio* 2012, *3* (6).
(27) Sezgin, E.; Schwille, P. Fluorescence Techniques to Study Lipid Dynamics. *Cold Spring Harb Perspect Biol* 2011, *3* (11).
(28) Reig, N.; van der Goot, F. G. About Lipids and Toxins. *FEBS letters* 2006, *580* (23), 5572–5579.
(29) Shogomori, H.; Futerman, A. H. Cholera Toxin Is Found in Detergent-Insoluble Rafts/Domains at the Cell Surface of Hippocampal Neurons but Is Internalized via a Raft-Independent Mechanism. *Journal of Biological Chemistry* 2001, *276* (12), 9182–9188.
(30) Heinemann, F.; Vogel, S. K.; Schwille, P. Lateral Membrane Diffusion Modulated by a Minimal Actin Cortex. *Biophys J* 2013, *104* (7), 1465–1475.
(31) Raghunathan, K.; Wong, T. H.; Chinnapen, D. J.; Lencer, W. I.; Jobling, M. G.; Kenworthy, A. K. Glycolipid Crosslinking Is Required for Cholera Toxin to Partition Into and Stabilize Ordered Domains. *Biophysical Journal* 2016, *111* (12), 2547–2550.
(32) Lingwood, D.; Ries, J.; Schwille, P.; Simons, K. Plasma Membranes Are Poised for Activation of Raft Phase Coalescence at Physiological Temperature. *PNAS* 2008, *105* (29), 10005–10010.
(33) Johnson, S. A.; Stinson, B. M.; Go, M. S.; Carmona, L. M.; Reminick, J. I.; Fang, X.; Baumgart, T. Temperature-Dependent Phase Behavior and Protein Partitioning in Giant Plasma Membrane Vesicles. *Biochimica et Biophysica Acta (BBA) - Biomembranes* 2010, *1798* (7), 1427–1435.
(34) Basit, H.; Maher, S.; Forster, R. J.; Keyes, T. E. Electrochemically Triggered Release of Reagent to the Proximal Leaflet of a Microcavity Supported Lipid Bilayer. *Langmuir* 2017, *33* (27), 6691–6700.
(35) Tabarin, T.; Martin, A.; Forster, R. J.; Keyes, T. E. Poly-Ethylene Glycol Induced Super-Diffusivity in Lipid Bilayer Membranes. *Soft Matter* 2012, *8* (33), 8743–8751.
(36) Bennett, W. F. D.; MacCallum, J. L.; Hinner, M. J.; Marrink, S. J.; Tieleman, D. P. Molecular View of Cholesterol Flip-Flop and Chemical Potential in Different Membrane Environments. *J. Am. Chem. Soc.* 2009, *131* (35), 12714–12720.
(37) Heinemann, F.; Schwille, P. Preparation of Micrometer-Sized Free-Standing Membranes. *ChemPhysChem* 2011, *12* (14), 2568–2571.
(38) Yokota, K.; Ogino, T. Phase Separation in Lipid Bilayer Membranes Induced by Intermixing at a Boundary of Two Phases with Different Components. *Chemistry and Physics of Lipids* 2015, *191*, 147–152.
(39) Becucci, L.; Martinuzzi, S.; Monetti, E.; Mercatelli, R.; Quercioli, F.; Battistel, D.; Guidelli, R. Electrochemical Impedance Spectroscopy and Fluorescence Lifetime Imaging of Lipid Mixtures Self-Assembled on Mercury. *Soft Matter* 2010, *6* (12), 2733–2741.
(40) Baumgart, T.; Hunt, G.; Farkas, E. R.; Webb, W. W.; Feigenson, G. W. Fluorescence Probe Partitioning between Lo/Ld Phases in Lipid Membranes. *Biochim Biophys Acta* 2007, *1768* (9), 2182–2194.
(41) Kahya, N.; Schwille, P. How Phospholipid-Cholesterol Interactions Modulate Lipid Lateral Diffusion, as Revealed by Fluorescence Correlation Spectroscopy. *J Fluoresc* 2006, *16* (5), 671–678.

(42) McMullen, T. P. W.; McElhaney, R. N. New Aspects of the Interaction of Cholesterol with Dipalmitoylphosphatidylcholine Bilayers as Revealed by High-Sensitivity Differential Scanning Calorimetry. *Biochimica et Biophysica Acta (BBA) - Biomembranes* 1995, *1234* (1), 90–98.
(43) Lin, Q.; London, E. Ordered Raft Domains Induced by Outer Leaflet Sphingomyelin in Cholesterol-Rich Asymmetric Vesicles. *Biophysical Journal* 2015, *108* (9), 2212–2222.
(44) Hill Reghan J.; Wang Chih-Ying. Diffusion in Phospholipid Bilayer Membranes: Dual-Leaflet Dynamics and the Roles of Tracer–Leaflet and Inter-Leaflet Coupling. *Proceedings of the Royal Society A: Mathematical, Physical and Engineering Sciences* 2014, *470* (2167), 20130843.
(45) Block, S. Brownian Motion at Lipid Membranes: A Comparison of Hydrodynamic Models Describing and Experiments Quantifying Diffusion within Lipid Bilayers. *Biomolecules* 2018, *8* (2).
(46) Kuimova, M. K.; Yahioglu, G.; Levitt, J. A.; Suhling, K. Molecular Rotor Measures Viscosity of Live Cells via Fluorescence Lifetime Imaging. *J. Am. Chem. Soc.* 2008, *130* (21), 6672–6673.
(47) Nojima, Y.; Iwata, K. Viscosity Heterogeneity inside Lipid Bilayers of Single-Component Phosphatidylcholine Liposomes Observed with Picosecond Time-Resolved Fluorescence Spectroscopy. *The Journal of Physical Chemistry B* 2014, *118* (29), 8631–8641.
(48) Ramadurai, S.; Holt, A.; Krasnikov, V.; van den Bogaart, G.; Killian, J. A.; Poolman, B. Lateral Diffusion of Membrane Proteins. *Journal of the American Chemical Society* 2009, *131* (35), 12650–12656.
(49) Adamson, K.; Spain, E.; Prendergast, U.; Moran, N.; Forster, R. J.; Keyes, T. E. Fibrinogen Motif Discriminates Platelet and Cell Capture in Peptide-Modified Gold Micropore Arrays. *Langmuir* 2018, *34* (2), 715–725.
(50) Nascimento, J. M.; Franco, O. L.; Oliveira, M. D. L.; Andrade, C. A. S. Evaluation of Magainin I Interactions with Lipid Membranes: An Optical and Electrochemical Study. *Chemistry and Physics of Lipids* 2012, *165* (5), 537–544.
(51) Juhaniewicz, J.; Sek, S. Interaction of Melittin with Negatively Charged Lipid Bilayers Supported on Gold Electrodes. *Electrochimica Acta* 2016, *197*, 336–343.
(52) Collins, M. D. Interleaflet Coupling Mechanisms in Bilayers of Lipids and Cholesterol. *Biophys J* 2008, *94* (5), L32–L34.
(53) Garg, S.; Rühe, J.; Lüdtke, K.; Jordan, R.; Naumann, C. A. Domain Registration in Raft-Mimicking Lipid Mixtures Studied Using Polymer-Tethered Lipid Bilayers. *Biophys J* 2007, *92* (4), 1263–1270.
(54) Kiessling, V.; Crane, J. M.; Tamm, L. K. Transbilayer Effects of Raft-like Lipid Domains in Asymmetric Planar Bilayers Measured by Single Molecule Tracking. *Biophys. J.* 2006, *91* (9), 3313–3326.
(55) Putzel, G. G.; Uline, M. J.; Szleifer, I.; Schick, M. Interleaflet Coupling and Domain Registry in Phase-Separated Lipid Bilayers. *Biophys J* 2011, *100* (4), 996–1004.
(56) Lauer, S.; Goldstein, B.; Nolan, R. L.; Nolan, J. P. Analysis of Cholera Toxin-Ganglioside Interactions by Flow Cytometry. *Biochemistry* 2002, *41* (6), 1742–1751.
(57) Bacia, K.; Scherfeld, D.; Kahya, N.; Schwille, P. Fluorescence Correlation Spectroscopy Relates Rafts in Model and Native Membranes. *Biophys J* 2004, *87* (2), 1034–1043.
(58) Kelly, C. V.; Wakefield, D. L.; Holowka, D. A.; Craighead, H. G.; Baird, B. A. Near-Field Fluorescence Cross-Correlation Spectroscopy on Planar Membranes. *ACS Nano* 2014, *8* (7), 7392–7404.
(59) Honigmann, A.; Mueller, V.; Ta, H.; Schoenle, A.; Sezgin, E.; Hell, S. W.; Eggeling, C. Scanning STED-FCS Reveals Spatiotemporal Heterogeneity of Lipid Interaction in the Plasma Membrane of Living Cells. *Nature Communications* 2014, *5*, 5412.
(60) Bezlyepkina, N.; Gracià, R. S.; Shchelokovskyy, P.; Lipowsky, R.; Dimova, R. Phase Diagram and Tie-Line Determination for the Ternary Mixture DOPC/ESM/Cholesterol. *Biophys. J.* 2013, *104* (7), 1456–1464.

(61) Levental, I.; Byfield, F. J.; Chowdhury, P.; Gai, F.; Baumgart, T.; Janmey, P. A. Cholesterol-Dependent Phase Separation in Cell-Derived Giant Plasma-Membrane Vesicles. *Biochem. J.* 2009, *424* (2), 163–167.
(62) Burns, A. R.; Frankel, D. J.; Buranda, T. Local Mobility in Lipid Domains of Supported Bilayers Characterized by Atomic Force Microscopy and Fluorescence Correlation Spectroscopy. *Biophys. J.* 2005, *89* (2), 1081–1093.
(63) Niemelä, P. S.; Ollila, S.; Hyvönen, M. T.; Karttunen, M.; Vattulainen, I. Assessing the Nature of Lipid Raft Membranes. *PLoS computational biology* 2007, *3* (2), e34.
(64) Brothers, M. C.; Ho, M.; Maharjan, R.; Clemons, N. C.; Bannai, Y.; Waites, M. A.; Faulkner, M. J.; Kuhlenschmidt, T. B.; Kuhlenschmidt, M. S.; Blanke, S. R.; Rienstra, C. M.; Wilson, B. A. Membrane Interaction of Pasteurella Multocida Toxin Involves Sphingomyelin. *FEBS J* 2011, *278* (23), 4633–4648.
(65) Bumb, A.; Sarkar, S. K.; Wu, X. S.; Brechbiel, M. W.; Neuman, K. C. Quantitative Characterization of Fluorophores in Multi-Component Nanoprobes by Single-Molecule Fluorescence. *Biomed Opt Express* 2011, *2* (10), 2761–2769.
(66) Day, C. A.; Kenworthy, A. K. Mechanisms Underlying the Confined Diffusion of Cholera Toxin B-Subunit in Intact Cell Membranes. *PLoS One* 2012, *7* (4).
(67) Wang, R.; Shi, J.; Parikh, A. N.; Shreve, A. P.; Chen, L.; Swanson, B. I. Evidence for Cholera Aggregation on GM1-Decorated Lipid Bilayers. *Colloids and Surfaces B: Biointerfaces* 2004, *33* (1), 45–51.
(68) Mou, J.; Yang, J.; Shao, Z. Atomic Force Microscopy of Cholera Toxin B-Oligomers Bound to Bilayers of Biologically Relevant Lipids. *J. Mol. Biol.* 1995, *248* (3), 507–512.
(69) Terrell, J.; Yadava, P.; Castro, C.; Hughes, J. Liposome Fluidity Alters Interactions Between the Ganglioside GM1 and Cholera Toxin B Subunit. *Journal of Liposome Research* 2008, *18* (1), 21–29.
(70) Shi, J.; Yang, T.; Kataoka, S.; Zhang, Y.; Diaz, A. J.; Cremer, P. S. GM $_1$ Clustering Inhibits Cholera Toxin Binding in Supported Phospholipid Membranes. *Journal of the American Chemical Society* 2007, *129* (18), 5954–5961.
(71) MacKenzie, C. R.; Hirama, T.; Lee, K. K.; Altman, E.; Young, N. M. Quantitative Analysis of Bacterial Toxin Affinity and Specificity for Glycolipid Receptors by Surface Plasmon Resonance. *J. Biol. Chem.* 1997, *272* (9), 5533–5538.
(72) Lencer, W. I.; Chu, S. H.; Walker, W. A. Differential Binding Kinetics of Cholera Toxin to Intestinal Microvillus Membrane during Development. *Infect. Immun.* 1987, *55* (12), 3126–3130.
(73) Šachl, R.; Amaro, M.; Aydogan, G.; Koukalová, A.; Mikhalyov, I. I.; Boldyrev, I. A.; Humpolíčková, J.; Hof, M. On Multivalent Receptor Activity of GM1 in Cholesterol Containing Membranes. *Biochimica et Biophysica Acta (BBA) - Molecular Cell Research* 2015, *1853* (4), 850–857.
(74) Bacia, K.; Majoul, I. V.; Schwille, P. Probing the Endocytic Pathway in Live Cells Using Dual-Color Fluorescence Cross-Correlation Analysis. *Biophys J* 2002, *83* (2), 1184–1193.
(75) Sagle, L. B.; Ruvuna, L. K.; Bingham, J. M.; Liu, C.; Cremer, P. S.; Van Duyne, R. P. Single Plasmonic Nanoparticle Tracking Studies of Solid Supported Bilayers with Ganglioside Lipids. *Journal of the American Chemical Society* 2012, *134* (38), 15832–15839.
(76) Hebbar, S.; Lee, E.; Manna, M.; Steinert, S.; Kumar, G. S.; Wenk, M.; Wohland, T.; Kraut, R. A Fluorescent Sphingolipid Binding Domain Peptide Probe Interacts with Sphingolipids and Cholesterol-Dependent Raft Domains. *Journal of Lipid Research* 2008, *49* (5), 1077–1089.
(77) Day, C. A.; Kenworthy, A. K. Functions of Cholera Toxin B-Subunit as a Raft Cross-Linker. *Essays In Biochemistry* 2015, *57*, 135–145.
(78) Moens, P. D. J.; Digman, M. A.; Gratton, E. Modes of Diffusion of Cholera Toxin Bound to GM1 on Live Cell Membrane by Image Mean Square Displacement Analysis. *Biophysical Journal* 2015, *108* (6), 1448–1458.

(79) Forstner, M. B.; Yee, C. K.; Parikh, A. N.; Groves, J. T. Lipid Lateral Mobility and Membrane Phase Structure Modulation by Protein Binding. *J. Am. Chem. Soc.* 2006, *128* (47), 15221–15227.

Chapter 3: Microcavity Array Supported Lipid Bilayer Models of Ganglioside – Influenza Hemagglutinin1 Binding

Published in *Chem. Commun.*, 2020, 56, 11251-11254.

Guilherme B. Berselli, Nirod Kumar Sarangi, Aurelien V. Gimenez, Paul V. Murphy, Tia E. Keyes.

Within this work, I was first author and contributor to the experimental design, execution, analysis and preparation of the manuscript. I specifically contributed towards the preparation and characterization of LUVs, PDMS microcavity arrays preparation and characterization, and FLCS studies. Dr. A. Gimenez assisted microcavity-gold array preparation. Supporting information associated with this chapter can be found in Appendix B.

3.1. Abstract

Microcavity supported Lipid Bilayers (MSLBs) are demonstrated as versatile platforms for modelling unit steps in viral-membrane interactions. The binding of influenza receptor (HA1) to membranes containing different glycosphingolipid receptors was investigated. We observed that HA1 preferentially binds to GD1a but the diffusion coefficient of the associated complex at lipid bilayer is approximately double that of the complexes formed by HA1 GM1 or GM3.

3.2. Introduction

Supported lipid membrane models (SLBs) are important biophysical tools to understand protein lipid/glycolipid interactions in controlled conditions.[1] Although highly stable, they typically exhibit reduced lipid lateral mobility, compared to liposomes, due to frictional substrate-membrane interactions.[2] Conversely, microcavity pore supported lipid membranes (MSLBs), offer liposome-like fluidity whilst maintaining much of the stability and versatility of SLBs, including the prospect of controlled asymmetric lipid leaflet composition inaccessible in liposomes.[3] MSLBs are therefore, particularly useful in the study of assembly processes at the lipid membrane that require lateral diffusion of constituent elements. This was exemplified recently in a study of cholera toxin (CTb)-GM1 recognition at asymmetric and symmetric MSLBs containing sphingomyelin and cholesterol.[4]

The influenza virus causes human respiratory illness and is responsible for seasonal and unpredictable pandemic infections.[5] To gain entry to the cytoplasm, influenza A viral protein hemagglutinin (HA) associates with sialylated receptors at the extracellular leaflet of the eukaryotic cell membrane.[6,7] Glycosphingolipids (GSLs) are an important group of hemagglutinin receptors comprised of hydrophobic ceramide backbone attached to oligosaccharide head groups.[8] Glycan microarrays have revolutionized understanding of HA glycan recognition.[9,10] However, artificial glycan arrays lack the cell membrane's fluidity which is intrinsic to the surface that HA encounters in-vivo.[11] There have been numerous investigations into the role of lipid membrane composition on influenza binding, at both cells and membrane models, including at supported lipid membrane models applied to HA1-GSL binding.[12] For instance, the fusion of the

H3N2 virions was demonstrated at SLBs comprised of PC/GM3 and H1N1 at liposomes comprised of PC/PE with GD1a as the HA1 receptor.[13,14] However, the role of the host cell membrane composition as well its fluidity in promoting or inhibiting influenza virus HA -glycan association has not been fully elucidated.[15–17] It has been shown, in liposomes, for example, that the transmembrane domain of HA partitions selectively to liquid ordered (Lo) domains, and in turn manifests clustering and budding of virus, a pathway for viral replication mediated potentially, by lipid rafts.[17–20] Other factors such as acyl chain and sugar head composition, can affect GSL-protein recognition, and thus are likely to affect HA binding.[21] Simple models that can deconvolute the unit constituents of membrane composition in viral and eukaryotic membranes can yield insights into receptor recognition that may prove useful in both advancing fundamental insights and also as biomedically relevant platforms for understanding affinities of key components in infection for drug targets. Here, we combine electrochemical impedance spectroscopy (EIS) with Fluorescence Lifetime Correlation Spectroscopy (FLCS) to assess the relative affinity of HA1 toward different GSLs within different membrane compositions at MSLBs. This study focuses on the monomeric globular head domain, HA1, of influenza HA (noting in its native form it is a homotrimeric glycoprotein).[22] HA1 contains the sialic acid receptor binding site responsible for cell membrane attachment and it is also an important epitope for neutralization antibodies against the influenza virus.[23] This analysis was carried out at the nanomolar concentration range of HA1.

3.3. Experimental Methods

3.3.1. Preparation of Microcavity arrays and MSLBs

A 1 cm^2 gold electrode imprinted with an ordered array of uniform semi-spherical pores of 1 μm diameter were prepared by gold electrodeposition following the method previously described (detailed in SI).[1,2] To enhance bilayer stability, the exterior, top, surface of the arrays was selectively functionalized with a monolayer of 6-mercaptohexanol (SI). For FLCS studies, MSLBs were assembled at optically transparent, polydimethylsiloxane (PDMS) microcavity arrays as previously reported.[1,2] Lipid bilayer was assembled by depositing a lipid monolayer at pre-aqueous filled pore arrays by the Langmuir Blodgett deposition, followed by vesicle fusion of the proximal monolayer. This approach, reported previously, permits ready preparation of asymmetric bilayer

compositions.3 In nature, glycosphingolipids are isolated to the outer leaflet of the cell membrane, thus, we assembled the GSLs only at the distal leaflet of the MSLBs by incorporating them into the liposomes used for the vesicle fusion step (See Fig. S1, SI). Whereas EIS measurements are label-free, for FLCS, fluorescently labelled DOPE-ATTO655 (0.01 mol%) was mixed into the lipid bilayer and the influenza HA1 was labelled with ATTO532 following the method described in Fig. S2, (SI). The experiments were conducted in triplicates.

3.4. Results and Discussion

3.4.1. Binding of HA1 to DOPC bilayers containing different GSLs

We first evaluated the affinity of HA1, using EIS, toward the individual GSLs; GM1, GM3 and GD1a, where each was doped at 1 mol% into model DOPC lipid bilayers (the most fluidic membrane) at gold-supported MSLBs. Figure 1a shows a representative Nyquist plot obtained from DOPC bilayer containing 1 mol % of GM1 at different concentrations of HA1. The relative Faradaic charge transfer resistance (RCT) was obtained from the diameter of the semicircle of the Nyquist plot by fitting the experimental data to an equivalent circuit model (ECM) (inset, Fig.2a), a heuristic model reported earlier by us for suspended bilayer over microcavity pores.1,3 Note that a constant phase element (CPE) was used instead of a pure capacitor to obtain the best fit. The relative change to membrane resistivity (ΔR) after exposure to HA1 was deduced from the initial membrane resistivity at 0 nM HA1. As expected HA1 binding increased membrane resistance, due to decreased admittance through the interfacial HA layer. This is also reflected in decreased membrane capacitance ($\Delta\boldsymbol{Q}$) values (cf. Fig. S3a, SI). Decreases to capacitance likely reflect increasing membrane thickness and may also reflect convolution of membrane thickness changes with changes to membrane roughness (or curvature), that impact the membrane area on HA association. The relative change in charge transfer resistance (ΔR) was plotted against HA1 concentration (0 - 100 nM), Fig.1b (filled symbols). From Fig.1b it can be seen that by ~100 nM saturation binding is reached for each GSL. We fit the experimental ΔR data (dashed lines, Fig.2b) to the Hill-Waud binding model (SI) which applies to cooperative protein-receptor binding (Hill coefficient, $\boldsymbol{n}$ dependency, see SI).4 From our fit, the empirical apparent equilibrium dissociation constant $\boldsymbol{K_D}$ values were estimated and indicate that HA1 has highest affinity for GD1a (17.47±2 nM, n=2.56) followed by GM3 (23.96±4 nM, n=1.45) with lowest affinity recorded for GM1

(41.3±9 nM, n=1.81) at DOPC membranes (cf. Table S1, SI). These differences in affinity are not surprising given each GSLs differs in their oligosaccharide group constitution. GD1a is notably different in that it terminates with two sialic acid (n-acetylneuraminic acid) residues compared to one for GM1 and GM3. In addition, the packing of the GSLs in the lipid bilayer may play a role in affinity. GM1 and GM3 are known to pack differently in the membrane, e.g., ganglioside aggregation balances hydrogen bond interactions and steric hindrance of the headgroups, causing differences to clustering of GSLs depending on the headgroup involved.5,6 The differences in packing are likely reflected in the very different magnitudes of ΔR response for the GSLs on HA binding.

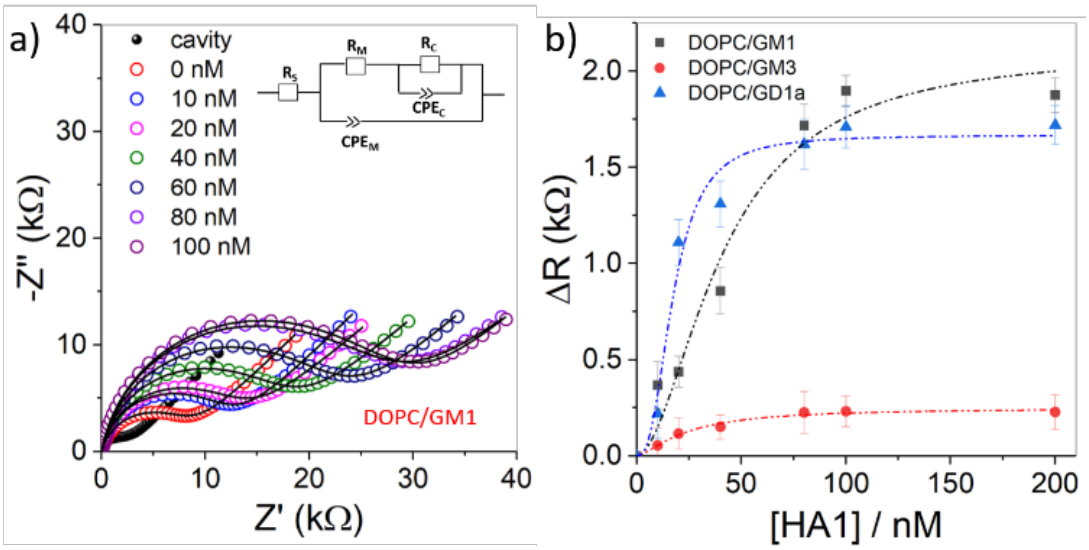

Figure 1. HA_1 binding to different GSLs in DOPC MSLBs formed in gold microcavities array. (a) Nyquist plot of cavity array before bilayer deposition (open black). EIS data of DOPC bilayer with GM1 (1 mol%) before HA1 red and after HA1 incubation (red: 0 nM, blue: 10 nM, pink: 20 nM, green: 40 nM, dark purple: 60 nM, light purple: 80 nM and violet: 100nM). Solid lines show the fit using ECM (inset). (b) Relative variation of the DOPC bilayer resistivity (ΔR) on HA1 binding to bilayers containing 1 mol% of different glycolipids. The dashed curves were fit to the Hill-Waud model. All the EIS spectra recorded in the presence of 1 mM Fe(CN)6 3-/4- and 0.1 M KCl at a bias potential of +0.26 V vs. Ag/AgCl (1 M KCl) with an amplitude 10 mV and frequency range of 104 to 10-2 Hz. All the measurements were carried out at 22±1 °C. The error bars in b, are ± SD, and the measurements are from triplicate.

Control experiments to evaluate non-specific binding in the absence of GSLs were carried out. And, as expected, no impedance changes were evident on incubation of HA1 across any of the membranes explored in the absence of GSL. This observation was further confirmed from fluorescence data (Fig S4, SI). Next, the interaction of HA1 with each GSL at DOPC membrane was investigated using fluorescence lifetime correlation spectroscopy (FLCS) at PDMS-MSLB platform, to evaluate the lateral diffusivity of fluorescently labelled HA1 (HA1-ATTO532).

Figure 2 shows representative autocorrelation function (ACF) data obtained for HA1-ATTO532 after incubation with an MSLB of DOPC/GM1 (1 mol%) (blue circles), DOPC/GD1a (1 mol%) (orange circles) and DOPC/GM3 (1 mol%) (green circles). Free HA1 (in the absence of bilayer) HA1-ATTO532 (red) and ATTO532 (black) dye in PBS solution. The diffusion coefficients of ATTO532 (Fig.2, black circles) and labelled HA1 (Fig.2, red circles) in PBS solution (pH 7.4) (each at 10 nM) were calculated by fitting the ACFs to a 3D model (See SI) as 385 $\mu m^2.s^{-1}$ and 90 $\mu m^2.s^{-1}$ respectively, which indicates a HA1 hydrodynamic radius of approximately 2.4 nm. The lateral diffusion coefficient of HA1-ATTO532 at GSL-containing MSLB was obtained by fitting the ACFs to a 2D diffusion model (See SI) and was determined as 13 $\mu m^2.s^{-1}$ for DOPC/GD1a and 5 $\mu m^2.s^{-1}$ for DOPC/GM1 and DOPC/GM3. The anomalous coefficient (α) value was obtained as ~1 in all cases, indicating Brownian diffusion.

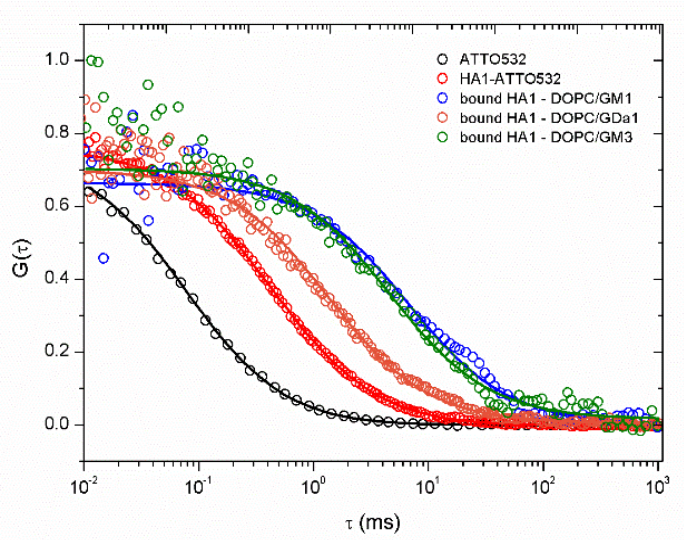

Figure 2 FLCS fitted autocorrelation functions (ACFs) obtained for free ATTO532 (black circles) and labelled HA1-ATTO532 (red circles) in PBS (pH 7.4). After incubating labelled HA1-ATTO532 to MSLBs comprised of DOPC containing 1 mo%l of GM1 (blue circles), GM3 (green circles) and GD1a (orange

circles). The bound fraction of HA1 was obtained by fitting the data to a one diffusing component model using 10 nM of dye/labelled protein.

The distinction in the lateral diffusion of HA1 bound to GD1a and GM1 or GM3 is notable, given the ceramide tails of each glycolipid are analogous, the anticipated 1:1 binding would be expected to yield similar diffusion coefficients at a homogenous DOPC bilayer. The distinction indicates, interestingly, that the radius of the final membrane bound HA1-GSL complex is different for GD1a compared to GM1 or GM3. The diffusion value was therefore used to estimate the diameter of membrane associated complex, from the Saffman-Delbrük (SD) model (SI). Using the SD model, we obtained a radius of 0.30 nm for GD1a, which corresponds well with that expected for diffusion of a single GD1a lipid. In contrast, a radius of 7.0 nm for the assembly formed by GM1/GM3 binding was estimated. As HA1 is monomeric and presents a single binding site, the differences in size/diffusion value cannot be ascribed to multivalency. However, the distinctions may be attributed to variation in penetration of HA into the membrane as it accommodates the glycolipid binding, or may be due to self-association of glycolipids within the membrane. Although no evidence of lateral aggregation of HA1 was observed even after prolonged incubation with GSL-containing membrane at saturation coverage of HA1 as reflected in the homogeneity of the intensity-time traces (Fig. S5, SI). And, binding of HA1-ATTO532 (10 nM, 40 nM or 80 nM, see Fig. S5, SI) at the membrane, was found not to influence membrane diffusivity significantly.

3.4.2. Membrane fluidity affects HA1-GSL recognition

Other parameters such as physical properties of membrane and phase, which are affected by membrane composition can influence the lateral organisation of GSLs and their clustering. And there is significant evidence that ordered domains and rafts can promote HA-glycan binding.7–9 Furthermore, the lateral organization of GSLs can be affected by the membrane composition in purely liquid disordered (Ld) membranes which may also influence affinity for HA1.5,10 We, therefore used the MSLBs to investigate the impact of the membrane composition and Lo and Ld phase-separated domains on HA1 binding to GM1. The membrane diffusivity for each composition was assessed from the lateral mobility of DOPE-ATTO655 lipid tracer in the absence of protein, and the protein diffusivity was determined with HA1-ATTO532 at bilayers of DOPC, POPC and DOPC/SM/Chol (4:4:2) (mol/mol/mol) doped with 1 mol% GM1 at the distal leaflet.

In parallel, the effect of HA1 association was evaluated using EIS at gold arrays. The Faradaic charge transfer resistance (***R***CT) of the aforementioned membranes and their relative change on exposure to HA1 interactions are shown in Fig.3. Interestingly, the binding constant, roughly estimated from ΔR at 50% saturation, is essentially unchanged by membrane composition. Whereas in contrast, the relative magnitude of membrane resistance change varies widely with composition on association with HA1 (Fig. 3). ΔR is most pronounced for DOPC MSLB, compared with POPC, and HA1 exerted least impact on the resistance of the ternary DOPC/SM/Chol membrane. For instance, at a fixed concentration of HA1 (100 nM), corresponding to saturation binding, the ΔR obtained for DOPC (ΔRDOPC = 1.9 kΩ) shows respectively 2 and 10 fold greater resistivity change compared to POPC membranes (ΔRPOPC = 0.9 kΩ) and DOPC/SM/Chol (ΔR = 0.2 kΩ) membrane. This is attributed to the much tighter packing of cholesterol-containing membranes. The diffusivity data for labelled DOPE from FLCS (Table S2) in the absence of HA1 and for bound labelled HA1 are given in (Figure 4b, Table S2).

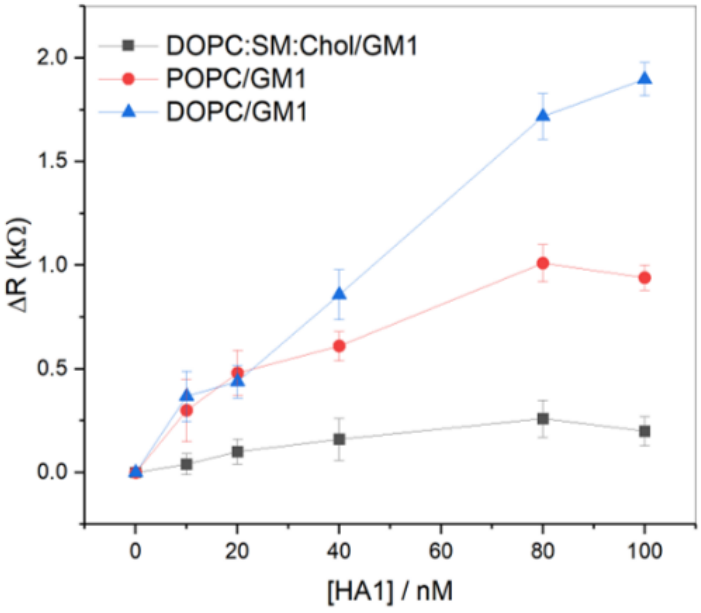

Figure 3 Representative resistance changes on HA1 binding to GM1 (1mol%) at MSLBs of different lipid compositions. The addition of sphingomyelin and cholesterol reduces the clustering of Influenza receptor in comparison to the highly fluidic DOPC lipid bilayer. The asymmetric lipid bilayers are comprised of a DOPC layer (proximal leaflet) and DOPC/SM/Chol (4:4:2) (distal leaflet).

In the absence of HA1, the lateral diffusion of labelled DOPE-ATTO655 was recorded as 10 μm2.s-1 for DOPC, consistent with previous reports,11 6.0 μm2.s-1 for POPC and 3.5 μm2.s-1 for DOPC/SM/Chol (4:4:2) membrane. The presence of 1 mol% GM1 at the distal leaflet did not affect measured fluidity. As expected, the data confirms membrane fluidity decreases in the order; DOPC > POPC > DOPC/SM/Chol (4:4:2), attributed in the latter case to mixed domain formation.12 Within experimental error, the diffusivity of the lipid marker did not change upon HA1-ATTO532 (10 nM) incubation irrespective of membrane composition. For the ternary DOPC/SM/Chol (4:4:2) composition, the diffusivity of the ordered lipid regions was obtained separately by measuring the lateral diffusion of labelled sphingomyelin (SM-ATTO647n), as 2.5 μm2.s-1, which is 3.5-fold lower than its diffusivity in DOPC membranes, 8.8 μm2.s-1 (Fig. S6, SI). The lateral diffusion of membrane bound HA1-ATTO532 is influenced profoundly by membrane composition and found to be 5.0 μm2.s-1 for DOPC, 3.3 μm2.s-1 for POPC and 1.6 μm2.s-1 for ternary lipid bilayers.

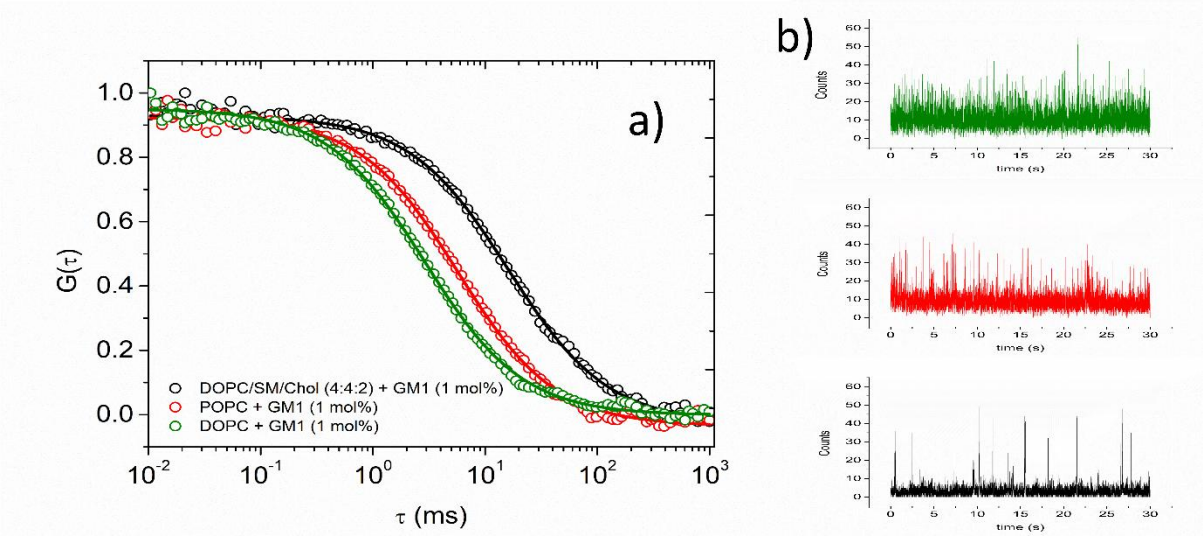

Figure 4 – a) Normalized autocorrelation function of HA1-ATTO532 obtained from MSLBs of DOPC (green), POPC (red) and DOPC/SM/Chol (black). All lipid bilayers contain GM1 (1 mol%) in the distal lipid leaflet. (b) Illustrates corresponding fluorescence intensity time trace of labelled HA1 at designated bilayer composition.

Notably, for DOPC and POPC the diffusion coefficient is roughly half that of the lipid label. Whereas for the ternary composition, the diffusion rate is lower than half, which suggests an association with ordered domains, consistent with previous report.13 The number of labelled HA1 molecules in the confocal volume may indicate that HA1 has a higher preference to bind to GM1

in more fluidic membranes but based on EIS data the difference is not dramatic (Figure 4b, Table S2). It is worth mentioning that the curvature, as well as thermal fluctuation of membrane lipid, may affect the diffusivity of proteins, as observed in a previous study.14 Our results from EIS as well as FLCS revealed that HA1 has an important predilection for binding GSLs in more fluidic membranes.

3.5. Conclusion

In summary, the affinity of three prevalent glycosphingolipids for influenza subunit HA1 were compared. GD1a showed highest affinity at DOPC bilayers, but diffusivity of the resulting GSL-HA1 complex was roughly half of that GM1 and GM3- HA1 complexes indicating surprising differences in the assembly dimensions or associated HA1 penetration into the lipid bilayer. The affinity of HA1 for GM1 appears unaffected by bilayer composition. But the lower mobility of bound HA1 in SM/Chol membranes suggests association with Lo domains. Overall, the data demonstrates that MSLBs are versatile platform for modelling unit steps in viral-membrane interactions. These studies will next be extended to multivalent HA subtypes and related viral models.

3.6. Supporting Material

Supplementary data associated with this chapter can be found in Appendix B.

3.7. References

(1) Carton, I.; Lucy Malinina; Richter, R. P. Dynamic Modulation of the Glycosphingolipid Content in Supported Lipid Bilayers by Glycolipid Transfer Protein. *Biophys J* 2010, *99* (9), 2947–2956.
(2) Siontorou, C. G.; Nikoleli, G.-P.; Nikolelis, D. P.; Karapetis, S. K. Artificial Lipid Membranes: Past, Present, and Future. *Membranes* 2017, *7* (3), 38.
(3) Berselli, G. B.; Sarangi, N. K.; Ramadurai, S.; Murphy, P. V.; Keyes, T. E. Microcavity-Supported Lipid Membranes: Versatile Platforms for Building Asymmetric Lipid Bilayers and for Protein Recognition. *ACS Appl. Bio Mater.* 2019, *2* (8), 3404–3417.
(4) Taubenberger, J. K.; Morens, D. M. The Pathology of Influenza Virus Infections. *Annu Rev Pathol* 2008, *3*, 499–522.
(5) Steinhauer, D. A. Role of Hemagglutinin Cleavage for the Pathogenicity of Influenza Virus. *Virology* 1999, *258* (1), 1–20.

(6) Gamblin, S. J.; Skehel, J. J. Influenza Hemagglutinin and Neuraminidase Membrane Glycoproteins. *Journal of Biological Chemistry* 2010, *285* (37), 28403–28409.
(7) Degroote, S.; Wolthoorn, J.; van Meer, G. The Cell Biology of Glycosphingolipids. *Seminars in Cell & Developmental Biology* 2004, *15* (4), 375–387.
(8) Stevens, J.; Blixt, O.; Paulson, J. C.; Wilson, I. A. Glycan Microarray Technologies: Tools to Survey Host Specificity of Influenza Viruses. *Nature Reviews Microbiology* 2006, *4* (11), 857–864. h
(9) Huang, M. L.; Cohen, M.; Fisher, C. J.; Schooley, R. T.; Gagneux, P.; Godula, K. Determination of Receptor Specificities for Whole Influenza Viruses Using Multivalent Glycan Arrays. *Chem. Commun.* 2015, *51* (25), 5326–5329.
(10) Ji, Y.; White, Y. J.; Hadden, J. A.; Grant, O. C.; Woods, R. J. New Insights into Influenza A Specificity: An Evolution of Paradigms. *Curr Opin Struct Biol* 2017, *44*, 219–231.
(11) Müller, M.; Lauster, D.; Wildenauer, H. H. K.; Herrmann, A.; Block, S. Mobility-Based Quantification of Multivalent Virus-Receptor Interactions: New Insights Into Influenza A Virus Binding Mode. *Nano Lett.* 2019, *19* (3), 1875–1882.
(12) Ramalho-Santos, J.; Pedroso De Lima, M. C. The Role of Target Membrane Sialic Acid Residues in the Fusion Activity of the Influenza Virus: The Effect of Two Types of Ganglioside on the Kinetics of Membrane Merging. *Cell. Mol. Biol. Lett.* 2004, *9* (2), 337–351.
(13) Godefroy, C.; Dahmane, S.; Dosset, P.; Adam, O.; Nicolai, M.-C.; Ronzon, F.; Milhiet, P.-E. Mimicking Influenza Virus Fusion Using Supported Lipid Bilayers. *Langmuir* 2014, *30* (38), 11394–11400.
(14) Leiva, R.; Barniol-Xicota, M.; Codony, S.; Ginex, T.; Vanderlinden, E.; Montes, M.; Caffrey, M.; Luque, F. J.; Naesens, L.; Vázquez, S. Aniline-Based Inhibitors of Influenza H1N1 Virus Acting on Hemagglutinin-Mediated Fusion. *J. Med. Chem.* 2018, *61* (1), 98–118.
(15) Sun, X.; Whittaker, G. R. Role for Influenza Virus Envelope Cholesterol in Virus Entry and Infection. *Journal of Virology* 2003, *77* (23), 12543.
(16) Scheiffele, P.; Rietveld, A.; Wilk, T.; Simons, K. Influenza Viruses Select Ordered Lipid Domains during Budding from the Plasma Membrane. *J. Biol. Chem.* 1999, *274* (4), 2038–2044.
(17) Scolari, S.; Engel, S.; Krebs, N.; Plazzo, A. P.; Almeida, R. F. M. D.; Prieto, M.; Veit, M.; Herrmann, A. Lateral Distribution of the Transmembrane Domain of Influenza Virus Hemagglutinin Revealed by Time-Resolved Fluorescence Imaging. *J. Biol. Chem.* 2009, *284* (23), 15708–15716.
(18) Veit, M.; Thaa, B. Association of Influenza Virus Proteins with Membrane Rafts. *Adv Virol* 2011, *2011*, 370606.
(19) Takeda, M.; Leser, G. P.; Russell, C. J.; Lamb, R. A. Influenza Virus Hemagglutinin Concentrates in Lipid Raft Microdomains for Efficient Viral Fusion. *PNAS* 2003, *100* (25), 14610–14617.
(20) Malinina, L.; Malakhova, M. L.; Kanack, A. T.; Lu, M.; Abagyan, R.; Brown, R. E.; Patel, D. J. The Liganding of Glycolipid Transfer Protein Is Controlled by Glycolipid Acyl Structure. *PLoS Biol* 2006, *4* (11).
(21) Jegaskanda, S.; Reading, P. C.; Kent, S. J. Influenza-Specific Antibody-Dependent Cellular Cytotoxicity: Toward a Universal Influenza Vaccine. *The Journal of Immunology* 2014, *193* (2), 469–475.
(22) Lee, C.-C.; Yang, C.-Y.; Lin, L.-L.; Ko, T.-P.; Chang, A. H.-L.; Chang, S. S.-C.; Wang, A. H.-J. An Effective Neutralizing Antibody Against Influenza Virus H1N1 from Human B Cells. *Scientific Reports* 2019, *9* (1), 1–11.
(23) Maher, S.; Basit, H.; Forster, R. J.; Keyes, T. E. Micron Dimensioned Cavity Array Supported Lipid Bilayers for the Electrochemical Investigation of Ionophore Activity. *Bioelectrochemistry* 2016, *112*, 16–23.
(24) Jose, B.; Mallon, C. T.; Forster, R. J.; Blackledge, C.; Keyes, T. E. Lipid Bilayer Assembly at a Gold Nanocavity Array. *Chem. Commun.* 2011, *47* (46), 12530–12532.

(25) Shi, J.; Yang, T.; Kataoka, S.; Zhang, Y.; Diaz, A. J.; Cremer, P. S. GM $_1$ Clustering Inhibits Cholera Toxin Binding in Supported Phospholipid Membranes. *Journal of the American Chemical Society* 2007, *129* (18), 5954–5961.
(26) Gu, R.-X.; Ingólfsson, H. I.; de Vries, A. H.; Marrink, S. J.; Tieleman, D. P. Ganglioside-Lipid and Ganglioside-Protein Interactions Revealed by Coarse-Grained and Atomistic Molecular Dynamics Simulations. *J. Phys. Chem. B* 2017, *121* (15), 3262–3275.
(27) Lee, D. W.; Hsu, H.-L.; Bacon, K. B.; Daniel, S. Image Restoration and Analysis of Influenza Virions Binding to Membrane Receptors Reveal Adhesion-Strengthening Kinetics. *PLOS ONE* 2016, *11* (10), e0163437.
(28) Wilson, R. L.; Frisz, J. F.; Klitzing, H. A.; Zimmerberg, J.; Weber, P. K.; Kraft, M. L. Hemagglutinin Clusters in the Plasma Membrane Are Not Enriched with Cholesterol and Sphingolipids. *Biophysical Journal* 2015, *108* (7), 1652–1659.
(29) Nikolaus, J.; Scolari, S.; Bayraktarov, E.; Jungnick, N.; Engel, S.; Plazzo, A. P.; Stöckl, M.; Volkmer, R.; Veit, M.; Herrmann, A. Hemagglutinin of Influenza Virus Partitions into the Nonraft Domain of Model Membranes. Biophys J 2010, 99 (2), 489–498.
(30) Goronzy, I. N.; Rawle, R. J.; Boxer, S. G.; Kasson, P. M. Cholesterol Enhances Influenza Binding Avidity by Controlling Nanoscale Receptor Clustering. Chem. Sci. 2018, 9 (8), 2340–2347.
(31) Fricke, N.; Dimova, R. GM1 Softens POPC Membranes and Induces the Formation of Micron-Sized Domains. Biophys. J. 2016, 111 (9), 1935–1945.
(32) Marsh, D. Cholesterol-Induced Fluid Membrane Domains: A Compendium of Lipid-Raft Ternary Phase Diagrams. Biochimica et Biophysica Acta (BBA) - Biomembranes 2009, 1788 (10), 2114–2123.
(33) Nicolau, D. V.; Burrage, K.; Parton, R. G.; Hancock, J. F. Identifying Optimal Lipid Raft Characteristics Required To Promote Nanoscale Protein-Protein Interactions on the Plasma Membrane. Mol Cell Biol 2006, 26 (1), 313–323.

Chapter 4: A Robust Photoelectric Biomolecular Switch at a Microcavity Support Lipid Bilayer

---

Published in *Appl. Mat. Inter.*, 2021, 13, 29158-29169.

Guilherme B. Berselli, Aurelien V. Gimenez, Alexandra O'Connor, Tia E. Keyes.

Within this work I was the primary author and contributor to the experimental design, execution, analysis, and preparation of the manuscript. I specifically contributed towards the following sections: preparation and characterization of LUVs and proteoliposomes, PDMS and Gold

microcavity arrays preparation, FLCS and electrochemical studies. Dr. A. Gimenez carried out microcavity arrays SEM/FESEM imaging and Alexandra O'Connor assisted in protein activation experiments. Supporting information associated with this chapter can be found in Appendix C.

4.1. Abstract

Biomolecular devices based on photo-responsive proteins have been widely proposed for medical, electrical, energy storage and production applications. And, bacteriorhodopsin has been extensively applied in such prospective devices as a robust photo addressable proton pump. As it is a membrane protein, in principle it should function most efficiently when reconstituted into a fully fluid lipid bilayer but in many model membranes, lateral fluidity of membrane and protein is sacrificed for electrochemical addressability because of the need for an electroactive surface. Here, we reported a biomolecular photo-active device based on light activated proton pump, bacteriorhodopsin (bR) reconstituted into highly fluidic Microcavity Supported Lipid Bilayers, MSLBs, at functionalised gold and polydimethylsiloxane (PDMS) cavity arrays substrates. The integrity of reconstituted bR at the MSLBs along with the lipid bilayer formation were evaluated by Fluorescence Lifetime Correlation Spectroscopy (FLCS), yielding protein lateral diffusion coefficient that was dependent on bR concentration, and consistent with Saffman-Delbrück model. The photo-electrical properties of bR-MSLBs were evaluated from the photocurrent signal generated by bR under temporal and transient light illumination. The optimal conditions for a self-sustaining photo-electrical switch were determined in terms of protein concentration, pH and light frequency of activation. Overall, a significant increase in the transient current was observed for lipid bilayers containing approximately 0.3 mol% bR with a measured photo-current of 250 nA/cm2. These results demonstrate that the platforms provide an appropriate lipid environment to support the proton pump, enabling its efficient operation. The bR reconstituted MSLB model serves both as a platform to study the protein in a highly addressable biomimetic environment but also serves as a demonstration of reconstitution of seven-helix receptors into MSLBs, opening the prospect of reconstitution of related membrane proteins including G-protein-coupled receptors at these versatile biomimetic substrates.

4.2. Introduction

Molecular machines, capable of reversible molecular motion or vectorial charge transport in response to optical or electrochemical stimuli are widely proposed as constituents of Boolean logic

gates for high density data storage and processing or for signal processing in imaging and sensing. As recently discussed by Leigh et al, there are two approaches generally taken in design of molecular machines, Technomimetics and Biomimetics, where the structures are inspired by real world mechanical machines in the latter and by molecular biological switches and signals in the latter.[1] The advantage of biomimetics is that such systems are already molecularly based, and biology offers the advantage of iteratively evolved structures and mechanisms to produce nanomechanical devices that offer robust addressable by light or changes to potential. Such biological molecular machines include functions such ATP synthase, neural transport, force generation, cell motility and division, membrane channels and ions pumps. All offer opportunities for the development of smart switchable materials.[2] And, the manipulation of such biological structures in engineered self-assembled biomolecular devices is emerging as a domain with extensive potential for advances in nanoengineering, materials science as well as an avenue to new biological insights.[3–6] However, the majority of biological molecular machines are membrane proteins, thus their structure and conformation, which is intrinsically linked to their efficient operation, relies on their proper insertion or orientation at the lipid membrane. Thus, the reconstitution of such biomaterials into bioengineered structures that closely mimic the key elements of the biological membrane are crucial to achieving optimal and stable response.

In biology, signal transduction and cell signaling frequently relies on biomolecular switches such as protein conformational change to create membrane proton gradients, instigate processes such protein aggregation, and cellular viral entry.[7–9] Many applications of biomolecular machines in artificial devices particularly rely in the ability of biomaterials to respond electrically under light irradiation. Among them, particular attention has been paid to biohybrid engineered devices focused on self-assembled protein-based photonic devices, such ion channel and transporter proteins in artificial membranes.[10–13] Such retro-bioengineering of photochromic biological machines are finding application in in photochemical cells, biosensors, solar fuel and energy storage/conversion.[14]

Bacteriorhodopsin (bR) is one of the most studied biological machines in this regard. It is a photo-initiated proton pump of the *Halobacterium Salinarum* membrane. bR converts solar into chemical energy by pumping protons against a proton gradient from the cytosolic to the extracellular side

of the cell membrane. The bR photocycle which completes in about 10 ms at room temperature, occurs through a series of 7 spectroscopically distinguishable steps bR→K↔L↔M1→M2↔N↔O→bR. The first is initiated by the photoinduced all-trans-to-cis isomerization at C13=C14 of the retinal, culminating in proton transfer across the bacterial membrane.[15,16] Because of its relatively robust structure, bR has been studied with demonstrable retention of photoactivity, outside of its native membrane environment in thin solid films. So bR is an attractive model for hybrid bioelectronic devices.[17] across diverse applications including optical memories, photovoltaic cells, artificial cells, and artificial retina prostheses.[14,18–20]

However, like most biological machines, bR is a membrane protein. It is a 7-pass integral protein, meaning that, in nature, it is integrated into the cell membrane of the organism through 7 topogenic α-helices that also encase the photoactive retinal trigger. For such integral proteins, the membrane environment is intrinsic to their conformation and function. And for bR, as the retinal is encapsulated within the membrane bound helices in its native environment its coupling to these helices and the conformational changes that retinal instigates occur within the membrane and so the dynamics are likely evolutionarily optimized for operation in this native environment And, while bR is remarkably robust compared to other membrane proteins, to the extent that many hybrid applications have not required the protein to be embedded in its native environment, there are significant advantages to bR integration into functional hybrid devices that encompass the lipidic environment and intra and extracellular analogues. Not least, using a membrane enables use of wild-type and thus inexpensive bR directly without need for genetic modification.[14] But, furthermore, given the complexity of the photocycle, ensuring conformational integrity of the protein should ensure closest biomimicry so that the evolutionarily iterated dynamics of the photoswitch apply. Indeed, distinct changes to the dynamics of the photocycle are observed depending on the protein microenvironment.[21] In addition, stable, interfacial hybrid devices that incorporate integral proteins in true, fluidic lipid membranes, while rare, offer opportunities to diversify from robust proteins such as bR to other less studied membrane proteins, broadening potential access to a wide range of molecular machines.[22,23]

Ideally, a lipid/protein based artificial model must exhibit controllable lipid composition, good addressability, by interfacial (electrochemical) and spectroscopic methods, and crucially, maintain

lipid membrane lateral fluidity, avoiding frictional interactions with the underlying substrate and also potentially protein denaturing surface interactions.[24–26] This combination of properties is not trivial to accomplish. Solid supported lipid membranes and associated cushioned/tethered variants are robust and stable lipid models with excellent addressability and are therefore widely used as artificial membrane models. For bR where the solid support is conducting, the interface provides a means to study the photocurrent.[27–29] However, reconstituted membrane proteins rarely show mobility. Liposomes and more recently lipid nanodisks are excellent platforms for ensuring a native like environment for reconstituted protein but suffer issues with addressability. However, solid-supported lipid membranes have some fundamental drawbacks, for example, they typically exhibit reduced lipid lateral mobility and the membrane-substrate distance is usually not sufficiently large to avoid direct contact between transmembrane proteins.

To avoid substrate-membrane interactions, new and more biomimetic artificial lipid models based on pore-suspended lipid membranes have been proposed, which combine the versatility of substrate-supported lipid bilayers with the membrane fluidity observed with freestanding membranes. For instance, the photoelectrical response of bR has been studied in black lipid membranes[23], nanopore-supported lipid bilayers[11] and nanodiscs.[30–32] Such approaches offer membrane is not in contact with a solid interface. A potentially useful lipid-based device in this regard for molecular machines are microcavity supported lipid bilayers (MSLBs), which combine the membrane fluidity observed in free-liposomes with the versatility and addressability of supported lipid bilayers. The pore-suspended character of MSLBs in contrast to classical SLBs have bulk aqueous environment at both interfaces of the bilayer. that at the microcavity interface can as a reservoir, encapsulating the lipid bilayer in an environment suitable for transmembrane proteins. The deep aqueous reservoir of the well, ensure reconstituted membrane proteins attain full lateral mobility. And, although single pass proteins; including integrin and glycophorin, have been reconstituted into MSLBs,[33] multi-pass proteins have not to date. Thus also light addressable ion channel proteins such bR to artificial membranes spanned over microdimensioned cavity arrays and their electrical activity was not yet explored. Reconstitution of protein into such devices is of value because they combine the qualities of true, compositionally versatile lipid bilayer with fluidity, including that of the reconstituted protein and optical and electrochemical addressability.

Herein, we report a method a new format for lipid membrane reconstituted bR at an MSLB using a hybrid two-step method involving fusion of proteoliposomes containing bR to pre-deposited lipid monolayer spanned over aqueous filled microcavity arrays. This method could be reliably used to reconstitute different densities of bR to the MSLB permitting investigation of the biophysical properties of formed artificial membranes and the photoelectrical activity of bR as a function of concentration. The lipid bilayer formation, as well the reconstituted bR to MSLBs were evaluated using Fluorescence Lifetime Cross Correlation Spectroscopy (FLCCS) and Fluorescence Lifetime Correlation Spectroscopy (FLCS). The photoactivity of bR was confirmed through chronoamperometry and affirming that bR retains its functionality forming a micro-photoactive device with stable and notably high and reproducible photocurrent switching over wide range of flicker frequencies overall indicating that bR-MSLBs represent a novel artificial biomolecular device.

4.3. Experimental Section

4.3.1. Materials

1,2-dioleoyl-sn-glycero-3-phosphocholine (DOPC) was purchased with maximum degree of purity (> 99%) from Avanti Polar Lipids (Alabama, USA) and used without further purification. 1,2-dioleoyl-sn-glycero-3-phosphoethanolamine labelled ATTO655 (DOPE-ATTO655) and NHS-ester-ATTO532 were purchase from ATTO-TEC GmbH (Siegen, Germany). Bacteriorhodopsin (lyophilized purple membrane) was purchased from Bras del Port S.A. (Alicante, Spain). Bacteriorhodopsin structure and purity was manufacturer-guaranteed, as presented in Figures S1 and S2. Phosphate buffer saline (PBS) tablets and Triton X-100 were purchased from Sigma-Aldrich (Wicklow, Ireland). Bio-beads SM-2 were purchased from Bio-Rad laboratories (Hercules, CA, USA). Aqueous solutions were prepared using Milli-Q water (Millipore Corp., Bedford, USA). Polydimethylsiloxane silicon elastomer (PDMS) was purchased from Dow Corning GmbH (Wiesbaden, Germany) and mixed following supplier instructions. Silicon wafers coated with a 100 nm layer of gold on a 50 Å layer of titanium were purchased from Platypus Technologies (New Orleans, LA, USA). The monodisperse polystyrene latex sphere with a diameter of 1 μm and 4.61 μm was obtained from Bangs Laboratories Inc. (Fishers, IN, USA).

The commercial cyanide free gold plating solution (TG-25 RTU) was obtained from Technic Inc. (Cranston, RI, USA).

4.3.2. Preparation and fluorescent labelled bacteriorhodopsin

Bacteriorhodopsin from purple membrane was solubilized in PBS buffer (pH 7.4) in presence of Triton X-100 (5 mM) and kept under gentle shaking for 24h at room temperature in the dark. The solution was then centrifuged for 1h at 10000 rpm to ensure insoluble particles or impurities were removed. The supernatant was collected and stored at 4°C and used within 30 days. For FLCS studies, bR was labelled with ATTO-532 by NHS-ester coupling following the protocol provided by ATTO-TECH. Briefly; 1 ml of bR (1 mg/ml) in PBS buffer (pH 8.3) was reacted with NHS-ester-ATTO-532 (1 mg/ml, DMSO) at a molar ratio of protein to dye of 1:3. The protein/dye mixture was gently agitated for 1h in the dark at 20°C. Unreacted dye was dialyzed from the labelled protein solution with a size exclusion membrane (10 kDa) (Milipore, Ultracel 10) by centrifugation at 10000 RPM for 30 min. This process was repeated 5 times and the labelling efficiency of the final bR-ATTO532 was verified by UV-Vis (See Figure S1).

4.3.3. Reconstitution of bR into large unilamellar vesicles

Reconstitution of bacteriorhodopsin into liposomes was accomplished using a a protocol previously reported by Jean-Louis Rigaud *et al*.[34] Briefly; bR was inserted into detergent-destabilized pre-formed DOPC liposomes. Detergent was subsequently removed by adsorption on polystyrene beads (biobeads) (See Scheme S1). First, a DOPC lipid film (4 mg) was dried in an amber glass under a gentle nitrogen flow and further dried under vacuum for 1h. For fluorescence studies, DOPE-ATTO655 was add to the lipid film at concentration of 0.01 (mol %) before drying the lipids under nitrogen flow. The lipid film was suspended by vortexing the lipid film in 1 mL of PBS buffer (pH 7.4) to achieve a liposomal concentration of 4 mg/mL for about 60 seconds. The obtained liposomal solution was extruded 11 times through 100 nm polycarbonate membrane (Avanti polar lipids). The resulting LUVs were then destabilized with Triton-X100.[35] The optimal detergent concentration was determined using DLS and UV-Vis (See Figure S2) as 4.5 mM Triton X100 which was combined with the DOPC liposomes 10 min under gentle stirring. Then, the

appropriate quantities of bR were added to the stirred solution to achieve a desired lipid/protein (L/P) ratio and the mixture kept under gentle agitation for 1h. The detergent was removed from the proteoliposomes by the sequential addition of 4 aliquots of pre-washed polystyrene beads (80 mg/mL) every 1.5h each. The proteoliposomes containing labelled bR-ATTO532 were characterized by DLS and Fluorescence Lifetime Cross-Correlation Spectroscopy (FLCCS), UV-Vis spectroscopy and relevant data compared to the properties of the liposomes prior to bR reconstitution (See Schematic S1).

4.3.4. Fabrication of PDMS and Gold microcavity arrays

The lipid bilayers were suspended across buffer-filled microcavity arrays prepared using a highly closed packed arrays substrates. Briefly, gold microcavity arrays were prepared by gravity-assisted convective assembly of microsized polystyrene spheres (PS) microsphere lithography and selectively modified with a self-assembled monolayer (SAM) of 1 mM 6-Mercapto-1-hexanol as described elsewhere.[36–38] The gold-microcavity arrays were prepared by drop casting polystyrene (PS) microspheres with 1 μm of diameter followed by gold electroplating, as described in the schematic presented in Scheme 1a. To obtain a highly packed microcavity array, a highly closed packed monolayer of polystyrene (PS) microspheres were casted using gravity assisted method onto pre-cut rectangles of gold coated silicon wafers. Then, gold was electrodeposit to the interstitial surface between the PS microspheres by applying a reduction potential (-0.6V, Ag/AgCl) to the gold array in presence of a cyanide free gold solution. The electrodeposition was controlled by the evolution of the current at the gold array until the current reached a minimum value corresponding to the closer distance between the spheres, indicating that the electrodeposition of gold has reached the hemisphere of PS (Figure S6a). After the gold electrodeposition the arrays were electrochemically cleaned using cyclic voltammetry in sulfuric acid (10 mM) for 6 cycles (-0.2 to 1.8V) and rinsed with deionized water, ethanol and dried gently under nitrogen flow (Figure S6b). The top surface of the gold microcavity arrays was then selectively functionalized with a self-assembled monolayer of 6-mercaptohexanol (1 mM) for at least 24 h in ethanol (Figure S6c).

The PDMS microcavity arrays were prepared by drop casting 50 μL of ethanol containing 0.1% of 4.61 μm polystyrene spheres (Bangs Laboratories) onto a 1 cm x 1 cm hand cleaved mica sheet.

After ethanol evaporation, PDMS was poured onto the PS spheres array and cured at 90 °C for 1h. The microcavities array is then formed after removing the inserted PS spheres by sonicating the PDMS substrate in tetrahydrofuran (THF) for 15 min. The substrates were then left to dry overnight. Prior to lipid bilayer formation, the substrates were plasma cleaned using oxygen plasma for 5 min and microcavities were buffer filled before to lipid monolayer deposition by sonicating PDMS substrate in PBS buffer (pH 7.4) for 1h. As previously reported, this step is important to increase the hydrophilicity of the substrate.[33]

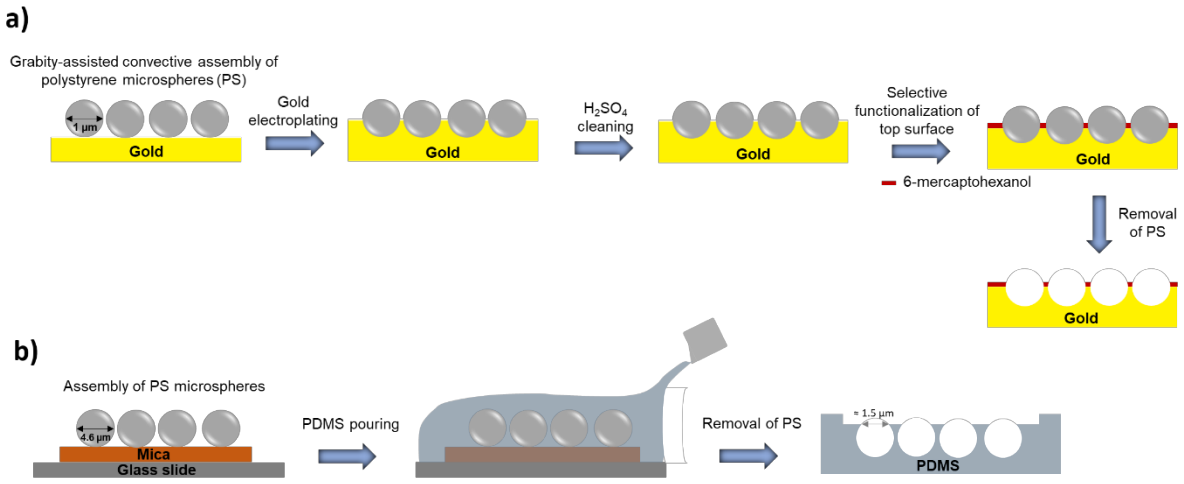

Figure 39. Schematic representation of step-by-step fabrication of Gold and PDMS microcavity arrays. a) To obtain a hemisphere microcavity array gold was electroplated until the equator of PS, gold microcavity arrays were prepared using Gravity-assisted convective assembly of polystyrene microspheres followed by gold electroplating. The substrates were functionalized with self-assemble monolayer (SAM) of 6-mercaptohexanol. b) The microcavity arrays used in FLCS were prepared by pouring PDMS to pre-deposit PS spheres following by PS removal.

4.3.5. Characterization of Au/PDMS µcavity arrays

Shape and size of formed microcavities arrays was characterize by Scanning Electron Microscopy (SEM) and Field Emission Scanning Electron Microscope (FESEM). SEM images of PDMS arrays were collected using a Hitachi S3400n, Tungsten system using 5.00 kV accelerating voltage. FESEM images of gold arrays (top view, tilted and profile) were obtained using a Hitachi S5500. All images were acquired using secondary electron mode.

4.3.6. Preparation of Microcavities Supported Lipid Bilayers containing bacteriorhodopsin

Microcavity supported lipid bilayers containing bacteriorhodopsin (bR-MSLBs) were spanned across buffer filled micro-cavity arrays following a combination of Langmuir-Blodgett (LB) and vesicle fusion as described previously.[36] Briefly and approximately 50 µL of 1,2-Dioleoyl-sn-glycero-3-phosphocholine (DOPC) (1 mg/mL in chloroform) were deposited onto the air-water interface of LB trough (NIMA 102D) and allowed to evaporate for 15 min and the resulting lipid monolayer at the air water interface was compressed four times to a surface pressure of 36 mN/m at 15 mm/min (See Figure S2). Then, micro-cavity arrays were immersed into the LB trough until all of the cavities were submerged completely into the subphase. The micro-cavity array was withdrawn from the trough at a rate of 5 mm/s whilst the surface pressure of the lipids was retained at 32 mN/m to ensure an adequate transfer of DOPC monolayer (See Figure S2). To assemble the upper leaflet of the bilayer and incorporate bacteriorhodopsin, the lipid monolayer was exposed to preformed DOPC/bR proteoliposomes (0.25 mg/ml) and allow to incubate for 3 hours in the dark. The integrity of lipid bilayers was acceded by Fluorescence Lifetime Correlation Spectroscopy (FLCS) and the photo-electrical response of bR-MSLBs was studied by chronoamperometry.

4.3.7. Fluorescence Lifetime Cross-Correlation Spectroscopy (FLCCS) and Fluorescence Lifetime Correlation Spectroscopy (FLCS) measurements

Single point FLCCS was performed in preformed proteoliposomes containing labelled bR-ATTO532 and DOPE-ATTO655 to assess the incorporation of bR to liposomes and the formation of proteoliposomes. FLCS was performed to evaluate the lipid bilayer formation over micropores after proteoliposomes fusion by accesing the diffusivity of DOPE-ATTO655 and to evaluate the bR integrity in MSLBs by monitoring the diffusivity of bR-ATTO532. Fluorescence measurements were performed on a MicroTime 200 lifetime (PicoQuant GmbH, Berlin, Germany) using a water immersion objective (NA 1.2 UPlanSApo 60 x 1.2 CC1.48, Olympus). The detection unit comprises of two single photon avalanche diode (SPAD) from PicoQuant. Labeled lipid membrane marker DOPE-ATTO655 was excited with 640 nm LDH-P-C-640B (PicoQuant) and bR-ATTO532 was excited with 532 nm PicoTA laser from Toptica (PicoQuant). To exclude scattered or reflected laser light, emitted fluorescence was collected through a HG670lp AHF/Chroma or HQ550lp AHF/Chroma band pass filter for 640 or 532 nm laser respectively. To

exclude scattered or reflected laser light, emitted fluorescence was collected through an HG670lp AHF/Chroma or HQ550lp AHF/Chroma band pass filter for 640 or 532 nm lasers, respectively. A 50 μm pinhole was used to eliminate photons from outside the confocal volume. Before FCLS measurement, backscattered images of the substrate were taken using an OD3 density filter to ensure the optimal positioning of the focus to the center of the microcavity. Then, the bilayer position was determined by z-scanning until the point of maximal fluorescence intensity of DOPE-ATTO655 was found. At this point, the fluctuating fluorescence intensity of labelled lipid marker or bR-ATTO532 were measured for 30 to 60 seconds per cavity, and replicate data from 20 to 30 cavities were measured per sample. To assess simultaneously the diffusion time (ms) and the fluorescence lifetime (ns) the emitted photons were analyzed by a time-correlated single photon counting system (TCSPC) (PicoHarp 300 from Picoquant). The fluorescence fluctuations obtained are then correlated with a normalized autocorrelation function (Equation 1):

$$G(\tau) = \frac{\langle \delta F(t).\, \delta F(t+\tau) \rangle}{\langle F(t) \rangle^2} \qquad \text{(Eq.1)}$$

The auto-correlation curves obtained from the fluorescence fluctuations of DOPE-ATTO655 and bR-ATTO532 were fitted to a 2-D model (Equation 2) using the software SymphoTime (SPT64) version 2.4 (PicoQuant).

$$G(\tau) = \frac{1}{N}\left[1 + \left(\frac{\tau}{\tau_D}\right)^{\alpha}\right]^{-1} \qquad \text{(Eq.2)}$$

Here, ρ represents the amplitude at G(τ) and is defined as the inverse of number of molecules (1/N) and α is the anomalous parameter; τD is the diffusion time of the fluorescent marked molecules in the lipid membrane. The diffusion coefficient is related to the correlation time τD by the relation $D = \omega^2/4\tau D$, where ω is the 1/e2 radius of the confocal volume i.e. the waist of the exciting laser beam. ω was measured for each excitation using a reference solution of free dye for which the diffusion coefficient is known. The ω was determined by calibration using reference dyes; ATTO-655 (Atto TEC, GmbH) for 640nm laser and Rhodamine 6G for 532 nm laser at 20°C in water.

.

4.3.8. Photocurrent generated by BR-MSLBs

To measure the photoelectrical activity of bR-MSLBs, lipid bilayers spanned over gold-microcavities arrays were investigated using chronoamperometry performed on a CHI 760B bipotentiostat (CH Instruments Inc., Austin, TX). The measurements were performed in 0.1 M KCl as supporting electrolyte solution using a three-electrode system consisting of a Ag/AgCl (1 M KCl) reference electrode, platinum coiled wire as a counter electrode and the gold-MSLB as the working electrode at 0V potential. The photocurrent of the self-sustaining switch was generated by photo-activating bR-MSLBs with a 2 mW LED (λ=555 nm) (Thor Labs, England) kept inside the Faraday cage and the LED was operated using a microcontroller "Arduino Uno" (Arduino, Italy). The source of light was kept 1 cm away from the substrate. Experimental setup is shown in Figure 2. The experiments were conducted in triplicates.

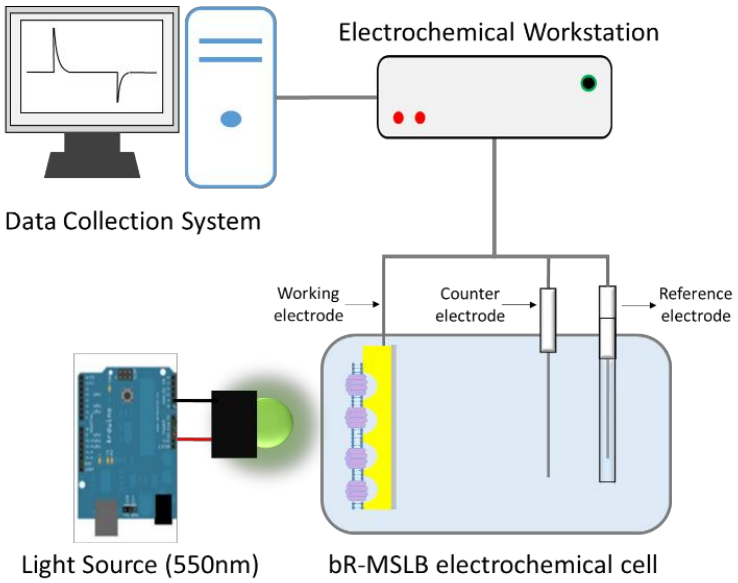

Figure 40. Schematic representation of the experimental setup of used for photocurrent measurements of Microcavity Supported Lipid Bilayers containing Bacteriorhodopsin (bR-MSLBs). The electrochemical apparatus consisted of a Ag/AgCl reference electrode (R.E), a platinum wire as counter electrode (C.E). The working electrode (W.E) is comprised of the MSLB-bR.

4.4. Results and Discussion

4.4.1. Preparation and Characterization of fluid Microcavity Supported Lipid Bilayers containing bacteriorhodopsin (bR-MSLBs)

The microcavity supported lipid bilayers were prepared and characterized as reported in detail previously.[33,36,39–41] Previous data confirm that surface modified pore arrays in gold and PDMS, that are pre- aqueous filled with buffer support stable, hydrated lipid bilayers, where the bilayers are fluidic and span the cavity apertures. And, that both lipid and any reconstituted protein exhibit liposome-analogous diffusion coefficients.[33,36,39–41] It was also confirmed previously that the method of bilayer preparation results in a single bilayer[42] and that the bilayer has sustained integrity, denying access to non-permeable species into the cavity.[43] Here, the LB monolayer and liposome fusion method reported previously was used to create the MSLBs, but in this instance the liposomes contained reconstituted bacteriorhodopsin.[33,36] The bR proteoliposomes used for fusion were characterized by DLS (See SI) and the protein reconstitution into liposome was confirmed in solution (PBS, pH 7.4) before the liposomes were then used for bilayer formation, using Fluorescence Lifetime Cross-Correlation Spectroscopy (FLCCS).

To confirm the bR was reconstituted into the liposomes, the proteoliposomes were labelled with a lipid marker and the signal from this was cross-correlated the FCS signal from the bR label, to ensure that they co-diffuse, i.e. to confirm that they are both reconstituted into the same liposome. Using FLCCS, the diffusivity of the green labelled bR and red labelled DOPE though the confocal volume was evaluated simultaneously. The relative cross-correlation amplitude indicates that bR is reconstituted into the DOPC liposomes along with the DOPE label, and we can conclude that the proteoliposomes are properly formed.[44] The Figure 3 shows the FLCCS of proteoliposomes tagged with DOPE-ATTO655 and bR-ATTO532 (Figure 3, schematic). The amplitude of the cross-correlation signal G(τ) (Figure 3, black line) is characteristic of concomitant movement of protein and tagged liposomes and indicates that both labelled DOPE and bR are diffusing together within the laser confocal spot consistent with protein reconstitution into proteoliposomes.[44,45] After proteoliposome fusion to the DOPC monolayer to form lipid bilayer, signal cross-correlation

G(τ) is lost, as expected, indicating lipid and protein mixing into the MSLB and rupture of the proteoliposome.

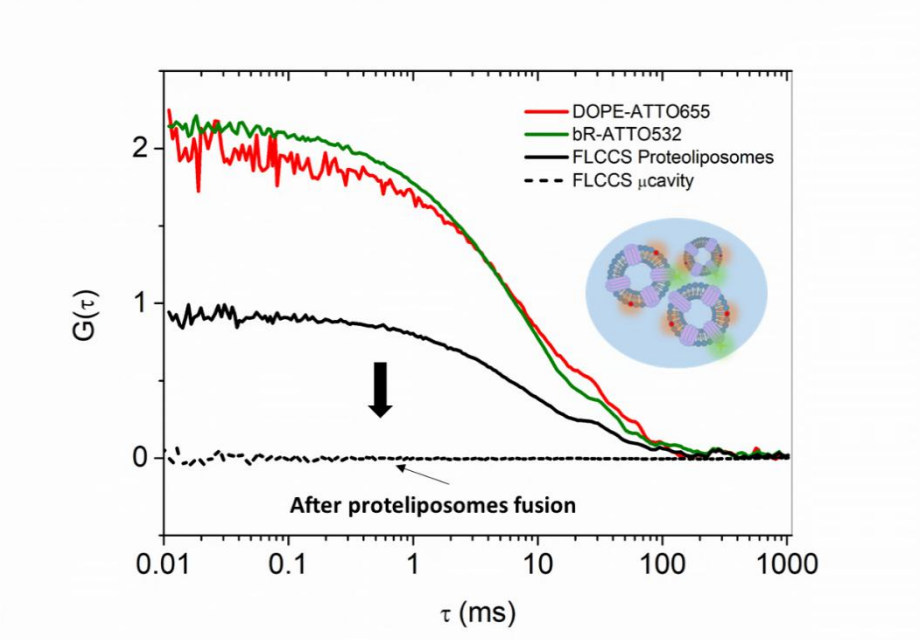

Figure 3. Auto-Correlation Functions (ACFs) from bR reconstituted DOPC proteoliposomes monitoring the DOPE-ATTO655 (0.01 mol %)(red) and bR-ATTO532 (0.01 mol %) labels (green) before disruption at the microcavity lipid monolayer interface. The Black lines show the cross-correlation curves before (solid line) and after (dashed line) proteoliposome fusion to DOPC monolayer i.e. following lipid bilayer formation. The insertion represents the proteoliposomes after bR reconstitution containing labelled DOPE-ATTO655 (red spots) and bR-ATTO532 (green spots). The insert shows the proteoliposomes containing labelled bR-ATTO532 (green tagged purple protein) and DOPE-ATTO655 (red tagged lipid)..demonstrating how cross correlation signal is only observed if the bR is reconstituted into the liposomes.

Membrane proteins provide outstanding opportunities for purposing sophisticated molecular switches. However, their membrane environment is key to their function. In this context, the fluidity of microcavity supported lipid bilayers is a key advantage of MSLBs over solid supported lipid membranes. Therefore, to investigate the photo-activity of bR in the MSLBs, the lipid bilayers were spanned across microcavity arrays using a hybrid method combining Langmuir-Blodgett (LB) lipid monolayer deposition with proteoliposome fusion reported previously.[33] Proteoliposomes comprised of DOPC and reconstituted with different concentrations of bR were disrupted at the aqueous filled microcavity arrays modified with an LB transferred DOPC

monolayer (Figure 4a). The formation of the microcavity supported lipid bilayer was evaluated by Fluorescence Lifetime Imaging (FLIM) and by monitoring the lateral diffusion of labelled DOPE-ATTO655 using Fluorescence Lifetime Correlation Spectroscopy (FLCS). Imaging and diffusion values conformed to previous reports for MSLBs with FLIM images of DOPE-ATTO655 obtained for DOPC/bR reconstituted lipid membranes confirming a continuous lipid bilayer spans the PDMS microcavity array and that the bilayer was faithfully formed with controlled concentrations of bR reconstituted. The rim of the microcavity is marked in the figure by the red circle (Figure 4b I-IV) and the fluorescence from the labelled protein evident above the microcavity pores indicating that the bR is reconstituted into the membrane spanned over the micropores.

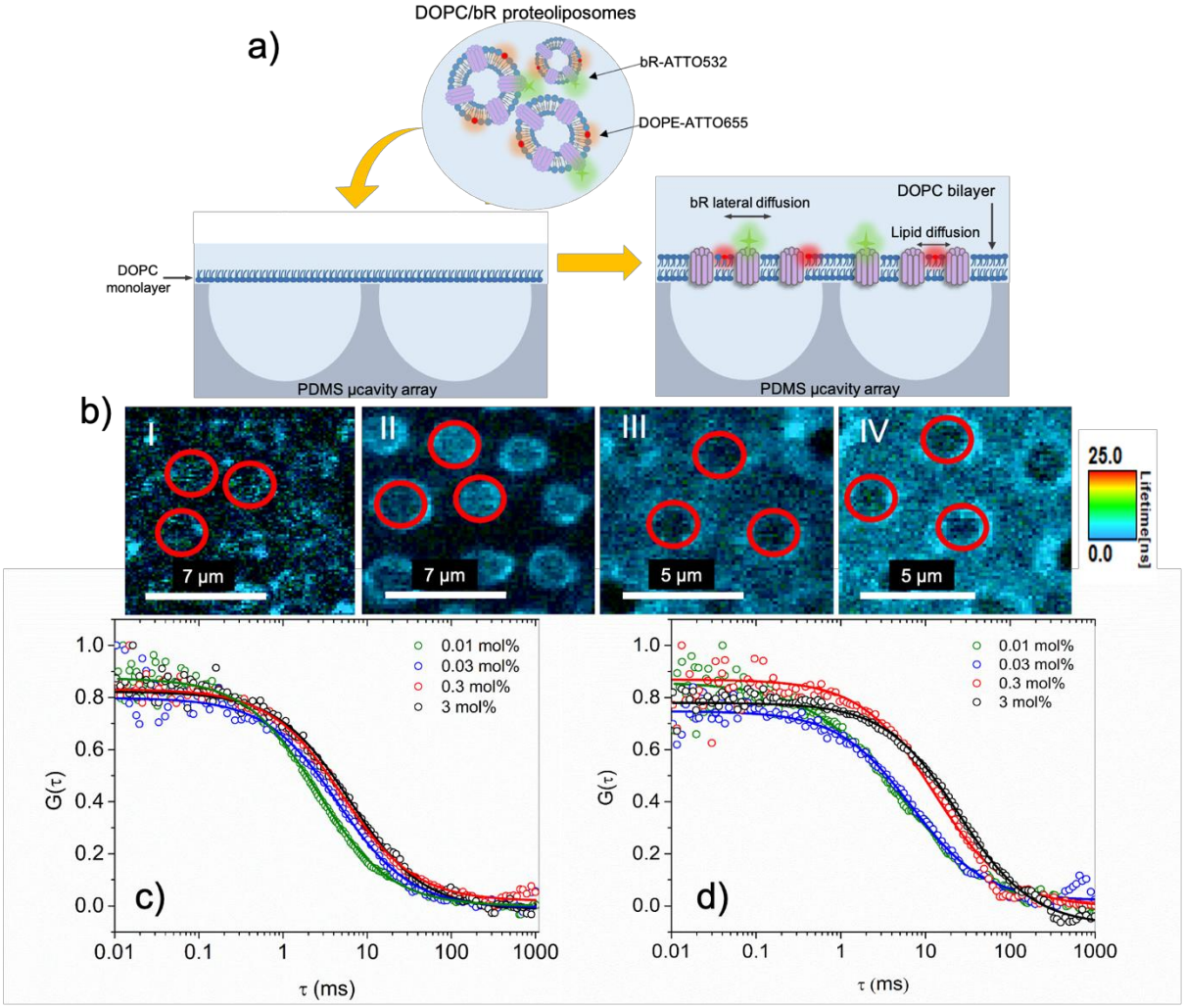

Figure 4. a) Schematic representation of preparation of MSLBs containing bR spanned over aqueous buffer filled PDMS microcavity arrays using LB/Proteoliposome fusion. (b) (I – IV) Fluorescence Lifetime

Imaging (FLIM) of DOPE-ATTO655 obtained for bR-MSLBs obtained after proteoliposome fusion containing different concentrations of bR, for 0.01mol%, 0.03mo%, 0.3mol% and 3mol%, respectively. The red circles indicate the rim of microcavities from within which the FLCS signals were collected, (c) and (d) Fluorescence Lifetime Correlation Spectroscopy (FLCS) obtained using labelled DOPE-ATTO655 and bR-ATTO532.

Using FLCS, a highly sensitive single molecule technique, the lateral diffusion coefficient of DOPE-ATTO655 obtained at DOPC/bR bilayers show that the reconstitution of bR into the DOPC membrane affects the diffusivity of DOPE. This effect scales with the protein concentration, where DOPE lateral diffusion decreases as protein content increases in the bilayer (Table 1). The lateral diffusion coefficient obtained for a DOPC lipid bilayer without bR (bare DOPC) was measured as approximately 10 $\mu m^2 s^{-1}$. This value is consistent with previously reported our group for DOPC MSLBs as well as for other reported free-standing DOPC bilayers and liposomes.[33,36,46] The lateral diffusion of labelled DOPE was approximately 9.8 ± 0.5 $\mu m^2.s^{-1}$, 8.4 ± 0.6 $\mu m^2.s^{-1}$, 6.5 ± 0.4 $\mu m^2.s^{-1}$, 5.5 ± 0.6 $\mu m^2.s^{-1}$, for lipid bilayers containing 0.001 mol%, 0.03 mol%, 0.3 mol% and 3 mol% of bR respectively. These values confirm lipid bilayer formation and indicate the insertion of the protein to the lipid membranes. The progressive decrease in lipid diffusion with increasing bR content is consistent with behavior noted for bR at liposome models and attributed to the impact of increasing protein/lipid ratio on membrane viscosity.[47] For the MSLB reconstituted bR-ATTO532 (Figure 4c), a diffusion coefficient of 4.2 ± 0.3 $\mu m^2.s^{-1}$ was measured for the lowest bR concentration (0.01 mol%) explored. The reduced diffusion coefficient of bR compared to lipid is consistent with large radius of this protein which as described is a 7-pass transmembrane protein spanning both lipid leaflets of the membrane. Translational diffusion of proteins in biological membranes has been described by the Saffman-Delbrűck (SD)relation, a hydrodynamic model that treats the bilayer as a 2 dimensional, viscous continuum interfaced with an infinite volume of fluid through which a solid cylindrical shape (representing the protein) diffuses (Equation 3).[48,49] The model suffers a number of limitations both when dimensions and density of protein exceed certain limits and in models that show reduced fluidity like SLBs, but was used here as our platform offers close to a continuous planar membrane decoupled from the surface.[50] Using the SD model we estimated the hydrodynamic radius of bR within the DOPC MLSB of 4 nm for 0.01mol% and 4.7 nm to 0.03mol%[49] and our measured diffusion coefficient agrees well with those determined in freestanding membranes of pore-spanning membranes, GUVs and BLMs.[51–53]

$$D = \frac{KT}{4\pi\mu h}\ (ln\left(\frac{\mu h}{\mu' r}\right) - \gamma)$$ (Eq. 3)

The diffusion coefficient of bR was observed to decrease with increasing bR concentration in the membrane (Figure 4d). This correlated with reduced labelled DOPE diffusion with increasing protein concentration described above (Table 1). It is notable that the anomalous co-efficient, α remained approximately 1 across all protein concentration, indicating, that the effect is from viscosity changes rather than for example, protein aggregation. In conclusion, our results clearly demonstrate that bR reconstitutes properly into the MSLB and that the membrane components of MSLBs show high lateral mobility in the freestanding microspore array, an important requisite to guarantee protein mobility and function.

Table 3. Diffusion co-efficient of labelled bR-ATTO532 (D_{bR}) and DOPE-ATTO655 (D_{DOPE}) introduced in the lipid bilayer comprised of DOPC using LB lipid transfer followed by proteoliposome fusion. The concentration of bR was varied during proteoliposomes preparation. The α co-efficient was determined as approximately 1.0 for all measurements.

bR concentration (mol %)	D_{bR} ($\mu m^2/s$)	D_{DOPE} ($\mu m^2/s$)
0.01	4.2 ± 0.3	9.8 ± 0.5
0.03	3.4 ± 0.6	8.4 ± 0.6
0.3	1.2 ± 0.4	6.5 ± 0.4
3	1.0 ± 0.5	5.5 ± 0.6

4.4.2. Photo-activation of bR incorporated to DOPC lipid bilayers and time resolution of light-induced current

To determine that protein functionality is intact and to characterize light induced proton flow, bR reconstituted bilayers spanned over gold microcavity arrays were evaluated under dynamic light activation by chronoamperometry. For chronoamperometric measurements, the 3-electrode

system, illustrated in Figure 2, was placed in a closed Faraday cage and the electrochemical cell was allowed to equilibrate for 300 s in the dark before photoactivation of bR. Then, the current in the electrochemical cell was measured for 60 s to obtain a dark current of approximately 0.1 nA/cm^2 prior to irradiating the sample with an LED light (2mW, λ_{em} 555nm) for approximately 10 s. The dark current was subtracted from the generated photocurrent measured for the bR-MSLBs. The photocurrent was related to the area of substrate covered by the lipid bilayer, which was approximately 1 cm^2. Therefore, the current per cm^2 was calculated similarly to previously reported by porous substates.[23] Figure 5b shows a characteristic photocurrent response from the bR-MSLBs. On light switch on, an anodic photocurrent evolves to a peak current maximum of approximately 240 nA/cm^2 that then decays to a steady state current of 0.1 nA/cm^2. Under illumination, bR retinal isomerizes with a high quantum yield, from the all-trans confomer to the 13-cis isomer initiating the proton transport process, the entire cycle takes roughly 15 ms, leading to proton transfer from the distal to proximal side of the bilayer. Given the cycle time, bR is expected to undergo multiple cycles of photoexcitation during an illumination which lasts approximately 10 s. Therefore, the regeneration of bR reaches saturation where proton release and uptake reaches an equilibrium. When the light is switched OFF, the concentration of excited state rapidly diminishes as proton reuptake takes place.[29]

Under continuous illumination, the decay of the peak current can be attributed to accumulation of the M intermediate and saturation of proton transport. In switching off the light a cathodic current evolves with a maximum of density of -125 nA/cm^2 which also decays to baseline. The decay data were analyzed by fitting each peak current (ON/OFF) to a biexponential function $\boldsymbol{I(t) = I_0 + I_{fast}e^{-\left(t/\tau_{fast}\right)} + I_{slow}e^{-(t/\tau_{slow})}}$ (Eq. 4), where I_0 represents the base line of the photocurrent at steady state, I_{fast}/I_{slow} indicate the amplitude of the intermediate decay, t the duration of the decay and τ the decay constant of current signal The data for the kinetic decay of the photocurrent peaks obtained after fitting to Eq. 4 are displayed in Table S2 and the fitted decays are shown in Figure S6. For the photoactivation process, the fast component of the decay is below the limit of the resolution of the measurement but both components of the decay, within experimental error showed, no dependence on protein concentration and the photocurrent amplitude of I_{fast} corresponds to approximately 85% to 90% of the photocurrent signal. This independence is anticipated, as the decay time is expected to depend on the incident light intensity and is a

convolution of kinetic response from the proton pump and the electrical circuit so is specific to the system.

To confirm that the current signal is coming from the bR proton pump, control experiments were carried out under analogous conditions to confirm that, by comparison, negligible photovoltaic current is observed on irradiation of the bilayer/electrode in absence of the protein (Figure S6b). Contributions from conductive artifacts were excluded by evaluation of the electrochemical photo-activation apparatus, such as changing the position of the light source while monitoring the current, we did not observe any other contributions to the photoelectrical signal. The photoelectric signal observed after photo activation of bR-MSLBs is attributed to proton displacement from the bulk solution across the lipid bilayer toward the interior of the microcavities (Figure 5a), and is similar the bR photocurrent previously reported in supported structures.[23,54,55] The stationary light-induced electric current observed (Figure 5b) is likely capacitive current from the underlying gold array and indicates non-random orientation of bR at the membrane.[56] Crucially, the observation of the characteristic transient photocurrent confirms that bR retains its functionality when integrated into the MSBLs and the observation of two transient peaks suggests in each case vectorial proton transport is occurring. The observed photocurrent and low leakage current, (0.1 nA cm^{-1}) also indicates that the MSLB membrane is intact and proton impermeable.[11,23] This is confirmed further below, in experiments where pH of the contacting solution at the distal leaflet is changed.

It is notable, in the dynamic photocurrent response, Figure 5c that the difference in peak magnitude of the light on versus light off currents is approximately 1.8. Notably, the photocurrents, normalized to electrode area, observed are comparable or indeed significantly higher than related reported systems, particularly given the light intensity in our experiments is low, compared to other reports. For instance, at optimal conditions and using high power systems (250 Watts), Horn *et al* obtained a photocurrent of 250 nA/cm^2, Guo *et al* obtained 350 nA/cm^2 and Lu et al obtained and 120 nA/cm^2.[23,57,58] This we tentatively attributed to the fact that in the present system the bR is reconstituted into a single bilayer rather than a layer by layer assembly so bR light activation directly pumps the proton across the membrane between bulk and cavity solution, with no intervening structures such as additional bilayer or multilayer impeding the proton transport.

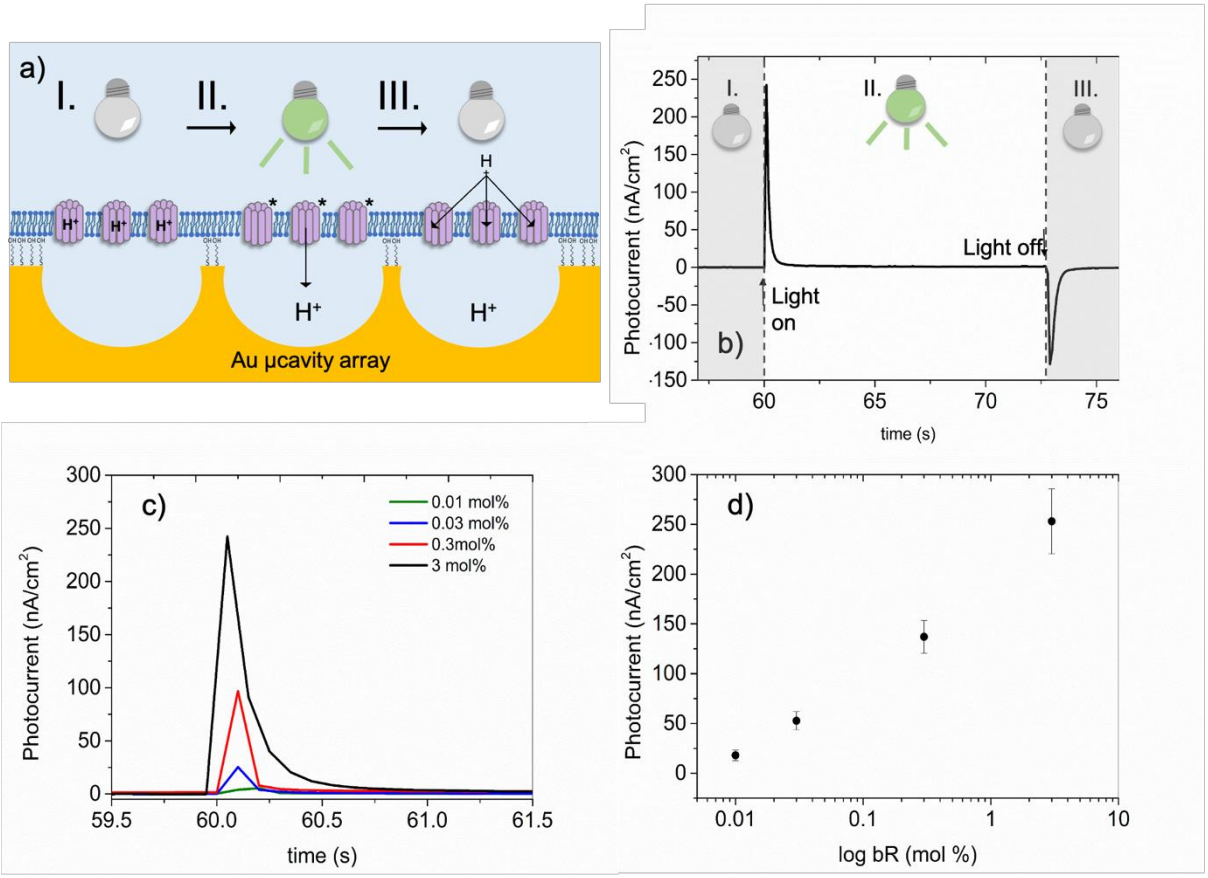

Figure 5. Representative photocurrents recorded from bR-MSLBs. (a) Schematic representation of photo-cycle mechanism of bR at MSLBs: I. represents the ground state of bR without presence of light, II. indicates the photo-switch of bR in presence of light, represented by its excited state and the subsequent proton release, and III. the return of bR to the ground state when light is switched off. (b) typical photocurrent decay of bR-MSLBs comprised of DOPC/bR (3 mol%) (KCl 0.1M, pH 5.6) (I.) before photo-activation, (II.) photoelectrical response of proton release and (III.) proton uptake. (c) photo-electrical response of proton release generated with different bR concentrations (KCl 0.1M, pH 5.6). (d) shows the photocurrent of bR-MSLBs indicating a logarithm dependence of i versus bR concentration,

The magnitude of the photocurrent is influenced by the concentration of bR in the proteoliposomes used to prepare the MSLB. As shown by the overlay of the photocurrent response from four MSLBs prepared from liposomes with different protein concentration (Table 2, Figure 5c), a logarithmic correlation is observed with concentration of protein (log [bR]), Figure 5d. The quantitative relationship between current and bR concentration in the fusion proteoliposomes result speaks to the robustness of the reconstitution method, indicating complete transfer of reconstituted protein to the bilayer and retention of is electro/photoactivity within the bilayer. As

noted, for DOPC only (bare MSLB) the photovoltaic response contributes less than 2% contribution to the photocurrent generated by bR (Figure S6b).

Table 2. Photocurrent activity of bacteriorhodopsin incorporated at gold-MSLBs activated with 2mW LED (555nm) in KCl (0.1M, pH 5.5).

bR concentration (mol %)	$i_{release}$ (nA/cm^2)	i_{uptake} (nA/cm^2)
0.01	18.6 ± 5.4	- 10.1 ± 3.7
0.03	52.7 ± 9.2	- 32.1 ± 1.6
0.3	137.4 ± 16.4	- 86.9 ± 6.5
3	253.5 ± 32.3	- 129.5 ± 16.8

4.4.3. Photoelectronic response of bR-MSLBs to asymmetric pH

The bacteriorhodopsin proton pump cycles cycle is initiated by photoisomerization of all-*trans* to 13-*cis* retinol caged at the center of the bR within the membrane.[59,60] This photoinduced conformational change initiates a photocycle that through a series of spectroscopically distinguishable intermediates, that lead to proton release at the extracellular side of the membrane between the L and M steps of the cycle that is then followed by the re-protonation of the Schiffs base that is preceded by a step whereby water is inserted temporarily into the proton channel and protonates through a proton chain mechanism.[61–63] This process requires significant conformation/structural changes to the channel helices. The pH of the contacting solution can not only alter the proton concentration in the bulk solution but also influences the proton release of bR. For instance, several studies have shown that the rate of deprotonation of bR decreases with decreasing pH.[64–66]

To investigate the proton switching of bacteriorhodopsin at MSLBs as a function of pH the photoelectrical response of bR was analyzed whereby, the pH of contacting electrolyte solution in the electrochemical cell was modified by addition of HCl (1 mM) or NaOH (1 mM) over the range of 3.5 – 9.5 (Figure 6a). Note that in these experiments, the solution in the microcavity, at the proximal membrane interface is pH 7.4 and it is only the pH of the contacting solution at the distal leaflet that is changed. Following pH adjustment, the samples were allowed to equilibrate at each new pH for 300 s in the dark before exposure to light before the photo-activity of bR was recorded

as before. We and others have reported previously that a pH gradient can be sustained at artificial bilayers[37] for windows of about an hour and here, the samples here were analyzed within 300 s to ensure the gradient is sustained within the experimental window.[67] As expected, the photo-activity of bR in DOPC MSLBs is strongly influenced by the pH of the contacting solution. The lowest photocurrent was observed at basic pH (> 8.5) and maximum photocurrent was recorded at pH 5.5 which actually decreased at more acidic pHs (< 5.5) as shown in Figure 6b. This pattern is similar to previous reports for supported lipid bilayers systems.[29,68,69] However, the maximal photocurrent here is observed at an order of magnitude more acidic environment than pH (pH ≈5.5) previously reported (pH≈6.5).[29] We can relate this effect to the pH gradient that is maintained using the MSLBs and .[58] it also confirms, consistent with the low dark current described, the excellent insulating properties of MSLBs indicating their suitability for such artificial proton pump devices.[70]

To understand if pH alters the kinetics of the electrodic response for the photoactivated and dark initiated states the current decays post light and dark steps were fit to exponential decay curves represented by equation 4 (Figure S7). The results are shown in Table S3. The data fit best to biexponential decays for the photoactivated process and as before, the fast decay, is at the limit of resolution of our measurement so showed no pH dependence. However, the slow step, although only contributing 2% of current amplitude, did show a pH dependence, consistent with photoelectric behavior of bR expressed on cells.[71]

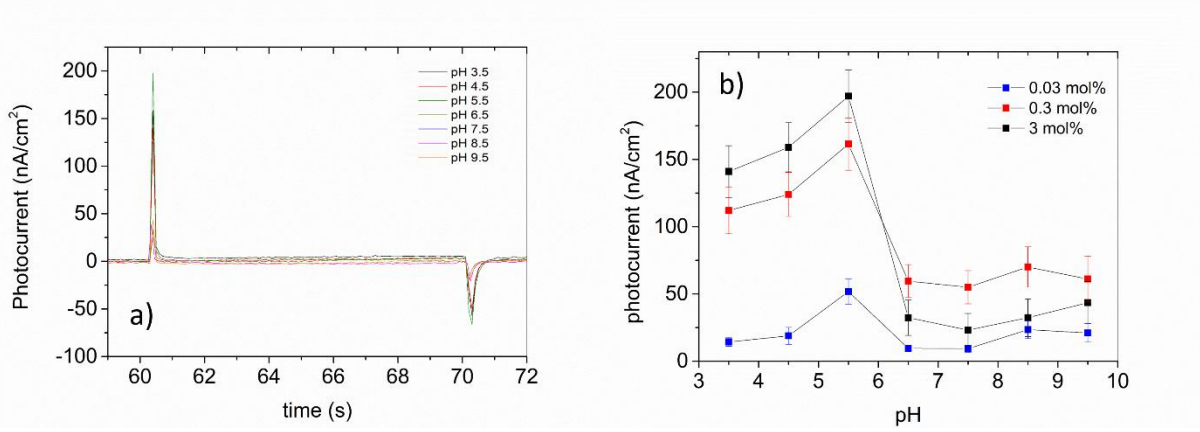

Figure 6. Photocurrent obtained after activation of bacteriorhodopsin at different bulk pHs. (a) Illustrates the photocurrent obtained for bR-MSLBs comprised of DOPC and doped with bR (3 mol%). (b) show the

photo-activity of bR-MSLBs at different bR concentrations. The solid lines are guides for the eye. These measurements were taken at 20 ± 2 °C.

4.4.4. Photo-current of bR-MSLBs response of transient light activation

Photo-switch devices that operate under flickering light conditions are important in the development of artificial biocomponents, such biotransistors, biocapacitorsors and biomimetic artificial retina.[18,58,72–74] The quasi-stationary photocurrent generated by bR-MSBLs under transient light activation illustrates an important characteristic of the molecular switch in MSLBs. Given the high photocurrent signals under relatively low light intensity we were interested to evaluate the photo-activity of bR-MSLBs under oscillating light activation, the devices were exposed to a flickering light (1 Hz – 20 Hz) and the photocurrent obtained as displayed in Figure 7.1 Here, a pulse of light represents the complete circle of light activation/deactivation (ON/OFF), for instance 1 Hz (1 pulse per sec) represents light ON for 0.5 s, followed by light OFF for 0.5 s, 2 Hz represents 0.25 s of light ON followed by 0.25 s of light OFF and so on for the other frequencies. The photo activity of bR incorporated to DOPC MSLB (0.3 mol%) increases with for frequency 2 Hz and 4 Hz, when compared to 1 Hz. This is possibly due to a synergic effect, as for 1 Hz the full photo-circle takes approximately 1 s (Figure 7.2a), it is possible to that for 2Hz bR excitation is enhanced, indicating that the concentration of excited bR is further increased, with similar period of the synodical photocurrent approximately 0.25ms (Figure 7.2b). As for 4 Hz, first cycle is not completed, forming a hybrid pattern combining a high amplitude of 200nA/cm2 with a low amplitude with approx. 82 nA/cm2 (Figure7.2c). The period of the synodical photocurrent was 0.12ms. At 8 Hz (Figure 7.2d) the wave period of photocurrent increased by a factor of 2 when compared to 1 Hz indicating that the lifetime of excited bR was increased, therefore the steady-state was prolonged. At long time scales, the photocurrent showed a synodical wave pattern with period of 3.3 s and A_{max} of 150 nA/cm^2 and A_{min} of 126 nA/cm^2 (Figure 7.1). At 16 Hz (Figure 7.2e), the photocurrent showed multiple amplitudes, with period of 2.1 s, A_{max} of 92 nA/cm^2 and A_{min} of 48 nA/cm2. At 18 Hz (Figure 7.2f) the period of the synoidal photocurrent was 2.5 s with A_{max} of 95 nA/cm^2 and A_{min} of 89 nA/cm^2. At 20 Hz (Figure 7.2g), the photocurrent showed two distinct phases, an initial peak of approx. 90 nA/cm^2 followed by a decrease until a steady-state. In this case, the steady state was at 50 nA/cm^2. This indicates that the proton pump has reached

and equilibrium, similar to what was to observed in Figure 5b. However, the photocurrent does not decay to base line, indicating that the flux of protons may reach a steady-state of 50 nA/cm^2.

Photocurrent maximizes at 4 Hz and by 8 Hz photocurrent is observed to decreases as, kinetically, the photo-cycle of bR is not completed at the arrival of photons, similarly to previous reports.[68] However, it is important to note that the device reported by Lu *et al* is formed by a thick multilayered bR structure, whereas here, bR is reconstituted into a single biomimetic lipid bilayer. The photocurrent continues to decrease with increasing frequencies until 20 Hz. The current dependence across the range of light activation frequencies shows a pattern observed for a photo-biocapacitor as the current decreases with light alternation state (ON to OFF). Here, the bR-MSLBs system is demonstrated to convert flickering light impulses below 20 Hz into distinguishable patterns of photocurrent, and a stationary photocurrent was observed at 20 Hz indicating that bR is continuously active. By controlling the incident light flicker frequency in this way we have the opportunity to fast switch between amplitude and period could be used to create a pH gradient across MSLBs.[75] As previously discussed, this proton gradient observed for the bR containing bilayer is only present momentarily. In order to maintain the proton gradient across the bilayer, fast flicker rates can be instigated.

1

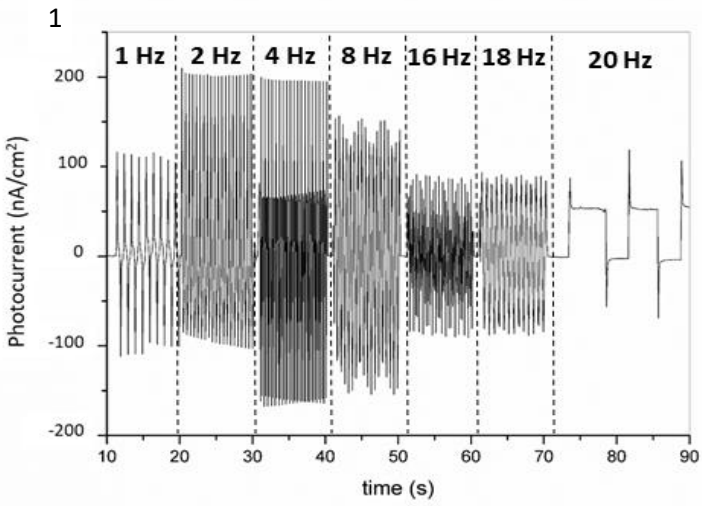

11

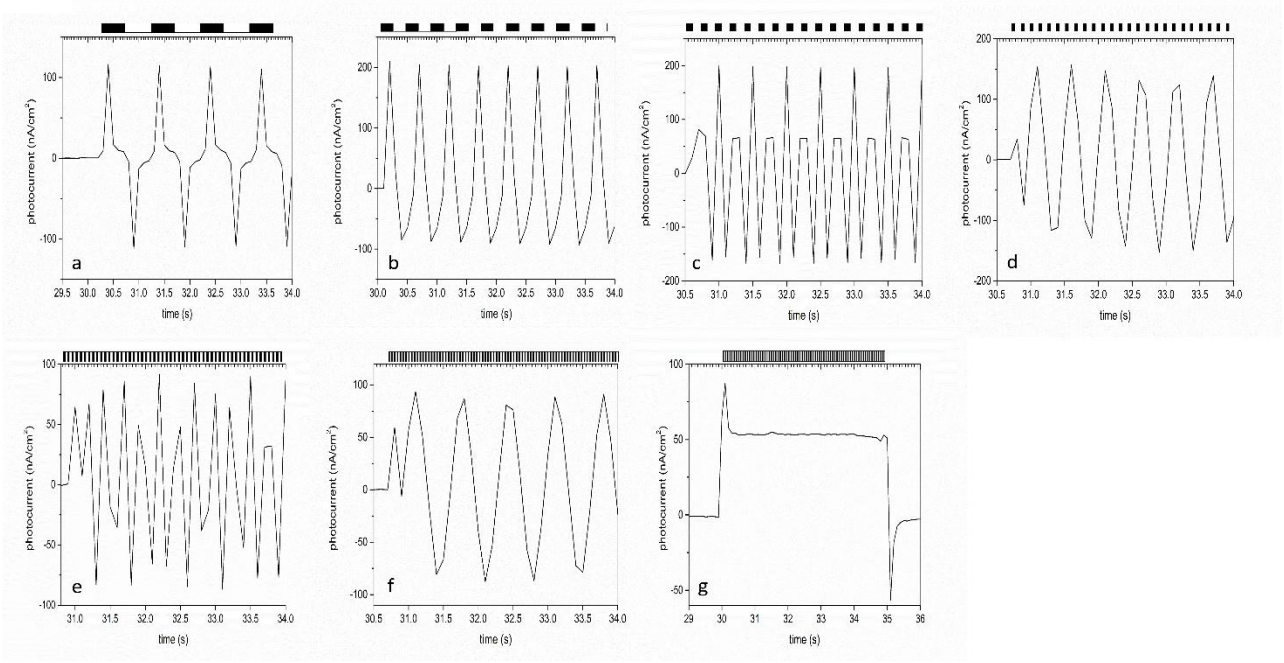

Figure 7. Photocurrent of bR-MSLB generated on application of a flickering light source. 1) The electrochemical current increases at 2 and 4 Hz but decreases for higher frequencies. At 20 Hz a stationary photocurrent was observed. 2) Individual i-t curves for photo-activation at different frequencies (a) 1 Hz, (b) 2 Hz, (c) 4 Hz , (d) 8 Hz , (e) 16 Hz , (f) 18 Hz and (g) 20 Hz. The bar over the graphs represent the state of activation light (on, black; off, white).

4.5. Conclusions

A new approach to a switchable photoelectric device is described based photo activated light driven proton transfer across bacteriorhodopsin reconstituted into a microcavity supported lipid bilayer. Exploiting an MSLB enables reconstitution of native biological switches into a strongly biomimetic and fluidic environment, with interfacial addressability without the need for laborious preparation of mutants and the associated changes that may occur to function. A reliable method for reconstituting this seven pass protiein into the MSLB is described exploiting Langmuir Blodgett monolayer over pore assembly followed by proteoliposome fusion. FLCS of labelled bR, following proteoliposome fusion indicate that the protein was successfully incorporated to MSLBs where it was found to diffuse retain a high degree of lateral fluidity within the device, with diffusion coefficient of 4.2 ± 0.3 $\mu m^2.s^{-1}$ for reconstituted bR-ATTO532 at 0.01 mol% (in the protoeoliposome preparation) at membranes that exhibited a lipid label diffusion coefficient of 9.8 ± 0.5 $\mu m^2.s^{-1}$. The diffusion coefficient of both membrane and bR decreased linearly with bR concentration, attributed to viscosity changes to the membrane indicating faithful reconstitution of different concentrations of bR into the MSLB using the reported reconstitution method.

The photo-electrical properties of bR-MSLBs were evaluated by studying the photocurrent signal generated by bR under temporal and transient light illumination and bR concentration, pH and light flicker frequency were all found to influence the photocurrent generated. Overall, large photocurrents were observed considering this is a single bilayer device and the signal scaled with bR concentration. In addition, the chronoamperometry assays demonstrated a direct relationship between the protein concertation and the electrical current response. The approach offers a robust and addressable platform that should facilitate further spectroscopic study of the mechanism and dynamics of bR proton transport at a lipid membrane, but more broadly, as bR is a 7 pass its reliable reconstitution into MSLBs suggests comparable proteins of pharmaceutical interest including G-protein-coupled seven-helix receptors and offer a new approach to building molecular switches with broad prospects for components and for applications. In terms of device application, the cavity array offers the opportunity of introcucing pH gradients and bR photoactivity, and the opportunity to model photoactivated drug-delivery or artificial endosomal capture and for the study of self-repairing optical switches. The fluidity and addressability of the substrate can also

in future offer the prospect of building complex membrane switches where initiation of aggregation processes requiring lateral fluidity are enabled.

4.6. Supporting Information

Supporting information can be found in the appendix C.

4.7. References

(1) Zhang, L.; Marcos, V.; Leigh, D. A. Molecular Machines with Bio-Inspired Mechanisms. *PNAS* 2018, *115* (38), 9397–9404.
(2) Palanco, M. E.; Skovgaard, N.; Hansen, J. S.; Berg-Sørensen, K.; Hélix-Nielsen, C. Tuning Biomimetic Membrane Barrier Properties by Hydrocarbon, Cholesterol and Polymeric Additives. *Bioinspir. Biomim.* 2017, *13* (1), 016005.
(3) Hess, H.; Saper, G. Engineering with Biomolecular Motors. *Acc. Chem. Res.* 2018, *51* (12), 3015–3022.
(4) Fang, Y.; Meng, L.; Prominski, A.; Schaumann, E. N.; Seebald, M.; Tian, B. Recent Advances in Bioelectronics Chemistry. *Chem. Soc. Rev.* 2020.
(5) Jin, Y.; Honig, T.; Ron, I.; Friedman, N.; Sheves, M.; Cahen, D. Bacteriorhodopsin as an Electronic Conduction Medium for Biomolecular Electronics. *Chem. Soc. Rev.* 2008, *37* (11), 2422–2432.
(6) Saaem, I.; Tian, J. E-Beam Nanopatterned Photo-Responsive Bacteriorhodopsin-Containing Hydrogels. *Advanced Materials* 2007, *19* (23), 4268–4271.
(7) Knipe, P. C.; Thompson, S.; Hamilton, A. D. Ion-Mediated Conformational Switches. *Chem. Sci.* 2015, *6* (3), 1630–1639.
(8) Harris, J. D.; Moran, M. J.; Aprahamian, I. New Molecular Switch Architectures. *PNAS* 2018, *115* (38), 9414–9422.
(9) Lentz, B. R.; Malinin, V.; Haque, M. E.; Evans, K. Protein Machines and Lipid Assemblies: Current Views of Cell Membrane Fusion. *Current Opinion in Structural Biology* 2000, *10* (5), 607–615.
(10) Wise, K. J.; Gillespie, N. B.; Stuart, J. A.; Krebs, M. P.; Birge, R. R. Optimization of Bacteriorhodopsin for Bioelectronic Devices. *Trends in Biotechnology* 2002, *20* (9), 387–394.
(11) Schmitt, E. K.; Nurnabi, M.; Bushby, R. J.; Steinem, C. Electrically Insulating Pore-Suspending Membranes on Highly Ordered Porous Alumina Obtained from Vesicle Spreading. *Soft Matter* 2008, *4* (2), 250–253.
(12) Garg, K.; Raichlin, S.; Bendikov, T.; Pecht, I.; Sheves, M.; Cahen, D. Interface Electrostatics Dictates the Electron Transport via Bioelectronic Junctions. *ACS Appl. Mater. Interfaces* 2018, *10* (48), 41599–41607.
(13) Palazzo, G.; Magliulo, M.; Mallardi, A.; Angione, M. D.; Gobeljic, D.; Scamarcio, G.; Fratini, E.; Ridi, F.; Torsi, L. Electronic Transduction of Proton Translocations in Nanoassembled Lamellae of Bacteriorhodopsin. *ACS Nano* 2014, *8* (8), 7834–7845.
(14) Wagner, N. L.; Greco, J. A.; Ranaghan, M. J.; Birge, R. R. Directed Evolution of Bacteriorhodopsin for Applications in Bioelectronics. *J R Soc Interface* 2013, *10* (84).
(15) Bondar, A.-N.; Elstner, M.; Suhai, S.; Smith, J. C.; Fischer, S. Mechanism of Primary Proton Transfer in Bacteriorhodopsin. *Structure* 2004, *12* (7), 1281–1288.
(16) Váró, G. Analogies between Halorhodopsin and Bacteriorhodopsin. *Biochimica et Biophysica Acta (BBA) - Bioenergetics* 2000, *1460* (1), 220–229.

(17) He, J.-A.; Samuelson, L.; Li, L.; Kumar, J.; Tripathy, S. K. Bacteriorhodopsin Thin-Film Assemblies—Immobilization, Properties, and Applications. *Advanced Materials* 1999, *11* (6), 435–446.
(18) Li, Y.-T.; Tian, Y.; Tian, H.; Tu, T.; Gou, G.-Y.; Wang, Q.; Qiao, Y.-C.; Yang, Y.; Ren, T.-L. A Review on Bacteriorhodopsin-Based Bioelectronic Devices. *Sensors (Basel)* 2018, *18* (5).
(19) Greco, J. A.; Fernandes, L. A. L.; Wagner, N. L.; Azadmehr, M.; Häfliger, P.; Johannessen, E. A.; Birge, R. R. Pixel Characterization of a Protein-Based Retinal Implant Using a Microfabricated Sensor Array. *Int. J. Hi. Spe. Ele. Syst.* 2017, *26* (03), 1740012.
(20) Pandey, P. C. Bacteriorhodopsin—Novel Biomolecule for Nano Devices. *Analytica Chimica Acta* 2006, *568* (1), 47–56.
(21) Efremov, R.; Gordeliy, V. I.; Heberle, J.; Büldt, G. Time-Resolved Microspectroscopy on a Single Crystal of Bacteriorhodopsin Reveals Lattice-Induced Differences in the Photocycle Kinetics. *Biophysical Journal* 2006, *91* (4), 1441–1451.
(22) Schuster, B. S-Layer Protein-Based Biosensors. *Biosensors (Basel)* 2018, *8* (2).
(23) Horn, C.; Steinem, C. Photocurrents Generated by Bacteriorhodopsin Adsorbed on Nano-Black Lipid Membranes. *Biophys J* 2005, *89* (2), 1046–1054.
(24) Espinosa, G.; López-Montero, I.; Monroy, F.; Langevin, D. Shear Rheology of Lipid Monolayers and Insights on Membrane Fluidity. *PNAS* 2011, *108* (15), 6008–6013.
(25) Engelman, D. M. Membranes Are More Mosaic than Fluid. *Nature* 2005, *438*, 578–580. https://doi.org/10.1038/nature04394.
(26) Daleke, D. L. Regulation of Transbilayer Plasma Membrane Phospholipid Asymmetry. *J. Lipid Res.* 2003, *44* (2), 233–242.
(27) Puu, G.; Gustafson, I.; Artursson, E.; Ohlsson, P.-Å. Retained Activities of Some Membrane Proteins in Stable Lipid Bilayers on a Solid Support. *Biosensors and Bioelectronics* 1995, *10* (5), 463–476.
(28) Steinem, C.; Janshoff, A.; Höhn, F.; Sieber, M.; Galla, H.-J. Proton Translocation across Bacteriorhodopsin Containing Solid Supported Lipid Bilayers. *Chemistry and Physics of Lipids* 1997, *89* (2), 141–152.
(29) Dolfi, A.; Tadini-Buoninsegni, F.; Moncelli, M. R.; Guidelli, R. Photocurrents Generated by Bacteriorhodopsin Adsorbed on Thiol/Lipid Bilayers Supported by Mercury. *Langmuir* 2002, *18* (16), 6345–6355.
(30) Lee, T.-Y.; Yeh, V.; Chuang, J.; Chung Chan, J. C.; Chu, L.-K.; Yu, T.-Y. Tuning the Photocycle Kinetics of Bacteriorhodopsin in Lipid Nanodiscs. *Biophys J* 2015, *109* (9), 1899–1906.
(31) Yeh, V.; Hsin, Y.; Lee, T.-Y.; Chan, J. C. C.; Yu, T.-Y.; Chu, L.-K. Lipids Influence the Proton Pump Activity of Photosynthetic Protein Embedded in Nanodiscs. *RSC Adv.* 2016, *6* (91), 88300–88305.
(32) Huang, H.-Y.; Syue, M.-L.; Chen, I.-C.; Yu, T.-Y.; Chu, L.-K. Influence of Lipid Compositions in the Events of Retinal Schiff Base of Bacteriorhodopsin Embedded in Covalently Circularized Nanodiscs: Thermal Isomerization, Photoisomerization, and Deprotonation. *J. Phys. Chem. B* 2019, *123* (43), 9123–9133.
(33) Basit, H.; Gaul, V.; Maher, S.; Forster, R. J.; Keyes, T. E. Aqueous-Filled Polymer Microcavity Arrays: Versatile & Stable Lipid Bilayer Platforms Offering High Lateral Mobility to Incorporated Membrane Proteins. *The Analyst* 2015, *140* (9), 3012–3018.
(34) Rigaud, J. L.; Paternostre, M. T.; Bluzat, A. Mechanisms of Membrane Protein Insertion into Liposomes during Reconstitution Procedures Involving the Use of Detergents. 2. Incorporation of the Light-Driven Proton Pump Bacteriorhodopsin. *Biochemistry* 1988, *27* (8), 2677–2688.
(35) Geertsma, E. R.; Nik Mahmood, N. A. B.; Schuurman-Wolters, G. K.; Poolman, B. Membrane Reconstitution of ABC Transporters and Assays of Translocator Function. *Nature Protocols* 2008, *3* (2), 256–266.

(36) Berselli, G. B.; Sarangi, N. K.; Ramadurai, S.; Murphy, P. V.; Keyes, T. E. Microcavity-Supported Lipid Membranes: Versatile Platforms for Building Asymmetric Lipid Bilayers and for Protein Recognition. *ACS Appl. Bio Mater.* 2019, *2* (8), 3404–3417.
(37) Maher, S.; Basit, H.; Forster, R. J.; Keyes, T. E. Micron Dimensioned Cavity Array Supported Lipid Bilayers for the Electrochemical Investigation of Ionophore Activity. *Bioelectrochemistry* 2016, *112*, 16–23.
(38) Basit, H.; Maher, S.; Forster, R. J.; Keyes, T. E. Electrochemically Triggered Release of Reagent to the Proximal Leaflet of a Microcavity Supported Lipid Bilayer. *Langmuir* 2017, *33* (27), 6691–6700.
(39) Robinson, J.; Berselli, G. B.; Ryadnov, M. G.; Keyes, T. E. Annexin V Drives Stabilization of Damaged Asymmetric Phospholipid Bilayers. *Langmuir* 2020, *36* (19), 5454–5465.
(40) Ramadurai, S.; Kohut, A.; Sarangi, N. K.; Zholobko, O.; Baulin, V. A.; Voronov, A.; Keyes, T. E. Macromolecular Inversion-Driven Polymer Insertion into Model Lipid Bilayer Membranes. *Journal of Colloid and Interface Science* 2019, *542*, 483–494.
(41) Ramadurai, S.; Sarangi, N. K.; Maher, S.; MacConnell, N.; Bond, A. M.; McDaid, D.; Flynn, D.; Keyes, T. E. Microcavity-Supported Lipid Bilayers; Evaluation of Drug-Lipid Membrane Interactions by Electrochemical Impedance and Fluorescence Correlation Spectroscopy. *Langmuir* 2019, *35* (24), 8095–8109.
(42) Jose, B.; Mallon, C. T.; Forster, R. J.; Blackledge, C.; Keyes, T. E. Lipid Bilayer Assembly at a Gold Nanocavity Array. *Chem. Commun.* 2011, *47* (46), 12530–12532.
(43) Kho, K. W.; Berselli, G. B.; Keyes, T. E. A Nanoplasmonic Assay of Oligonucleotide-Cargo Delivery from Cationic Lipoplexes. *Small* 2021, *17* (12), 2005815.
(44) Simeonov, P.; Werner, S.; Haupt, C.; Tanabe, M.; Bacia, K. Membrane Protein Reconstitution into Liposomes Guided by Dual-Color Fluorescence Cross-Correlation Spectroscopy. *Biophysical Chemistry* 2013, *184*, 37–43.
(45) Bacia, K.; Schwille, P. Practical Guidelines for Dual-Color Fluorescence Cross-Correlation Spectroscopy. *Nature Protocols* 2007, *2* (11), 2842–2856.
(46) Heinemann, F.; Schwille, P. Preparation of Micrometer-Sized Free-Standing Membranes. *ChemPhysChem* 2011, *12* (14), 2568–2571.
(47) Peters, R.; Cherry, R. J. Lateral and Rotational Diffusion of Bacteriorhodopsin in Lipid Bilayers: Experimental Test of the Saffman-Delbrück Equations. *PNAS* 1982, *79* (14), 4317–4321.
(48) Hughes, B. D.; Pailthorpe, B. A.; White, L. R. The translational and rotational drag on a cylinder moving in a membrane. *Journal of Fluid Mechanics* 1981, *110*, 349–372.
(49) Saffman, P. G.; Delbruck, M. Brownian Motion in Biological Membranes. *Proceedings of the National Academy of Sciences* 1975, *72* (8), 3111–3113.
(50) Camley, B. A.; Brown, F. L. H. Diffusion of Complex Objects Embedded in Free and Supported Lipid Bilayer Membranes: Role of Shape Anisotropy and Leaflet Structure. *Soft Matter* 2013, *9* (19), 4767–4779.
(51) Ramadurai, S.; Holt, A.; Krasnikov, V.; van den Bogaart, G.; Killian, J. A.; Poolman, B. Lateral Diffusion of Membrane Proteins. *Journal of the American Chemical Society* 2009, *131* (35), 12650–12656.
(52) Weiß, K.; Neef, A.; Van, Q.; Kramer, S.; Gregor, I.; Enderlein, J. Quantifying the Diffusion of Membrane Proteins and Peptides in Black Lipid Membranes with 2-Focus Fluorescence Correlation Spectroscopy. *Biophysical Journal* 2013, *105* (2), 455–462.
(53) Schwenen, L. L. G.; Hubrich, R.; Milovanovic, D.; Geil, B.; Yang, J.; Kros, A.; Jahn, R.; Steinem, C. Resolving Single Membrane Fusion Events on Planar Pore-Spanning Membranes. *Scientific Reports* 2015, *5* (1), 12006.
(54) Hildebrandt, V.; Fendler, K.; Heberle, J.; Hoffmann, A.; Bamberg, E.; Büldt, G. Bacteriorhodopsin Expressed in Schizosaccharomyces Pombe Pumps Protons through the Plasma Membrane. *Proc. Natl. Acad. Sci. U.S.A.* 1993, *90* (8), 3578–3582.

(55) Bamberg, E.; Apell, H.-J.; Dencher, N. A.; Sperling, W.; Stieve, H.; Läuger, P. Photocurrents Generated by Bacteriorhodopsin on Planar Bilayer Membranes. *Biophys. Struct. Mechanism* 1979, *5* (4), 277–292.
(56) Barabás, K.; Dér, A.; Dancsházy, Z.; Ormos, P.; Keszthelyi, L.; Marden, M. Electro-Optical Measurements on Aqueous Suspension of Purple Membrane from Halobacterium Halobium. *Biophys J* 1983, *43* (1), 5–11.
(57) Guo, Z.; Liang, D.; Rao, S.; Xiang, Y. Heterogeneous Bacteriorhodopsin/Gold Nanoparticle Stacks as a Photovoltaic System. *Nano Energy* 2015, *11*, 654–661.
(58) Lu, S.; Guo, Z.; Xiang, Y.; Jiang, L. Photoelectric Frequency Response in a Bioinspired Bacteriorhodopsin/Alumina Nanochannel Hybrid Nanosystem. *Advanced Materials* 2016, *28* (44), 9851–9856.
(59) Heberle, J. Proton Transfer Reactions across Bacteriorhodopsin and along the Membrane. *Biochimica et Biophysica Acta (BBA) - Bioenergetics* 2000, *1458* (1), 135–147.
(60) Lee, Y.-S.; Krauss, M. Dynamics of Proton Transfer in Bacteriorhodopsin. *J. Am. Chem. Soc.* 2004, *126* (7), 2225–2230.
(61) Ming, M.; Lu, M.; Balashov, S. P.; Ebrey, T. G.; Li, Q.; Ding, J. PH Dependence of Light-Driven Proton Pumping by an Archaerhodopsin from Tibet: Comparison with Bacteriorhodopsin. *Biophysical Journal* 2006, *90* (9), 3322–3332.
(62) Freier, E.; Wolf, S.; Gerwert, K. Proton Transfer via a Transient Linear Water-Molecule Chain in a Membrane Protein. *PNAS* 2011, *108* (28), 11435–11439.
(63) Friedrich, D.; Brünig, F. N.; Nieuwkoop, A. J.; Netz, R. R.; Hegemann, P.; Oschkinat, H. Collective Exchange Processes Reveal an Active Site Proton Cage in Bacteriorhodopsin. *Commun Biol* 2020, *3* (1), 1–9.
(64) Balashov, S. P.; Lu, M.; Imasheva, E. S.; Govindjee, R.; Ebrey, T. G.; Othersen, B.; Chen, Y.; Crouch, R. K.; Menick, D. R. The Proton Release Group of Bacteriorhodopsin Controls the Rate of the Final Step of Its Photocycle at Low PH. *Biochemistry* 1999, *38* (7), 2026–2039.
(65) Balashov, S. P. Protonation Reactions and Their Coupling in Bacteriorhodopsin. *Biochimica et Biophysica Acta (BBA) - Bioenergetics* 2000, *1460* (1), 75–94.
(66) Wang, J.-P.; Yoo, S.-K.; Song, L.; El-Sayed, M. A. Molecular Mechanism of the Differential Photoelectric Response of Bacteriorhodopsin. *J. Phys. Chem. B* 1997, *101* (17), 3420–3423.
(67) Kleineberg, C.; Wölfer, C.; Abbasnia, A.; Pischel, D.; Bednarz, C.; Ivanov, I.; Heitkamp, T.; Börsch, M.; Sundmacher, K.; Vidaković-Koch, T. Light-Driven ATP Regeneration in Diblock/Grafted Hybrid Vesicles. *ChemBioChem* 2020, *21* (15), 2149–2160.
(68) Lv, Y.; Yang, N.; Li, S.; Lu, S.; Xiang, Y. A Novel Light-Driven PH-Biosensor Based on Bacteriorhodopsin. *Nano Energy* 2019, *66*, 104129.
(69) Miyazaki, S.; Matsumoto, M.; Brier, S. B.; Higaki, T.; Yamada, T.; Okamoto, T.; Ueno, H.; Toyabe, S.; Muneyuki, E. Properties of the Electrogenic Activity of Bacteriorhodopsin. *Eur Biophys J* 2013, *42* (4), 257–265.
(70) Jeong, S.; Nguyen, H. T.; Kim, C. H.; Ly, M. N.; Shin, K. Toward Artificial Cells: Novel Advances in Energy Conversion and Cellular Motility. *Advanced Functional Materials* 2020, *30* (11), 1907182.
(71) Geibel, S.; Friedrich, T.; Ormos, P.; Wood, P. G.; Nagel, G.; Bamberg, E. The Voltage-Dependent Proton Pumping in Bacteriorhodopsin Is Characterized by Optoelectric Behavior. *Biophys J* 2001, *81* (4), 2059–2068.
(72) Sode, K.; Yamazaki, T.; Lee, I.; Hanashi, T.; Tsugawa, W. BioCapacitor: A Novel Principle for Biosensors. *Biosensors and Bioelectronics* 2016, *76*, 20–28.
(73) Matsumoto, A.; Miyahara, Y. Current and Emerging Challenges of Field Effect Transistor Based Bio-Sensing. *Nanoscale* 2013, *5* (22), 10702–10718.
(74) Ariga, K.; Makita, T.; Ito, M.; Mori, T.; Watanabe, S.; Takeya, J. Review of Advanced Sensor Devices Employing Nanoarchitectonics Concepts. *Beilstein J. Nanotechnol.* 2019, *10* (1), 2014–2030.

(75) Verchère, A.; Ou, W.-L.; Ploier, B.; Morizumi, T.; Goren, M. A.; Bütikofer, P.; Ernst, O. P.; Khelashvili, G.; Menon, A. K. Light-Independent Phospholipid Scramblase Activity of Bacteriorhodopsin from Halobacterium Salinarum. *Scientific Reports* 2017, *7* (1), 9522.

Chapter 5: A Nanoplasmonic Assay of Oligonucleotide-Cargo Delivery from Cationic Lipoplexes

---

Published in *Small,* 2021, 17, 2005815.

Kiang W. Kho, Guilherme B. Berselli, Tia E. Keyes.

Within this work I was second author, I contributed towards experimental design, execution and manuscript preparation. I carried out lipoplexes characterization though DLS and completed all FLCCS, FLCS and FLIM studies on PDMS microcavity arrays. I have written complete sections with significant contribution to overall manuscript preparation. Gold array preparation, cysteine functionalization, Raman and SE(R)S were carried out by Dr. K. W. Kho. Supporting information associated with this chapter can be found in Appendix D.

5.1. Abstract

Over the past decades, the difficulties in precisely engineering the release mechanism of large therapeutic molecules from their nanocarrier have been the major bottleneck of intracellular delivery. With the dearth of detailed insights into such a mechanism and the lack technique to probe the release process *in-vitro*, the development of an efficient delivery vector remains elusive. To facilitate a rational design approach, a platform with the potential to screen the release mechanism of a huge array of vectors in parallel is highly desirable. The proof-of-concept study presented here, aims to achieve exactly that by demonstrating a nano-photonic biophysical endosome model as an assay to study cargo escape from nanocarrier following fusion with endosomal membrane. More importantly, through the combined use of plasmonic hot-spots and fluorescence lifetime correlation spectroscopy (FLCS), our model enabled identification of an intermediate endosomal-escape mechanism facilitated by positively-charged oligonucleotide-binding membrane domain that dictates the rate of oligonucleotide release. This work reveals a hitherto unreported release mechanism as a complex multi-step interplay between the oligonucleotide cargo and the target membrane, rather than solely on lipid-mixing at the fusing site as previously proposed, substantiating the observations that lipid-mixing is unnecessarily correlated with the rate of cargo release. This presents a new paradigm for assessment of vector delivery at model membranes using a plasmonic well to mark molecular permeation across a micropores suspended lipid bilayer that promises to have wide application within the drug delivery design application space.

5.2. Introduction

Delivery vectors hold tremendous potential as a platform for conveying treatment for a broad range of diseases, particularly where targeting is inhibited by challenging membrane barriers or where the therapeutic cargo is toxic or fragile. However, the inability to precisely engineer the release mechanism of cargo from the abyss of endosomal trap has limited its escape rate to at most about 1%.[1] This is especially true for large therapeutic molecules (LTMs), particularly biologics and gene-based drugs, which currently account for up to 40% of drugs under development. Aside from realising novel treatment possibilities such as vaccination against cancer,[2, 3] or treatments for orphan diseases,[4]and recently, the potential use of gene-editing tool for treating viral infections.[5, 6] an in-depth understanding of the mechanism of intracellular delivery is also key from a safety

and regulatory standpoint, as outlined in the European Medicines Agency guidelines on gene therapy products.[7] While *In-vitro* and *in-vivo* assays have traditionally been the methods of choices in vector design, these techniques are typically laborious and expensive,[8] and so inefficient for iterative design approaches in such highly complex problems as vector design. Another concern for cell transfection assays is their reliance on 'down-stream signals', i.e. gene-expression, for assessment of delivery. Such an approach is indirect and interpretation can be confounded by a plethora of factors including the physiological state, cell-lines and antibiotics used,[9] thus obscuring crucial intracellular events, such as the rate-limiting endosomal escape (EE).[1, 10]Another crucial obstacle to understanding EE is the dearth of studies regarding the exact mechanism of oligonucleotide-cargo release (OCR) from an endosome.[11]In the case of cationic lipoplex, although fusion with the endosomal membrane is understood to be a pre-requisite for transfection, the extent of lipid-mixing was sometime found to not correlate with OCR rate.[12, 13, 14]As such, the capability to probe CR is highly desirable in any vector development.

Biophysical membrane models comprised of artificially-prepared phospholipid-bilayers could serve as a surrogate for endosome. The benefits of such membrane models are manifold, including in modularity, customizability, conduciveness to short-range probing such as atomic-force mapping and plasmonically enhanced spectroscopy. For instance, correlations were found between the interaction of poly(amidoamine) (PAMAM) dendrimer with supported 1,2-dimyristoyl-sn-glycero-3-phosphocholine (DMPC) lipid bilayers and cell-based experiments in terms of cellular internalization mechanism.[15]In light of cell-penetrating peptide's role in EE, De Shayes, et al. investigated the effect of the conformational-state of a peptide on its interactions with membrane using supported lipid bilayers (SLBs).[16] However, assays based on SLBs are insensitive to OCR due to space constraints imposed by the underlying support. It should be stressed that, in contrast to previous assumptions, and also as will be shown in this report, the occurrence of liposome-membrane fusion is by no means an indicator of OCR,[17]i.e. in instances where cargo may remain bound to the membrane following fusion. Recently, Diao, J. et al., devised a content-mixing assay through which hybridization of complementing DNA contents in two fusing SNARE-decorated sub-micron vesicles can be detected via Fluorescence Resonance Energy Transfer (FRET).[18]While the objective of Diao, J. et al. study was not intended to elucidate OCR, this particular approach

would may be inappropriate for OCR study, since the detection of content-mixing does not necessarily correlate with oligonucleotide dissociation from the vesicles membrane.

To address the challenge of assaying for OCR, a proof-of-concept demonstration of a platform that combines high-throughput screening (HTS) potentiality with direct OCR detection capability is reported. Specifically, a microcavity suspended membrane model (MSLB) is used to study the delivery and release of oligonucleotide-cargo from lipoplexes. MSLB was chosen for a number of attractive features: firstly, the underlying pore support eliminates space constraints seen in models like SLBs, rendering MSLB useful for observing OCR; secondly, MSLB is amenable to microfluidic adaptation, providing an attractive route to realising an affordable HTS platform in the future.[19]Previous pore-supported lipid bilayer assays, have focussed on nanodimensioned apertures and so have been confined to small-molecule studies due to the restricted area of the suspended-membrane.[19, 20] For instance, lipid bilayer supported over cylindrical nano-pores as described by Urban M., et. al. are limited to interrogation of species less than about 80nm diameter(i.e. the size of the pores),[19] which is smaller than a typical delivery vector (Ø ~ 100nm – 300nm). A key problem arises from the fact that pore-supported SLBs formed at cylindrical pores can become highly unstable with larger pore-diameters. Recently, Keyes, et al. circumvented this issue by suspended lipid bilayer over semi-spherical Au and PDMS voids that are buffer filled.[21] The high MSLB stability attained, which last for up to 21hrs on gold and for many days on PDMS was attributed to the rounded edge along the rim of the supporting voids and the hydrophillicty of the interface, which can be selectively surface modified to promote hydrophobic character and aqueous filling also plays a key role. Pore-SLs formed over large voids with diameters up to 5µm have been prepared with this particular method,[22] and with micron dimensioned pore supports, the pore starts to approach the dimensions of a cell, making the models amenable to study by microscopy enabling in OCR study methods, such as fluorescence correlation spectroscopic (FCS) for interrogation of vector-interaction at the suspended membrane. More importantly, in the present context in metallic pore supports the opportunistic exploitation of the plasmonic hot-spots at the bottom of the semi-spherical Au void can allow for Surface Enhanced (Resonance) Raman Scattering (SE(R)RS) based arrival-time monitoring of the released oligonucleotide-cargo from the membrane suspended on the void. Here, such a setup is detailed and new insights into the effects of lipoplex compositions on OCR revealed.

5.3. Methods

5.3.1. Materials

1,2-Dioleoyl-sn-glycero-3-phosphocholine (DOPC), porcine brain N-(octadecanoyl)-sphing-4-enine-1-phosphocholine(SM), cholesterol, 1,2-dioleoyl-sn-glycero-3-phospho-L-serine (DOPS), 1,2-dioleoyl-3-trimethylammonium-propane (DOTAP), and 1,2-dioleoyl-sn-glycero-3-phosphoethanolaminewere purchased with a maximum degree of purity (>99%) from Avanti Polar Lipids (Alabaster, Alabama) and used without further purification. 1,2-Dioleoyl-sn-glycero-3-phosphoethanolamine-labeled Atto532 (Atto532-DOPE) was purchased from ATTO-TEC (Siegen, Germany). {hosphate-buffered saline (PBS)tablets were purchased from Sigma-Aldrich (Wicklow, Ireland). Aqueous solutions were prepared using Milli-Q water (Millipore,Bedford, MA). Polydimethylsiloxane silicon (PDMS) elastomer was purchased from Dow Corning (Wiesbaden, Germany) and mixed following the supplier's instructions. Silicon wafers coated with a 100nm layer of gold on a 50 Å layer of titanium were obtained from AMS Biotechnology. The monodisperse polystyrene latex spheres with a diameter of 750nm, and 4.6μm were obtained from Bangs Laboratories. The commercial cyanide-free gold-plating solution (TG-25 RTU) was obtained from Technic. Pur-A-Lyzer Dialysis kit (MWCO 3.5KDa) was purchased from Sigma-Aldrich and used as per instruction.

5.3.2. Fabrication and functionalization of SERS substrates.

Large hexagonally-packed Au cavity arrays were prepared by the method of templated Au deposition. Briefly, a flat Au-coated Si chip was first cleaned with THF followed by a 10min plasma-treatment (1000mTorr), before a uniform nano-sphere template as large as 6mm (Ø) was deposited via convection-assisted self-assembly of 750nm polystyrene spheres as described elsewhere. Au is then electrochemically deposited through the template at a bias-voltage of -0.46V for 6.6min. The as prepared sample was then soaked in THF for 3min to remove the nano-sphere template. The Au-cavity array imprint was then cleaned by applying 20 votlammetric oxidation reduction cycles in 0.05mM H_2SO_4 to remove any surface residues. The cleaned substrate was then placed in 10mM Cysteamine solution(in H_2O) for 18hours before rinsing profusely with

water, and kept in dried condition until use. Schematics depicting the process can be found in supplementary document.

5.3.3. Preparation of lipoplex

Chloroform solution of lipids with a total volume of 40ul was dried under a steady flow of nitrogen followed by the removal of solvent under high vacuum for 30mins. When preparing for DOTAP lipoplex, 40ul of 1mMDOTAP was used, while for DOTAP/DOPE lipoplex, about equal amount of DOTAP and DOPE, each at 1mM concentration, was used. For labelled DOTAP and DOTAP-DOPE lipoplexes, about 1ul of Atto532 (10µg/ml) was added to the lipid solution prior to drying. Lipids were then rehydrated with 1ml PBS (filtered with 0.2um pore-size membrane) containing 0.26µM Cy5-labeled ssDNA. This mixture was then thoroughly mixed for 2min with a vortex mixer. To ensure the ssDNA adequately complexes with the cationic lipids, the samples were further agitated using a rotating mixer for 30min. Finally, the suspensions were extruded through a 100nm-pore size polycarbonate filter 13 times followed by 3hr-dialylsis to remove unbound ssDNA using the pur-A-lyzerkit. Size distributions and zeta-potentials of the lipoplexes were determined by DLS on a Zeta-Sizer 5000, Malvern Instruments. All extruded samples were kept at 4ºC and were stable up to at least 5 days.

5.3.4. Microcavity Supported Lipid Bilayer Preparation

Pore suspending lipid bilayers were spanned across buffer filled micro-cavity arrays using Langmuir-Blodgett (LB) transfer. Briefly, an LB trough (NIMA 102D) was filled with MiliQ water (18.2 MΩ.cm^{-1}) and approximately 50 µL of lipid mixture containing DOPC (52 mol%), SM (7 mol%), DOPS (8 mol%) and cholesterol (33mol %) (1 mg/mL in chloroform) were deposited onto the air-water interface until surface pressure of >1 mN/m was obtained. For FLCS studies, labelled DOPE-ATTO532 was add to the lipid mixture at 0.01 mol % and transferred to the distal lipid leaflet only. Gold or PDMS micro-cavity were immersed into the LB trough until all of the cavities were submerged completely into the subphase. The chloroform was allowed to evaporate and the resulting lipid monolayer at the air water interface was compressed four times to a surface pressure of 36 mN/m each time. The micro-cavity array was withdrawn from the trough at a rate of 5 mm/s whilst the surface pressure of the lipids was retained at 36mN/m to ensure adequate transfer of

lipid monolayer. To assemble upper leaflet of the bilayer, the substrates were submerged into the trough at a rate of 5 mm/s.

5.3.5. Preparing PDMS chamber

Prior to lipoplex fusion, PDMS thin chamber was sealed to a cover glass with rapid adhesive glue (Araldite). The microfluidic device was formed after insertion of two silicon tubes to the sealed chamber containing microcavity array by punching two holes through the PDMS into cavity chamber (see SI). Care was taken to ensure that at no stage during the preparation or measurements the bilayer was exposed to air. In this work, the proximal leaflet refers to the LB deposited lipid leaflet next to the substrate and the distal leaflet is the outer lipid layer facing toward the bulk solution. The integrity of lipid bilayers were acceded by FLCS.

5.3.6. Electrochemical Impedance Spectroscopy (EIS) measurements

Electrochemical impedance measurements were performed with a CHI 760Bbipotentiostat (CH Instruments, Austin, TX) in a three-electrode cell configuration. This comprises of a Ag/AgCl (1 M KCl) reference electrode, a platinum coiled wire as a counter electrode, and the gold substrate with a microcavity array as the working electrode. 1 mM K3[Fe(CN)6]/K4[Fe(CN)6] (1:1 mol/mol) dissolved in PBS containing additional 0.1 M KCl as the supporting electrolyte was used as a redox probe. The EIS were recorded in the frequency region between0.02 Hz to 10^4Hz with a bias potential of 0.26 V vs Ag/AgCl. All samples were left to equalize in the buffer for at least 5min before commencing measurements.

5.3.7. SE(R)RS and SERS measurements

All Raman measurements were done with HORIBA spectrometric system with an Olympus 50X 0.55NA objective lens. A 633nm laser line (4.5uW) was used for arrival-time measurement of the Cy5-labelled ssDNA delivered across the lipid membrane. This particular excitation wavelength was chosen as it was closer to the surface-plasmon resonance of the 750nm Au cavity-array. The membrane-bearing cavity-array was always kept at a fixed distance of about 300um from the cover-glass with a PVA-spacer. Prior to the introduction of the lipoplex solution, Raman spectra were obtained of the membrane-bearing array. Time-series SE(R)RS measurement commenced within 1min upon application of lipoplex with 30min interval for a period of 2hr. All experiments

were carried out immediately after LB-LB membrane deposition. 'Leak-test' was also performed on membrane-bearing arrays with membrane-impermeable probe, DRAQ7, to verify absence of any leaky defects in the membrane. 'Leak-test' were performed after each delivery study to ensure membrane integrity remained uncompromised throughout the experiment. All leak-tests were carried out at 785nm laser (5uW). All obtained spectra were de-noised with a 3-point moving-points averaging.

5.3.8. Fluorescence Lifetime Correlation Spectroscopy (FLCS) and Fluorescence Lifetime Cross-Correlation Spectroscopy (FLCCS)

Single point FLCS and FLCCS were primarily used to characterize the DNA incorporation to lipoplexes comprised of DOTAP and DOTAP/DOPE (1:1 mol:mol). Then, to assess both the diffusion of lipid marker and DNA prior and after delivery of DNA, the lateral diffusion of DNA-Cy5 and DOPE-ATTO532 was measured by FLCS. Fluorescence measurements were performed on a MicroTime 200 lifetime (PicoQuant GmbH, Berlin, Germany) using a water immersion objective (NA 1.2 UPlanSApo 60 x 1.2 CC1.48, Olympus). The detection unit comprises of two single photon avalanche diode (SPAD) from PicoQuant. Labeled lipid marker DOPE-ATTO532was excited with 532 nm PicoTA laser from Toptica (PicoQuant). Labelled DNA-Cy5 was excited with 640 nm LDH-P-C-640B (PicoQuant). To exclude scattered or reflected laser light, emitted fluorescence was collected through an HG670lp AHF/Chroma or HQ550lp AHF/Chroma band pass filter for 640 or 532 nm lasers, respectively. A 50 μm pinhole was used to eliminate photons from outside the confocal volume. Before FCLS measurement, backscattered images of the substrate were taken using an OD3 density filter to ensure the optimal positioning of the focus to the centre of the microcavity. Then, the bilayer position was determined by z-scanning until the point of maximal fluorescence intensity of DOPE-ATTO532 was found. At this point, the fluctuating fluorescence intensity of labeled lipid marker or DNA-Cy5 were measured for 30 to 60 seconds per cavity, and replicate data from 20 to 30 cavities were measured per sample. To assess simultaneously the diffusion time (ms) and the fluorescence lifetime (ns) the emitted photons were analyzed by a time-correlated single photon counting system (TCSPC) (PicoHarp 300 from Picoquant). The fluorescence fluctuations obtained are then correlated with a normalized autocorrelation function (Equation 1):

$$G(\tau) = \frac{\langle \delta F(t).\, \delta F(t+\tau) \rangle}{\langle F(t) \rangle^2} \qquad \text{(Eq.1)}$$

The auto-correlation curves obtained from the fluorescence fluctuations of DOPE-ATTO532 were fitted to a 2-D model (Equation xx) using the software SymphoTime (SPT64) version 2.2 (PicoQuant).

$$G(\tau) = \frac{1}{N}\left[1 + \left(\frac{\tau}{\tau_D}\right)^{\alpha}\right]^{-1} \qquad \text{(Eq.2)}$$

DNA-Cy5 autocorrelation data were fitted using 2-D/3-D diffusion model for two diffusing moieties by adding a second component to equation 2, (Equation 3).

$$G(\tau) = \frac{1}{N}\left[1 + \left(\frac{\tau}{\tau_{2D}}\right)^{\alpha 1}\right]^{-1}\left[1 + \left(\frac{\tau}{\tau_{3D}}\right)^{\alpha 2}\right]^{-1} \qquad \text{(Eq.3)}$$

Here, ρ represents the amplitude at G(τ) and is defined as the inverse of number of molecules (1/N) and α is the anomalous parameter; $\tau_{2D}$and τ_{2D} are the diffusion time of the DNA molecules in the lipid membrane and in solution, respectively. The diffusion coefficient is related to the correlation time τ_D by the relation $D = \omega^2/4\tau_D$, where ω is the $1/e^2$ radius of the confocal volume i.e. the waist of the exciting laser beam. ω was measured for each excitation using a reference solution of free dye for which the diffusion coefficient is known. The ω was determined by calibration using reference dyes; ATTO-655 (Atto TEC, GmbH) for 640nm laser and Rhodamine 6G for 532 nm laser at 20°C in water. Detailed description of the experimental set up is shown below.

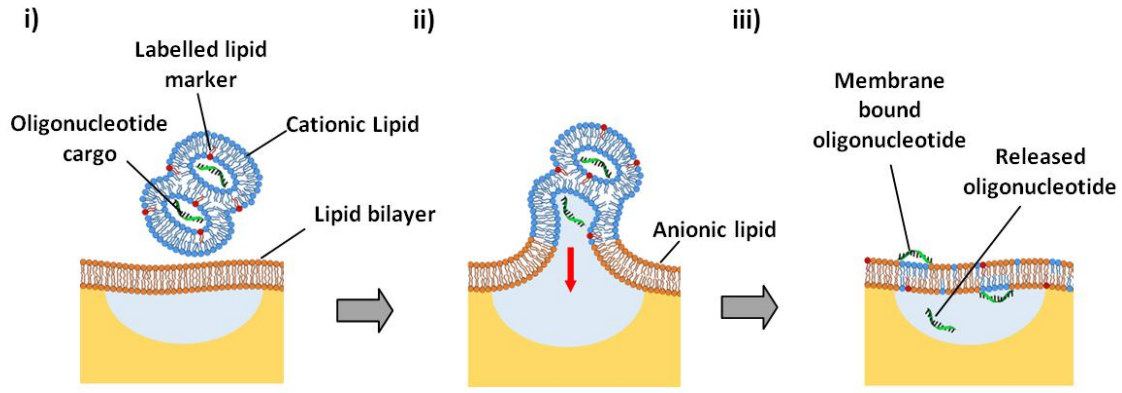

Scheme 1. Schematic representation of DNA delivery to MSLBs. i) lipoplex is exposed to buffer filled micro cavity arrays; ii) lipoplex fusion against the lipid bilayer; iii) DNA is delivered and encapsulated inside the microcavities.

5.4. Results

5.4.1. Suspended lipid-bilayers over hemi-spherical Au cavities

Au substrates consisting of uniform, hexagonally-packed Au hemispherical pores with 750nm apertures were used for all surface enhanced Raman experiments. This size was selected as their plasmon-resonance peak match well to the excitation lines used in the experiment (633nm and 785nm). To maximize detection sensitivity of Cy5-ssDNA, the substrate surface was rendered positively charged by Cysteamine-(Cyst)-functionalization (due to the amino group at pH 7.4) so as to promote binding the anionic oligonucleotide (the model cargo here) to the surface where the plasmonic fields were strongest.[23] Electrochemical impedance spectroscopic (EIS) measurements were performed to confirm the presence of Cyst–monolayer using a three electrode cell, with the cavity array serving as working electrode. Figure1a shows representative Nyquist plot obtained in PBS (pH 7.4) containing 1mM $K_3[Fe(CN)_6]/K_4[Fe(CN)_6]$ (1:1 mol/mol) as a redox probe containing 0.1 M KCl as supporting electrolyte for bare Au-cavities (i.e. without Cyst), and Cyst-treated ones. The observed decrease of R_{ct} in Cyst-Au is a reported characteristic of the electrochemistry of the Cyst -monolayer, attributed to electrostatic interaction between the Cyst-

monolayer and the negatively charged redox-probe. It is thus helpful in confirming association and that the film can interact electrostatically with reagent.[24] Figure 1b shows the SE(R)RS spectra of the Cy5-tag, demonstrating the enhanced detection sensitivity for Cy5-ssDNA with a Cyst-treated substrate.

It should be noted that, aside from promoting Cy5-ssDNA binding, the Cyst-monolayer also serves to improve the hydrophilicity of the Au substrate, and thus support the stability of the suspended lipid bilayer. The lipid membrane composition used throughout this study comprised of1,2-Dioleoyl-sn-glycero-3-phosphocholine(DOPC, 51.7 mol%),cholesterol (33.3 mol%), 1,2-dioleoyl-sn-glycero-3-phospho-L-serine (DOPS, 8.3 mol%) and porcine brain N-(octadecanoyl)-sphing-4-enine-1-phosphocholine (SM, 6.7 mol%), selected in order to model a typical mammalian plasma membrane.[25] The bilayer was deposited via Langmuir-blodgett (LB) transfer onto the cavity array, followed by EIS measurements carried out at 15min and 3hrs time-points. As can be seen from the Figure 1c, the R_{ct} remained stable at ~90KΩ lasting over well beyond the 2 hour window that is the typical length of the gene-delivery experiments studied here. The large resistance value observed here, which contrasts strongly with the Cysteamine modified array is attributed to the low charge-transfer efficiency caused by electrostatic repulsion between $Fe(CN)_6]^{3-/4-}$and the negatively-charged membrane. Importantly, in the absence of the Cysteamine modification, bilayer at the gold membrane was unstable.

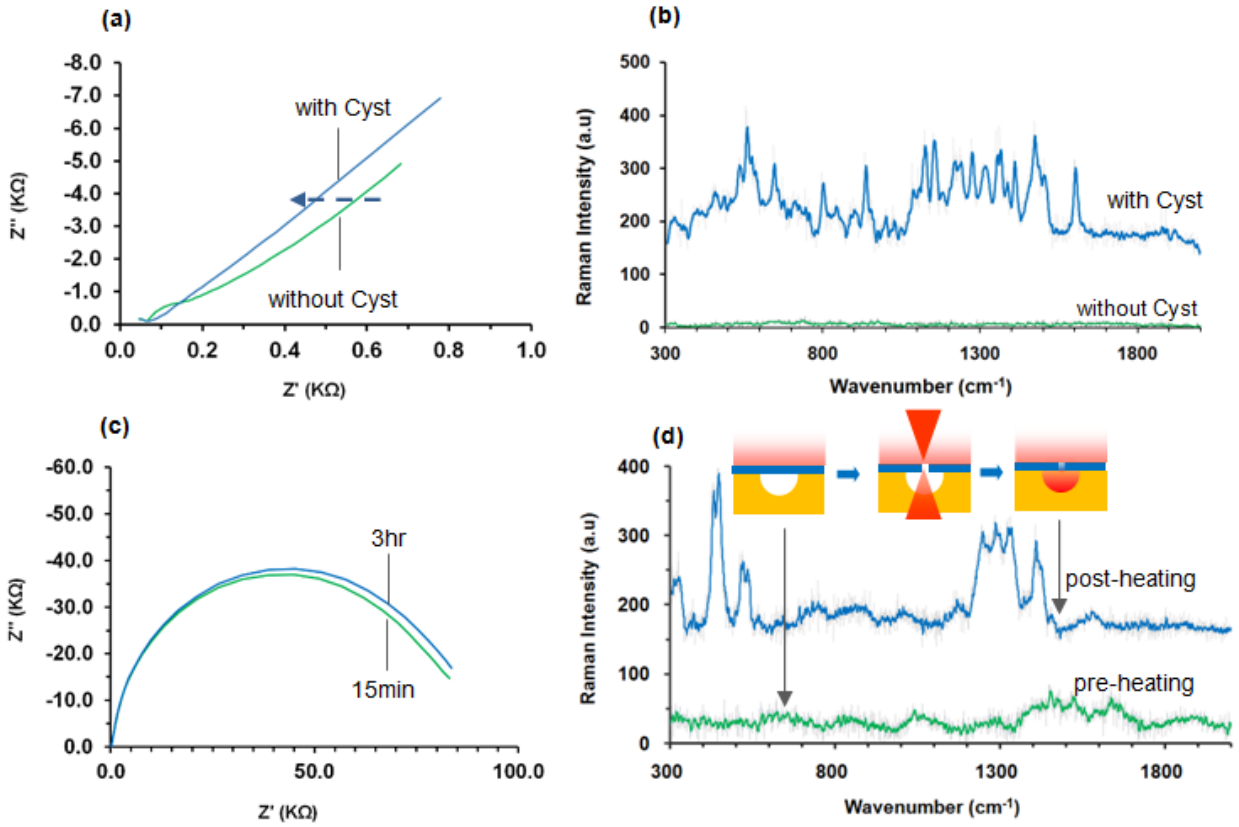

Figure 1. (a) EIS of bare Au cavities, and Cyst-functionalized Au cavities; (b) SE(R)RS spectra of Cy5-tage from Cy5-ssDNA in Cyst-functionalized and bare substrate; (c). EIS spectra of microcavity supported lipid bilayer obtained at 15min and 3hrs post deposition demonstrate stability over the experimental window;(d)'leak-test' with DRAQ7confirms the MSLB seals the cavity from access by non-membrane permeable species. The schematic depicts membrane disruption by local heating; The membrane composition is DOPC (51.7 mol%), Cholesterol (33.3 mol%), DOPS (8.3 mol%) and N-(octadecanoyl)-sphing-4-enine-1-phosphocholine (6.7 mol%). Excitation wavelength for Figure 1b is 633nm, and 1d 785nm. EIS measurements were carried out with a Ag/AgCl (1 M KCl) reference electrode, a platinum coil wire as a counter electrode, and the gold substrate with a microcavity array as the working electrode under 1 mM K3[Fe(CN)6]/K4[Fe(CN)6] in PBS between 0.02Hz and 104HZ operating frequency.

It is critical to establish that the lipid membrane suspended across the pore array does behave as a barrier to non-membrane permeable cargo. To confirm this, the sealing quality of the MSLB bearing Au-voids (MSLB-Au) was examined by exposing them to 5μM DRAQ7, a membrane-

impermeable probe, with a strong Raman signature, resonantly enhanced at 785 nm. As can be seen in Figure 1d, which shows Raman spectrum from the array following incubation of the MSLB withDRAQ7 no Raman signal from DRAQ7 (see S1 for DRAQ SE(R)RS spectrum) is observed. This indicates that the probe is prevented from entering the cavity in the presence of the MSLB confirming the bilayer seals the SERS active Au-voids. To establish that DRAQ permeation would be evident if it were occurring, the lipid membrane was then deliberately thermally disrupted by illuminating it at increased laser power (by 10×) for 2-min before acquiring another SE(R)RS spectrum at a lower excitation intensity. Notably, the spectrum acquired post-heating now shows an intense and well resolved SE(R)RS signal corresponding to DRAQ7 (see post-heating curve in Figure 1d)indicating thermal membrane disruption enabled entry of the DRAQ7 into plasmonic field of the cavity. Taken together, one can conclude that a stable sealed microcavity supported lipid bilayer was obtained and that using the most intense region of plasmonic field which is located below the level of the lipid membrane, is a valid and useful means of determining membrane permeation. It should be stressed that the ability to preserve the suspended-membrane's integrity over a large pore size array for a prolonged period of time is a crucial feature of this platform that is precisely what enables the OCR study presented herein.

5.4.2. Delivery of oligonucleotide-cargo across suspended lipid bilayer with lipoplex

Two lipoplexes, 1,2-dioleoyl-3-trimethylammonium-propane (DOTAP) and DOTAP/1,2-Dioleoyl-sn-glycero-3-phosphoethanolamine (DOPE)were used to study the effect of composition on delivery efficiency of fluorescently labelled oligonucleotide cargo. Dynamic Light Scattering (DLS) analysis revealed the Cy5-ssDNA loaded lipoplexes to be 146 +/- 1.5nm (@PDI=0.12), and 135+/- 1nm (@PDI=0.12) in diameter respectively, with zeta-potentials of34.96 +/- 2mV and 20.5 +/- 1mV respectively. On the basis of particle size and zeta-potential, both DNA-loaded lipoplexes were found to be stable for at least 5days.

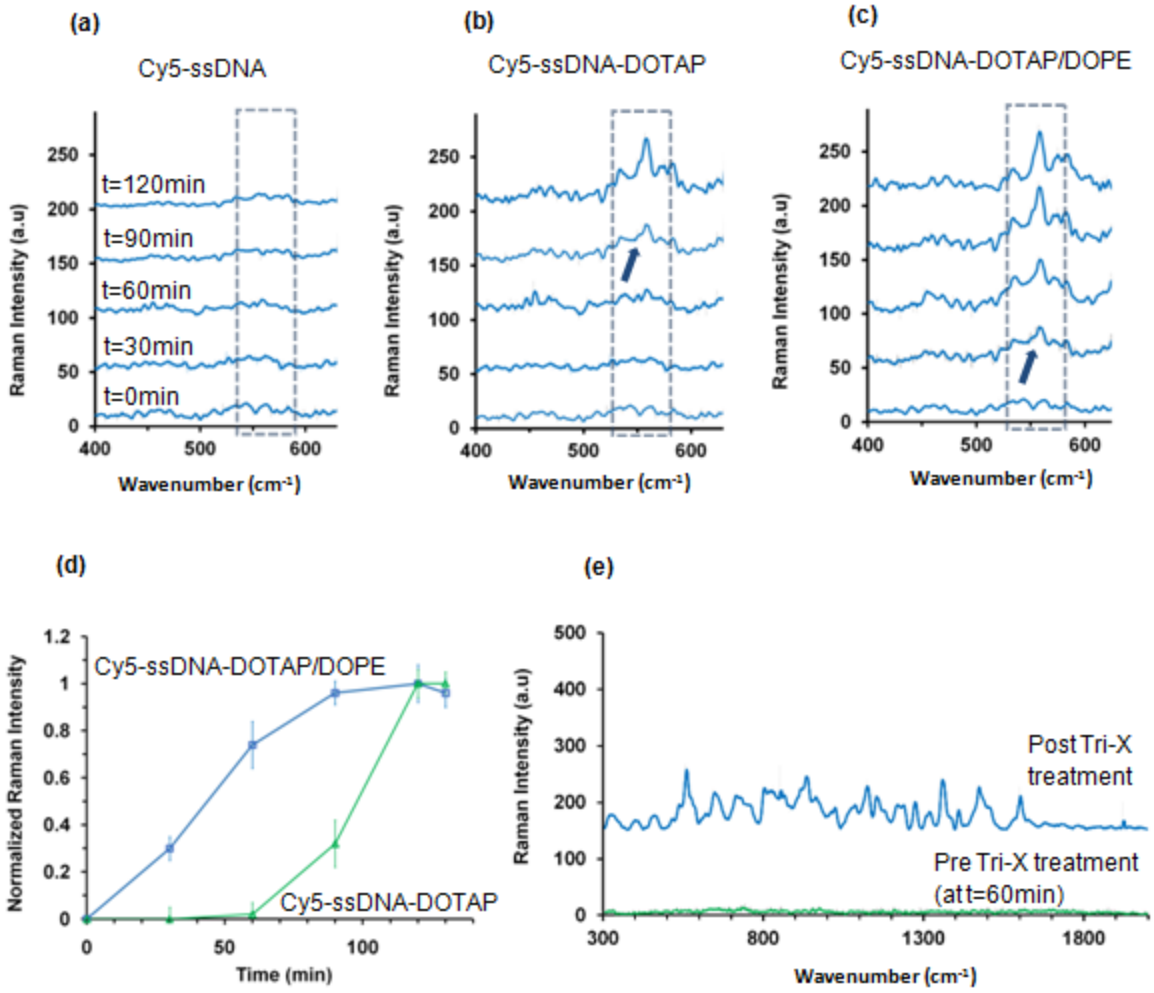

Figure 2. (a), (b), and (c) Evolution of SE(R)RS spectra of Cy5-tag from naked Cy5-ssDNA, Cy5-ssDNA-DOTAP lipoplex, and Cy5-ssDNA-DOTAP/DOPE lipoplex respectively. SE(R)RS peak at 560cm-1, which correspond to polymethine-bridge stretching mode, is shown. (d) SE(R)RS response curve showing the OCR kinetic. (e) same as (c) except the experiment is terminated at 60min time point. SE(R)RS spectra of Cy5-tag from Cy5-ssDNA-DOTAP lipoplex became discernible after membrane disruption by Tri-X. Excitation wavelength = 633nm.supercripted

For these experiments,633nm excitation was used to match the electronic absorption peak (@670nm) of the Cy5-tag and this wavelength is also expected, as for 785 nm, to elicit a SERS effect.[26]First, background Raman spectra were collected, from the MSLB. As can be seen in Figure 2a - c, no SE(R)RS signals were detectable before administrating the samples (t=0min).Then,

about 60µl of lipoplex was incubated with substrate surface, and the time-series measurement commenced within 3 min of sample administration. The growth of the Cy5-ssDNA concentration in the cavity was tracked by monitoring the SE(R)RS intensity of the polymethine-bridge stretching mode at ~560cm^{-1},[27] which is the most intense Raman peak in the Cy5-SE(R)RS spectrum. As can be seen from Figure 2b (for DOTAP lipoplex), 2c (for DOTAP-DOPE lipoplex) and also in the normalized response-curves (Figure 2d), Raman signal intensity from Cy5-ssDNA on exposure to the lipid bilayer modified voids increased, and followed a sigmoidal trend, reaching a plateau at120min, and 60min, respectively for DOTAP and DOTAP/DOPE lipoplex. A prominent distinction between the DOTAP and DOTAP/DOPE SE(R)RS response-curves is the time-point at which signals began to rise: DOTAP/DOPE lipoplex begins to 'deliver' Cy5-ssDNA as early as 30min, while it takes approximately90min for the DOTAP counterpart to instigate release. To ensure that the MSLB remained intact throughout the experiment, 'leak tests' were performed with membrane impermeable DRAQ7 exciting at 785nmin an analogous way as described earlier at the end of each experiment. This was completed to ensure that the SE(R)RS signal from Cy5-ssDNA was derived from lipoplex facilitated delivery of the OC to the cavity interior and was not due to degradation of the membrane overtime. Correspondingly, at the end of each experiment the DRAQ7 was confirmed to remain impermeable to the cavities and no leakage was detectable. (see S2).In addition, no SE(R)RS signals were observed on incubation of free Cy5-DNA with the MSLBs (Figure 2a), i.e. without lipoplex, confirming as expected that no passive transport of the DNA across the lipid bilayer occurs during the experimental window.

As can be seen in Figure 2d, the lipoplex composition does indeed influence the overall delivery kinetics, with the Cy5-ssDNA-DOTAP/DOPE lipoplex being the most efficient vector in consistent with previous cell-based studies.[28] To gain insights into the long time lag (up to 60 - 70min) in the Cy5-ssDNA-DOTAP kinetic curve (green), SE(R)RS experiments were repeated with Cy5-ssDNA-DOTAP lipoplex, but now terminated prematurely at 60min time point. In agreement with Figure 2d, no SE(R)RS signals were discernible during the experiment (green spectrum in Figure 2e). However, when the membrane was subsequently disrupted with (1mM) Triton-X, strong SE(R)RS signals from Cy5-ssDNA became detectable (blue spectrum in Figure 2e). It was thus hypothesized that Cy5-ssDNA was predominantly anchored at the membrane lumen within the first 60min interval, thereby preventing it from reaching the plasmonic hot spot

at the bottom of the cavity. To further elucidate this observation, Fluorescence Lifetime Correlation Spectroscopy (FLCS) was used to probe the lipoplex-membrane fusion activities.

5.4.3. Fluorescence Studies of Microcavity Supported lipid bilayer formation and fusion of lipoplex

FLCS was used in support of the SE(R)RS measurements to provide further insights into the lipoplex-mediated delivery process. Prior to OCR experiments, the amenability of FLCS to probe the fusion process for the lipoplex at a free-standing membrane was first assessed by monitoring the diffusion coefficients (DCs) of membrane-bound lipid Atto532-DOPE.Following deposition of MSLBs, reflectance and FLIM imaging (Fig. 3) were used in conjunction with z-scanning to precisely locate the suspended lipid bilayer at the center of the cavities. Point FLCS measurements were then performed to determine the lateral DCs of Atto532-DOPE, before and after incubation with Cy5-ssDNA-DOTAP-lipoplexes. The DCs of labeled Atto532-DOPE, thus obtained, are displayed in Table 1.

Prior to incubation with lipoplex, the diffusivity of Atto532-DOPE within the lipid bilayer was determined as 6.0 ± 0.7 $\mu m^2/s$, which decreased to $3.8 \pm 0.9 \mu m^2/s$ post 15 min incubation, before equilibrating at $4.8 \pm 0.2 \mu m^2/s$ by120 min. It should be noted that partial recovery of the DCs toward their initial value is typical of the fusion experiments studied in this report. It is tempting to speculate that this observation stems from the formation of diffusion-limiting negatively-curved nano-domains formed by pairing between the cationic DOTAP-lipid and the anionic DOPS-lipid from the target membrane.[29] Notwithstanding its origin, this result indicates that the fusion of lipoplexes exerts a small but measurable influence on the mobility of lipids. Most importantly, FLCS, consistent with Raman leak tests with DRAQ7 described above, confirms membrane integrity is uncompromised by the lipoplex fusion, which corroborates the SE(R)RS measurements discussed above (see also S2). This is also further confirmed from FLIM imaging of the membrane shown in Figure 3c.

Table 1. Diffusion co-efficient of Atto532-DOPE introduced in the lipid bilayer comprised ofDOPC (51.7 mol%), cholesterol (33.3 mol%), DOPS (8.3 mol%) and SM (6.7 mol%) using LB-LB lipid transfer after fitting. The α co-efficient was approximately 1.0 for all measurements.

Time (min)	D_{DOPE} ($\mu m^2/s$)
0	6.0 ± 0.7
15	3.8 ± 0.9
45	4.0 ± 1.1
60	4.5 ± 1.5
120	4.8 ± 0.2

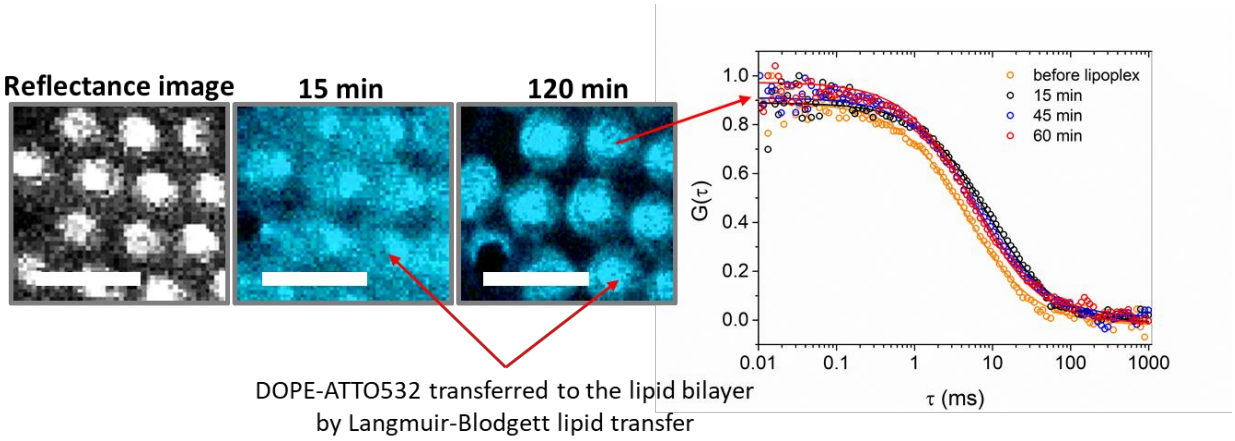

Figure 3. Fluorescence lifetime images (FLIM) of labelled DOPE-ATTO532 in MSLBs comprised of DOPC (51.7 mol%), cholesterol (33.3 mol%), DOPS (8.3 mol%) and SM (6.7 mol%) after exposing the lipid bilayer to lipoplexes at early (15 min) and late (120 min) stage. The reflectance image was in the left was obtained with and OD3 filter and shows the buffer filled microcavities (bright spots). The arrows indicate the point of FLCS measurement at the centre of microcavities. The fitted autocorrelation functions (ACFs) indicate the lateral diffusion of DOPE-ATTO532 within the lipid bilayer before and after exposing to lipoplexes.

Next, the delivery of Cy5-ssDNA by the lipoplexes was investigated. For such a study, the Atto532-DOPE lipid was incorporated into the Cy5-ssDNA-loaded lipoplexes instead of the membrane. In a similar manner as above, point FLCS measurements were performed on the suspended lipid bilayer at the center of the cavities to monitor the evolution of the DCs during fusion. The corresponding FLCS curves are shown in Figure 4. As can be seen in Figure 4a and

4d, the cross correlation G(t) is strong before fusion (at t=0min) confirming co-diffusion of Cy5-ssDNA and Atto532-DOPE. A distinct observation following lipoplex incubation is the diminishing of G(t) at t=15min (Figure 4a and d), which is indicative of lipid-mixing between the docked lipoplex and the membrane when the Atto532-DOPE lipid no longer associated with the lipoplex (an hence Cy5-ssDNA). To assess the populations of free and bound Cy5-ssDNA, the autocorrelation G(t) (Figure 4b - c and 4e - f) were fitted using a 2D-diffusion equation (Seq1), and as a control reference, the diffusivity of free Cy5-ssDNA in PBS (pH 7.4) was also acquired and estimated to be approximately 170 $\mu m^2/s$ (see S4).

Cy5-ssDNA-DOTAP lipoplex

Cy5-ssDNA-DOTAP/DOPE lipoplex

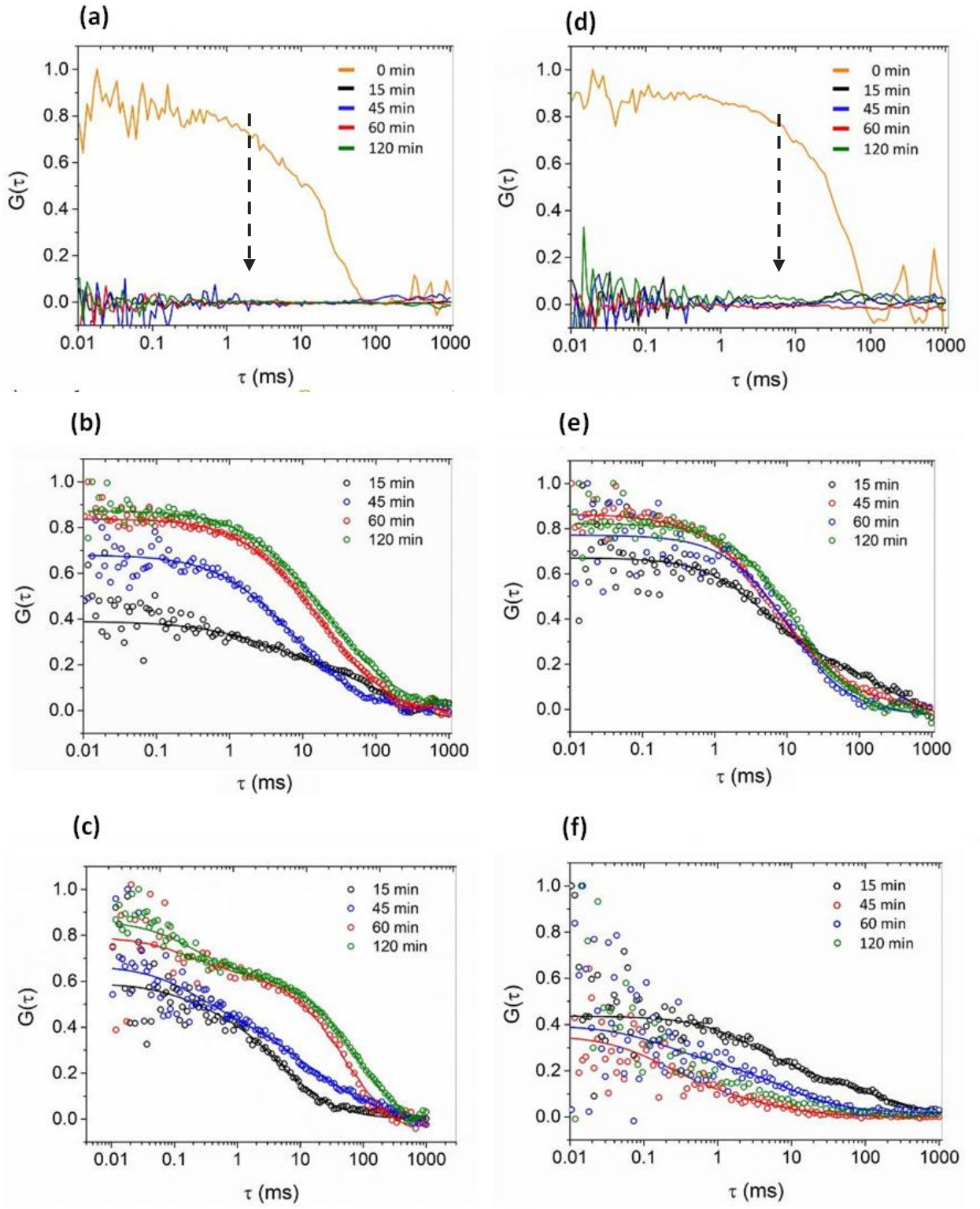

Figure 4. Cross-correlation and auto-correlation traces show fusion of Cy5-ssDNA-DOTAP- and Cy5-ssDNA-DOTAP/DOPE lipoplexes to target membrane. Both lipoplexes are doped with Atto532-DOPE lipid for lipix-mixing assay. Figures on the left column, i.e. (a), (b), and (c), correspond to Cy5-ssDNA-DOTAP lipoplex, while the right column, i.e. (d), (e), and (f) Cy5-ssDNA-DOTAP/DOPE lipoplex. The cross-correlation curves shown in (a) and (d) show lipid-mixing at t=15min and onward for both lipoplex. (b) and (e) correspond to auto-correlation traces of Atto532-DOPE lipids in DOTAP- and DOTAP/DOPE lipoplex, respectively.(c) and (e) auto-correlation traces for Cy5-ssDNA, i.e. the OC.

Table 2 shows the DCs of Atto532-DOPE and Cy5-ssDNA assembled into both DOTAP- and DOTAP/DOPE-lipoplex. Typically, the DCs for the Atto532-DOPE lipid fluctuated during fusion between t=15min and 60min regardless of the lipoplex composition. This can be attributed to the unpredictable residence time of the Atto532-DOPE lipids within the detection volume as they occasionally encountered, and diffused around the 3D structure of the fusing lipoplexes[30]. As with the case shown in Figure 3, the DCs for the fast Atto532-DOPE diffusion component (5.30$\mu m^2/s$ and 2.2$\mu m^2/s$ for DOTAP- and DOTAP/DOPE-lipoplex respectively) at 120minonly partially recovers to its initial value (9.5$\mu m^2/s$ and 5.2$\mu m^2/s$ for DOTAP- and DOTAP/DOPE-lipoplex respectively at t=15min). This is again speculated to be due to the formation of negatively-curved nano-domains triggered by DOTAP-DOPS pairing. Additionally, the two lipoplexes also contrast each with other in terms of the number of diffusion components. While the DCs for DOTAP-lipoplex comprise of two components, those for DOTAP/DOPE lipoplex are predominantly single-component, implying the absence of mixed phases once the lipoplex has incorporated into the membrane, attributed to the membrane destabilizing effect of DOPE owing to its conical shape.[31, 32]

The DCs for Cy5-ssDNA are more predictable and show opposing trends for both lipoplexes (see table 2). To illustrate this, the ratio %fast/%slow (β) is defined and plotted in Figure 5. As can be seen, the β value for DOTAP-lipoplex began at 0.9 and decreased asymptotically to 0.4 (see blue curve in Figure 4b). On examining the DCs, one can observe the presence of two Cy5-ssDNA species; solution phase (unbound) species (D_{fast}=170$\mu m^2/s$) and membrane-bound species (D_{slow}=0.2 - 1.8$\mu m^2/s$). At t=120min, about 70% of the Cy5-ssDNA is membrane-bound, i.e. β=0.4. On the other hand, the β value for DOTAP/DOPE-lipoplex was initially 1.5, followed by a temporary decrease to 1.0 before reaching 2.3 (see red curve in Figure 5). It should be noted that the high β value of 1.5 at t=15min corresponds to a fusion stage, known as Hemifusion-Diaphragm

(HD) in which lipid-mixing between the docked DOTAP/DOPE-lipoplex with the membrane has led to pore formation,[33] i.e. the Cy5-ssDNA remained trapped inside the lipoplex. This is evident from the low DCs of the trapped Cy5-ssDNA at t=15min time point, and the concomitant reduction of G(t) to zero(see Figure 4d). According to table 2, only about 30% of Cy5-ssDNA remained anchored to the membrane when DOPE was added to the lipoplex formulation.

Table 2. Diffusion coefficients of Cy5-ssDNA and Atto532-DOPE as measured from the lipid bilayer comprised of DOPC (51.7 mol%), cholesterol (33.3 mol%), DOPS (8.3 mol%) and SM (6.7 mol%). The upper sub-table shows DCs for Cy5-ssDNA-DOTAP-lipoplex, and the lower sub-table Cy5-ssDNA-DOTAP/DOPE lipoplex. Excitation wavelengths for Cy5-ssDNA and Atto532-DOPE are 640nm, and 532nm respectively. All measurements were carried out with a water-immersion lens, NA 1.2 UPlanS Apo 60 x 1.2 CC1.48, Olympus.

DOTAP-lipoplex

	D_{DOPE} ($\mu m^2/s$)		%DOPE Pop		D_{ssDNA} ($\mu m^2/s$)		%DNA Pop	
Time (min)	D_{fast}	D_{slow}	%fast	%slow	D_{fast}	D_{slow}	%fast	%slow
15	9.5 ± 0.56	0.21 ± 0.10	25 ± 10	75 ± 10	175.0 ± 25.5	1.80 ± 0.28	48 ± 15	52 ± 15
45	4.10 ± 45	0.55 ± 0.20	70 ± 15	30 ± 15	170.2 ± 17.3	1.18 ± 0.66	34 ± 9	66 ± 9
60	3.01 ± 0.56	0.26 ± 0.11	46 ± 20	54 ± 20	175.3 ± 15.2	0.72 ± 0.36	30 ± 10	70 ± 10
120	5.30 ± 0.28	0.50 ± 0.25	38 ± 3	62 ± 3	170.5 ± 10.7	0.29 ± 0.05	29 ± 4	71 ± 4

Cy5-ssDNA-DOTAP/DOPE-lipoplex

	D_{DOPE} ($\mu m^2/s$)		%DOPE Pop		D_{ssDNA} ($\mu m^2/s$)		%DNA Pop	
Time (min)	D_{fast}	D_{slow}	%fast	%slow	D_{fast}	D_{slow}	%fast	%slow
15	5.2 ± 1.7	0.5 ± 0.2	50 ± 10	50 ± 10	12.0 ± 2.8	0.4 ± 0.2	60 ± 15	40 ± 12
45	3.4 ± 0.8	-	100	-	170.1 ± 10.5	2.7 ± 1.2	51 ± 19	49 ± 19
60	2.4 ± 0.3	-	100	-	170.2 ± 8.8	3.3 ± 0.3	70 ± 10	30 ± 10
120	2.2 ± 0.2	-	100	-	168.4 ± 9.8	3.6 ± 0.5	70 ± 9	30 ± 9

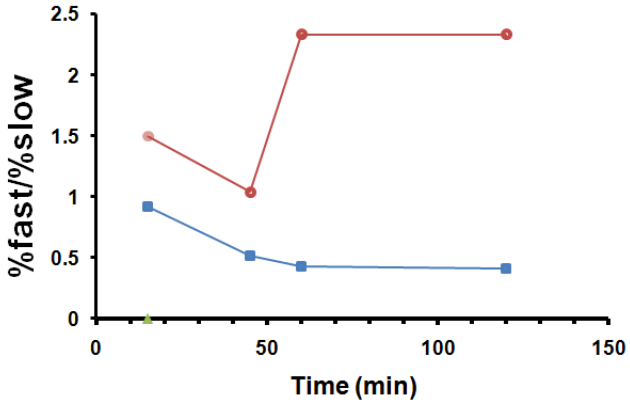

Figure 5. Time trace of β (ratio of Cy5-ssDNA fast-diffusing to slow-diffusing component, %fast/%slow) for DOTAP-lipoplex (blue) and DOTAP/DOPE-lipoplex (red). β values for DOTAP-lipoplex decrease from 0.9 to 0.5 asymptotically, suggesting the majority of the Cy5-ssDNA is bound. In contrast, β values for DOTAP/DOPE-lipoplex commence at 1.5, and decrease to 1.0 before reaching a plateau at 2.3. The β value at t=15min corresponds to the Hemifusion-Diaphragm (HD) fusion stage.

5.4.4. Fusion of membrane with fluorescently-labelled lipoplexes

To visualize the fusion process, FLIM images of the Atto532-DOPE distributions in the membrane spanning over the cavity apertures were acquired. Representative images are shown in Figure 6a and 6b, that depict the distribution dynamic for DOTAP- and DOTAP/DOPE-lipoplex respectively. In the case of DOTAP-lipoplex, the distribution of Atto532-DOPE appears granular over the cavities (circled) between t=15min - 60min, before transitioning to a relatively more diffusive and homogeneous distribution at t=120min. These speckled features are attributed to regions where Atto532-DOPE lipids resided longer as they diffused into or around the 3D volume of fused lipoplexes.[30]Eventually, as more lipoplexes collapse into the membrane at t=120min, Atto532-DOPE distribution becomes relatively more homogenous. Similar dynamics are observed for the DOTAP/DOPE lipoplex (Figure 6b) except the transition is faster and Atto532-DOPE appears more uniformly distributed earlier on in the sequence. This implies an enhanced fusion rate for this liposome formulation attributed to the membrane de-stabilizing effect of the DOPE lipids.[31] This observation also agrees well with the SE(R)RS response curves shown in Figure 2d, in which OC delivery occurred sooner with DOTAP/DOPE lipoplex.

(a) Cy5-ssDNA-DOTAP lipoplex

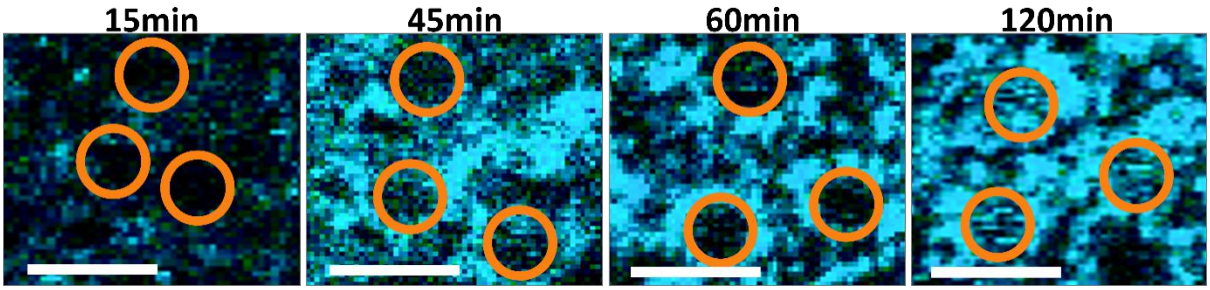

(b) Cy5-ssDNA-DOTAP/DOPE lipoplex

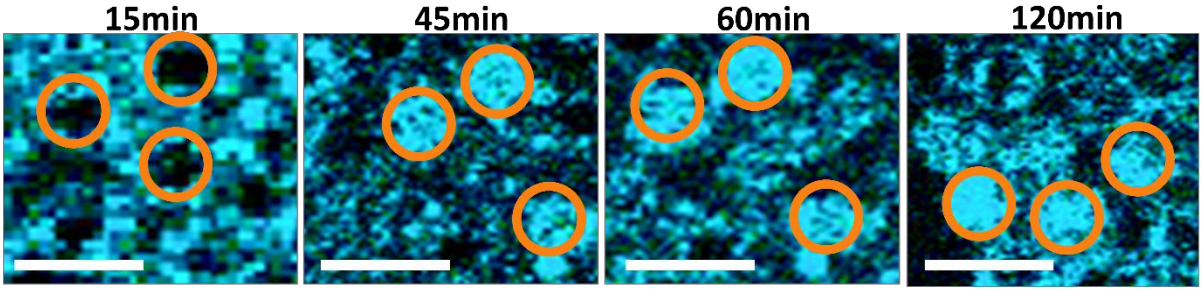

Figure 6. Fluorescence lifetime images (FLIM) showing the distribution of Atto532-DOPE lipids in membrane suspended over the cavity apertures. (a) depicts the dynamical changes of Atto-532-DOPE distribution when Cy5-ssDNA-DOTAP-lipoplex is fused to the membrane. Atto532-DOPE became relatively more homogeneous at t=120min. (b) depicts Atto532-DOPE distribution when Cy5-ssDNA-DOTAP/DOPE lipoplex fused with the membrane. In contrast to the case of DOTAP-lipoplex, Atto532-DOPE becomes more homogenously distributed at an earlier time point, when DOPE is included in the lipoplex. Membranes used in these experiments were deposited on a PDMS cavity array with a 2μm pore size. Scale bar is 3μm.

5.5.Discussion

5.5.1. Endosomal escape mechanism as a multi-step process

The cell membrane is generally impermeable to most large molecules, including to therapeutic oligonucleotides, which have the additional disadvantage in this regard, of being negatively charged. Where large molecules are permeable, the majority of such species penetrate the membrane through activated mechanisms particularly endocytosis, which eventually leads them to the abyss of endosomal entrapment. Unfortunately, the bottleneck of extremely low endosomal-escape rate has long hindered progress in intracellular therapy; sufficient molecules must break out of endosome in order to elicit therapeutic effects. To this end, various EE schemes have since

been studied, to facilitate delivery including sponge effect,[34, 35] flip-flop, and the use of pH-sensitive cell-penetrating peptide.[36]

Whereas transfection assays are normally used to assess the delivery efficiency of a vector, the method is essentially blind to EE as many compounding factors can influence expression level, e.g. cell-state, generation, mechanism of release of oligonucleotide in the endosome.[9]To overcome the rate-limiting EE challenges in intracellular delivery, a direct means to probe EE must be devised to enable informed decisions during the rational design of nanocarrier. To this end, the objective of the current study is two-fold. Firstly, the possibility of a high-throughput photonic-based endosomal-escape assay conducive for rational nanocarrier design approach was explored based on a bio-mimetic endosomal membrane model. As described above, Urban M. et al. previously proposed suspended membrane over pore as a potential HTS platform for permeability study,[19] but the sensitive membrane area (~80nm) is not compatible with atypical vector's size (100-300nm). The platform described herein on the other hand, and as shown in Figure 1a - d, allows for stable lipid membrane to be spanned over large pore diameters (500nm to 5μm).[22]

Secondly, oligonucleotide release at the fusing site was studied. The current study focused primarily on cationic lipid-based nano-carrier, or lipoplex, because of its wide application as a non-viral gene vectors as well as its clinical importance.[28, 37, 38]However, in spite of the many well-documented reports on this particular vector, very little is known about the exactly mechanism through which the oligonucleotide cargo become completely dissociated from the fusing site, and subsequently enter the cytoplasm.[18, 39] In the case of cationic lipoplex, it was proposed that the release of OC was a result of neutralization of the cationic lipids from the lipoplex by the anionic lipids from the target membrane.[40] However, previous studies (e,g, by Olivier Le Bihan, et al,) on lipoplex-mediated transfection have found no correlation between the extent of fusion(in terms of lipid-mixing) and gene expressionlevel.[14] This observation thus hints at more complex interactions between the cargo and the fusing lipid membranes.

The current study intends to probe OCR with a membrane model. To mimic a typical mammalian endosomal membrane as closely as possible, a quaternary membrane composition DOPS/DOPC/SM/Chol was used at a molar ratio of 8:52:7:33[25]. The inclusion of DOPS has been

shown to be essential in enhancing lipoplex-membrane binding fusion.[41]It should be stressed that the use of a symmetric lipid bilayer (i.e. identical lipid composition for both leaflets) here also renders the current study more relevant to pathological membranes.[42]Another important consideration for the experiments herein is the stability of the partitioning membrane between the cavity chamber and the aqueous exterior. To establish this is stable during our experimental window, EIS measurements demonstrated that the membrane remained intact for at least 3hrs, which exceed the length of most experiments (~2hrs) carried out here. Proper sealing of the membrane-bearing cavity is equally crucial and was verified by a negative control study against a membrane impermeable probe DRAQ7 (see Figure 1d).

Having established the integrity and impermeability of the lipid bilayer at the MSLB, two types of lipoplexes were examined in this study: DOTAP-lipoplex and DOTAP/DOPE lipoplex. DOTAP is a common transfection re-agent, and DOPE is well documented as a 'helper-lipid' that enhances delivery efficiency by promoting hemifusion stalk as well as inverted hexagonal phase due to its conical-shape.[43, 44, 45, 46] A negative control study was also carried out with naked Cy5-ssDNA. As shown in Figure 2b and c, the arrival of the released Cy5-ssDNA to the bottom (~175nm away from the suspended membrane) of the cavity where the plasmonic hot-spots reside was readily monitored via the intense SE(R)RS peak of Cy5 @ 560cm^{-1}, which corresponds to the polymethine-bridge stretching mode.[27, 47]From Figure 2a - c, one can observe distinct delivery dynamics among the three lipoplex species. DOTAP/DOPE (Figure 2c) was the most efficient delivery vehicle whereas unsurprisingly, the naked Cy5-ssDNAdid not permeate the membrane at all.[1] In contrast, 'delivery' of Cy5-ssDNA by the DOTAP-lipoplex commenced only at 60min post administration (see green curve in Figure 2d). This observation corroborates previous cell-based assays, which showed a 2×or more improvement in EE rate when DOPE is included in the lipoplex formulation.[43]As mentioned above, delayed release of OC from the endosome when lipoplex fusion was expected was not uncommon in cell-transfection experiments.[12, 14, 48] Yet, the exact mechanism of OCR has been overlooked.[18, 39]To this end, the time lag in OC delivery with DOTAP-lipoplex were examined further by repeating the SE(R)RS experiments up to the 60min time point, i.e. before SE(R)RS signals became discernible. As before, no SE(R)RS signals were discernible during the experiment (green spectrum in Figure 2e). However, when the membrane was subsequently disrupted with (1mM) Triton-X, strong SE(R)RS signals from Cy5-ssDNA

became detectable (blue spectrum in Figure 2e). This suggests the delay in DOTAP-lipoplex mediated OCR was likely caused by the Cy5-ssDNA being arrested at the membrane, preventing it from entering the cavity where it was able to reach the plasmonic hot spot. It is important to emphasize that for SE(R)RS signals to be detectable, it was demonstrated that the Cy5-ssDNA molecules must be fully dislodged from the lipoplex (see S3). Absence of SERRS from the lipoplex boundCy5-ssDNA is attributed to volume exclusion (the lipoplexes are about 120nm in size) of the lipoplex particles from the plasmonic hot-spots. This observation also demonstrates the power of the novel plasmonic assay approach.

To further investigate the role of membrane in oligonucleotide release, the techniques of FLCCS and FLCS were employed. The Cy5-ssDNA-loaded lipoplexes were labelled with Atto532-DOPE to allow for lipid-mixing to be monitored. As can be seen in Figure 4a and 4d, lipid-mixing led to diminishing cross-correlation curves at t = 15min, when the cationic lipids from the lipoplex began to diffuse into the lumen of the target membrane, and thus no longer co-diffused with the Cy5-ssDNA cargo. This indicates two possible fusion stages: the Hemifusion-Diaphragm (HD) stage (where the outer-leaflets fuse but the content remains trapped) and the Fused-State (FS) (where a stable neck stalk and pores formed) and cargo is released.[33]On the basis of the fast diffusion-components of Cy5-ssDNA (D_{fast} under D_{ssDNA} in table 2), one can conclude the DOTAP/DOPE-lipoplex was at the HD stage as the OC predominantly remained trapped (D_{fast} = 12μm^2/s) albeit lipid-mixing had occurred, while DOTAP-lipoplex in FS stage where some free Cy5-ssDNA 'leaking' out via the fusion pores (D_{fast} = 170μm^2/s @ 30% fraction) could be observed. These fusion stages are also shown in Figure7c with respect to the OCR curves. From this point onward, the release kinetics for both lipoplexes proceeds in a markedly different way. Particularly, the OCR kinetic curve for DOTAP-lipoplex (the green curve) which exhibits a sigmoidal trend with a lag-time of about 75min. To fully understand the OCR dynamic, a 2-step kinetic reaction scheme as employed by Bentz in his study of vesicle fusion,[49](see Figure 7b) is used to describe the transfer of trapped oligonucleotide, $X_o(t)$, to the membrane lumen, $X_{OC\text{-}bound}(t)$, and finally the interior of the cavity, $X_{OC\text{-}free}(t)$.Initial attempts to model the sigmoidal curve as a simple 2-step 1st-order-process failed to replicate the long lag-time observed. It is therefore concluded that the OCR must be nonlinear and gradual between t = 15min - 60min, before increasing abruptly, i.e. before $X_o(t)$ decreasing abruptly at 60min. This was attributed to the fact that OCR was more rapid with

decreasing lipoplex size (FS_b stage in Figure 7c) as observed in molecular simulations.[50]This is further substantiated by the Atto532-DOPE (Figure 6a) images taken of the Cy5-ssDNA-DOTAP-lipoplex fused membrane patches over the cavity apertures. They typically showed a transition from granular features between 15min - 60min to homogeneity at t = 120min (C-stage in Figure 7c). The speckled features are tentatively attributed to increased residence time of the Atto532-DOPE lipids within the confocal volume whenever they encountered a fused lipoplex and diffused around its 3D geometry.[30]

Next, to gain insights into the OCR pathway from the DOTAP-lipoplex, the trajectory of the corresponding β (blue curves in Figure 5) values was traced over the course of the fusion process. At t=15min, β (=%fast/%slow) is about 0.9. This however does not indicate that 50% of the oligonucleotide content has already been released. Since Cy5-ssDNAs trapped within a sub-diffraction-limited lipoplex would be 'perceived' as a single particle by FLCS, a small fraction of free Cy5-ssDNA could artificially inflate the β value. As the lipoplex continued to inject its content into the surrounding membrane, β dropped asymptotically to 0.4, indicating an increase in the population of slow-diffusion component (reaching 70% at t=120min), which corresponds to the membrane bound Cy5-ssDNAs. Interestingly, anchoring of oligonucleotide to membrane upon release from a cationic lipoplex was predicted by Bruiniks et al. in their molecular simulation experiments.[50] This was a result of Cy5-ssDNAs failing to fully de-complex from the DOTAP lipids, and therefore remaining bound to the membrane lumen.

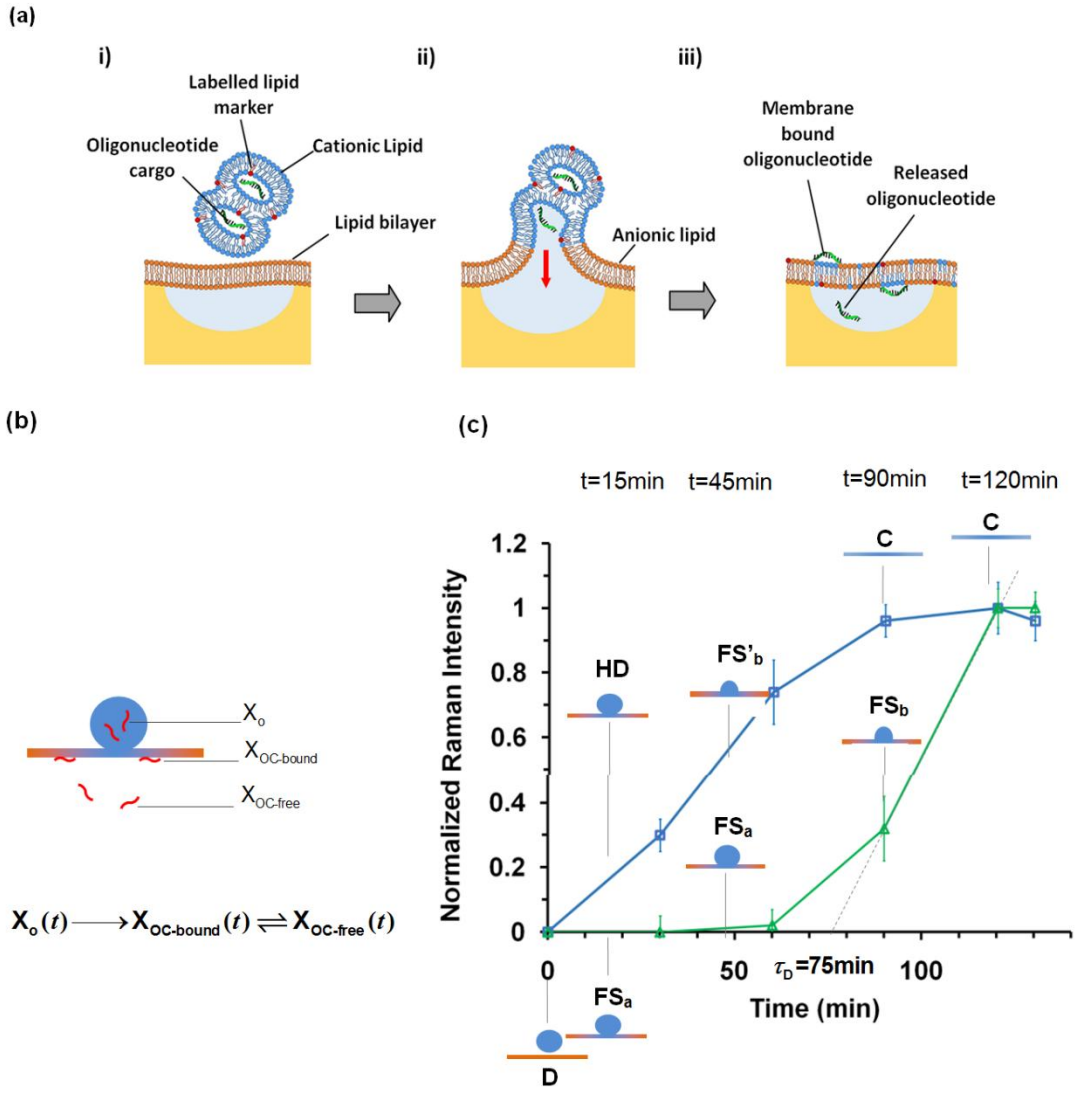

Figure 7. OCR pathway. (a) Schematic showing the sequence of fusion events; (i) lipoplex docking the target membrane; (ii) a fused state where a stable stalk is formed and pore exposes the Cy5-ssDNA fragments (i.e. the OC); (iii) lipoplex fully collapsed into the membrane. Note also the fractions of DNA fragments remained anchored to the membrane. (b) a kinetic reaction scheme showing OCR as a multi-step process; $X_0(t)$ denotes the total amount of Cy5-ssDNA fragments trapped within the lipoplexes; $X_{OC\text{-}bound}(t)$ is the total amount of membrane-bound Cy5-ssDNA; $X_{OC\text{-}free}(t)$ fully-released Cy5-ssDNA (c). OCR kinetic curves and the various fusion stages. lag-time of OCR is shown to be 75min. D: docking; HD: Hemifusion-Diaphragm stage; FS_a: slow-releasing fused state; FS_b: fast-releasing fused state; C: lipoplex fully collapsed.

In contrast, no lag-time was observed in DOTAP/DOPE lipoplex mediated oligonucleotide delivery; the OC appeared to be delivered within the first 30min of the experiment. The β value, however, began at 1.5 at t=15min (see red curve in Figure 5), with the corresponding Cy5-ssDNA diffusion-rates ranging between 0.4 to 12.0μm^2/s (much slower compared to free Cy5-ssDNA species). This suggests a HD stage in which lipid-mixing occurred but without the formation of stable pores that connected the trapped oligonucleotide content to the interior of the cavity. The β value then dropped to 1.0 before rapidly reaching a plateau at 2.3, which is accompanied by a fast Cy5-ssDNA diffusing component (170μm^2/s, see Table 2), signifying a FS stage where the majority (up to 70%) of the oligonucleotides departing the lipoplex are completely released, i.e. %fast > %slow. This scenario is aptly reflected in the FLIM image shown in Figure 6b, which depicts a rapid transition of Atto532-DOPE lipids from a granular distribution (at t=15min) over the cavity apertures to more homogeneously distributed ones (at t=45-120min). Two factors may contribute to the improved transfection efficiency of DOTAP/DOPE lipoplex. Firstly, a reduced concentration of DOTAP in the lipoplex facilitates de-complexing of OC from the lipoplex/membrane. Secondly, the introduction of DOPE (the so-called helper lipid) enhances membrane fluidity, and aids de-stabilization of the lipoplex, encouraging stalk formation.[31, 32] Furthermore, the inverted hexagonal phase induced by DOPE is also likely to play a role in the release of OC to some extent as suggested by Zelphati O. et al. and Du Z. et al.[28, 43] Such a de-stabilizing effect of DOPE is evident from the absence of slow Atto532-DOPE diffusion component at t=120min for DOTAP/DOPE lipoplex mediated OCR (see Table 2) as compared to the case of DOTAP-lipoplex where different membrane domains persist following delivery as evident from the presence of two diffusion components.

5.6. Conclusions

In conclusion, the current study reveals the mechanism of OCR in lipoplex mediated transfection, shedding light on the interplay between fusion and OCR. The trade off between the stability of a DOTAP-based lipoplex and the ability of the OC to sufficiently de-complex from the membrane lumen must be considered in a transfection experiment. Other functional component, such as a helper lipid or peptide, may be required in the composition of a cationic vector in order to assist OCR. More importantly, while cell-based HTS techniques have conventionally been the cornerstone for drug-delivery assay in the pharmaceutical industry, the high average cost/sample

($1,000) render their use in vector development prohibitively uneconomical given the ever increasingly-complex design-landscape of a delivery nanocarrier.[51] Crucially, this study was enabled by a new approach to membrane permeability assay that monitors cargo arrival to the plasmonic field within the microcavity interior and below the lipid membrane, providing signal enhancement to the cargo only after it has permeated the lipid membrane. The assay, presented in microfluidic format, opens up the prospect of high-throughput and sensitive low-cost cell-free alterative to understanding cell membrane permeation dynamics and mechanistic insights into cargo delivery in drug delivery design.

5.7. Supporting Information

Supporting information can be found in the Appendix D.

5.8. References

(1) Dowdy SF. Overcoming cellular barriers for RNA therapeutics. Nat Biotech 2017, 35, 222-229.
(2) Stevenson FK. DNA vaccines against cancer: from genes to therapy. Ann Oncol 1999, 10, 1413-1418.
(3) Lopes A, Vandermeulen G, Préat V. Cancer DNA vaccines: current preclinical and clinical developments and future perspectives. J Exp Clin Cancer Res 2019, 38,
(4) Tambuyzer E, Vandendriessche B, Austin CP, Brooks PJ, Larsson K, Needleman KIM, Valentine J, Davies K, Groft SC, Preti R, Oprea TI, Prunotto M. Therapies for rare diseases: therapeutic modalities, progress and challenges ahead. Nat Rev 2020, 19, 93-1111.
(5) Puschnik AS, Majzoub K, Ooi YS, Carette JE. A CRISPR toolbox to study virus–host interactions. Nat Rev 2017, 15, 351-364.
(6) Kennedy EM, Cullen BR. Gene Editing: A New Tool for Viral Disease. Ann Rev Med 2017, 68, 401-411.
(7) European Medicines Agency. Quality, preclinical and clinical aspects of gene therapy medicinal products.http://www.ema.europa.eu/ema/index.jsp?curl=pages/regulation/general/general_content_000873.jsp&mid=WC0b01ac058002956b.
(8) Rinkenauer AC, Vollrath A, Schallon A, Tauhardt L, Kempe K, Schubert S, Fischer D, Schubert US. Parallel High-Throughput Screening of Polymer Vectors for Nonviral Gene Delivery: Evaluation of Structure−Property Relationships of Transfection. ACS Comb Sci 2013, 15,
(9) Homann S, Hofmann C, Gorin AM, Nguyen HCX, Huynh D, Hamid P, Maithel N, Yacoubian V, Mu W, Kossyvakis A, Roy SS, Yang OO, Kelesidis T. A novel rapid and reproducible flow cytometric method for optimization of transfection efficiency in cells. PLOS One 2017, 12, e0182941.
(10) Liu F, Huang L. Development of non-viral vectors for systemic gene delivery. J Control Release 2002, 78, 259-266.
(11) Degors IMS, Wang C, Rehman ZU, Zuhorn IS. Carriers Break Barriers in Drug Delivery: Endocytosis and Endosomal Escape of Gene Delivery Vectors. Acc Chem Res 2019, 52.
(12) Elouahabi A, Ruysschaert J-M. Formation and Intracellular Trafficking of Lipoplexes and Polyplexes. Mol Ther 2005, 11, 336-347.
(13) Stegmann T, Legendre J-Y. Gene transfer mediated by cationic lipids: lack of a correlation between lipid mixing and transfection. Biochim Biophys Acta 1991, 1325,

(14) Bihan OL, Chevre R, Mornet S, Garnier B, Pitard B, Lambert O. Probing the in vitro mechanism of action of cationic lipid/DNA lipoplexes at a nanometric scale. Nucleic Acids Res 2011, 39,
(15) Hong S, Bielinska AU, Mecke A, Keszler B, Beals JL, Shi X, Balogh L, Orr BG, Jr. JRB, Holl MMB. Interaction of Poly(amidoamine) Dendrimers with Supported Lipid Bilayers and Cells: Hole Formation and the Relation to Transport. Bioconjugate Chem 2004, 15, 774-782.
(16) Deshayes S, Morris M, Divita G, Heitz F. Interactions of primary amphipathic cell penetrating peptides with model membranes: consequences on the mechanisms of intracellular delivery of therapeutics. Curr Pharm Des 2005, 11, 3629-3638.
(17) Chan YH, Lengerich Bv, Boxer SG. Eff ects of linker sequences on vesicle fusion mediated by lipid-anchored DNA oligonucleotides . PNAS 2009, 106, 979-984.
(18) Diao J, Su Z, Ishitsuka Y, Lu B, Lee KS, Lai Y, Shin Y-K, Ha T. A single-vesicle content mixing assay for SNARE-mediated membrane fusion. Nat Commun 2010, 1,
(19) Urban M, Kleefen A, Mukherjee N, Seelheim P, Windschiegl B, Brüggen MVd, Koçer A, Tampé R. Highly Parallel Transport Recordings on a Membrane-on-Nanopore Chip at Single Molecule Resolution. Nano Lett 2014, 14, 1674-1680.
(20) Im H, Wittenberg NJ, Lesuffleur A, Lindquist NC, Oh S-H. Membrane protein biosensing with plasmonic nanopore arrays and pore-spanning lipid membranes. Chem Sci 2010, 1,
(21) Berselli GB, Sarangi NK, Ramadurai S, Murphy PV, Keyes TE. Microcavity-Supported Lipid Membranes: Versatile Platforms for Building Asymmetric Lipid Bilayers and for Protein Recognition. ACS Appl Bio Mat 2019, 2, 3404-3417.
(22) Basit H, Gaul V, Maher S, Foster RJ, Keyes TE. Aqueous-filled polymer microcavity arrays: versatile & stable lipid bilayer platforms offering high lateral mobility to incorporated membrane proteins. Analyst 2015, 140,
(23) Oćwieja M, Maciejewska-Prończuka J, Adamczyk Z, Roman M. Formation of positively charged gold nanoparticle monolayers on silica sensors. J Colloid Interface Sci 2017, 501, 192-201.
(24) Shervedani R, Farahbakhsh A, Bagherzadeh M. Functionalization of gold cysteamine self-assembled monolayer with ethylenediaminetetraacetic acid as a novel nanosensor. Anal Chim Acta 2007, 587, 254-262.
(25) Nelson GJ. Lipid composition of erythrocytes in various mammalian species. Biochim Biophys Acta, Lipids Lipid Metab 1967, 144,
(26) Cole RM, Baumberg JJ, Abajo FJGd, Mahajan S, Abdelsalam M, Bartlett PN. Understanding Plasmons in Nanoscale Voids. Nano Lett 2007, 7, 2094-2100.
(27) Mahajan S, Baumberg JJ, Russella AE, Bartlett PN. Reproducible SERRS from structured gold surfaces. Phys Chem Chem Phys 2007, 9, 6016-6020.
(28) Zelphati O, Jr FCS. Mechanism of oligonucleotide release from cationic liposomes. PNAS 1996, 93, 11493-11498.
(29) Schubert T, Römer W. How synthetic membrane systems contribute to the understanding of lipid-driven endocytosis. Biochim Biophys Acta 2015, 1853,
(30) Schwenen LLG, Hubrich R, Milovanovic D, Geil B, Yang J, Kros A, Jahn R, Steinem C. Resolving single membrane fusion events on planar pore-spanning membranes. Sci Rep 2015, 5,
(31) Farhood H, Serbina N, L.Huang. The role of dioleoyl phosphatidylethanolamine in cationic liposome mediated gene transfer. BBA 1995, 1235, 289-295.
(32) Felgner JH, Kumar R, Sridhar CN, Wheeler CJ, Tsai YJ, Border R, Ramsey P, Martin M, Felgner PL. Enhanced gene delivery and mechanism studies with a novel series of cationic lipid formulations. J Bio Chem 1994, 269, 2550-2561.
(33) Marrink SJ, Mark AE. The Mechanism of Vesicle Fusion as Revealed by Molecular Dynamics Simulations. JACS 2003, 125, 11144-11145.
(34) Pack DW, Hoffman AS, Pun S, Stayton PS. Design and Development of Polymers for Gene Delivery Nat Rev 2005, 4, 581-593.
(35) Sonawane N, Szoka FJ, Verkman A. Chloride accumulation and swelling in endosomes enhances DNA transfer by polyamine-DNA polyplexes. J Bio Chem 2003, 278, 44826-44831.

(36) Simões S, Slepushkin V, Pires P, Gaspar R, Lima MPd, Düzgüneş N. Mechanisms of gene transfer mediated by lipoplexes associated with targeting ligands or pH-sensitive peptides. Gene Ther 1999, 6, 1798-1807.
(37) Lechanteur A, Sanna V, Duchemin A, Evrard B, Mottet D, Piel G. Cationic Liposomes Carrying siRNA: Impact of Lipid Composition on Physicochemical Properties, Cytotoxicity and Endosomal Escape. Nanomaterials 2018, 8, 270.
(38) Semple SC, Akinc A, Chen J, Sandhu AP, Mui BL, Cho CK, Sah DWY, Stebbing D, Crosley EJ, Yaworski E, Hafez IM, Dorkin JR, Qin J, Lam K, Rajeev KG, Wong KF, Jeffs LB, Nechev L, Eisenhardt ML, Jayaraman M, Kazem M, Maier MA, Srinivasulu M, Weinstein MJ, Chen Q, Alvarez R, Barros SA, De S, Klimuk SK, Borland T, Kosovrasti V, Cantley WL, Tam YK, Manoharan M, Ciufolini MA, Tracy MA, Fougerolles Ad, MacLachlan I, Cullis PR, Madden TD, Hope MJ. Rational design of cationic lipids for siRNA delivery. Nat Biotech 2009, 28, 172-176.
(39) Mochizuki S, Kanegae N, Nishina K, Kamikawa Y, Koiwai K, Masunaga H, Sakurai K. The role of the helper lipid dioleoylphosphatidylethanolamine (DOPE) for DNA transfection cooperating with a cationic lipid bearing ethylenediamine. Biochim Biophys Acta 2013, 1828, 412-418.
(40) Hafez I, Maurer N, Cullis P. On the mechanism whereby cationic lipids promote intracellular delivery of polynucleic acids. Gene Ther 2001, 8, 1188-1196.
(41) Berezhnaa S, Schaefer S, Heintzmann R, Jahnz M, Boese G, Deniz A, Schwill P. New effects in polynucleotide release from cationic lipid carriers revealed by confocal imaging, fluorescence cross-correlation spectroscopy and single particle tracking. BBA 2005, 1669, 193-207.
(42) Zalba S, Hagen TLMt. Cell membrane modulation as adjuvant in cancer therapy. Cancer Treat Rev 2017, 52.
(43) Du Z, Munye MM, Tagalakis AD, Manunta MDI, Hart SL. The Role of the Helper Lipid on the DNA Transfection Efficiency of Lipopolyplex Formulations. Sci Rep 2014, 4.
(44) Hart SL. Multifunctional nanocomplexes for gene transfer and gene therapy. Cell Bio Tox 2010, 26, 69-81.
(45) Ewert KK, Ahmad A, Evans HM, Safinya CR. Cationic lipid-DNA complexes for non-viral gene therapy: relating supramolecular structures to cellular pathways. Expert Opin Bio Ther 2005, 5, 33-53.
(46) Wasungu L, Hoekstra D. Cationic lipids, lipoplexes and intracellular delivery of genes. J Control Release 2006, 116, 255-264.
(47) Owens NA, Pinter A, Porter MD. Surface-enhanced resonance Raman scattering for the sensitive detection of a tuberculosis biomarker in human serum. J Raman Spectrosc 2018, 50, 15-25.
(48) Rehman Zu, Hoekstra D, Zuhorn IS. Mechanism of Polyplex- and Lipoplex-Mediated Delivery of Nucleic Acids: Real-Time Visualization of Transient Membrane Destabilization without Endosomal Lysis. ACS Nano 2013, 7, 3767-3777.
(49) Bentz J. Intermediates and kinetics of membrane fusion. Biophys J 1992, 63.
(50). Bruininks BM, Souza PC, Ingolfsson H, Marrink SJ. A molecular view on the escape of lipoplexed DNA from the endosome. Elife 2020, 9, e52012.
(51). Halford B. How DNA-Encoded Libraries Are Revolutionizing Drug Discovery. Chem Eng News 2017.

Chapter 6: Galectin-3 targets the inactive α5β1 integrin to oligomerize and trigger membrane reorganization in a GSLs-dependent manner

6.1. Introduction

Integrins, a family of heterodimeric glycoproteins, of which 24 are known in eukaryotes. They are receptors for extracellular matrix (ECM) molecules such laminin, fibronectin and collagen.1 Integrins consist of a non-covalent linked α and β units comprised of an extracellular domain and a short cytoplasmic tail. They are essential for the normal function of organisms being involved in several cell functions including cell migration, proliferation and apoptosis.2 In addition, integrins are receptors for lectins. Galectins, a component of ECM, are a family of N-glycan-binding proteins that closely interacts with integrins modulating cell adhesion or migration.3 Galectin-3 (Gal3) is a unique member of galectin family, containing a C-terminal carbohydrate recognition domain (CRD) and N-terminal that favours the formation of Gal3 oligomers of the lectin (Figure 6.1a).[4,5] Gal3 binds to carbohydrate groups of glycoproteins at the cell membrane as a monomer. The oligomerization of N-terminus of Gal3 increases its capacity to recruit and interact with GSLs at cell membrane, as shown in Figure 1b.[6]

Evidence has been accumulating that glycoproteins and glycolipids are involved in endocytic uptake of adhesion molecules in a clathrin-independent way, of which the association of Gal3 might be a trigger. Recently, the role of Gal3 in endocytic trafficking has been investigated. For example, oligomerized Gal3 is capable of inducing the formation of narrow membrane invaginations in interactions with glycosphingolipids. The formation of clathrin-independent carries (CLICs) is believed to involve the oligomerization of Gal3 in presence of glycosphingolipids and β1-integrin (

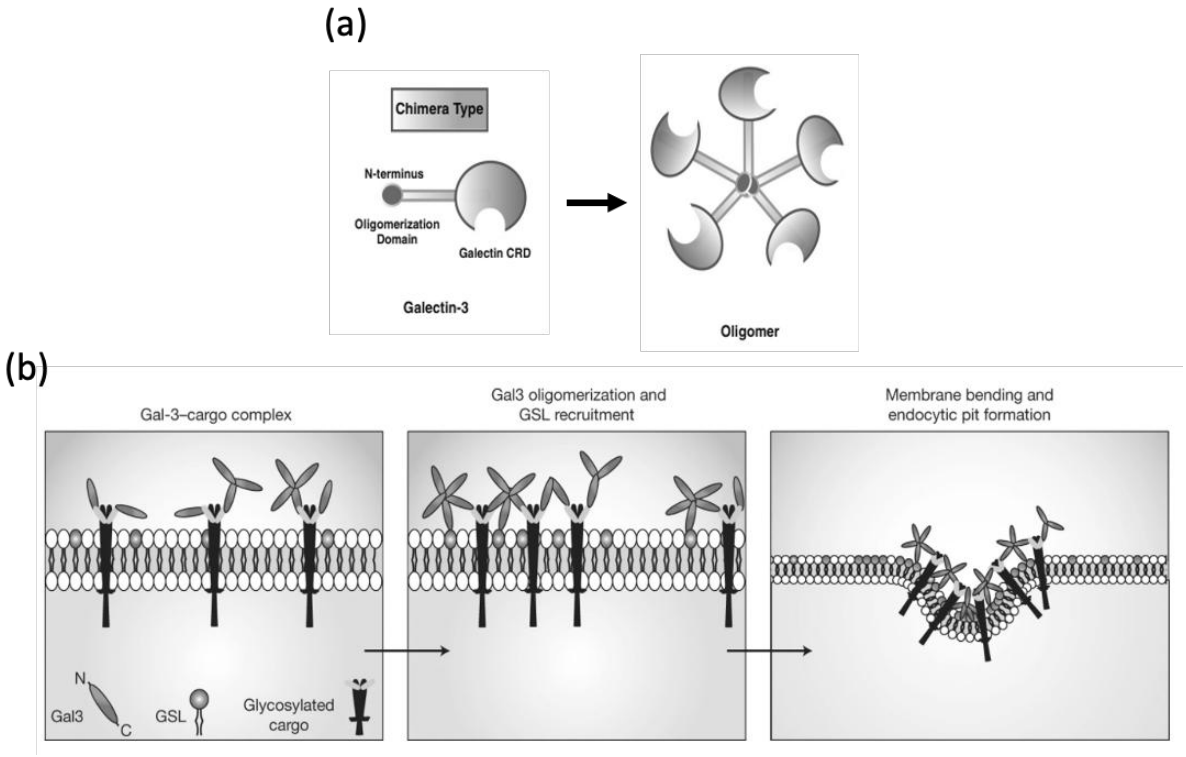

Figure 6.41b) which were not observed in presence of N-terminus truncated Gal3 containing only CRD region.[6] Most of the information related to CLICs was been obtained studying cells. For instance, this process has been observed in breast carcinoma cells where galectin-3 mediates the endocytosis of β1 integrins in presence of glycans and lead to the reduction of integrins in the cell surface.[7] Further evidence was observed as transcytosis across enterocytes in mouse intestine was demonstrated to be mediated though Gal3 binding to the glycoprotein lactotransferrin in a glycosphingolipid-dependent manner.[8] However, the direct role of integrin/GSLs in CLICs still remain to be elucidated.

In this context, this work aims to address the role of integrin galectin interaction and to understand the role of glycolipid and activation of α5β1-integrin in promoting this interaction. This project is ongoing but here, the preliminary results of α5β1-integrin reconstitution and binding of Gal3 are presented. The study was conducted using wild-type galectin-3, here referred to as Gal3, and the truncated at N-terminus of Gal3 and contains only the CRD domain (Gal3ΔNter). Integrin was reconstituted to MSLBs using a two-step method, first integrin was reconstituted into proteoliposomes that was later fused against a pre-deposit lipid monolayer. The preliminary results shown that the diffusion coefficient of reconstituted α5β1-integrin measured by FLCS increased after reaction with Gal3 but were not affected by the Gal3ΔNter. Also, the presence of GLSs enhanced this effect, by increasing the binding of Gal3 and Gal3ΔNter. In addition, the electrochemical results indicate that the binding of Gal to integrin is more dominant when GSLs are present suggesting that Gal3 binds to integrin /GSLs in a cooperative manner. Together, these results indicate that

the platform was effective for modelling GSL-integrin-lectin interactions which enables the advancement of the project into more biological relevant conditions.

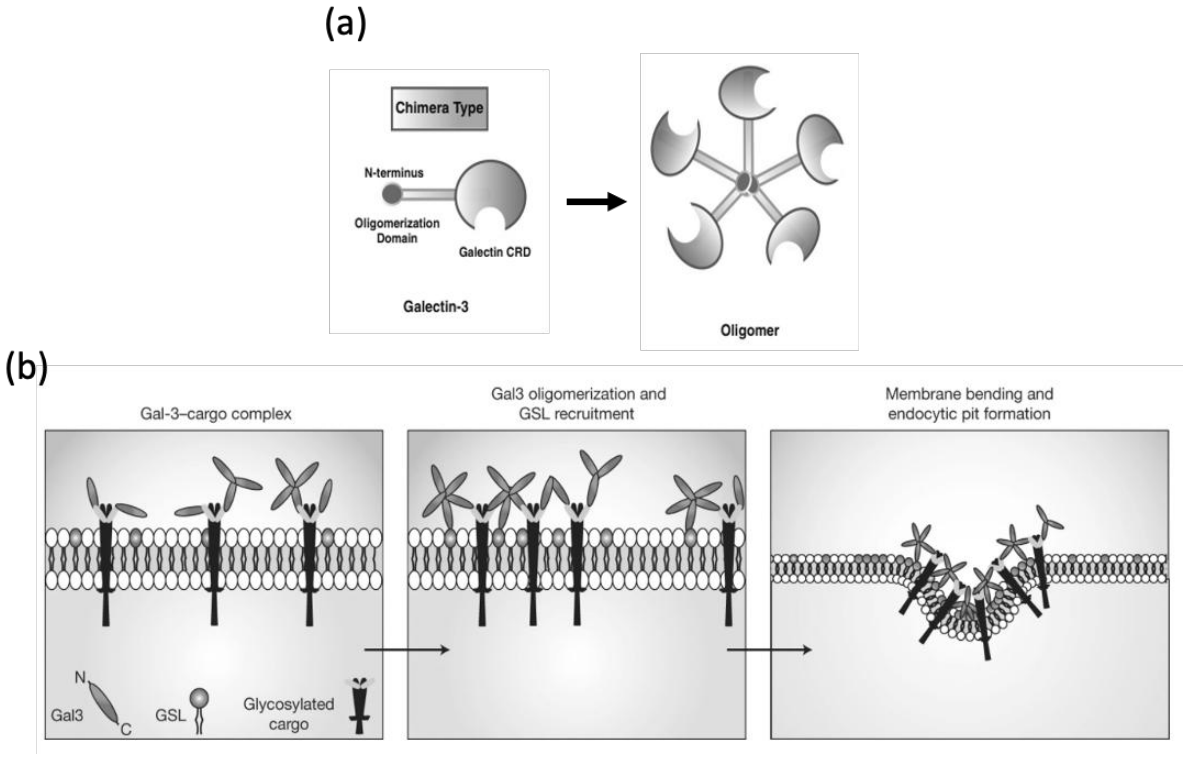

Figure 6.41. (a) Oligomerization of Gal3 occurs through the N-terminus of the lectin. (b) Mechanism proposed for the clathrin independent carrier (CLIC) formation and biogenesis. Monomeric galectin-3 is recruited to membrane by binding to glycosylated cargo proteins, such β_1 integrins. Membrane bound galectin-3 oligomerizes and gains functional GSL binding capacity. Clustering of cargo protein and GSL generates mechanical stress forming endocytic invaginations. Figure reproduced from reference.[6]

6.2. Experimental

6.2.1. Integrin reconstitution into proteoliposomes

Integrin $\alpha_5\beta_1$ was incorporated to proteoliposomes comprised of eggPC/eggPA (90:10) or eggPC/eggPA/GSLs (85:10:5) using detergent-mediated according the protocol used by Johannes' group at the Marie Curie Institute, Paris (FR). Briefly, lipid films were prepared with 18 µL of 10 mg/ml eggPC and 2 µL of 10 mg/ml eggPA in chloroform dried under nitrogen flow and further

dried under vacuum for 1h. For liposomes containing GSLs, 20 µL of brain extracted GSLs (1 mg/ml) was mixed with eggPC and eggPA prior to solvent evaporation. For fluorescence studies, DOPE-ATTO655 was add to the lipid film at concentration of 0.01 (mol %). The lipid film was suspended in 200 µL in TrisHCl (10mM, pH 7.4, NaCl 150 mM) to achieve liposomal concentration of 1 mg/mL Large Unilamellar Vesicles (LUVs) obtained after vortex the lipid film. The liposomes were destabilized with 5 µL Triton X-100 (10% v/v) for approximately 10 minutes. Then, a combination of free labelled and labelled ATTO488-integrin $\alpha_5\beta_1$ was add to obtain a ratio lipid to protein of 10 (w/w). The mixture containing lipids and proteins was allow to equilibrate at room temperature for 10 min before removal of detergent. This was obtained by adding 3 aliquots of 10 mg of hydrated bio-beads with an hour of interval between each addition. Finally, the proteoliposomes were separated from biobeads by using a micropipette. The proteoliposomes were diluted with PBS (pH 7.4) to the final concentration of 0.25 mg/ml and their size distribution was evaluated by DLS. Liposomes and proteoliposomes were analysed by DSL before and after reconstitution of integrin. Proteoliposomes containing labelled DOPE-ATTO655 and ATTO488-$\alpha_5\beta_1$ were characterized by Fluorescence Lifetime Cross-Correlation Spectroscopy (FLCCS).

6.2.2. Gold and PDMS microcavity array preparation

The lipid bilayers were spanned over PDMS and Gold arrays prepared as indicated in the previous chapters. The experiments were conducted in triplicates.

6.2.3. Lipid Bilayer preparation

Pore suspending lipid bilayers containing bacteriorhodopsin were spanned across buffer filled micro-cavity arrays following the method described previously.[9] Briefly, a combination of Langmuir-Blodgett (LB) and vesicle fusion was used. The LB trough (NIMA 102D) was filled with MiliQ water (18.2 $M\Omega.cm^{-1}$) and approximately 50 µL of eggPC (1 mg/mL in chloroform) were deposited onto the air-water interface until surface pressure of >1 mN/m was obtained. Micro-cavity arrays comprised of PDMS or gold were immersed into the LB trough until all of the cavities were submerged completely into the subphase. The chloroform was allowed to evaporate and the resulting lipid monolayer at the air water interface was compressed four times to a surface

pressure of 36 mN/m each time. The micro-cavity array was withdrawn from the trough at a rate of 5 mm/s whilst the surface pressure of the lipids was retained at 32 mN/m to ensure transfer of eggPC monolayer. To assemble upper leaflet of the bilayer and incorporate integrin-$\alpha_5\beta_1$, the face containing the microcavities were exposed to preformed proteoliposomes at 0.25 mg/ml. Substrate was incubate for at 1.5 hours in the dark to allow the protein-bilayer formation. Here, asymmetric lipid bilayer comprised of eggPC//eggPC/PA or eggPC//eggPC/eggPA/GSLs are shown as PC/PA or PC/PA/GSLs for simplicity. The integrity of lipid bilayers was acceded by Fluorescence Lifetime Correlation Spectroscopy (FLCS) and Electrochemical Impedance Spectroscopy (EIS).

6.2.4. Fluorescence Lifetime Imaging and Correlation Spectroscopy

In this work, labelled DOPE-ATTO655, CRD-Alexa647 and Gal3-Alexa647 were excited with 640 nm laser (LDH-P-C-640B (PicoQuant)). Integrin ATTO488-$\alpha_5\beta_1$ was excited with a 532 nm laser (PicoTA laser from Toptica (PicoQuant)). Fluorescence light was collected through a HG670lp AHF/Chroma or HQ550lp AHF/Chroma band pass filter for 640 or 532 nm laser respectively. The lipid bilayer position was determined at the pore of microcavities by z-scanning until the point of maximal fluorescence intensity of labelled DOPE or integrin was found. At this point, the fluorescence intensity of was measured for 30 to 60 seconds per cavity, and replicate data from 20 to 30 cavities were measured per sample. After MSLB preparation, Gal3-Alexa647 or CRD-Alexa647 at designated concentration range were titrated in the microfluidic MSLB device. Each concentration was allowed to equilibrate for at least 30 min. FLCS data was fitted to the 2D or 3D diffusion model as previously described in chapter 2, 3 and 4.

6.2.5. Electrochemical Impedance Spectroscopy

Electrochemical Impedance Spectroscopy (EIS) was performed as previously described in chapter 3. The electrochemical cell was kept in PBS buffer (pH 7.4) and for each concentration of CRD/Gal3 a lag time of ~30 min incubation was maintained before EIS were recorded. From the EIS data, the change in resistance and capacitance values were extracted by fitting the EIS data as previously described in chapter 3. The resistance and capacitance changes are given as there is some batch-to-batch variation in absolute electrochemical values due to the substrate, but absolute

resistance of the membrane was evaluated before study to ensure it confirmed to that expected for stable lipid bilayer.

6.3. Results and Discussion

6.3.1. Incorporation of integrin in proteoliposomes and MSLBs

Integrin $\alpha_5\beta_1$ was incorporated into proteoliposomes comprised of eggPC/eggPA (90:10) or eggPC/eggPA/GSLs (85:10:5) using detergent-mediated protocol. To evaluate the reconstitution of integrin to the proteoliposomes, DOPE-ATTO655 was added to the lipid mixture to permit two laser excitation Fluorescence Lifetime Cross Correlation Spectroscopy (FLCCS). To do so, both liposome and integrin were labelled with fluorescent markers with different excitation wavelengths. Liposomes were tagged with DOPE-ATTO655 prior to the incorporation of labelled $\alpha_5\beta_1$-ATTO488. The Figure 6.2 shows the DLS and FLCS results obtained for the incorporated integrin to proteoliposomes and to the incorporated to MSLBs.

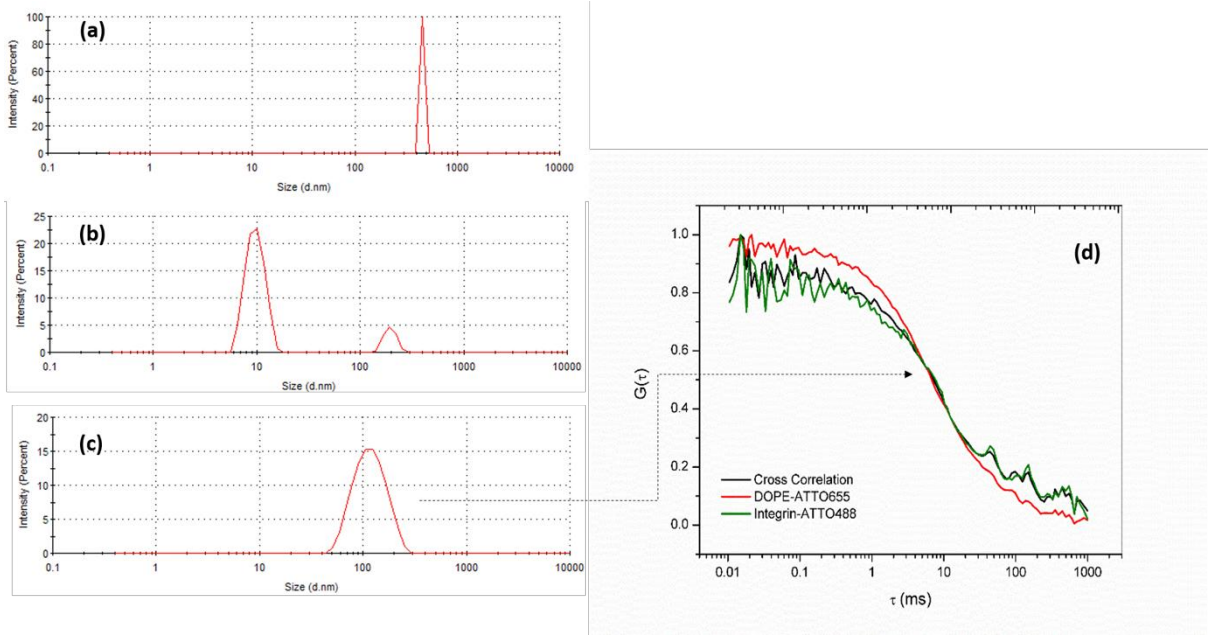

Figure 6.42. Dynamic Light Scattering (DLS) and Auto correlation functions (ACFs) obtained for Fluorescence Lifetime Cross-Correlation Spectroscopy (FLCCS) of proteoliposomes after reconstitution

integrin using two independent fluorophores. DLS represents (a) liposomes after resuspension into solution (a), (b) after destabilization with Triton X-100 and (c) after detergent removal using bio-beads. (d) Shows the FLCCS of integrin and DOPE. The red and the green line represent the labelled ATTO488-$\alpha_5\beta_1$ and DOPE-ATTO655, respectively. The black line indicates the cross-correlation between the two dyes.

Dynamic Light Scattering shows that liposomes resuspended in Tris buffer formed vesicles with diameter of around 500 nm, as indicated in Figure 6.42a. After addition of Triton X-100, the vesicles were disrupted as indicated by the change in the size distribution of the resulting solution of lipids/Triton X-100 (Figure 6.42b). The 3 aliquoted additions of bio-beads and detergent removal, the reconstructed lipid vesicles containing integrin generate proteoliposomes of approximately 120 nm (Figure 6.42c). Using FLCCS, the diffusion of proteoliposomes was evaluated following the dual excitation of labelled integrin-ATTO488 and DOPE-ATTO655 (Figure 6.42d). It can be observed that both molecules shown co-diffusion within the reconstituted proteoliposomes, indicating that integrin was well inserted in the formed liposomes after detergent removal.

6.3.2. Characterization of MSLBs containing α5β1 integrin

We first evaluated the incorporation of integrin $\alpha_5\beta_1$ into MSLBs after sample preparation using the hybrid method of Langmuir-Blodgett lipid deposition followed by proteoliposomes disruption similar to chapter 4. Reconstitution of integrin into MSLB was monitored by FLCS by studying the lateral diffusion of labelled integrin-488. Here, FLCS data was fitted to a 2D model, as described in chapter 4. We observed that after reconstitution to PC/PA bilayers, the diffusion coefficient of labelled ATTO488-$\alpha_5\beta_1$ was 1.8 ± 0.4 $\mu m^2/s$ with α coefficient of 0.86 ± 0.05. The diffusion value of integrin-488 is slightly slower than the diffusivity previously reported for integrin in GUVs, to be 2.6 ± 0.3 $\mu m^2/s$.[10] By comparison Gaul reported platelet integrin αIIbβ3 reconstituted into simple DOPC MSLB exhibited a diffusion coefficient of 2.80 ± 0.59 $\mu m^2/s$ and an alpha value of 1. The diffusion coefficient of the same integrin in "natures own" GUV was 2.5 $\mu m^2/s$ so could be related to the composition of the lipid membrane.[10] We observed that the diffusion of labelled DOPE-ATTO655 was lower in PC/PA bilayers, determined to be 7.1 ± 0.5

$\mu m^2/s$. This value is significantly lower that previously reported for DOPC bilayers, to be around 10 $\mu m^2/s$, indicating that PC/PA bilayers are less fluid, which could explain the lower integrin diffusion. Alternatively, the relatively low diffusion value for the integrin may indicate that it, as reconstituted, is dimerized or aggregated to some degree, this has been observed in integrin previously and may also account for the alpha value, which in previous reports on integrin has been 1. Nonetheless overall, the diffusivity of integrin indicates that its reconstitution was stably achieved at MSLBs, where in control experiments, there no evidence for change in diffusivity or α during this window (*Figure 6.43*).

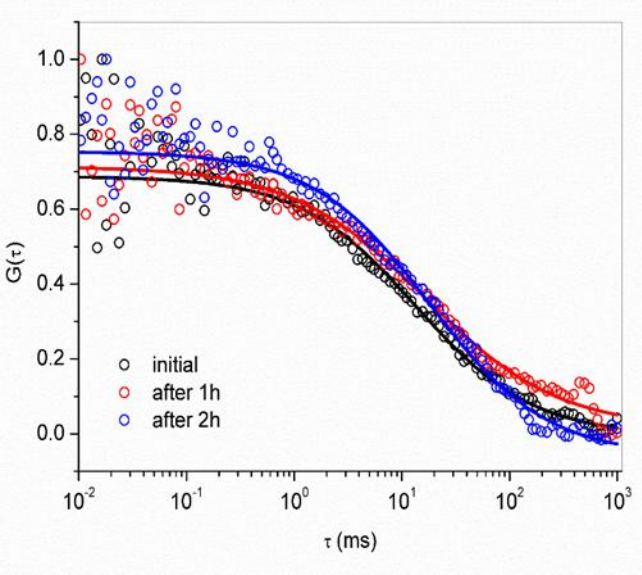

Figure 6.43. ACFS for labelled α5β1 Integrin-488. Integrin was reconstituted into PC/PA-integrin-488 (LP 10), PBS Buffer ACFs were collected over time for reconstituted integrin and show no changes over 3 - 4 hours windows.

6.3.3. Interaction of Gal3 and CRD with α5β1 integrin in absence of GSLs

To evaluate the effect of oligomerization of Gal3 and network formation to membranes containing α5β1 integrin, experiments were carried out using Gal3 (wild type) and a N-terminus truncated Gal3 (Gal3ΔNter) containing the carbohydrate recognition domain (CRD) but lacking the N-terminus responsible for oligomerization and clustering of Gal3. Initially, the diffusion of labelled Gal3-Alexa647 and CRD-Alexa64 was evaluated by FLCS in PBS (pH 7.4) as indicated in the

Figure 6.44. We observed that the diffusion of Ga3-Alexa647 and CRD-Alexa647 were approximately 100 $\mu m^2/s$ after fitting to a 3D diffusion model as indicated in the appendix B.

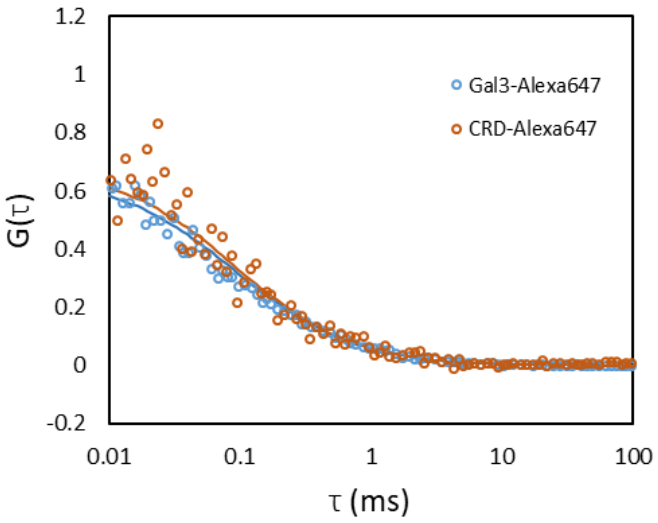

Figure 6.44. ACF curves obtained for labelled Gal3-Alexa647 (blue circles) and CRD-Alexa647 (orange circles) in PBS (pH 7.4). The data was fitted to a 3D diffusion model (solid lines).

Initially, the binding of labelled CRD and WT-Gal3 with Alexa647 were evaluated at MSLBs comprised of PC/PA contain integrin α5β1 (LP 10 wt:wt) using FLIM/FLCS. The FLIM images obtained after the reaction of labelled CRD-Alexa647 are shown in Figure 6.45. The samples were exposed to CRD-Alexa647 at 6.66, 33.3 and 66.6 nM, represented by the Figures 5a, 5b, and 5c, respectively. We observed that in absence of GSLs, the binding of CRD was weak and limited to the rim of microcavities, which could indicate adsorption of CRD to the less mobile parts of the membrane. The diffusion coefficient of CRD-647 was approximately 24 $\mu m^2/s$. This is indicated by the absence of mobile molecules at the center of the microcavities, as shown in the Figure 6.6 (right) and could indicate the CRD might bind to α5β1 immobilized protein.

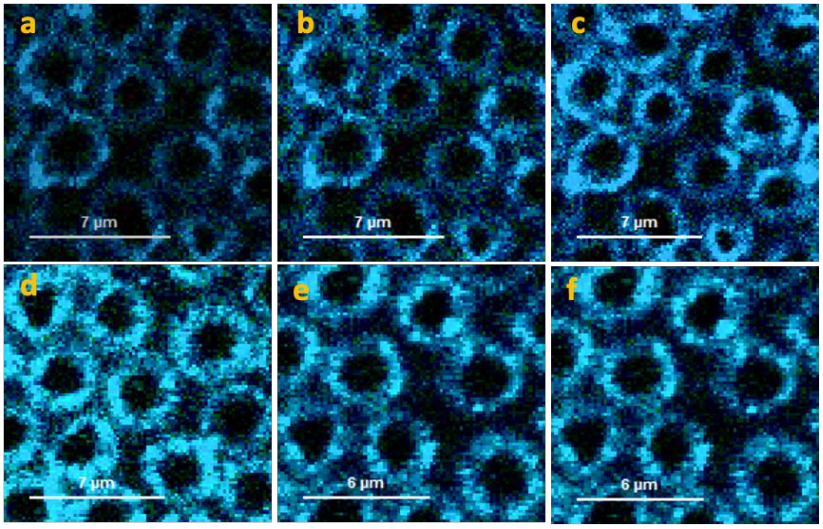

Figure 6.45. FLIM of MSLBs comprised of PC/PA (90:10) containing α5β1 (LP 10 wt:wt) after reaction with CRD-Alexa647. Figures (a), (b) and (c) represent the FLIM obtained for CRD-Alexa647 at 6.6, 33.3 and 66.6 nM. (d), (e) and (f) represent the FLIM images obtained for α5β1-ATTO488.

The FLIM images obtained for labelled-integrin shown a constant fluorescence intensity with brighter areas nearby the rim of the microcavities, as shown in same conditions as indicated by the Figures 5d, 5e and 5f. As well, the ACFs curves obtained for labelled integrin $\alpha_5\beta_1$ above microcavities (Figure 6.46, left) indicated that the association of CRD to the membrane, which corresponds to low binding to integrin as shown in the FLIM images displayed in Figure 6.45. The truncated CRD lacks the N-terminus which is what leads to self-oligomerization of Galectin 3. However a variation on the diffusion coefficient of integrin was observed, which increased from 1.9 $\mu m^2/s$ to 2.7 $\mu m^2/s$ after addition of CRD, as indicated in Figure 6.46, right.

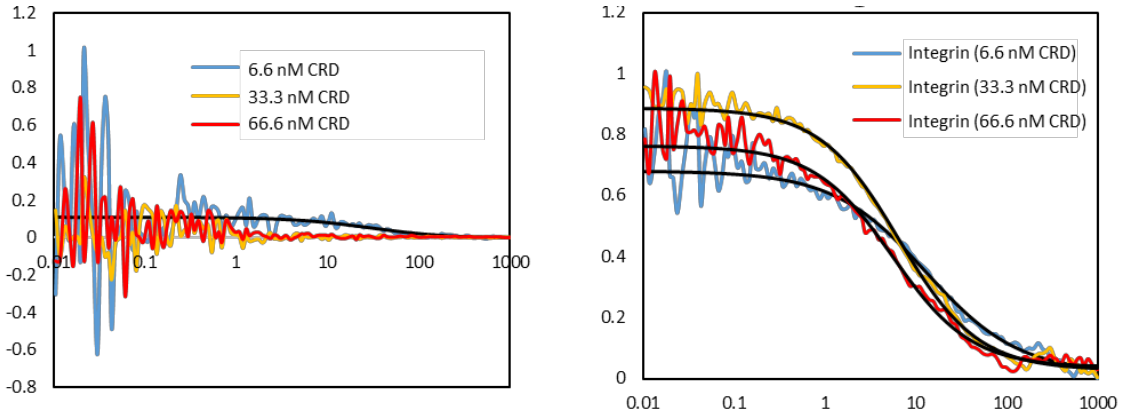

Figure 6.46. FLCS obtained for PC/PA (90:10 mol%) + α5β1 (LPR 10) after reaction with CRD-Alexa647. The ACF curves represent the diffusion of the labelled CRD-Alexa647 (left) and α5β1-ATTO488 (right) as function of CRD concentration. ACFs of CRD (right) indicate poor association to $\alpha_5\beta_1$ at cavities as indicated by the lower correlation of the curves.

Next, the lipid bilayers comprised of PC/PA + contain integrin α5β1 (LP10) were exposed to labelled WT-Gal3-Alexa647. In absence of GSL, the FLIM images obtained after the addition of Gal3-Alexa647 shown a significant increase in intensity at center of microcavities, when compared to CRD as shown in the Figure 6.47 (a-c). This could indicate a higher association of Gal3 to integrin as the N-terminus allows lectin-oligomerization, which could lead to uptake of integrin is more efficient way. The ACFs curves obtained for Gal3 shown that the diffusion coefficient of Gal3 decreases with concentration from approximately 0.9 $\mu m^2/s$, indicating association as the solution phase values confirm the binding to the membrane. Also, the very low diffusivitity likely indicates network or lattice formation, as indicated in

Figure 6.48, left, in accordance with FLIM.

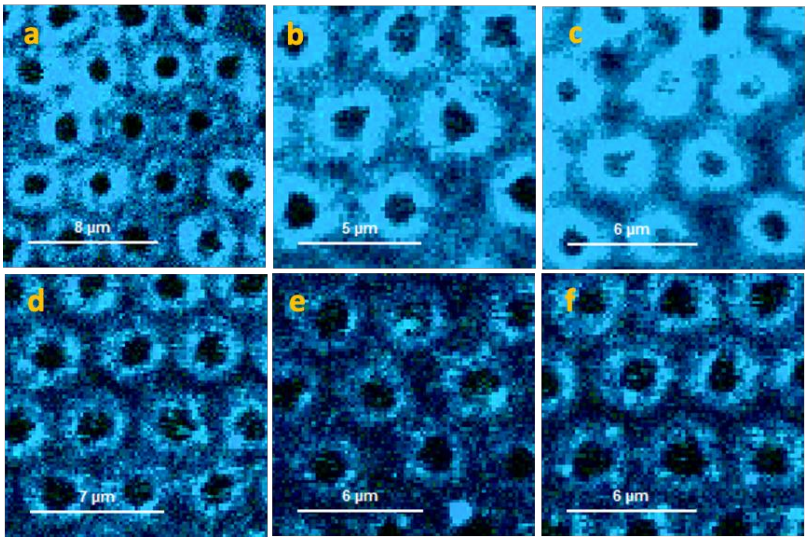

Figure 6.47. FLIM of MSLBs comprised of PC/PA (90:10) containing α5β1 (LP 10 wt:wt) after reaction with Gal3-Alexa647. Figures (a), (b) and (c) represent the FLIM obtained for Gal3-Alexa 647 at 3.7, 18.5 and 37 nM, respectively. Figures (d), (e) and (f) indicate the FLIM obtained for α5β1-ATTO488.

In case of labelled integrin α5β1-ATTO488, FLIM images of shown a relatively constant brightness as indicated in Figure 6.47 (d-f). Conversely, the addition of Gal3 causes integrin diffusivity to increase, as indicated in

Figure 6.48, right. The diffusion coefficient of integrin increased from 1.8 $\mu m^2/s$ to 5.6 $\mu m^2/s$ after Gal3 binding. This suggests disaggregation of the integrin or perhaps change in resting status and could indicate a variation in local membrane diffusivity due to curvature change. This is accompanied by an increase in the Brownian α coefficient to approximately 1, which indicates reversion from anomalous to close to Brownian motion on Gal3 treatment and taken together may suggest that Gal3 imposes disaggregation of the integrin at the membrane, possibly due to inhibition of inter-integrin interactions or change of activation status. Our data is strongly consistent with studies reported by Yang et al. that Gal3 alters the lateral mobility and clustering of α5β1-integrins in HeLa cells using SPT. They observed that the truncated CRD showed only minor reductions in lateral mobility while WT-Gal3 induced higher diffusivity of integrin.[11] To the best of our knowledge, this is the only observation of a change in mobility of integrin after Gal3 binding.

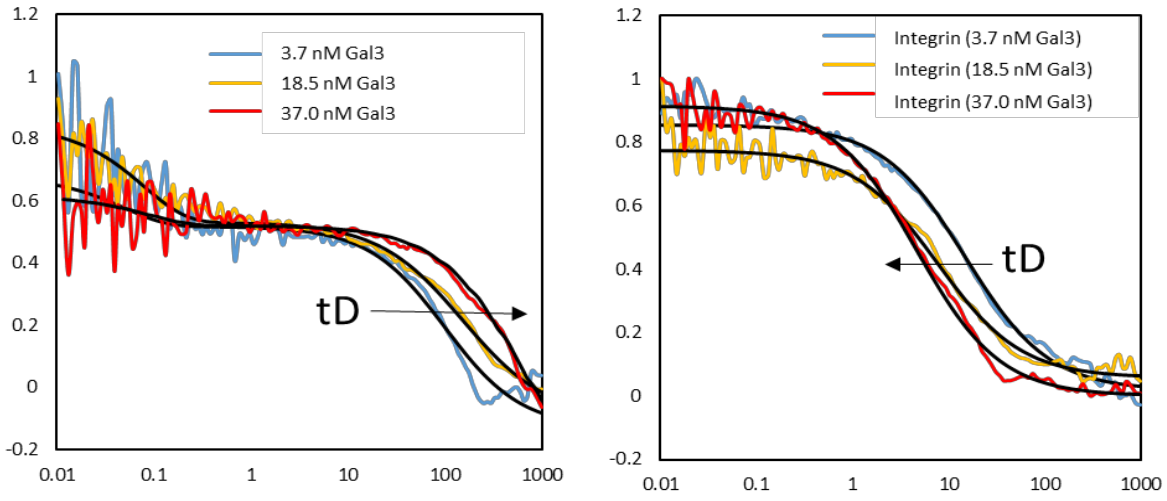

Figure 6.48. PC/PA (90:10 mol%) + α5β1 (LPR 10) + Gal3-Alexa647. Data is collected for the same experiment but left shows diffusion of the labelled Gal3 and Right shows ACFs for α5β1 as function of Gal3 concentration.

Additionally, complementary studies conducted with EIS shown a different behavior of Gal3 and CRD at membranes containing integrin as indicated in Figure 6.49. We observed that both Gal3 and CRD cause a decrease in resistance of the integrin reconstituted to PC/PC bilayer, which extent of change is consistently larger for Gal3 (Figure 6.49a). However, the Gal3 was observed to increase the membrane capacitance at lower concentrations, around 10 nM, which decreased for higher concentration at 40 nM. On the other hand, we observe a systematic decrease in capacitance for concentration of up to 10 nM. After, the capacitance remained constant and unvaried with CRD concentration (Figure 6.49b). This difference indicates Gal3-oligomerization at lipid membrane, which could cause an increase in membrane capacitance due to the additional protein layer, in accordance with FLCS/FLIM observations.

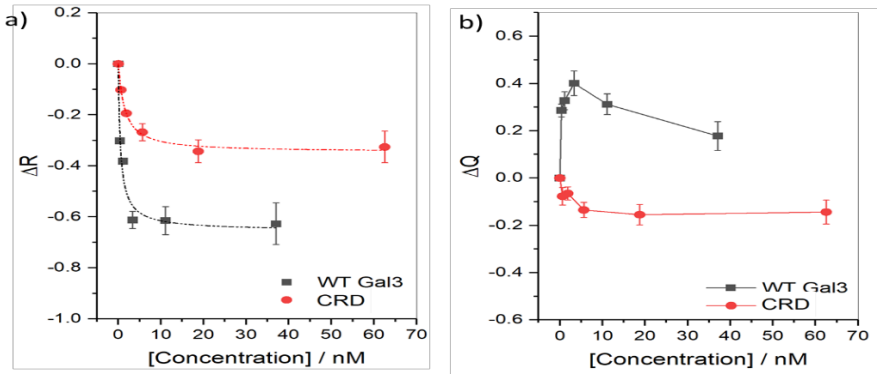

Figure 6.49 Impact of Gal3 and CRD on PC/PA lipid membrane containing Integrin. Figures a and b illustrate the change in resistance and capacitance of membrane. There values were extracted from the EIS fitted data.

6.3.4. Inhibition of Galectin-3 with $\alpha_5\beta_1$ integrin in absence of GSLs

To disrupt carbohydrate-mediated interactions of Gal3 with integrin, Gal3 was incubated in presence of lactose as inhibitor competitor as indicated by the ACF curves in Figure 6.50. Under these conditions, the diffusivity of integrin-488 obtained was 2.1 ± 0.5 $\mu m^2/s$ (black circles). The diffusivity of integrin in presence of β-lactose was 1.9 ± 0.7 $\mu m^2/s$, indicating that lactose did not affect integrin diffusion (red circles). Notably, from Figure 6.50, if the integrin is pre-incubated with lactose the galectin induced changes are not observed. After the addition of pre-incubated Gal3 with β-lactose (50mM), integrin diffusivity was not impacted, remaining around 2.2 ± 0.4 $\mu m^2/s$ (blue circles), indicating that Gal3 failed to bind to integrin. The bilayer was then rinsed with PBS (pH 7.4, 1 ml) to remove non-bound Gal3-lactose complex and exposed to Gal3 (1 μg/ml), which corresponds to 37 nM, the diffusivity of integrin was increased to 5.5 ± 0.8 $\mu m^2/s$. This important observation indicates that carbohydrate recognition domain binding is the interaction with integrin is required to alter the integrin mobility.

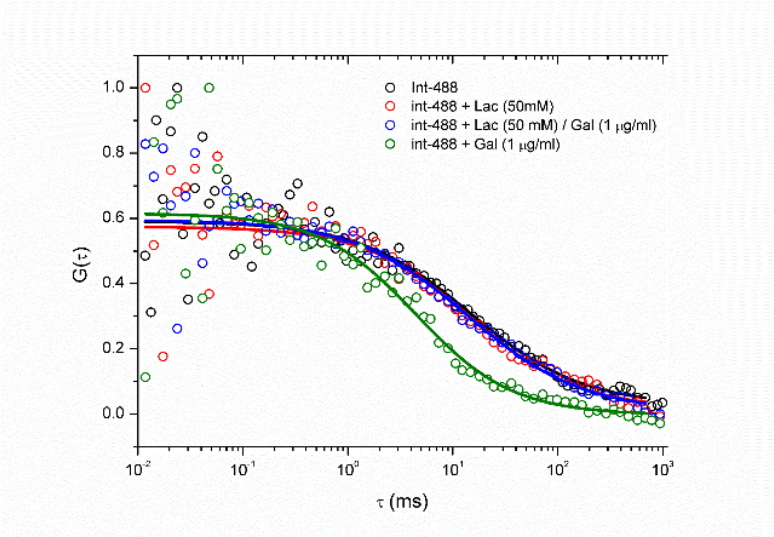

Figure 6.50 Diffusivity of integrin-atto488 before reaction with lactose (red circles), Gal3 pre-incubated with β-lactose (blue circles), WT-Gal3 (green circles). PBS, pH 7.4.

6.3.5. Interaction of Gal3 and CRD with α5β1 integrin in presence of GSLs

Next, to directly address the role of GSLs and integrin on Gal3 binding were investigated following using labelled Ga3 and CRD. To do so, MSLB containing 5 mol% of GSLs and integrin α5β1 were prepared following the proteoliposomes preparation previously described. The lipid bilayers exposed to labelled CRD-Alexa647 shown that the association of CRD was higher for the GSL/α5β1 than the results observed for α5β1 in absence of GSLs. This is observed as shown in the FLIM images in Figure 6.51 (a-c). It is possible to observe that FLIM images of CRD-Alexa647 shows increase in fluorescence intensity of CRD-Alexa647 above the microcavities which might indicate a better association of CRD to integrin/GSL. However, the diffusion coefficient of CRD was constant at approximately 2 $\mu m^2/s$ across the 3 concentrations tested as shown in Figure 6.52, right. This suggests that CRD does not from a network, as expected for the truncated Gal3, since the diffusion essentially matches that of the untreated integrin. Together, FLIM and FLCS of labelled CRD-Alexa647 shown that GSLs increase the ability of CRD to bind integrin membranes. Controls were conducted to lipid membranes containing only GSLs which shown poor association and indicates that GSL/integrin binding is cooperative.

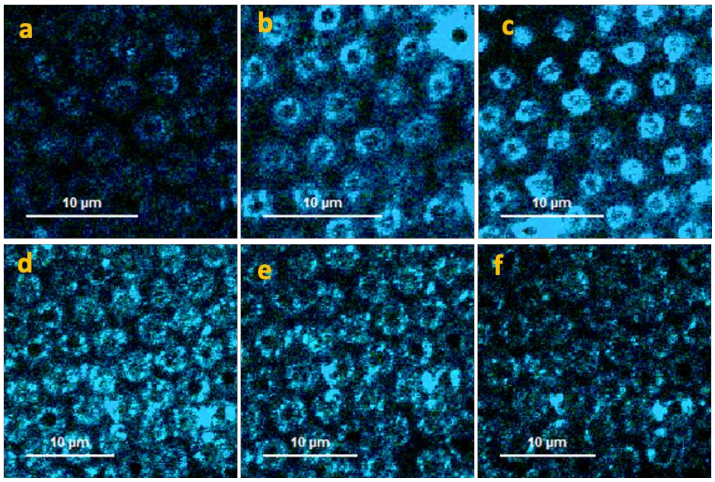

Figure 6.51 FLIM images of CRD-Alexa647 and Integrin-488 obtained for MSLBs comprised of PC/PA/GSL containing integrin. Figures (a), (b) and (c) represent the FLIM obtained for CRD-Alexa647 at 6.6, 33.3 and 66.6 nM. (d), (e) and (f) represent the FLIM images obtained for integrin-ATTO488.

FLIM images of integrin shown that the lipid membrane was stable throughout the experiment (Figure 6.51). The diffusivity of integrin remained constant at approximately 1.2 $\mu m^2/s$ with α coefficient of 0.8 (Figure 6.52, right). This either indicates that the association is mainly through the bilayer/GSL or that the CRD associates with the integrin but does not disaggregate it.

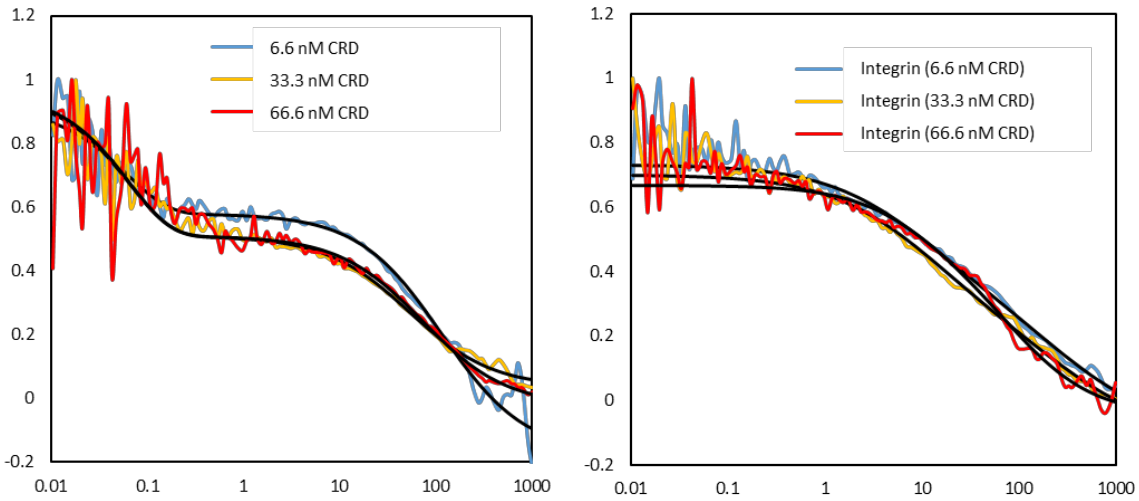

Figure 6.52 Fluorescence Correlation Data for PC/PA/GSL (85:10:5) + α5β1 (LP 10) + His-tagged ΔNter-Gal3 (CRD-Alexa647). ACFs obtained for CRD-Alexa647 (left) and α5β1-ATTO488 (right).

In presence of GSL, lipid bilayers containing integrin α5β1 show a very strong response to Gal3 as indicated by FLIM images obtained for Gal3-Alexa647 shown significant increase in brightness indicating extensive association of Gal3 to integrin/GSL bilayer (Figure 6.53 (a-c)), which could be related to network formation of Gal3. The FLCS results obtained for Gal3 (Figure 6.54, right) shown that the association of Gal3 might induce local clustering or aggregation of Gal3, as the protein diffusion decreased approximately 2 $\mu m^2/s$ to 0.1 $\mu m^2/s$. The diffusion of Gal3 is slightly faster than in absence of GSLs. This could suggest that GSLs promote stabilization of Gal3 aggregates in presence of integrin.

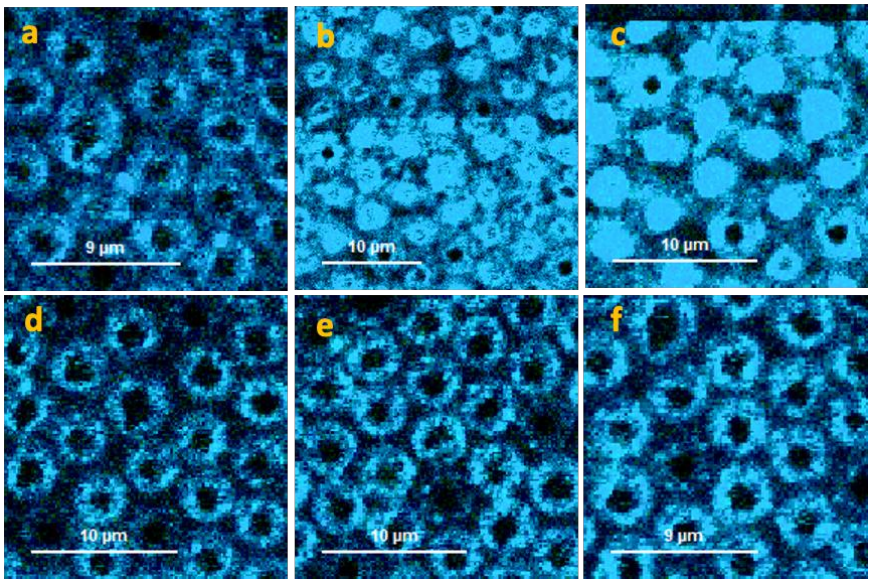

Figure 6.53 FLIM images of Gal3-Alexa647 and Integrin-488 obtained for MSLBs comprised of PC/PA/GSL containing integrin. Figures (a), (b) and (c) represent the FLIM obtained for Gal3-Alexa647 at 6.6, 33.3 and 66.6 nM. (d), (e) and (f) represent the FLIM images obtained for integrin-ATTO488.

On the other hand, FLIM images obtained for labelled Integrin-ATTO488 shown low variation in intensity indicating that integrin was associated to the lipid membrane across the experiment (Figure 6.53 (d-f)). Also, the diffusivity of integrin increased from 2.0 $\mu m^2/s$ to 4.1 $\mu m^2/s$ after reaction with Gal3 as indicated in Figure 6.53 (left). This values are slightly lower than previously

observed for integrin in absence of GSLs and might suggest that glycolipids stabilize the binding of Gal3 to integrin.

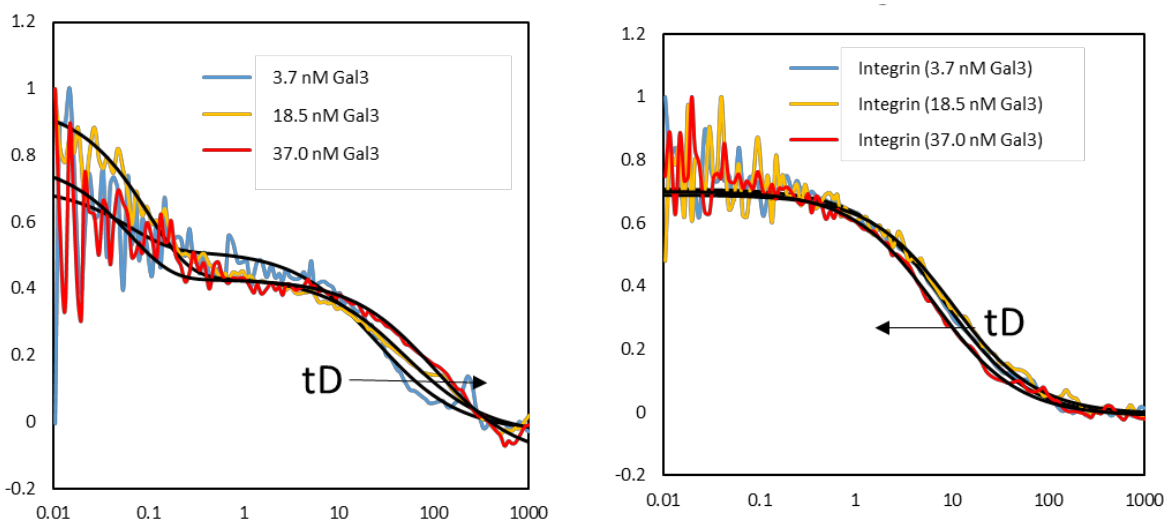

Figure 6.54. FLCS obtained for Gal3-Alexa647 and α5β1-ATTO488 at PC/PA/GSL (85:10:5) + α5β1 (LPR 10) bilayers. ACFs of Gal3-Alexa647 (left) indicated a reduction on Gal3 diffusion while ACFs of integrin-488 (right) indicates an increase of integrin diffusion.

The results obtained from EIS suggest that both Gal3 and CRD impact in membrane resistivity in a similar way. This is indicated by the decrease of the relative resistivity as shown in Figure 6.55a. This could be related to a better permeability of the lipid membrane caused by rearrangement of the lipids or integrin. Interestedly, the capacitance of lipid bilayers containing GSLS increased after reaction with CRD differently to lipid bilayers prepared in absence of GSLs (Figure 6.55b). This could be related to the binding of CRD observed in FLIM and FLCS measurements. The capacitance of lipid membranes after Gal3 was slightly affected in presence of GSLs and increased significantly at 40 nM. This could be related to a modulation of GSLs to Gal3 oligomerization, as indicated by FLCS.

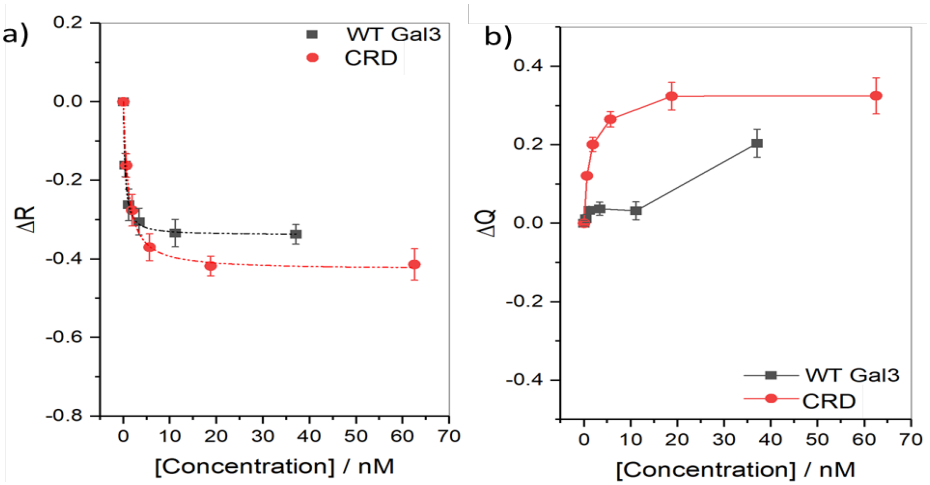

Figure 6.55 Impact of WT Gal3 and CRD on PC/PA/GSL(85:10:5) membrane containing Integrin. Integrin reconstitution were carried out at LP10. Figures (a) and (b) illustrate the change in resistance and membrane capacitance values extracted from the EIS fit.

6.3.6. Inhibition of Galectin-3 in presence of α5β1 integrin in presence of GSLs

In a similar manner, the inhibition studies ware performed with Gal3 (1 µg/ml) was pre-incubated with I3 inhibitor (Hakon Leffler, Lund University, Sweden) (10 µM) for 1h at RT. The inhibitor I3 function by blocking the carbohydrate recognition domain, similarly to lactose. The complex Gal3/I4 was allowed to react with lipid bilayer for 30 min before FLCS measurements, shown in Figure 6.56. The diffusivity of integrin increased modestly after reaction with pre-incubated Gal3, from 2.4 $\mu m^2/s$ to 2.6 $\mu m^2/s$, indicating that the inhibition was sufficient to prevent Gal3 binding to integrin/GSLs.

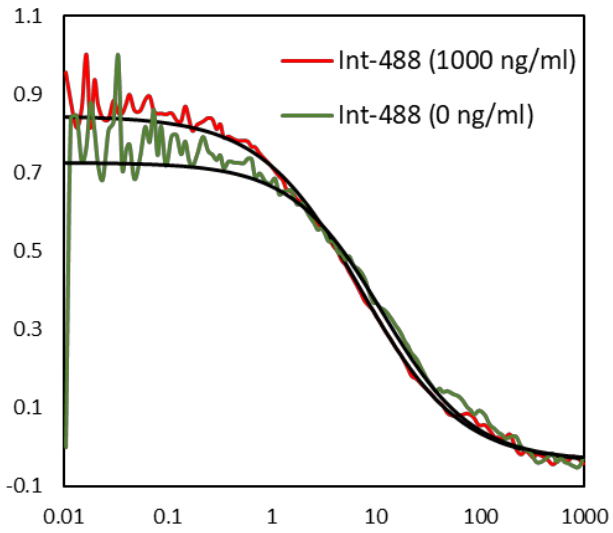

Figure 6.56. Inhibition binding of Gal3 to lipid bilayer containing GSL/α5β1 before (green line) and after (red line) addition of pre-incubated Gal3-I4.

6.4. Conclusion

The preliminary results indicate that α5β1 was incorporated to MSLBs using the two-step protocol based on LB transfer followed by proteoliposomes fusion, as indicated by the diffusivity of integrin and FLIM images. The role of the N-terminus of Gal3 on recruiting integrin at lipid membrane was investigated using a truncated CRD. The difference between CRD and Gal3 observed indicates that Gal3 requires GSLs along to integrin to promote binding and aggregation. This is related the N-terminus responsible for oligomerization galectin responsible for recruiting integrin, which is reflected on the increase of diffusion of integrin after binding to Gal3. This was further confirmed by the use of inhibitors such lactose and I4 shown that inactive galectin could not change diffusion of integrin However, the increase of lateral diffusion of α5β1 still remains to be further studied. This work focused on inactive form of α5β1. Future work is ongoing on activated integrin and in order to further elucidate the lattice formation of Gal3 and the consequence on α5β1.

6.5. References

(1) Hynes, R. O. Integrins: A Family of Cell Surface Receptors. *Cell* 1987, *48* (4), 549–554.
(2) Hood, J. D.; Cheresh, D. A. Role of Integrins in Cell Invasion and Migration. *Nature Reviews Cancer* 2002, *2* (2), 91–100.
(3) Le Mercier, M.; Fortin, S.; Mathieu, V.; Kiss, R.; Lefranc, F. Galectins and Gliomas. *Brain Pathol* 2010, *20* (1), 17–27.
(4) Hönig, E.; Ringer, K.; Dewes, J.; von Mach, T.; Kamm, N.; Kreitzer, G.; Jacob, R. Galectin-3 Modulates the Polarized Surface Delivery of B1-Integrin in Epithelial Cells. *Journal of Cell Science* 2018, *131* (11), jcs213199.
(5) Menon, R. P.; Hughes, R. C. Determinants in the N-Terminal Domains of Galectin-3 for Secretion by a Novel Pathway Circumventing the Endoplasmic Reticulum–Golgi Complex. *European Journal of Biochemistry* 1999, *264* (2), 569–576.
(6) Lakshminarayan, R.; Wunder, C.; Becken, U.; Howes, M. T.; Benzing, C.; Arumugam, S.; Sales, S.; Ariotti, N.; Chambon, V.; Lamaze, C.; Loew, D.; Shevchenko, A.; Gaus, K.; Parton, R. G.; Johannes, L. Galectin-3 Drives Glycosphingolipid-Dependent Biogenesis of Clathrin-Independent Carriers. *Nature Cell Biology* 2014, *16* (6), 592–603.
(7) Furtak, V.; Hatcher, F.; Ochieng, J. Galectin-3 Mediates the Endocytosis of β-1 Integrins by Breast Carcinoma Cells. *Biochemical and Biophysical Research Communications* 2001, *289* (4), 845–850.
(8) Ivashenka, A.; Wunder, C.; Chambon, V.; Sandhoff, R.; Jennemann, R.; Dransart, E.; Podsypanina, K.; Lombard, B.; Loew, D.; Lamaze, C.; Poirier, F.; Gröne, H.-J.; Johannes, L.; Shafaq-Zadah, M. Glycolipid-Dependent and Lectin-Driven Transcytosis in Mouse Enterocytes. *Communications Biology* 2021, *4* (1), 1–15.
(9) Berselli, G. B.; Sarangi, N. K.; Ramadurai, S.; Murphy, P. V.; Keyes, T. E. Microcavity-Supported Lipid Membranes: Versatile Platforms for Building Asymmetric Lipid Bilayers and for Protein Recognition. *ACS Appl. Bio Mater.* 2019, *2* (8), 3404–3417.
(10) Gaul, V.; Lopez, S. G.; Lentz, B. R.; Moran, N.; Forster, R. J.; Keyes, T. E. The Lateral Diffusion and Fibrinogen Induced Clustering of Platelet Integrin AIIbβ3 Reconstituted into Physiologically Mimetic GUVs. *Integrative Biology* 2015, *7* (4), 402–411.
(11) Yang, E. H.; Rode, J.; Howlader, M. A.; Eckermann, M.; Santos, J. T.; Armada, D. H.; Zheng, R.; Zou, C.; Cairo, C. W. Galectin-3 Alters the Lateral Mobility and Clustering of B1-Integrin Receptors. *PLOS ONE* 2017, *12* (10), e0184378.

Chapter 7: Conclusions and Future perspectives

In this study, we have shown that artificial lipid bilayer spanned over microcavity arrays are versatile and insightful models to better understand the complex nature of cell membrane and its interactions with membrane proteins and membrane associating proteins. In particular, MSLBs are a useful model of the cell membrane for applications and investigations of processes that require high lateral mobility of membrane components or transmembrane lipid asymmetry. In this thesis we aimed to fabricate reliable asymmetric lipid bilayers, to explore their interaction with peripheral and integral proteins through appropriate biophysical methods, such fluorescence, impedance and Raman spectroscopy.

One of the main focuses of this thesis has been on a demonstrating the versatility and breadth of applications of these fluidic models for membrane associating proteins spanned over microcavity arrays. Therefore, the study began with the characterisation of asymmetric lipid bilayers and their impact on lipid diffusion coefficient (chapter 2). The influence of transmembrane asymmetry on diffusion indicated that interdigitation of membrane leaflets affect the diffusion coefficient of lipids. The diffusion of DOPE-Atto655 lipid label was highest for fluidic bilayers comprised of DOPC alone and decreased in the following order: DOPC > DOPC/SM/Chol > DOPC/SM. These results has an important implication in the biophysical field of artificial lipid membranes as it is suggested that interdigitation of lipids influence the physical-chemical properties of the lipid membrane. Our results on MSLBs suggest, in agreement with recent studies on SLBs, that the interleaflet coupling of the lipid monolayers can modulate the overall membrane fluidity.

In chapter 2, the high fluidity of MSLBs enable the interrogation of binding of CTb to GM1 and CTb aggregation, evaluated as function of CTb concentration. As expected, diffusion coefficient of the couple GM1-labelled CTb-Alexa555 was slower for membranes containing SM or SM/Chol. Two populations were found to contribute to the diffusion model. The % contribution of the slow diffusing fraction scaled with CTb concentration, suggesting it is CTb-crosslinked aggregates and the diffusion of the fast component decreased, attributed to single CTb units anchored to 1, 2 or 3 GM1 units at the membrane, based on simple Saffman-Delbrück estimations of radii. Gangliosides such as GM1 participate in a wide range of recognition and signalling processes at the cell

membrane where signalling in many cases is driven by oligomerization or 2-dimensional network formation. Modelling of such processes at an artificial membrane requires capability to build transversally asymmetric bilayers but also lateral fluidity is crucial to enable bilayer organisation, both demands are fulfilled by MSLBs. The long term objective of this work is to apply the study the impact asymmetric MSLBs in highly relevant biological problems, for instance, how the loss of asymmetry affects the progression of Alzheimer's disease.

Chapter 3 further explored association of hemagglutinin (HA1) to MSLBs containing different receptors at lipid membrane. Very few studies have been reported to date of biophyiscal influenza models. In our platform, two parameters were varied, the membrane composition and the ganglioside identity, and both were shown to influence in the binding HA1. Using fluidic lipid membranes comprised of DOPC with 1 mol % of GSL asymmetrically distributed, in analogy to the plasma membrane, at the distal leaflet, we observed that HA1 bound preferentially to GDa1 than GM1 and GM3. The diffusion of bound HA1 to GDa1 was observed to be approximately two-fold the value obtained for GM1 and GM3 complexes, suggesting that GSL nature could affect the dimension of the associated HA1-GSLs complexes or penetration of bound HA1 to the lipid membrane. The binding of HA1 to ganglioside GM1 in Lo/Ld composition showed a lower mobility for HA1 assembly compared to more fluidic bilayers, indicating that the local membrane composition might influence hemagglutinin-GSL recognition. We also noted that HA1 has higher affinity at more fluidic membranes as elucidated by electrochemical studies, where the results obtained using EIS shown more affinity for fluidic DOPC membranes than complex composition. In agreement to that, FLCS results indicate that the mobility of bound HA1 in SM/Chol membranes is occurring in more fluidic domains. Overall, FLCS and EIS have shown that the fluidity of lipid membranes affects the HA1 binding to MSLBs. These results are expected to contribute to the influenza A understanding of viral binding and recognition to the cell membrane. A limitation of this work is that we used only the receptor of HA1 away from the viral particle.

In chapter 4, we sought to explore the application of MSLBs to incorporation of transmembrane protein. Chapter 4 explored the electrochemical photo-activation of bacteriorhodopsin reconstituted into MSLBs. This was accomplished after the incorporation of bR to proteoliposomes comprised of DOPC using a detergent-mediated method. In order to evaluate protein incorporation to proteoliposomes, bR was fluorescently labelled with Atto532. After reconstitution, the

diffusivity of the lipid bilayers was evaluated by FLCS, in which the lipid diffusion was obtained in respect of concentration of bR. The photocurrent generated after photoactivation shows that bR retained its functionality after incorporation to MSBLs and indeed the intensity of the photocurrent, given it is a single bilayer indicated it was highly efficient. This indicates that the lipidic environment provided by the spanned lipid bilayer is supportive of the protein and the utility of porous arrays. The photocurrent was determined to be related not only to the protein concentration but also external factors, such as pH and frequency of activation. These effects were demonstrated as the photocurrent signal detected was higher at more acidic pH. In addition, we were able to vary the frequency of activation by using a microcontroller indicating that the maximum photocurrent was detected at 4Hz. The rapid switching of the membrane bound bR indicates that the proteins is fully functional and efficient in the membrane and this approach offers the possibility to build sophisticated biomolecular switches based on membrane protein at MSLBs. These molecular switches could be used to investigate the impact of pH changes to lipid or proteins in real time. Also the incorporation of transmembrane protein to MSLBs open the possibility of study pore-forming proteins, involved in active permeation of molecules.

Chapter 5 focused on oligonucleotide delivery to MSLBs. Within Keyes lab, MSLBs are being used to study the drug permeability and a novel assay has been developed that monitors drug arrival below the membrane from its arrival at a plasmonic hotspot within the cavity using Raman spectroscopy. This work explored MSLBs as models of endosomal escape of ssDNA from cationic lipoplexes at MSLBs. In chapter 6, we attempted to prepare the lipid bilayers purely by LB: 1) LB transfer of lipid monolayer, and 2) LB transfer of subsequent monolayer. The results of point-FLCS shown that the bilayers were well spanned over MSLBs and retain fluidic. We observed that the maximum release of DNA was obtained when cationic lipoplexes contained a lipid helper, or DOPE. The results presented here indicate that the platform is suitable to be used as a test to new oligonucleotide-cargos, aiming the development of faster and more efficient gene delivery therapies. An example of a nanocargo is the use of virosomes, as suggested for chapter 3.

Further work is ongoing concerning the study of galectin-integrin assembly at MSLBs activation state of integrin that can impact the clathrin-independent endocytic mechanisms. In chapter 6 the thesis is rounded out and we described the preliminary studies of the incorporation of integrin to MSLBs using a two-step protocol of 1) LB transfer of lipid monolayer, and 2) proteoliposomes

rupture led to formation of lipid bilayer containing integrin. Confocal microscopy and point FLCS measurement confirmed the formation of lipid bilayers spanned over buffer filled microcavities. We were able to achieve this spanning with asymmetric lipid composition, including GSLs. Importantly, point measurements shown that the diffusivity of integrin was comparable to free-standing bilayers or GUVs. Next, we explore the association of Galectin-3 to lipid bilayers containing integrin. We observed that following administration of Galectin-3, the diffusion coefficient of integrin increased from its original value. The investigation of invaginations-like structures is to be determined by super-resolution microscopy and AFM.

From the success and challenges described in this thesis, the following sections outline possible areas of improvement that could be made to the future work. In conventional SLBs, as discussed in chapter 1, the lipid membrane constituents, such lipids and proteins, interact with the underlying substrate hindering their lateral mobility or interfering with their functionality. The results here presented indicate a great advantage of MSLBs over SLBs due to the lower interference of the substrate in the membrane fluidity. However, more work is to be done in order to stablish the loss of lipid asymmetry in MSLBs, the stability of lipid asymmetry and the influence of lipid membrane composition (Lo/Ld) in the dynamic of lipid flip-flop.

Future investigations circa the interaction of HA with MSLBs could be conducted using virosomes prepared via incorporation of HA into liposomes. The use of virosomes particles could to mimic the behaviour of the influenza virus particle, which affinity, kinetic of incorporation, and gene-delivery to MSLBS could be monitored through the biophysical techniques used in this thesis. This could unravel other insights about the influence of lipid membrane in the influenza infection. In addition, this study might suggest that MSLBs could be used as screening-tests for antiviral drugs, focusing in the inhibition process of viral infection.

The further development of a more reliable fabrication methods to obtain more reproducible substrates of PDMS microcavities is ongoing. The main drawback of dropcast of polystyrene spheres is the variation of structure arrays that can be obtained, particularly to the spontaneous formation of multilayers of spheres. The use of silicon or 3D-printed mould could facilitate the production of highly reproductible microfluidic chips, while varying the cavity size and depth and their impact in membrane properties and stability. In addition, AFM studies may provide further characterization of mechanical properties of microcavity supported lipid bilayers can be used to

determine lateral tension (σ) and spring constant (k) of membranes spanned over buffer-filled microcavity arrays.

In addition, a main drawback of MSLBs is the lack of extended temporal stability for membranes spanned over gold arrays. Similarly to liposomes, the bilayer are stable for hours, typically 1-10h, which might limit the application of MSLBs when compared to other lipid systems, such classic SLBs. This could be improved in our platform by the development of self-healing membranes, we the underlying cavity can act as cellular endosome to deliver lipids to the suspended membrane. In addition, the use of single frequency EIS measurements could be tested as a rapid and efficient way to measure the interaction of proteins/lipids with MSLBs, which would bring the platform into the direction of a commercial device for investigation of lipid models. This is particularly attractive for the development of new pharmaceutical drugs and would bring the technology developed by Keyes group into another level of sophistication and excellence.

Appendices A-D

Appendix A

Supporting information associated with Chapter 2.

Fabrication of gold microcavity array electrodes

Figure S1 represents step by step the procedure for gold microcavity array fabrication. In step-1, 1μm sphere PS (1 wt% v/v in milli-Q water) was self-assembled on plasma treated gold substrate using drop-cast approach. After evaporation of water (Figure S1a) in step-2, the electrode was subjected to gold deposition by submerging the electrode into electroplating solution. The growth was monitored until the film grown up to half of the PS sphere diameter in between the intestinal space of PS sphere and stopped (Figure S1b). In step-3, the electrode was washed with Milli-Q water, dried under N_2 gas and submerged in a 1mM ethanolic solution of 6-mercapto-1-hexanol (SH) and kept for the formation of self-assembled monolayer. After 2 days, the electrode was removed from thiol solution and washed gently with ethanol to remove excess unbound thiol. In step-4 the substrate was dipped in THF solution for 10 min. In this process, the PS is removed and the microcavity array is formed (Figure S1c). The substrate was kept in PBS buffer for more than 1 hr and ready for further use. Briefly, 1μm sphere PS (1 wt% v/v in milli-Q water) was self-assembled on plasma treated gold substrate using drop-cast approach. After evaporation of water (Figure S1a), the electrode was subjected to gold deposition by submerging the electrode into electroplating solutions. The growth was monitored using controlled potential deposition until the film has grown up to half of the PS sphere diameter in between the intestinal space of PS sphere and stopped (Figure S1b). Selective SAM formation at the top interface of the array was achieved by submerging the gold substrates in a 1 mM ethanolic solution of MH prior to the removal of the 1 μm polystyrene (PS) templating spheres. As described previously, the PS spheres could prevent the MH SAM forming at the pore interior, limiting the SAM to the interstitial planar regions at the top surface of the array between pores[1,2]. The chemical modification of MH treatment step improves the stability of the bilayer due to strong wettability of gold substrate with –OH functionalized interface. Next, the PS spheres were removed by submerging the gold substrate in THF for 10 min to form hemisphere microcavity arrays. As described previously, this step does not remove the SAM from the top surface and this further confirmed from EIS data (*vide supra*).[3]

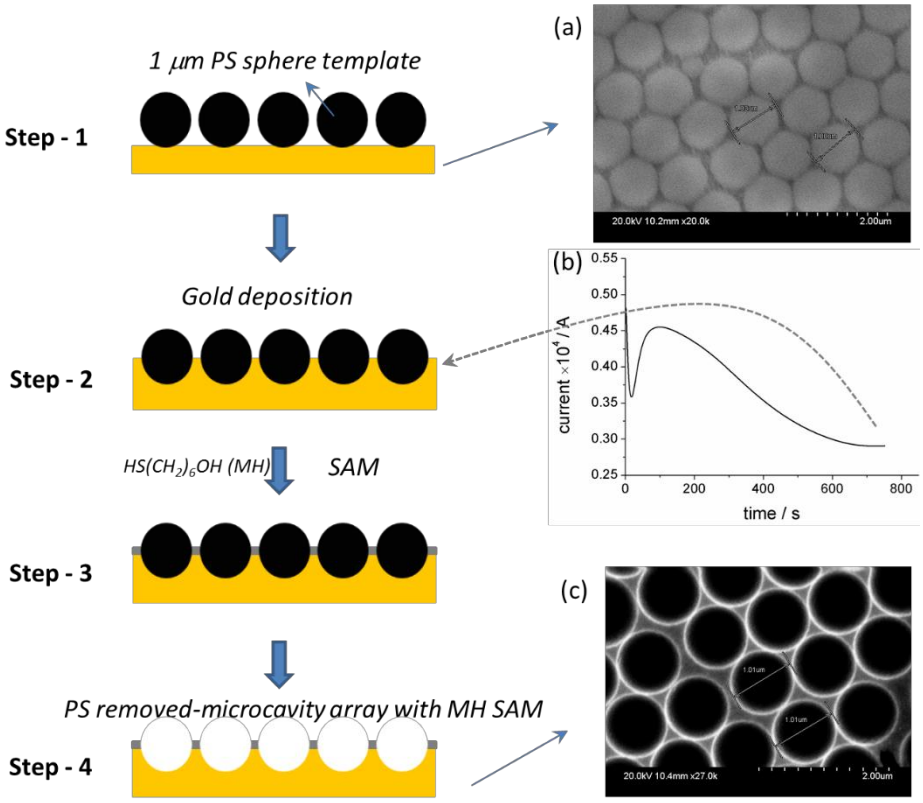

Figure S1. Schematic illustrations of step by step procedure for the fabrication of hemisphere microcavity array on gold substrate. (a) SEM image of PS sphere before gold deposition. (b) Represents the current-time curve during the electrodeposition of gold solution at -0.6 V vs Ag/AgCl. (c) Represents SEM image after PS removal. The scale bar of each image was 2 µm.

Fabrication of PDMS microcavity array

Figure S2 represents stepwise the procedure for the fabrication of microcavity array in PDMS substrate. Similarly to gold electrodes preparation, in step-1 approximately 50 µL of 4.61 µm polystyrene spheres (0.1 wt% v/v in ethanol) was self-assembled on 1 cm x 1 cm fresh cleaved mica sheet. The PDMS mixture (10:1 ratio) is degassed in a vacuum chamber for 30 min and the bubble-free mixture is poured into a handmade aluminum mould to be cured at 90°C for 30 minutes. After curing, PS spheres were removed by sonicating the substrates in THF for 15 minutes and leftover for solvent evaporation in fumehood overnight.

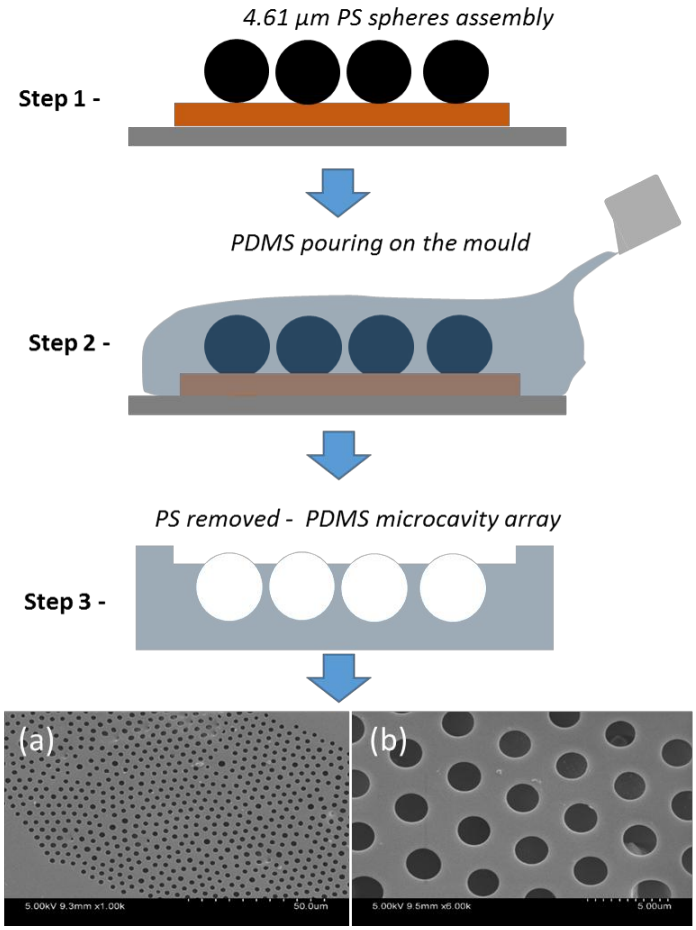

Figure S2. Schematic illustrations of step by step procedure for the fabrication of microcavity array on PDMS substrate. (a) and (b) SEM images of PDMS substrate after PS spheres removal. The scale bar of each image was 50µm and 5 µm, respectively.

Fluorescence Lifetime correlation spectroscopy (FLCS) calibration

The confocal volume was determined by prior calibration using Rhodamine 6G and Atto655, fitting the resulting autocorrelation function using the known diffusion coefficient of the dye at 20 °C. The free diffusion of the dyes in solution following the water viscosity correction expressed by equation (S1)[4] :

$$\mathbf{D(T) = D(25°C)\frac{T}{298.15K}\frac{8.9.10^{-4}\ Pa.s}{\eta(T)}} \qquad \text{(S1)}$$

Where D is the dye diffusion and η is the viscosity of water.

Lipid monolayer transfer using Langmuir-Blodgett films

Prior to filling the cavities with PBS buffer pH 7.4, the substrate is cleaned by oxygen plasma for 5 minutes and sonicated in PBS buffer for 1 hour. Usually, 50 µL of lipids (1 mg/ml in chloroform) is added drop by drop onto the sub phase (MiliQ water, 18.2 MΩ.cm) at room temperature, and chloroform is allowed to evaporate for 10 min. The monolayers were with 4 cycles of compression/decompression at barrier speed of 20 mm/min at final surface pressure (Π) of 35 $mN.m^{-1}$. Then, the monolayer is compressed up to 32 $mN.m^{-1}$ and held for at least 300 s before transfer. Lipid monolayers were transferred onto to hydrophilic gold or PDMS substrates vertically at 5 and 10 mm/min at room temperature.

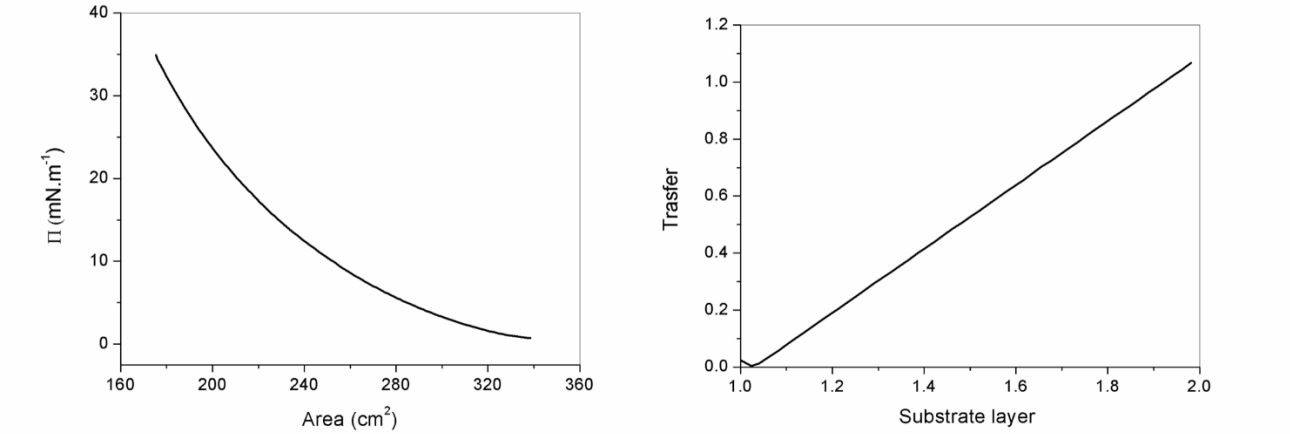

Figure S3. Lipid monolayer transfer using Langmuir-Blodgett lipid films. A typical DOPC isotherm (left) and transfer (right).

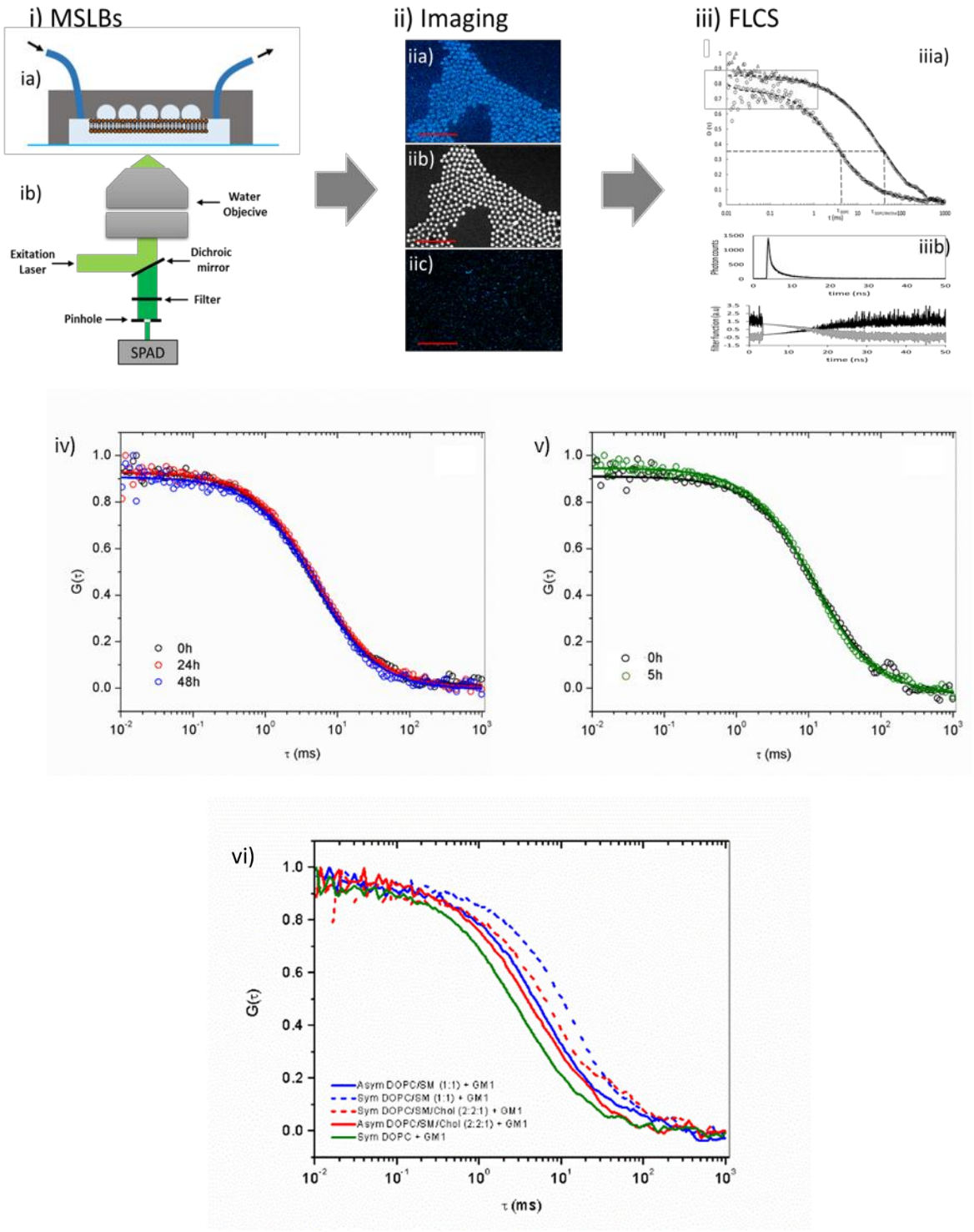

Figure S4. Schematic illustrations of FCS measurement on buffer filled suspended lipid bilayers. (ia) and (ib) represents the MSLBs microcavity array mounted on a confocal microscope and the microscope apparatus used to excite the fluorophores (DOPE and CTb), respectively. (iia)

represents fluorescence lifetime image obtained for DOPE-Atto655 on a DOPC/GM1 (1 mol%) lipid bilayer. (iib) shows the reflectance image obtained using and OD3 filter. (iic) shows the substrate exited with 532nm laser before incubation with CTb-A555 (no auto fluorescence is observed). (iiia) and (iiib) shows the typical ACF curves obtained for DOPE and CTb for DOPC/GM1 (1 mol%) lipid bilayers and the filters used in fluorescence lifetime correlation spectroscopy. Lipid bilayer stability spanned over PDMS microcavity array: (iv) FLCS data obtained for a DOPC bilayer containing GM1 (1 mol%) in the distal leaflet. Initial measurement after sample preparation (black), after 24 hours (red) and after 48 hours (blue). (v) FLCS data obtained for an asymmetric lipid bilayer comprised of DOPC (proximal leaflet) and DOPC/SM (1:1) containing GM1 (1 mol%) in the distal leaflet after sample preparation (0 hour, black) and after 5 hours (green). The lines represent the fitting to the 2D diffusing model. (vi) FLCS DOPE-Atto655 autocorrelation curves (ACFs) obtained for asymmetric and symmetric lipid bilayers spanned over microcavities arrays.

Cholera Toxin Controls with lipid bilayers lacking GM1

The diffusion of CTb in solution was calculated by fitting the ACF (black open circles) displayed in Figure S4a using a pure free diffusional model and found to be around 54 ± 3 $\mu m^2.s^{-1}$. This value was used to estimate the pentameric radius of CTb (rCTb) using Stokes-Einstein relation: $rCTb = KT/6\pi\mu'D$, for bulk solution viscosity (μ') of 0.001 Pa.s at 20°C (T), K is Boltzmann constant and D is the obtained CTb diffusion. rCTb obtained of approximately 3.7 nm is in agreement to CTb radius previously reported.[5] Table S1 shows the results of lipid bilayers without GM1 showing non-specific interaction to lipid bilayers containing sphingomyelin and cholesterol.

Table S1: Resistance and capacitance data for MSLBs at a fixed concentration (40 nM) of CTxB. Results presented reflect the change (Δ) recorded following CTb addition, relative to bilayer prior to CTb interaction and the non-specific adsorption to the lipid membrane were evaluated in presence of sphingomyelin and cholesterol.

Lipid composition	ΔR (kΩcm^2)	ΔC (μF/cm^2)	Slow CTb (μm^2. s^{-1})	Pop (%)
Sym DOPC	0.05±0.01	-0.4±0.01	11.12 ± 2.51	65
sym DOPC/SM/Chol (2:2:1)	0.66±0.02	-1.3±0.12	1.50 ± 0.20	80

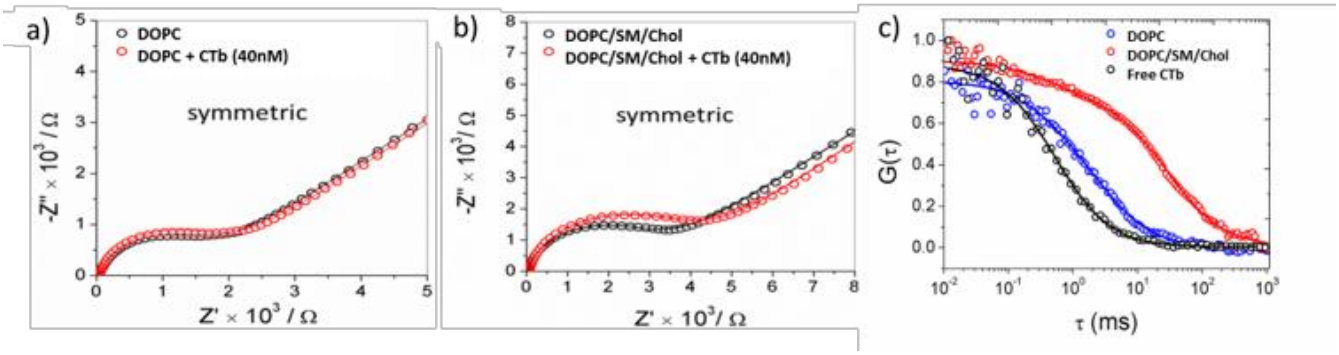

Figure S5. Electrochemical impedance spectra for microcavity array based supported lipid bilayers on gold electrodes with (red) and without (black) the presence of CTb. a) Illustrates EIS data of symmetric DOPC bilayers with and without CTb. b) Represents the respective EIS data without the presence of CTb for symmetric raft-composition bilayers comprised of DOPC/SM/Chol (2:2:1) (mol/mol/mol). The EIS data are recorded in the presence of 1 mM $[Fe(CN)_6]^{3-/4-}$ internal redox probe in 0.1 M KCl electrolyte solution in PBS buffer at the potential of +0.26 V vs. Ag/AgCl (1 M KCl). c) Shows the ACF curves obtained for free diffusion CTb-A555 in PBS (pH 7.4) (black circles), at the membrane surface of symmetric DOPC lipid bilayers (blue circles) and DOPC/SM/Chol (2:2:1) (mol/mol/mol) (red circles).

Fluorescence Lifetime Spectroscopy (FLIM) of bound CTb

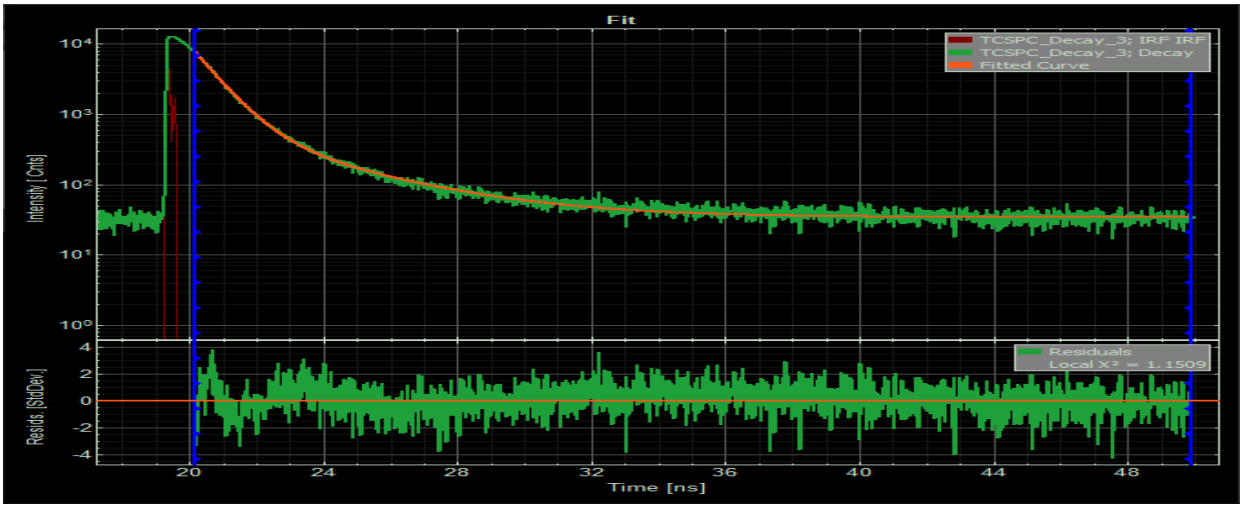

Figure S6. Fluorescent lifetime imaging decay of labelled CTb-Alexa555 for composition DOPC/SM/Chol (4:4:2 mol %) + GM1 (1 mol %).

Table S2. Fluorescence lifetime of CTb-A555 after binding to GM 1 in asymmetric and symmetric lipid bilayers.

	Ex/Em	Asym DOPC + GM1 (1 mol%)		Asym DOPC/SM/Chol (2:2:1) + GM1 (1 mol%)		Asym DOPC/SM (1:1) + GM1 (1 mol%)		Sym DOPC/SM/Chol 2:2:1 + GM1 (1 mol%)		Sym DOPC/SM (1:1) + GM1 (1 mol%)	
	λ (nm)	τ (ns)	τ_{Amp} (%)	τ (ns)	τ_{Amp} (%)	τ (ns)	τ_{Amp} (%)	τ (ns)	τ_{Amp} (%)	τ (ns)	τ_{Amp} (%)
CTb-A555	555/580	τ_1 = 3.12	20	τ_1 = 2.71	23	τ_1 = 3.00	20	τ_1 = 2.84	16	τ_1 = 3.34	26
		τ_2 = 0.67	80	τ_2 = 0.77	77	τ_2 = 0.74	80	τ_2 = 0.78	84	τ_2 = 1.03	74

Table S3. Lateral diffusion of labeled CTb-A555 and population of fast and slow diffusing against CTb unlabelled concentration. The asymmetric lipid bilayers comprised of DOPC +GM1 with 1mol% and 5%mol% of GM1 in the distal leaflet.

Distal leaflet composition	CTb (nM)	$D_{CTb}(\mu m^2 s^{-1})$	Population CTb		Number of molecules CTb (N_{CTb})
		D_{CTb} fast	$\%P_{CTb}$ fast	$\%P_{CTb}$ slow	
DOPC + 1% (mol) GM1	4	5.23 ± 3.29	100	-	5.54 ± 4.09
	10	4.43 ± 1.46	67.1 ± 24.3	32.9 ± 23.3	4.46 ± 1.51
	40	4.74 ± 0.89	28.3 ± 14.5	71.7 ± 14.4	5.34 ± 2.47
	80	2.51 ± 0.79	5.7 ± 2.3	94.3 ± 2.3	2.69 ± 1.12
DOPC + 5% (mol) GM1	4	8.18 ± 1.75	100	-	4.43 ± 1.13
	10	5.30 ± 1.09	100	-	5.07 ± 1.41
	20	4.72 ± 1.16	89.2 ± 1.2	10.8 ± 1.2	7.59 ± 2.02
	40	2.36 ± 1.12	8.2 ± 5.7	91.8 ± 5.7	4.02 ± 1.15
	80	1.93 ± 0.69	9.7 ± 8.9	90.2 ± 5.6	3.34 ± 1.98

Table S4. Lateral diffusion of labelled CTb-A555 and population of fast and slow diffusing against CTb unlabelled concentration. The asymmetric lipid bilayers comprised of DOPC/SM (1:1) (mol/mol) + GM1 with 1 mol% and 5 mol% of GM1 in the distal leaflet shown the effect of SM containing membrane in CTb diffusion within CTb concentration.

Distal leaflet composition	CTb (nM)	D_{CTb} ($\mu m^2.s^{-1}$)	Population CTb		Number of molecules CTb (N_{CTb})	D_{DOPE} ($\mu m^2.s^{-1}$)
		D_{CTb} fast	$\%P_{CTb}$ fast	$\%P_{CTb}$ slow		
DOPC/SM (1:1) + 1% (mol) GM1	4	1.76 ± 0.64	54 ± 27	55 ± 31	7.28 ± 2.67	5.4 ± 1.1
	10	1.10 ± 0.97	29 ± 26	71 ± 26	4.47 ± 3.81	5.0 ± 0.9
	20	0.87 ± 0.43	23 ± 25	77 ± 25	8.44 ± 7.31	4.0 ± 0.7
	40	0.36 ± 0.37	19 ± 19	81 ± 19	4.38 ± 3.37	2.0 ± 0.8
DOPC/SM (1:1) + 5% (mol) GM1	4	0.60 ± 0.19	36 ± 29	64 ± 29	4.86 ± 3.45	5.3 ± 1.0
	10	0.41 ± 0.21	18 ± 8	88 ± 12	3.21 ± 2.16	4.3 ± 1.1
	20	0.20 ± 0.29	7 ± 11	95 ± 5	3.13 ± 1.87	2.4 ± 0.4

References

(1) Mallon, C. T.; Jose, B.; Forster, R. J.; Keyes, T. E. Protein Nanopatterning and Release from Gold Nano-Cavity Arrays. *Chem. Commun.* 2010, *46* (1), 106–108.

(2) Adamson, K.; Spain, E.; Prendergast, U.; Moran, N.; Forster, R. J.; Keyes, T. E. Peptide-Mediated Platelet Capture at Gold Micropore Arrays. *ACS Appl Mater Interfaces* 2016, *8* (47), 32189–32201.

(3) Jose, B.; Mallon, C. T.; Forster, R. J.; Blackledge, C.; Keyes, T. E. Lipid Bilayer Assembly at a Gold Nanocavity Array. *Chem. Commun.* 2011, *47* (46), 12530–12532.

(4) Müller, C. B.; Loman, A.; Pacheco, V.; Koberling, F.; Willbold, D.; Richtering, W.; Enderlein, J. Precise Measurement of Diffusion by Multi-Color Dual-Focus Fluorescence Correlation Spectroscopy. *EPL (Europhysics Letters)* 2008, *83* (4), 46001.

(5) Miller, C. E.; Majewski, J.; Watkins, E. B.; Weygand, M.; Kuhl, T. L. Part II: Diffraction from Two-Dimensional Cholera Toxin Crystals Bound to Their Receptors in a Lipid Monolayer. *Biophysical Journal* 2008, *95* (2), 641–647.

Appendix B

Supporting information associated with Chapter 3.

Materials

1,2-dioleoyl-*sn*-glycero-3-phosphocholine (DOPC), porcine brain N-(octadecanoyl)-sphing-4-enine-1-phosphocholine (SM), cholesterol (Chol), ganglioside GM1, GM3 and GD1a were purchased with maximum degree of purity (> 99%) from Avanti Polar Lipids (Alabama, USA) and used without further purification. 1,2-dioleoyl-*sn*-glycero-3-phosphoethanolamine labelled Atto655 (DOPE-ATTO655), sphingomyelin-ATTO647n (SM-ATTO647n) and 532-ATTO-NHS-ester (ATTO532) were purchase from ATTO-TEC GmbH (Siegen, Germany). Hemagglutinin HA_1 sub-unit (Recombinant Influenza A virus proteins, subtype H3N2, A/Aichi/2/1968, His Tag) was purchased from Invitrogen ThermoFisher. Aqueous solutions were prepared using Milli-Q water (Millipore Corp., Bedford, USA). Polydimethylsiloxane silicon elastomer (PDMS) was purchased from Dow Corning GmbH (Wiesbaden, Germany) and mixed following supplier instructions. Silicon wafers coated with a 100 nm layer of gold on a 50 Å layer of titanium were obtained from AMS Biotechnology Inc. The monodisperse polystyrene latex sphere with a diameter of 1 μm was obtained from Bangs Laboratories Inc. The commercial cyanide free gold plating solution (TG-25 RTU) was obtained from Technic Inc. All other HPLC grade reagents were obtained from Sigma-Aldrich and used as obtained.

Liposome preparation

Briefly, in this work, liposome fusion was used to form the distal lipid leaflet of microcavity supported lipid bilayers (MSLBs). To prepare the liposomes, stock solutions of all vesicle components such as DOPC, brain sphingomyelin and cholesterol 50 mg/mL each, and GM1 (1 mg/mL), GM3 (1 mg/mL) and GD11 (1 mg/mL) were prepared in chloroform and stored in sealed glass vials at -20°C. Fluorescence labelled DOPE-ATTO655 was mixed in a ratio of 50000:1 mol/mol with unlabelled lipids for fluorescence correlation spectroscopy (FLCS) studies. For electrochemical measurements, as electrochemical impedance spectroscopy (EIS) is label-free, fluorescent probe was not included during the preparation of liposomes. Aliquots of the appropriate amounts of the stock solutions were mixed in clean amber glass vials and dried under

a gentle stream of nitrogen and placed under vacuum for 1 h. The lipids were rehydrated in 1 mL of PBS buffer (pH 7.4) and vortexed vigorously for at least 60 s. Large unilamellar vesicles (LUVs) were prepared by extruding the multilamellar vesicle suspension 11x against a polycarbonate membrane (0.1 µm pore size) using a mini-extruder (Avanti Polar Lipids). The LUVs were diluted to 0.25 mg/mL. Liposomes composed of SM were extruded at 45°C, above the SM transition temperature, to guarantee that vesicles are in the fluidic state. Figure S1 shows the size distribution of the liposomes obtained by dynamic light scattering (DLS) before (Figure S1a) and after extrusion (Figure S1b).

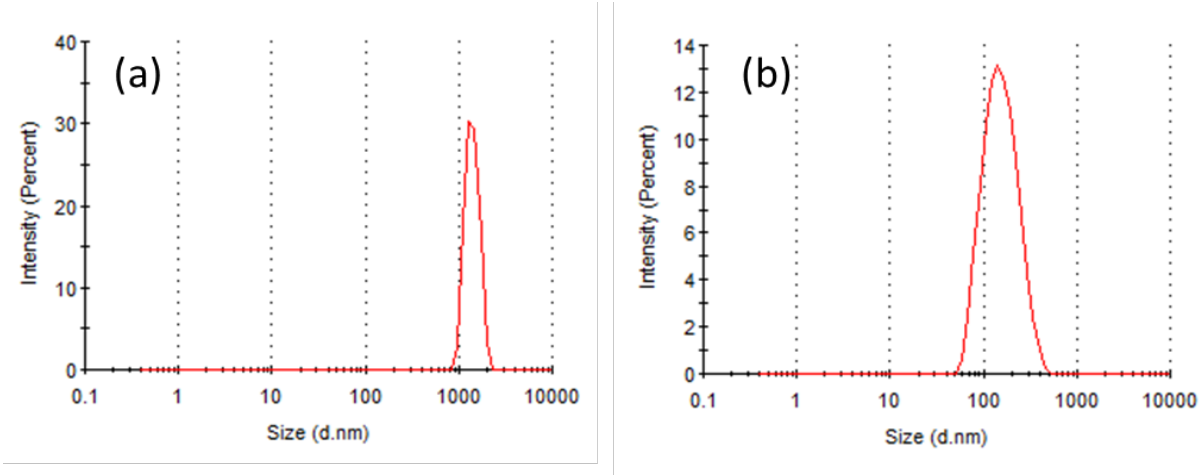

Figure S1 – Size distribution of liposomes obtained by DLS (a) before and (b) after extrusion against polycarbonate membranes of 0.1 µm diameter pore size. The average size of liposomes after extrusion was 120 nm with polydispersity index (PDI) of approximately 0.1.

Fluorescent labelling of HA_1

For FLCS measurements, HA_1 was labelled with ATTO532 NHS-ester (ATTO-Tec GmbH) following the method suggested by the seller. The conjugation was performed by reacting to the succinimidyl ester moiety of ATTO dye with terminal amines in the protein at basic pH. To avoid ester hydrolysis and therefore inactivation of the dye, ATTO532 NHS-ester was diluted in anhydrous DMSO (HPLC grade). Briefly, HA_1 was diluted in PBS buffer (pH 8.3) to the final concentration of 0.2 mg/mL. ATTO532 ATTO532 NHS-ester was added to 400 µL of HA_1 in a molar ratio of 3:1 of dye to protein to ensure adequate reaction with protein. The reaction was conducted under gentle agitation for 1 h at room temperature in the dark. The labelled protein was separated from unreacted dye by dialysis in a centrifugal filter membrane (AMICON 10 kDa) at

10000 RPM for 15 min. The process was repeated 6 times by the addition of 1 mL of PBS buffer pH 7.4 each time. The labelling of HA_1 was determined by UV-VIS spectroscopy (Figure S2) and by the lateral diffusion of the protein in solution measured by FLCS by fitting the autocorrelation functions (ACFs).

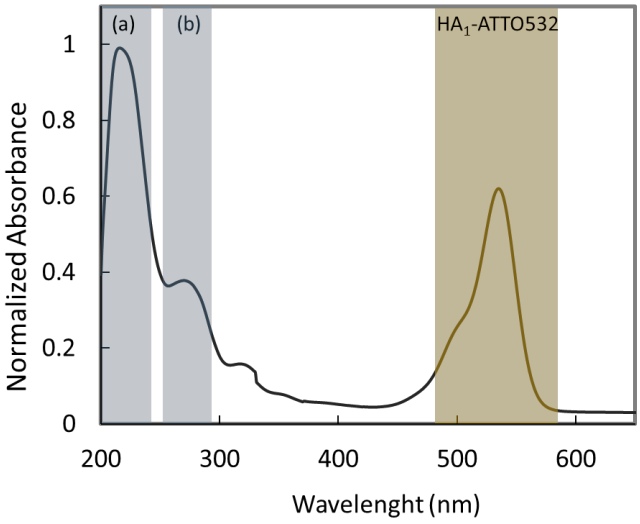

Figure S2 – Normalised Absorbance spectrum of labelled HA_1 after reaction with ATTO532-NHS-ester. The insertions (a) and (b) indicates the maximum absorbance of trypsin and tyrosine with the probe maxima marked in yellow.[1,2]

Electrochemical Impedance Spectroscopy

Electrochemical impedance measurements were performed on a CHI 760e bipotentiostat (CH Instruments Inc., Austin, TX) in a three-electrode cell consisting of a Ag/AgCl (1 M KCl) reference electrode, platinum coiled wire as a counter electrode and the gold substrate with microcavity array served as the working electrode. 1 mM $[Fe(CN)_6]^{3-/4-}$ was used as an internal redox probe in 0.1 M KCl electrolyte solution in PBS buffer. The EIS recording was performed in the frequency region between 10^4 and 0.01 Hz with a bias potential of 0.26 V vs Ag/AgCl. The impedance spectra were fit to an equivalent circuit model (ECM) as described previously [3] and the same has been shown in Figure 1a (inset) main text. In the circuit, $\boldsymbol{R_S}$ is the solution resistance, $\boldsymbol{R_M}$ and $\boldsymbol{CPE_M}$ represents the resistance and constant phase element of the membrane and $\boldsymbol{R_C}$ and $\boldsymbol{CPE_C}$ represents the cavity resistance and constant phase element of the gold substrate. The constant phase elements (CPE) were used in the equivalent circuit to provide to account for the heterogeneity of the SLBs in

microcavity array. The quality of fit was assessed from χ^2 values and visual inspection. The impedance of the CPE can be calculated using Eq. (S1);

$$\boldsymbol{Z_{CPE} = \frac{1}{Q(j\omega)^{\beta}}} \quad \text{(S1)}$$

where $\boldsymbol{Q}$ and the exponent $\boldsymbol{\beta}$ represent respectively the CPE and an empirical constant related to the frequency dispersion. When β close to 1, it behaves like an ideal capacitor, and when $\beta < 1$, the capacitance depends on the frequency. From our fitting using the ECM model, we obtained a β value in the range of 0.93-0.96. Note the membrane capacitance values are reported are not a true capacitance value rather it is CPE ($\boldsymbol{Q}$) values which do not depend on any particular frequency unlike a true capacitance value (which is frequency dependent). Note, the relative change in resistance and capacitance values are not normalized with respect to electrode surface area.

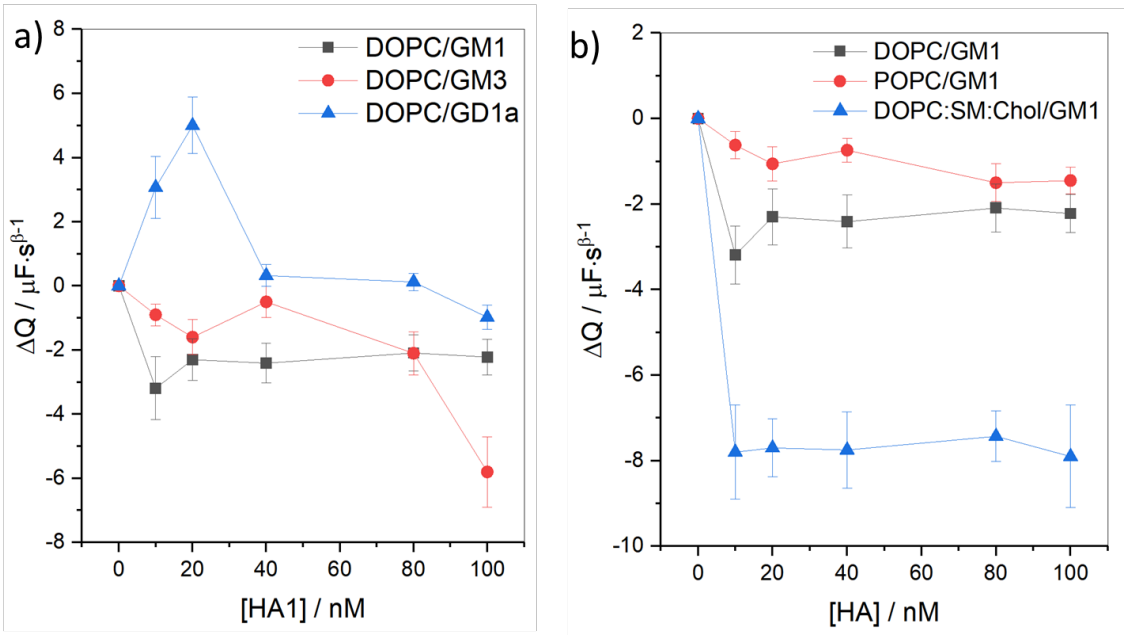

Figure S3 – a) Representative relative change in capacitance of DOPC membranes with varied embedded receptors upon HA_1 interaction. b) relative change in capacitance of different membrane compositions with GM1 receptor upon HA_1 interaction.

Hill-Waud binding model:

The relative change in membrane resistance from EIS data for different lipid compositions versus HA_1 binding concentrations (see Fig. 2a, main text) were fit iteratively to the Hill-Waud expression, as defined by equation (S2) and the extracted fit data are shown in Table S1.

$$\Delta \boldsymbol{R} = \frac{\Delta \boldsymbol{R_{sat}}(\boldsymbol{C})^{\boldsymbol{n}}}{(\boldsymbol{K_D})^{\boldsymbol{n}}+(\boldsymbol{C})^{\boldsymbol{n}}} \qquad \text{(S2)}$$

where $\Delta \boldsymbol{R}$ is the change in membrane resistance, defined by $\boldsymbol{R_M^0} - \boldsymbol{R_M^{HA1}}$, $\Delta \boldsymbol{R_{sat}}$ is absorption capacity or change in resistance at maximum surface loading that relates to the number of available binding sites, $\boldsymbol{K_D}$ is the empirical apparent equilibrium dissociation constant, $\boldsymbol{C}$ is the concentration of the HA_1 and $\boldsymbol{n}$ (dimensionless) is the Hill coefficient of cooperativity.[4] The "$\boldsymbol{n}$" constant in the Hill-Waud model (Eq. S2) relates to the strength of the adsorption or often relates to cooperative effect.[5] $\boldsymbol{n}$<1 indicates chemically mediated absorption i.e., multiple binding sites with a different affinity (negative cooperativity), $\boldsymbol{n}$ =1 reverts the expression to Langmuir isotherm, where all binding sites are equal, i.e. non cooperative equilibrium binding, and $\boldsymbol{n}$ > 1 indicates positive cooperativity.

Table S1. Data obtained for HA_1 by fitting relative change in resistance (ΔR) of different lipid compositions to Hill-Waud model.

membrane composition	K_D (nM)	ΔR_{sat} (MΩ)	n	R^2
DOPC/GM1	41.3±9	2.11±0.27	1.81	0.97
DOPC/GM3	23.96±4	0.25±0.02	1.45	0.98
DOPC/GD1	17.47±2	1.66±0.08	2.56	0.97

Binding of HA_1 to MSLBs in absence of GSLs

Control experiments were carried out to bare lipid membranes comprised of DOPC and DOPC/SM/Chol (4:4:2) without GSLs. The results obtained have not shown non-specific binding of HA_1 to MSLBs in absence of GSLs as the membrane resistivity remains constant after exposing the lipid bilayers to HA_1 for 30 min. Figure S4 shows the results obtained for bare DOPC bilayer (Figure S4a) and to the complex lipid bilayer (Figure S4b).

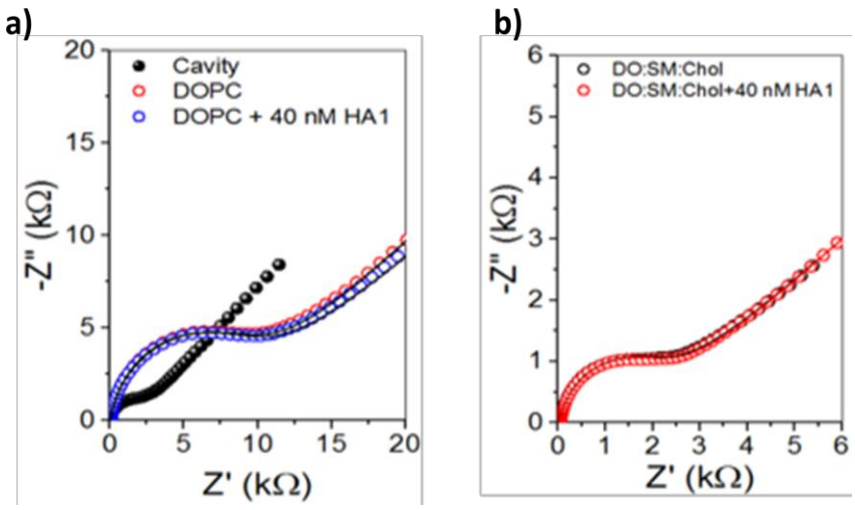

Figure S4 – Electrochemical Impedance Spectroscopy of control experiments without GSLs. (a) Symmetric DOPC lipid bilayers and (b) symmetric lipid bilayers comprised of DOPC/SM/Chol (4:4:2). Non-specific binding was not observed after reacting to the lipid bilayers with HA_1 (40 nM) for 30 min.

Fluorescence Lifetime Correlation Spectroscopy

FLCS measurements were performed at PDMS-MSLBs (Figure S5) platform where the labelled phospholipid DOPE-ATTO655 was introduced to the distal leaflet during the liposome fusion. The conjugated HA1-ATTO532 was inserted in the microfluidic device by the tubing port connection and was left to equilibrate for 1 hour. After, the microfluidic chamber was rinsed with 1 mL of PBS buffer in order to remove any unreacted protein. The autocorrelated data obtained for labelled DOPE-ATTO655 and bound HA1-ATTO532 were fitted to 2D diffusion model (Eq. S3).

$$G(\tau) = \frac{1}{N}\left[1 + \left[\frac{\tau}{\tau_D}\right]^{\alpha}\right]^{-1} \qquad \text{(S3)}$$

The lateral diffusion of labelled HA_1-ATTO532 and the free ATTO532, e.g. unbound dye in PBS buffer, were calculated by fitting the ACFs obtained in for 10 nM solution of each molecule to a 3D model (Eq. S4). The Equation S4 includes a κ term, which defines the shape of the confocal volume.

$$G(\tau) = \frac{1}{N}\left[1 + \left[\frac{\tau}{\tau_D}\right]^{\alpha}\right]^{-1}\left[1 + \left[\frac{\tau}{\tau_D}\right]^{\alpha}\frac{1}{\kappa^2}\right]^{-1/2} \quad \text{(S4)}$$

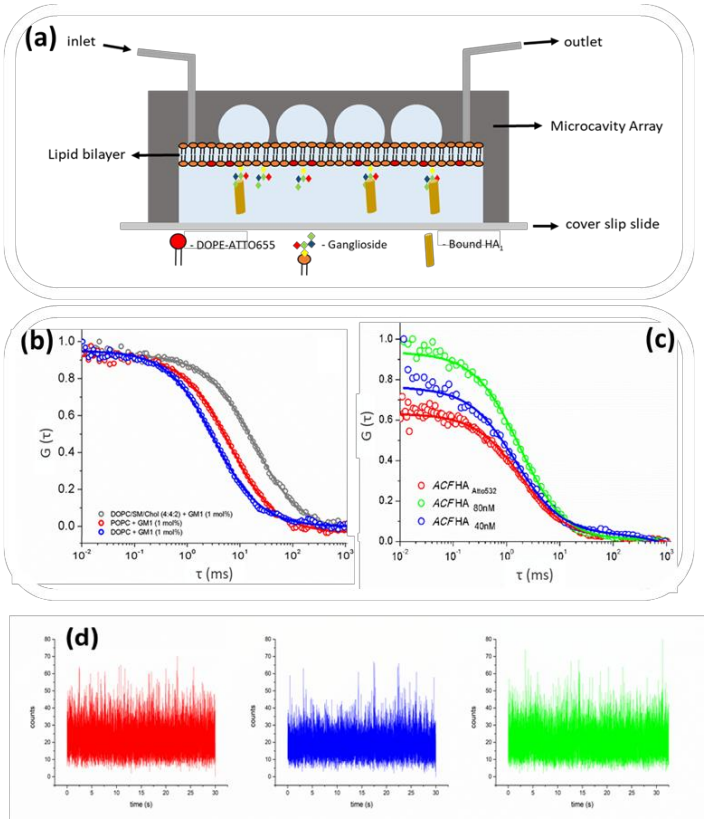

Figure S5 – (a) Schematic representation of bound HA_1 to gangliosides at MSLBs. (b) Representative autocorrelation functions (ACFs) obtained for labelled DOPE-ATTO655 incorporated into DOPC (blue circles), POPC (red circles) and DOPC/SM/Chol (4:4:2) (grey circles) MSLBs doped with GM1 (1 mol%). (c) Representative fitted ACFs of bound HA_1 to DOPC lipid bilayer doped with GD1a (1 mol%) at different HA_1 concentrations, indicating the absence of protein aggregation. (d) Intensity time-trace obtained at different concentrations of HA_1-ATTO532 (10 nM (red), 40 nM (blue), 80 nM (green)) to DOPC bilayer containing GM3 (1 mol%).

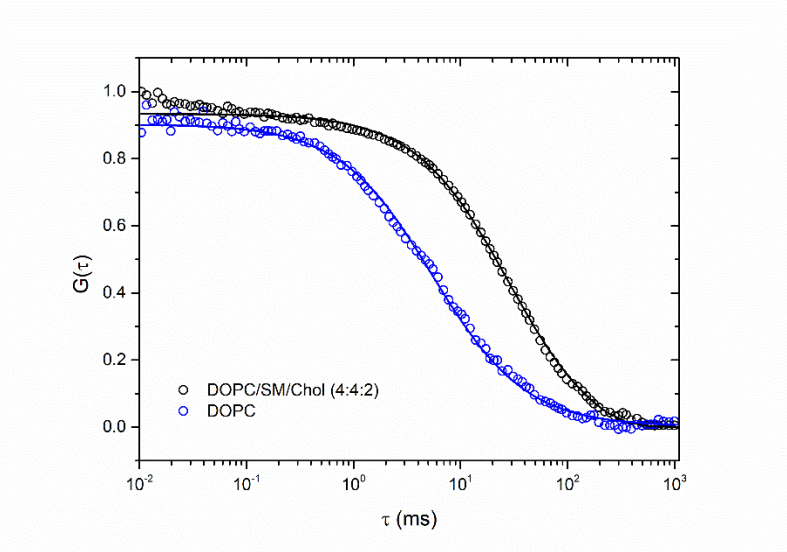

Figure S6 – FLCS of labelled SM-ATTO647n obtained from DOPC (blue circles) and DOPC/SM/Chol (4:4:2) (black circles) MSLBs.

Saffman-Delbrück (SD) model:

Due to the suspended character of planar MSLBs, where both leaflets are in contact with bulk aqueous phase, we assume the Saffman-Delbrück model (Equation S5) applies and this was used to estimate the diameter of the membrane associated complex.

$$D = \frac{KT}{4\pi\mu h}\left(ln\left(\frac{\mu h}{\mu' r}\right) - \gamma\right) \qquad \text{(S5)}$$

Where D is the lateral diffusion obtained from FLCS, K is Boltzmann constant, T is the absolute temperature, r is the radius of the cylindrical membrane inclusion, h is the membrane thickness, γ is Euler-Mascheroni constant (approx. 0.577), μ and μ' are the membrane viscosity and the bulk solution viscosity, respectively. The parameters used to estimate the membrane associated complexes were membrane height h = 3.8 nm, viscosity of the surrounding media μ' = 0.001 Pa.s and membrane viscosity μ = 0.05 Pa.s.

Table S2. Lateral diffusion of labelled HA_1-ATTO532 obtained after binding to lipid membranes containing GM1 (1 mol %) in different lipid systems, from FLCS. The lateral diffusion of DOPE-ATTO655 decreases with membranes fluidity, here expressed by the DOPE diffusivity.

Lipid bilayer + GM1 (1 mol %)	Lateral Diffusion ($\mu m^2 s^{-1}$)		N_{HA1}
	HA_1-ATTO532	DOPE-ATTO655	
DOPC	5.0 ± 0.4	10.0 ± 0.5	6.3 ± 0.6
POPC	3.3 ± 0.4	6.3 ± 0.6	3.5 ± 0.4
DOPC/SM/Chol (4:4:2)	1.8 ± 0.5	3.0 ± 0.4	2.0 ± 0.6

References

(1) Schmid, F.-X. Biological Macromolecules: UV-Visible Spectrophotometry. In *Encyclopedia of Life Sciences*; John Wiley & Sons, Ltd, Ed.; John Wiley & Sons, Ltd: Chichester, UK, 2001; p a0003142.

(2) Antosiewicz, J. M.; Shugar, D. UV–Vis Spectroscopy of Tyrosine Side-Groups in Studies of Protein Structure. Part 2: Selected Applications. *Biophys Rev* 2016, *8* (2), 163–177.

(3) Maher, S.; Basit, H.; Forster, R. J.; Keyes, T. E. Micron Dimensioned Cavity Array Supported Lipid Bilayers for the Electrochemical Investigation of Ionophore Activity. *Bioelectrochemistry* 2016, *112*, 16–23.

(4) Shi, J.; Yang, T.; Kataoka, S.; Zhang, Y.; Diaz, A. J.; Cremer, P. S. GM $_1$ Clustering Inhibits Cholera Toxin Binding in Supported Phospholipid Membranes. *Journal of the American Chemical Society* 2007, *129* (18), 5954–5961.

Appendix C

Supporting information associated with Chapter 4.

TECHNICAL DATA SHEET

BACTERIORHODOPSIN

Some microorganisms have adapted to the high salinity conditions of this environment, such as the species *Halobacterium salinarum*, from which **Bras del Port** has extracted **Bacteriorhodopsin** in the form of a high quality lyophilized purple membrane.

It is a photosensitive protein with important properties that will improve information storage and processing systems (manufacture of optical processors, 3D memories, biosensors, light energy converters in electric systems, among other uses).

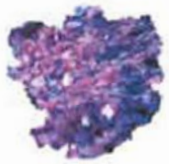

- **Product:** Bacteriorhodopsin in the form of lyophilized *Halobacterium salinarum* MP purple membrane
- **Appearance:** Purple powder
- **Information:**
  - ➢Bacteriorhodopsin MW: 26.5 KD
  - ➢Aminoacids: 248
  - ➢Extinction coefficient: 63,000 M^{-1} cm^{-1}

ANALYSIS* (for a homogenized suspension of 0.5 mg/ml of product in ultra-pure water)

PROTEIC PURITY
> 99% (evaluated in SDS-PAGE)

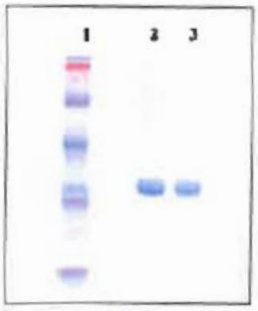

1. MW standard
3. MP-Bras-05

MAXIMUM ABSORPTION: 568 nm

A_{280}/A_{570} RATIO: 2.0

ABSORPTION SPECTRUM (250-700 nm)

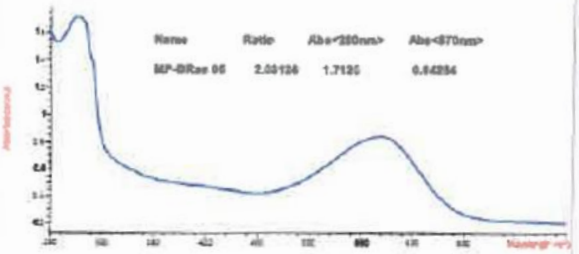

* Analysis January 18th, 2016 (Batch MP-Bras-05)

PACKAGING: 10 mg / 25 mg / 50 mg / 100 mg / 200 mg

CONSERVATION AND STORAGE: Lyophilized powder is very stable for prolonged periods of time being kept dry at room temperature. Aqueous suspensions can be stored at +4ºC for short time, but for longer periods, freezing at -20ºC is recommended.

HANDLING: Purple membrane in suspension tends to keep certain degree of aggregation. Homogenization (e.g. sonication) is recommended to obtain best accuracy.

1st European Maritime Salina certified with the ISO 9001:2008 in all product

BRAS DEL PORT, S.A.

SERVICIO DE CALIDAD

31.03.2020

BRAS DEL PORT, S.A.
Ctra. Cartagena-Alicante, km 85 | PO Box, 1 | 03130 SANTA POLA (Alicante)
Tfno. 96 541 33 47 Fax 96 541 35 13 | e-mail salinas@brasdelport.com | www.brasdelport.com

Labelling of bacteriorhodopsin for Fluorescence Lifetime (Cross)Correlation Spectroscopy - FLCCS/FLCS

The incorporation of bacteriorhodopsin (bR) to proteoliposomes and to MSLBs was conducted using fluorescence studies, such FLCCS and FLCS. To do so, bR was marked ATTO-532 using NHS-ester coupling to an amino residue to covalently bound the ATTO dye to the protein. The labelling procedure used was provided by ATTO-TECH and followed as it is. The labelling efficiency was evaluated by UV-Vis spectroscopy and the degree of labelling (DOL) was measured after dialysis of unreacted ATTO532 dye from the labelled protein. Figure S7 shows the UV-Vis absorption spectra of unlabelled bR (black line) and labelled bR-ATTO532 (green line). The DOL was calculated by comparing the absorbance of protein versus labelled protein using equation S1, indicating a DOL of approximately 60%.

$$DOL = \frac{A_{ATTO532} \cdot \varepsilon_{bR,280}}{(A_{bR,280} - A_{ATTO532}) \cdot \varepsilon_{ATTO532}} \qquad \text{eq. (S1)}$$

Here the extinction coefficient of ATTO532 at 532nm and bR at 280nm were $\varepsilon_{ATTO532} = 1.15 \times 10^5$ $M^{-1}cm^{-1}$ ([1]) and $\varepsilon_{bR280} \approx 63000$ $M^{-1}cm^{-1}$ ([2]), respectively.

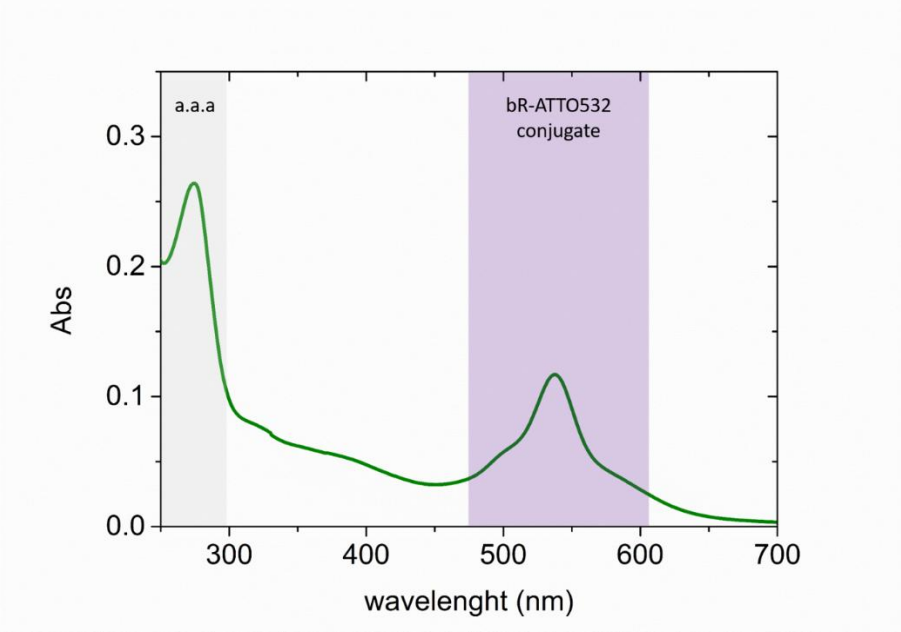

Figure S1. UV-Vis spectra of bR after NHS-ester coupling of bR with ATTO532. The grey insertion represents the aromatic amino acids (a.a.a) absorption region.[3] The purple insertion illustrates the bR-ATTO532 conjugate absorption with maximum absorbance 530-550 nm.

Determination of optimal Titron-X100 concentration for protein incorporation

The optimal concentration of Titron-X100 for the protein incorporation using liposomes comprised of DOPC was determined by the change on the optical density of the liposomes solution, as previously proposed ([4]). Additionally, the change on the liposomes size was monitored by Dynamic Light Scattering (DLS) (Malvern, Zetasizer). The objective of this method is to create spaces into the liposome with the detergent and fill the gaps with bR. The UV-Vis (Figure S5, open blue circles) shows that the optical density (OD) of the solution against 540 nm initially increases to around 2 mM of Triton X-100. Then OD linearly decreases until approximately 10.5 mM of Triton X-100. At this point, the liposomes are partially to completely dissolved by the detergent in solution.[4] The size of liposomes monitored against detergent concentration indicates that the liposomes swell due to the insertion of detergent to the lipid bilayer until disruption at 10 – 11 mM. (Figure S5, black circles) Therefore, to avoid partial disruption of the liposomes during bR incorporation, the concentration of Triton X-100 used in this work was 5 mM.

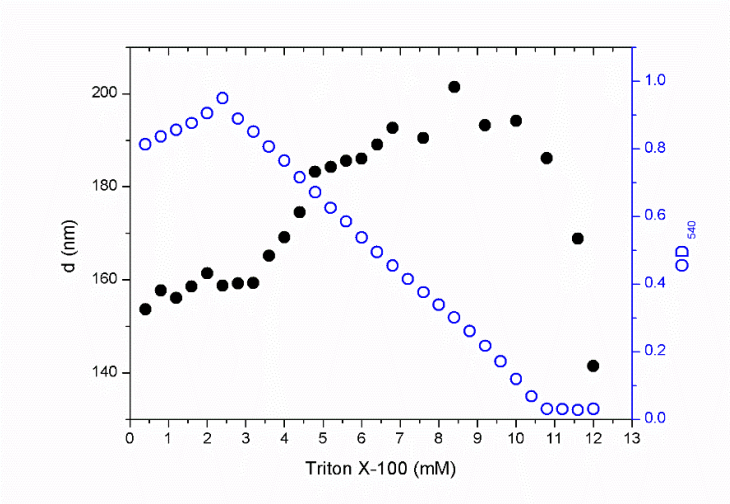

Figure S2. Titration of DOPC liposomes (4mg/ml) against Triton X-100. Blue open circles express the OD collected at 540nm. Full black circles correspond to the size of the liposomes measured by DLS.

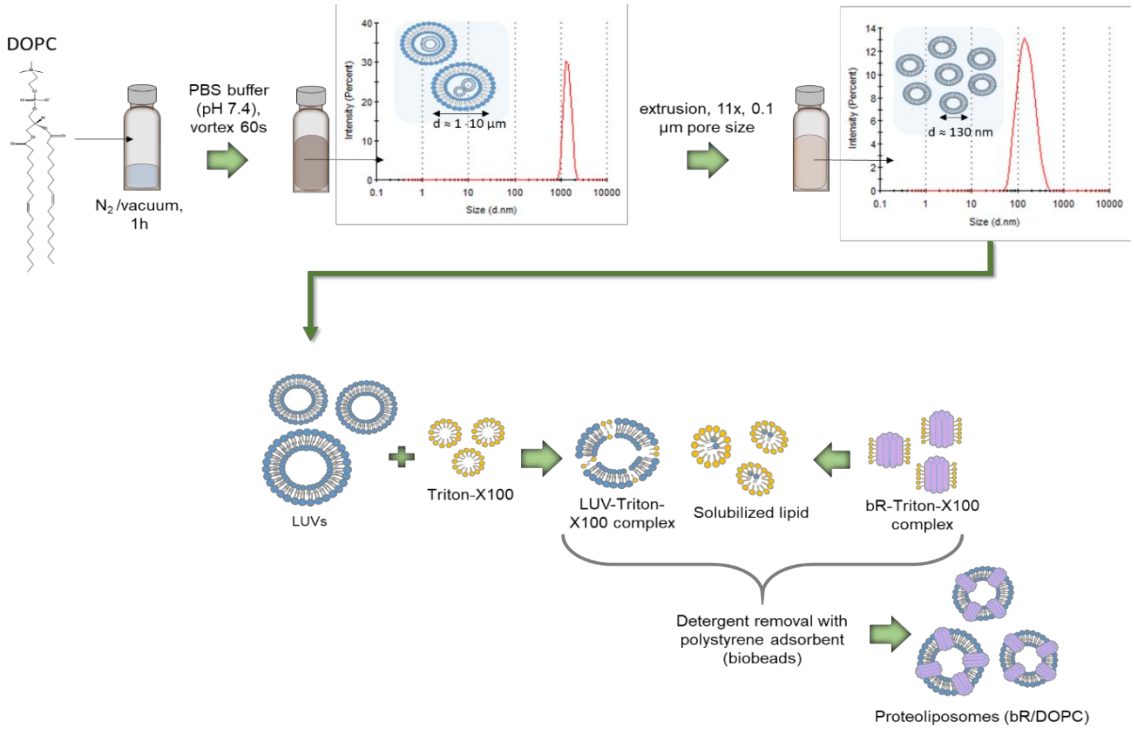

Schematic S1. Schematic illustration of proteoliposomes preparation comprised of DOPC and containing bR.

Electroplating of Gold

In order to obtain a semi-hemispherical gold microcavity array, gold was electrodeposit to pre-casted monolayer of polystyrene microspheres using a cyanide free electroplating solution (Technic Inc.) The gold solution was purged with nitrogen for at least 30 min before reaction. Gold was electrodeposited at -0.6 V (vs. Ag/AgCl) using a 3-electrod set up with the gold array as working electrode, Ag/AgCl (KCl 1M) as reference electrode and a platinum wire as counter-electrode. The gold deposition was controlled by the evolution of current over time (Figure S3a). The electrodeposition was stopped at the lower current, which represents when metal had grown to the hemispherical point of the PS spheres. To remove residual electroplating gold solution, the resulting substrate is rinsed with deionized water, ethanol and dried under nitrogen flow. Then, the substrates were electrochemically cleaned in H_2SO_4 (10mM) through cyclic voltammetry (Figure S3b). The substrates were then submerged in 1 mM 6-mercapto-1-hexanol in ethanol to allow self-assembled monolayer formation (SAM) overnight (Figure S3c). After SAM formation the PS spheres were removed by sonicating the substrates in THF for 5 min. To prefill the microcavities with the conducting electrolyte the substrates were sonicated in 0.1 M KCl for 10 minutes prior to lipid bilayer assembly.

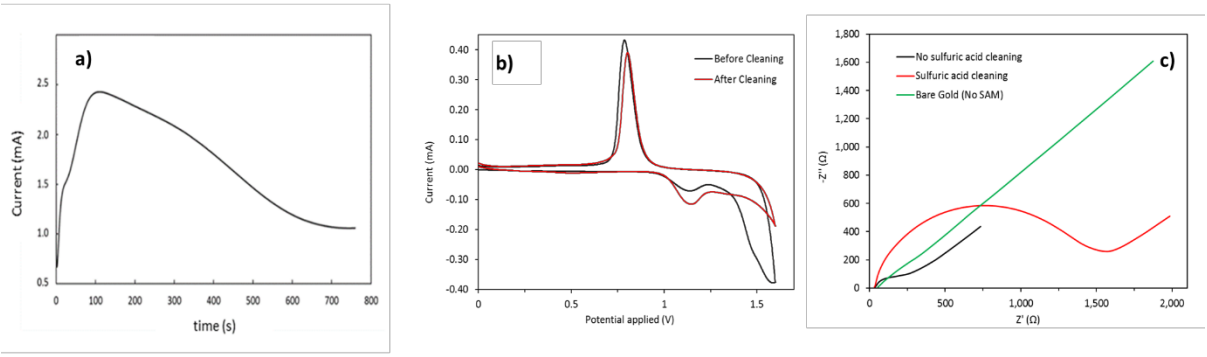

Figure S3. (a) Time-current of gold electroplating. (b) Sulphuric acid potential cycling cleaning of gold microcavity arrays before (black line) and after (red line) 6 cycles at 40 mV/s versus (Ag/AgCl) reference electrode. (c) Shows the Nyquist plots obtained after formation of self-assembled monolayer (SAM) of 6-mercapto-1-hexanol over gold-microcavity arrays before (black

line) and after (red line) potential cycling cleaning. Green line represents the impedance spectroscopy of a bare gold substrate without SAM. The impedance was evaluated in 1 mM of ferricianide/ferrocyanide ($Fe^{2+/3+}$) with 0.1M KCl at 0.26V against (Ag/AgCl) reference electrode. The frequency range of measurement was 10^4 Hz – 10^{-1} Hz.

Characterization of PDMS and Gold µcavity arrays

The lipid bilayers comprised of DOPC/bR were spanned across PDMS and Gold arrays prepared using polystyrene (PS) spheres templating. In order to obtain a highly closed packed array, the Gold arrays were prepared by gravity-assisted lithography of PS, followed by gold electroplating. The dimensions of microcavities were analyzed with FESEM as illustrated in Figures S4. Top line shows the microcavity arrays obtained after gold electroplating and PS removal, indicating the highly ordered closed packed arrays over micrometer range. In order to highlight the lateral structure and the individual cavities dimensions on gold-arrays, tilted (+25°) and profile images were collected (bottom line), indicating depth and diameter of approximately 0.5 µm and 1 µm, respectively.

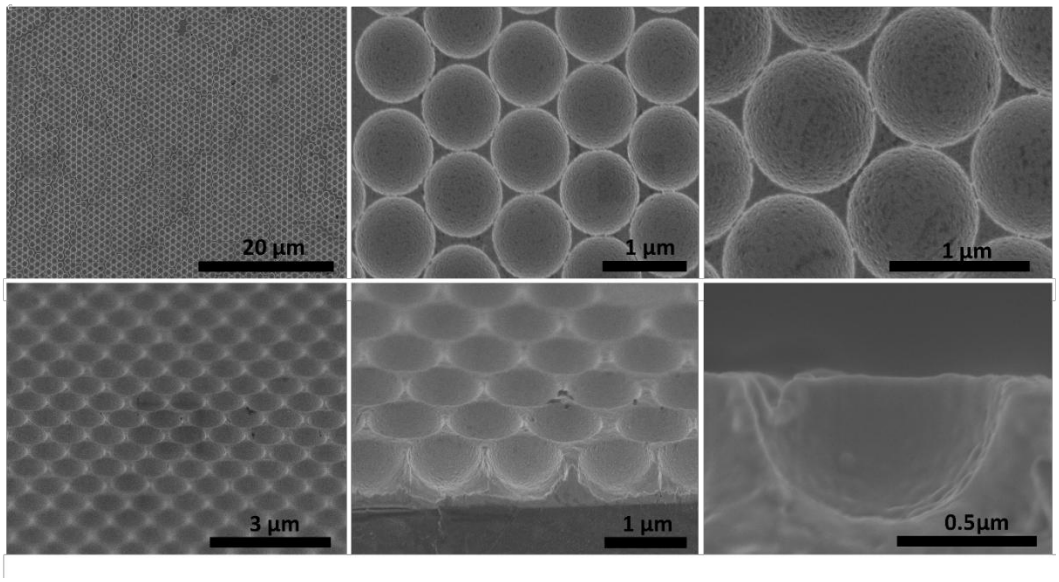

Figure S4. Field Emission Scanning Electron Microscopy (FESEM) of gold microcavity array formed by gold electrodeposition to pre-casted PS microspheres (1 um) monolayer. The top line shows the hexagonal highly ordered array from topview. The tilted and profile images in the

bottom line illustrates the lateral and axial dimensions obtained for gold microcavities to be approximately height = 0.50 µm and diameter = 1 µm.

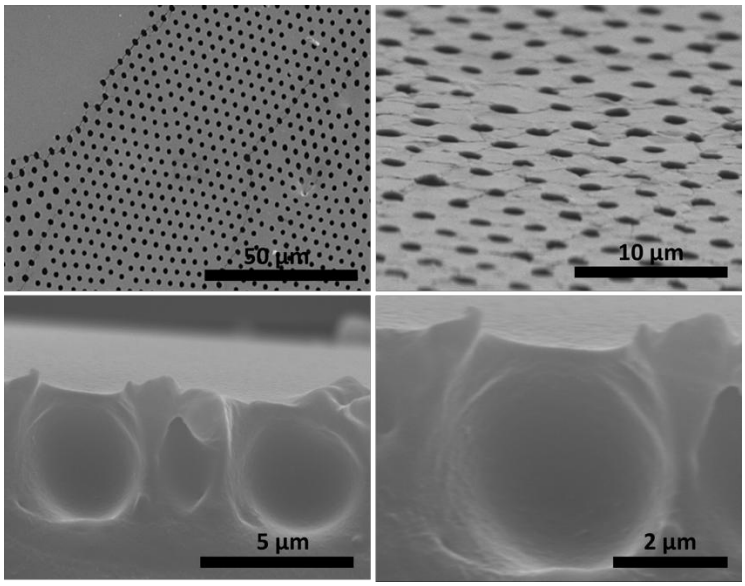

Figure S5. Scanning electron microscopy (SEM) of PDMS microcavity arrays. Top shows the microcavity array after PS removal over a large area and a tilted close to the array, respectively. Figures (c) and (d) show the profile structure of individual microcavities. The dimensions obtained for the microcavities were approximately height = 3.2 µm, diameter = 4.5 µm.

Electrochemical Impedance Spectroscopy and Chronoamperometry of DOPC lipid bilayers

Figure S6a shows the Nyquist plot obtained after incorporation of bR to MSLBs. The impedance was evaluated in 0.1 M KCl as supportting electrolyte (pH 5.5) at 0V (vs Ag/AgCl) using an AC amplitude of 0.01 V with a frequency range of 10^4 Hz to 10^{-1} Hz. The membrane resistivity (Rm) and capacitance (Cm) obtained for the lipid membranes after fitting to model previously reported are displayed in table S1. The membrane resistance and capacitance are in accordanc The values obtained from Rm and Cm of DOPC previously reported by DOPC lipid bilayer were approximately 6 MOhm and 6.1 µF.Sm-1. which is in good agreement with to previous values reported by our group[5] and those reported tethered supported lipid bilayers.[6]

Table S1. Electrochemical properties of lipid bilayers containing bR.

bR (mol %)	Rm (MΩ)	Cm (μF.S^{m-1})
0.01	4.8 ± 0.8	3.1 ± 0.1
0.03	3.7 ± 0.5	4.5 ± 0.1
0.3	2.2 ± 0.4	6.3 ± 0.2
3	1.2 ± 0.2	8.7 ± 0.3

Figure S6b shows the photocurrent response of a DOPC bilayer in absence of bR to the 2 mW LED at wavelength 550 nm. Here, a sharp photo-current signal of approximatly 7 nA/cm^2 was observed with LED switched on. This small contribution to a change in current may be an artifact of the photoelectric effect or due to static interference to the electronic aparatus.

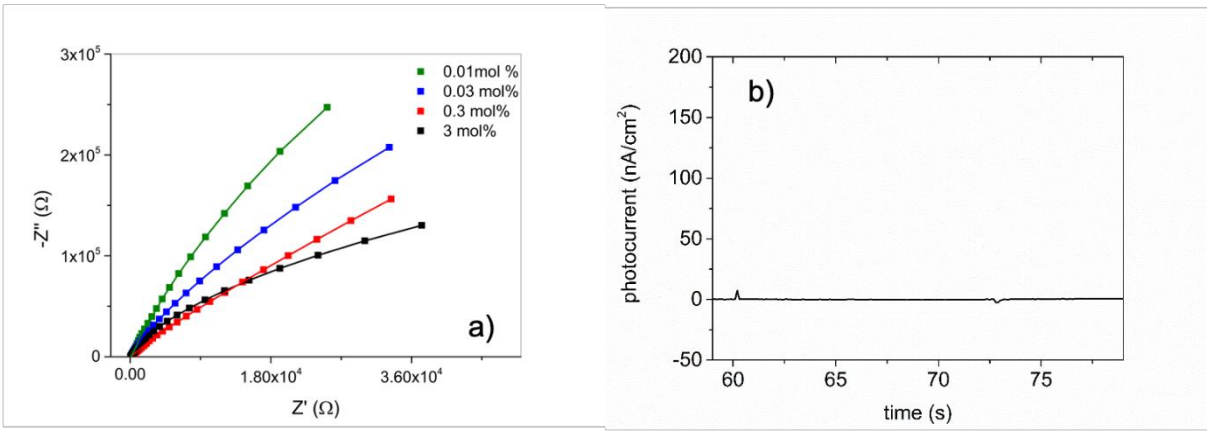

Figure S6. (a) EIS of MSLBs containing bR. (b) Photo-current of a gold-MSLB comprised of DOPC, i.e. background photocurrent in absence of reconstituted bR.

Table S2. Fitted decays of bR at different concentrations. A represents the amplitude and t decay time.

Concentration of bR (mol%)	Photoactivation				Photodeactivation	
	I_{fast} (nA/cm2)	τ_{fast} (s)	I_{slow} (nA/cm2)	τ_{slow} (s)	I (nA/cm2)	τ (s)
3	208.3 ± 31.2	0.037 ± 0.06	23.7 ± 5.4	0.365 ± 0.025	-133.5 ± 15.2	0.155 ± 0.057
0.3	88.9 ± 15.4	0.026 ± 0.04	5.67 ± 1.6	0.276 ± 0.024	-47.5 ± 10.7	0.122 ± 0.026
0.03	29.3 ± 7.5	0.031 ± 0.03	2.73 ± 0.4	0.321 ± 0.031	-23.2 ± 6.3	0.134 ± 0.018
0.01	4.37 ± 1.2	0.021 ± 0.02	0.47 ± 0.02	0.252 ± 0.012	-13.1 ± 4.2	0.112 ± 0.027

Table S3. Kinetics of photoactivation of bR-MSLBs containing 3 mol% of protein within a range of pH (3.5 – 9.5).

pH	Photoactivation (ON)			
	I_{fast} (nA/cm2)	t_{fast} (s)	I_{slow} (nA/cm2)	t_{slow} (s)
3.5	131.8 ± 27.2	0.021 ± 0.003	5.2 ± 1.6	0.178 ± 0.021
4.5	133.5 ± 25.4	0.029 ± 0.006	12.1 ± 3.3	0.192 ± 0.018
5.5	153 ± 31.7	0.027 ± 0.005	7.8 ± 2.5	0.272 ± 0.022
6.5	22.4 ± 9.8	0.031 ± 0.006	9.3 ± 2.2	0.306 ± 0.036
7.5	17.1 ± 3.6	0.029 ± 0.004	6.2 ± 1.5	0.421 ± 0.052
8.5	32.1 ± 7.5	0.032 ± 0.007	2.6 ± 1.1	0.698 ± 0.041
9.5	62.9 ± 13.7	0.029 ± 0.005	1.2 ± 0.8	0.783 ± 0.083

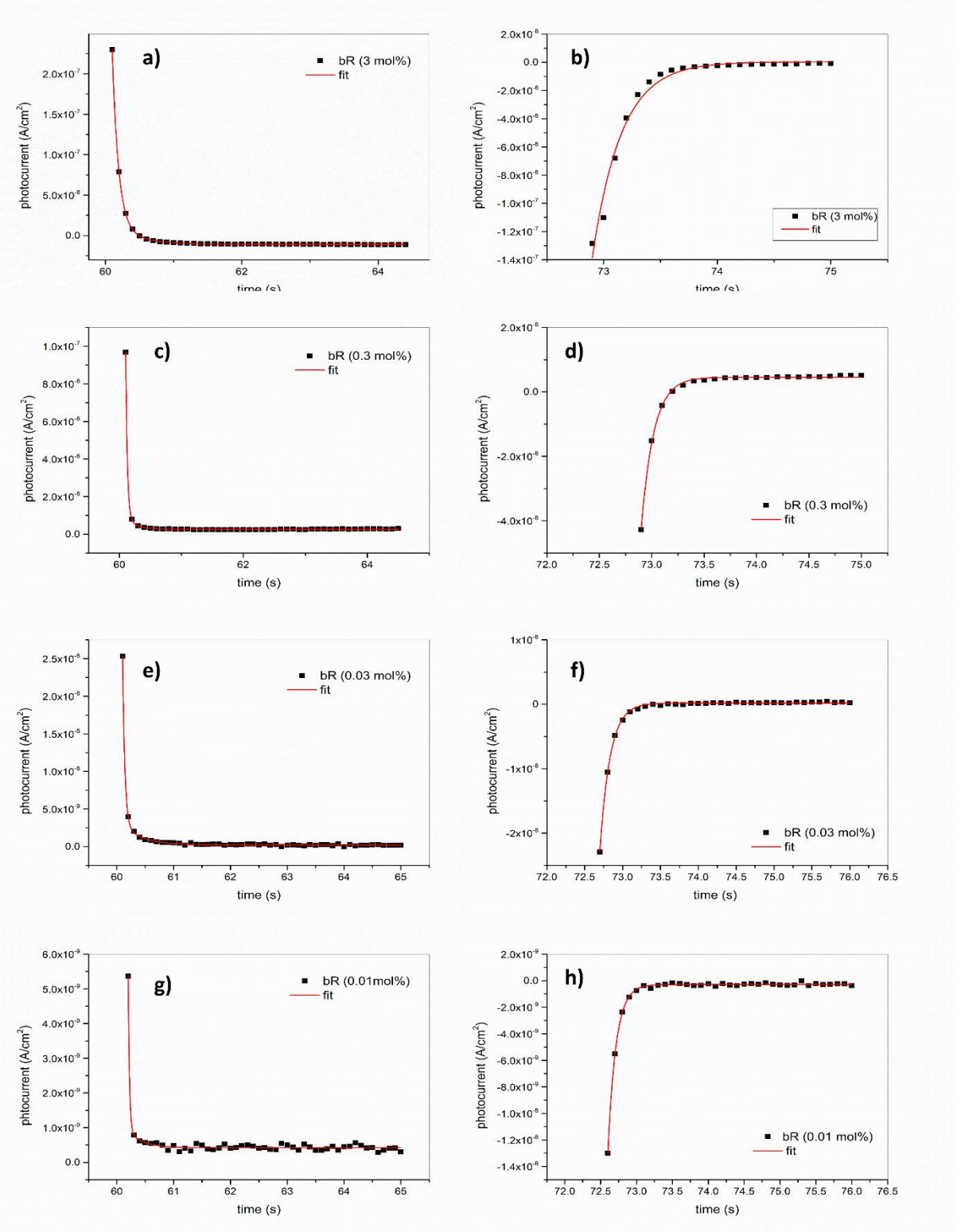
a)
bR (3 mol%)
fit
photocurrent (A/cm²)
time (s)
b)
bR (3 mol%)
fit
photocurrent (A/cm²)
time (s)
c)
bR (0.3 mol%)
fit
photocurrent (A/cm²)
time (s)
d)
bR (0.3 mol%)
fit
photocurrent (A/cm²)
time (s)
e)
bR (0.03 mol%)
fit
photocurrent (A/cm²)
time (s)
f)
bR (0.03 mol%)
fit
photocurrent (A/cm²)
time (s)
g)
bR (0.01mol%)
fit
phtocurrent (A/cm²)
time (s)
h)
bR (0.01 mol%)
fit
photocurrent (A/cm²)
time (s)

Figure S7. Fitted photocurrent decays of bR-MSLBs. (a) and (b), (c) and (d), (e) and (f), (g) and (h) show the fitted decays of activation and deactivation of bR-MSLBs containing 3 mol%, 0.3 mol%, 0.03 mol% and 0.01 mol% respectively.

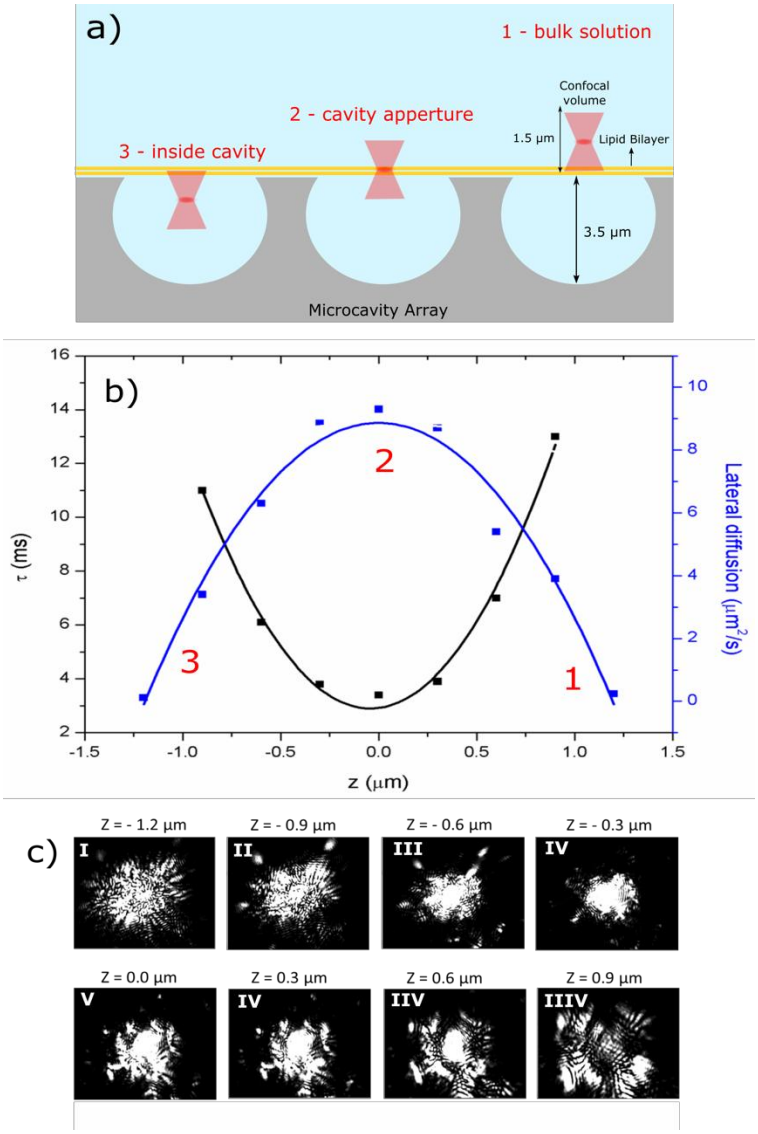

Figure S8. Z-scan obtained for Microcavity Supported Lipid Bilayers at a single cavity. a) Schematic representation of the position of the confocal volume within the substrate. b) Indicates the lateral diffusion of labelled DOPE-ATTO655 within the focal plan of the sample. c) Actual image obtained from the focal spot using a CCD camera.

Membrane impermeable probe pyranine was introduced in the pores of the array before assembly of the bilayer presonicating the microcavity arrays in 1 μM pyranine solution. After, we prepared a lipid bilayer using the method here, by LB followed by proteoliposomes fusion. The substrate was imaged using a confocal microscope (Leica TCS SP8, Ex: 405 nm, detection window 440 - 470nm). As shown in figure S9, we observed that after the bilayer preparation, the dye remain encapsulated within the microcavities, which indicate the bilayer is both suspended across the pore aperture and forms an effective impermeable seal, this persists in this way for several hours up to days

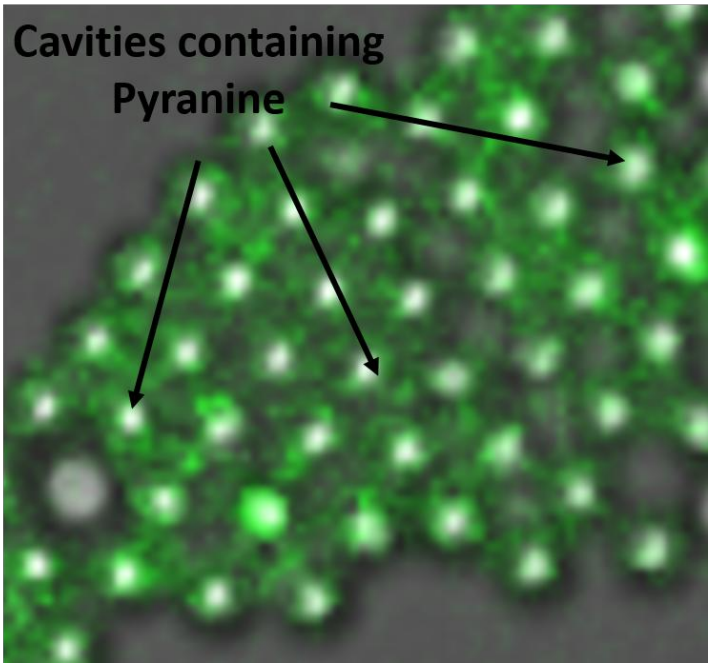

Figure S9. Membrane Leakage test using membrane impermeable probe pyranine. The pryanine is introduced by sonication in solution into the microcavities by prior to monolayer transfer and proteoliposomes fusion. We observed that once the bilayer is in place the pyranine was retained within the cavity with no loss of emission intensity over the window of our experiments confirming the bilayer was spanning and its integrity maintained during our experimental windows.

References

(1) Hughes, L. D.; Rawle, R. J.; Boxer, S. G. Choose Your Label Wisely: Water-Soluble Fluorophores Often Interact with Lipid Bilayers. *PLoS One* 2014, *9* (2).
(2) London, E.; Khorana, H. G. Denaturation and Renaturation of Bacteriorhodopsin in Detergents and Lipid-Detergent Mixtures. *J. Biol. Chem.* 1982, *257* (12), 7003–7011.
(3) Antosiewicz, J. M.; Shugar, D. UV–Vis Spectroscopy of Tyrosine Side-Groups in Studies of Protein Structure. Part 2: Selected Applications. *Biophys Rev* 2016, *8* (2), 163–177.
(4) Geertsma, E. R.; Nik Mahmood, N. A. B.; Schuurman-Wolters, G. K.; Poolman, B. Membrane Reconstitution of ABC Transporters and Assays of Translocator Function. *Nature Protocols* 2008, *3* (2), 256–266.
(5) Sarangi, N. K.; Stalcup, A.; Keyes, T. E. The Impact of Membrane Composition and Co-Drug Synergistic Effects on Vancomycin Association with Model Membranes from Electrochemical Impedance Spectroscopy. *ChemElectroChem* 2020, *7* (22), 4507–4507.
(6) Basit, H.; Van der Heyden, A.; Gondran, C.; Nysten, B.; Dumy, P.; Labbé, P. Tethered Bilayer Lipid Membranes on Mixed Self-Assembled Monolayers of a Novel Anchoring Thiol: Impact of the Anchoring Thiol Density on Bilayer Formation. *Langmuir* 2011, *27* (23), 14317–14328.

Appendix D

Supporting information associated with Chapter 5.

S1

A typical Surface-Enhanced Resonance Raman Spectroscopy (SE(R)RS) spectrum of a membrane impermeable dye, DRAQ7 (1μM) as measured in PBS solution. Excitation wavelength used is 785nm with a laser power of 5uW at the sample. Spectrum was de-noised with a 3-point moving-points averaging.

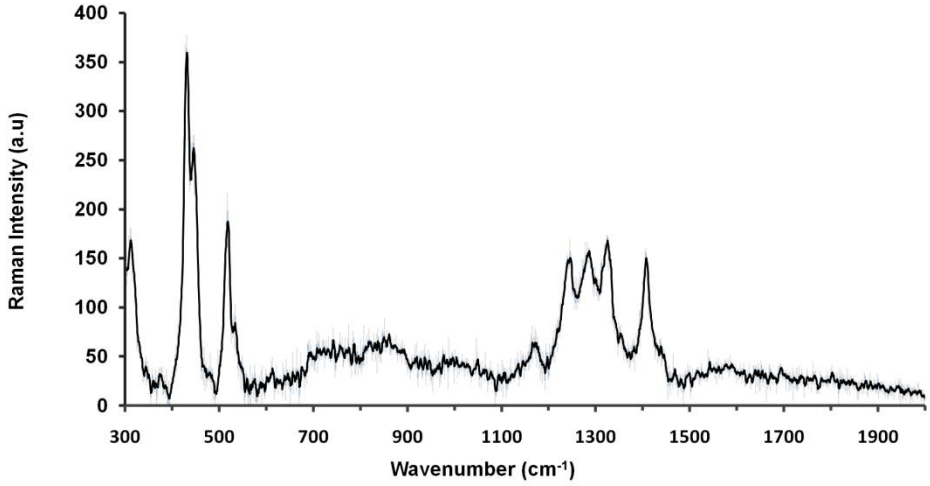

Fig. S1

S2

To confirm the membrane remained intact throughout the OCR experiments, 'leak test' was performed at t=120min post lipoplex administration. Briefly, at the end of each OCR experiment, about 60µl of DRAQ7 (1µM) was introduced into the microfluidic bearing the MSLB and incubated for about 1min. Raman measurements were then measured immediately at 785nm (5µW) (green curves in Fig. S2a and S2b) to verify the absence of DRAQ7 SE(R)RS signals from within the cavities as one would expect for a membrane impermeable dye. The MSLB was then irradiated further for 2min but with a 10× increased laser power to induce localized plasmonic heating at the laser spot that disrupt the membrane. Following this, the laser power was returned to 5µW, before a second spectrum was acquired (see schematic show in Fig.S2a). Fig. S2b and S2c show the 'leak test' results corresponding to Cy5-ssDNA-DOTAP and Cy5-ssDNA-DOTAP/DOPE lipoplexes, respectively. As can be seen, DRAQ7 spectra were only detected after the membrane has been disrupted.

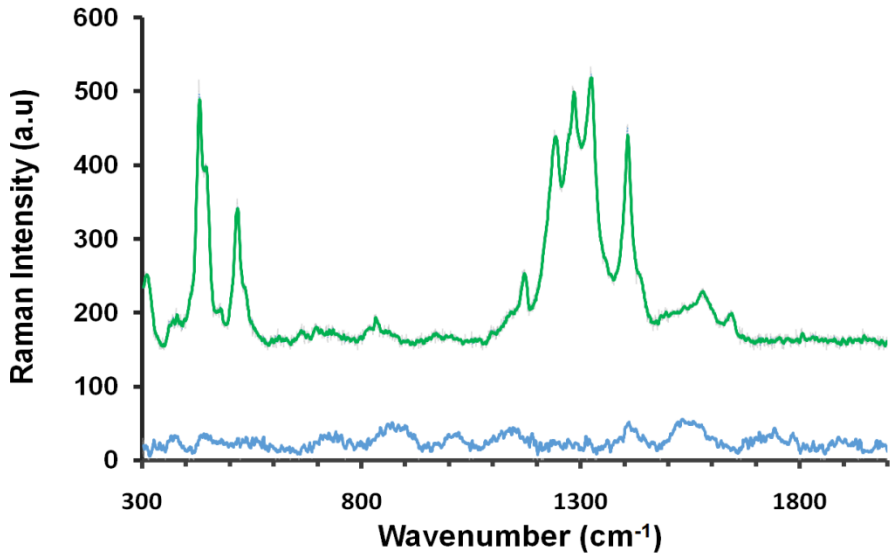

Fig. S2a

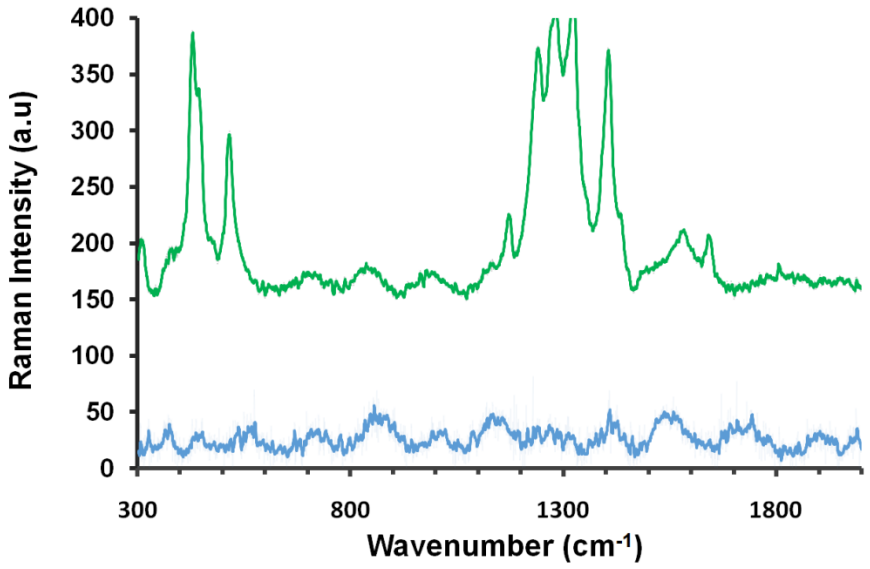

Fig. S2b

S3

To verify that Cy5-SE(R)RS spectrum was detectable only when Cy5-ssDNA was completely released or dislodged from the lipoplex, an array of Au 750nm cavities was incubated with 60µl Cy5-ssDNA loaded lipoplex solution (from the stock prepared as described in the Methods section and with no dilution) for about 3min before SE(R)RS measurements were performed on the array at 633nm (4.5µW). The same experiment was repeated, but with 60µl solution containing Cy5-ssDNA loaded lipoplex mixed with 1mM Trix-X, which lysed the lipoplex. Fig. 3a and 3b show the Cy5-SE(R)RS spectra for Cy5-ssDNA-DOTAP and Cy5-ssDNA-DOTA/DOPE lipoplex respectively. Cy5-SE(R)RS spectra agree with previously published results [*Physical Chemistry and Chemical Physics 9, 6016-6020 (2007)*].

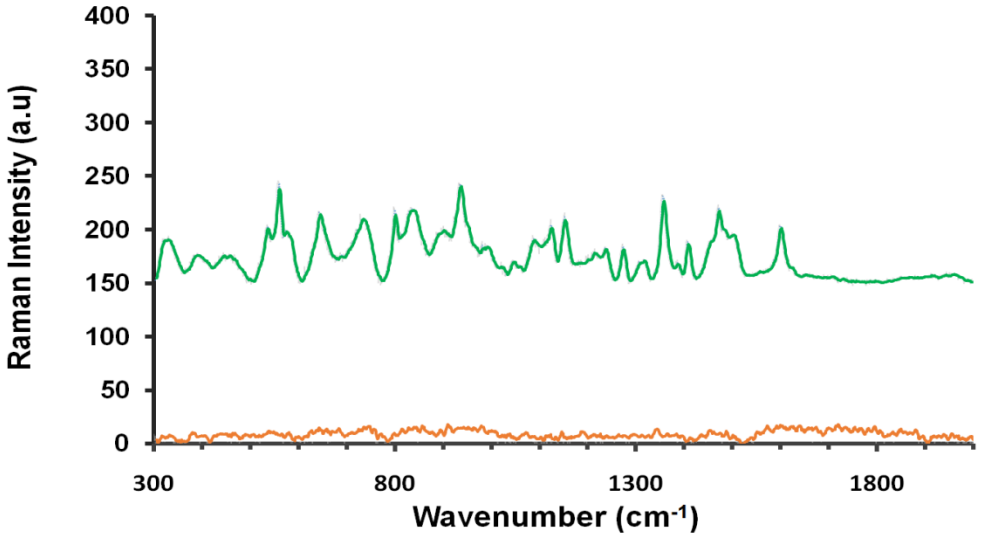

Fig. S3a

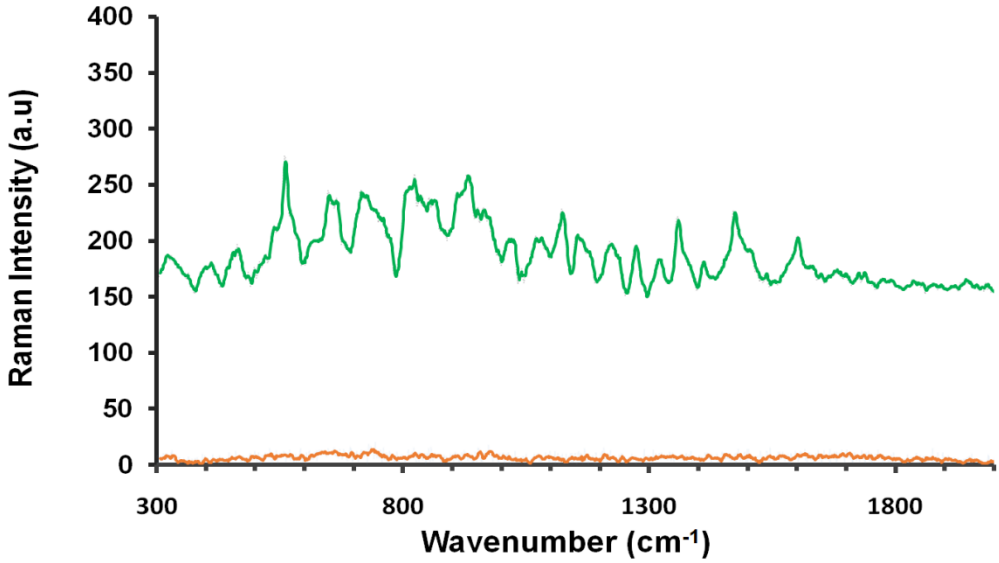

Fig. S3b

S4

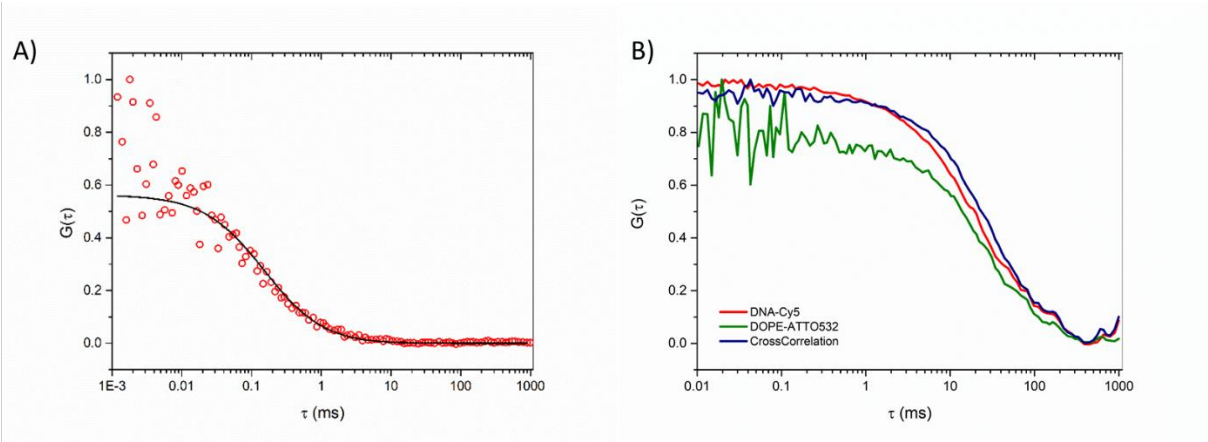

Figure S3 – A) Diffusivity of Cy5-ssDNA in PBS (pH 7.4) solution obtained by FLCS. The lateral diffusion of free ssDNA was determined to be approximately 170 $\mu m^2/s$. B) FLCCS of lipoplex after dialysis.

S5

Using Stokes-Einstein relation (Equation AR1.2) the hydrodynamic radii of ssDNA is therefore estimated to be approximately 4.5 nm.

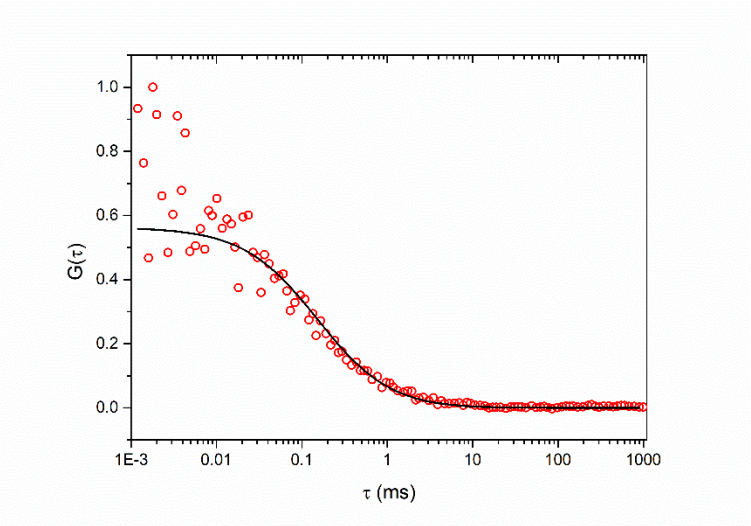

Fig. S5 – Diffusivity of Cy5-ssDNA in PBS (pH 7.4) solution obtained by FLCS. The lateral diffusion of free ssDNA was determined to be approximately 170 $\mu m^2/s$.